DEPARTMENT OF CIVIL ENGINEERING
UNIVERSITY OF STRATHCLYDE
GLASGOW

THE NUMERICAL SIMULATION OF TIDE AND STORM SURGE PROPAGATION IN TWO-DIMENSIONAL SPACE USING THE METHOD OF CHARACTERISTICS

THESIS SUBMITTED IN FULFILMENT OF THE REQUIREMENTS FOR THE DEGREE OF DOCTOR OF PHILOSOPHY

ALAN STEWART DONALD

1981

DEPARTMENT OF CIVIL ENGINEERING
UNIVERSITY OF STRATHCLYDE
GLASGOW

THE NUMERICAL SIMULATION OF TIDE AND STORM SURGE PROPAGATION IN TWO-DIMENSIONAL SPACE USING THE METHOD OF CHARACTERISTICS

THESIS SUBMITTED IN FULFILMENT OF THE REQUIREMENTS FOR THE DEGREE OF DOCTOR OF PHILOSOPHY

ALAN STEWART DONALD

1981

ABSTRACT

The non-linear hyperbolic partial-differential equations governing long-wave propagation in two spatial dimensions are postulated. Through the method of characteristics, specific conditions are developed for integrating the long-wave equations. By introducing finite difference approximations to the characteristic conditions, an explicit numerical scheme is developed as an alternative to more standard finite difference techniques. The modifications required at the open and closed boundary points are of particular importance and lead to a 45° characteristic numerical scheme.

A practical assessment of stability and consistency criteria associated with the numerical scheme is shown to be important for the successful simulation of free and forced tidal oscillations. Tests with motion prescribed by analytical solutions verify the accuracy of the integration procedure and lead to the correct form of interpolation coefficients. A method of subdivisions is developed for improving the simulation of free wave oscillation in a closed basin of trapezoidal profile. Analytical solutions for steady and unsteady wind surges are used to examine the effect of introducing wind stress terms into the numerical scheme.

A practical evaluation of the scheme is accomplished by simulating tidal propagation in the Clyde sea area. Tidal motion in this region is highlighted by the existence of an amphidromic point. Data for the model, provided by a tidal survey, confirm certain values of range and phase given in the Tide Tables (1979).

Two separate surge events are simulated in the Clyde sea area. The relative size of each surge component and the interaction between tide and surge are established. The forms of the surges and the meteorological conditions required for their propagation into the Clyde sea area are also assessed. Finally, a west coast shelf model is developed to overcome the problem of specifying the external surge as a boundary condition.

ACKNOWLEDGEMENTS

First and foremost, I am indebted to Dr J.M. Townson, Department of Civil Engineering for his supervision whilst carrying out this investigation. Dr Townson's guidance throughout the research and his constructive criticism of the preparation of this thesis are highly appreciated. My thanks also, to Dr P.H. Milne for initially bringing to my attention the problem of surge research in the Firth of Clyde and for supplying surge records.

The financial support of the Science Research Council, who founded this research and my M.Sc study, is most appreciated.

I am grateful to the University of Strathclyde for the use of computer facilities. My thanks are also due to the members of the Computer Advisory Service for their recommendations concerning the computational aspects.

I wish to thank everybody else who assisted in various ways towards the completion of this research, particularly Miss Marion Cochran for typing the thesis. Finally any credit must, in part be given to Lesley for her continued encouragement and unselfish support and whom, I cannot thank enough.

INDEX

NOTATION

a	channel length.
A	wave amplitude.
B	channel breadth.
c	long wave celerity.
c_{max}	maximum wave celerity calculated from $(g.H_{max})^{\frac{1}{2}}$.
$\bar{c}$	average celerity of a free wave travelling across the shelf.
C	Chezy resistance coefficient.
$\frac{d}{d}$	total or material derivative.
$\bar{d}$	standard (mean) deviation.
DS, DT	space and time increments used in the numerical model.
e	dynamic coefficient of eddy viscosity.
f	dimensionless wind stress (positive towards shore).
F_x, F_y	x,y components of the external forces presented in dimensionless form (see equation (2.38)).
F	fetch length.
g	gravitational acceleration.
H	equilibrium water depth.
H_o, H_1	equilibrium water depth at the head and mouth of a channel, also the equilibrium water depth at the shore and edge of the shelf model.
$\bar{H}$	equilibrium water depth at the mouth of a channel.
i	gradient of total energy line.
I,J	coordinate system for a mesh of grid points in 'x,y' space.
J	Bessel function of the first kind.
k	wave number , $2\pi/L$
k	wind stress coefficient used in conjunction with air density.
K	wind stress coefficient used in conjunction with water density.
L	wavelength.
m	average bed slope of Scottish West coast continental shelf.
m,n	m number of subdivisions up to a maximum number n, also the number of nodes along the x,y axes defining a particular mode of seiche.

M,N	number of grid points along the x,y axes of a channel or sea area.
p	pressure.
p_a	atmospheric pressure.
PE	semi-diurnal tidal period.
Q	interpolated variable.
r	correction factor (ratio of the exact steady state solution to Reid's approximate steady state solution).
S	displacement of free surface from equilibrium level as a result of an applied wind stress (wind surge).
S_c	computed value of S.
S_{mc}	maximum computed value of S.
t	independent time variable.
t'	t/T, dimensionless time variable.
t'_e	relative time of passage of end of fetch at shore.
t'_m	relative time of occurrence of maximum surge level at shore.
t'_w	relative time of maximum shoreward wind speed at shore.
T	waveperiod.
T_f	travel time for a free, long wave to cross the shelf.
u,v,w	x,y,z components of fluid velocity.
U,V	x,y components of mean, horizontal fluid velocity.
V_w	shoreward velocity of the storm.
W	surface wind speed at about ten metres above sea level.
W_m	maximum surface wind speed.
x,y	independent variables in horizontal plane.
x_o, y_o	x,y coordinates of grid point in question.
$x_1, x_2, ..$	x coordinates of characteristic points.
$y_1, y_2, ..$	y coordinates of characteristic points.
Y	Neumann function (Bessel function of the second kind).
Y	Weber function (Bessel function of the second kind).
z	independent variable in the vertical plane.
Z	total depth $(H+\eta)$.
Z_o	total depth at a grid point using linearised 45^o characteristics.

$\mathcal{Z}$	dynamic response factor (dimensionless water level variable).
$\mathcal{Z}_o$	Reid's value of $\mathcal{Z}$ at shore at time t'.
$\mathcal{Z}_m$	Reid's maximum value of $\mathcal{Z}_o$.
$\mathcal{Z}_{mc}$	computed maximum value of $\mathcal{Z}$ at shore.
$\mathcal{Z}_r$	Reid's value of $\mathcal{Z}_m$ adjusted by correction factor r.
β	wind direction measured clockwise from true north.
δ	Courant number $c.\Delta t/\Delta s$
$\delta x, \delta y$	x,y components of an infinitesimal space increment.
δt	infinitesimal time increment.
$\Delta s, \Delta t$	discrete values of space and time increment.
ϵ	free surface displacement from equilibrium level.
η	harmonic free surface displacement from equilibrium level.
$\bar{\eta}$	harmonic displacement at mouth of channel.
ϑ	angle at the vertex of the conoid of a characteristic projected onto a constant time plane measured anti-clockwise from the positive x-axis.
λ	root of characteristic equation.
ξ	Horizontal displacement of the free surface.
π	3.1415926.
ρ	fluid density.
σ	angular frequency of harmonic motion.
τ	shear stress (tangential force per unit area).
τ_{xb}, τ_{yb}	x,y components of bottom frictional stress.
τ_{xs}, τ_{ys}	x,y components of surface wind stress.
$\varkappa$	ratio of wavelength to channel length, L/a.
ω	angular velocity of the earth.
Ω	earth's rotation reduced by latitude.
$\frac{\partial}{\partial}$	partial derivative.
$\|\|$	modulus of a variable, also the determinant of a matrix.

Any quantity at the left hand side of a characteristic equation represents the value at $t = t + \Delta t$.

INTRODUCTION

With the advance of technological developments over the years, the impact of civil constructions on the immediate environment has become greater. Consequently, if these constructions have adverse effects, then usually it is impractical to attempt suitable alterations. The credibility of new proposals is therefore strongly dependent on being able to determine their effects with greater advance precision than was previously required. An important part of the design process may be the assessment of environmental impact using numerical models as a basis. In this context the numerical model can only provide important information if a satisfactory prior verification of the model's accuracy has been established.

Within the framework of hydraulic engineering, the construction of the Thames Barrier as a storm surge defence exemplifies the interaction of large projects. The development of numerical models as a research tool, such as that used by Rossiter and Lennon (1965) was important in determining a favourable location for the Barrier. To a large extent the underlying reasons for constructing the Thames Barrier arise from the increased attention given to the measurement and calculation of tidal movements in and around the British Isles. In fact most hydraulic engineering problems in maritime waters will require an assessment of the basic tidal motion in the surrounding waters. By considering the tidal motion as governed by the basic hydrodynamic equations, the foundation is laid for a more detailed investigation of any other maritime problems. In addition to determining the basic dynamics of tidal motion within the system concerned, an inclusion of the subsidiary natural peturbations and configuration effects which interact with the basic tide may have to be considered if they are not trivial. It may also be necessary to consider the interactive effect of the proposed construction on the basic tide if this is thought to be significant. These steps may be regarded as sufficient grounds for developing the numerical model. In seeking a numerical solution to the 'long wave' equations for tidal motion through repeated tests which are related to specific numerical aspects of the model, such as calibration the credibility of the model can be established. Once obtained, the numerical model can be applied to other problems in hydraulic

engineering. Therefore the basic hypothesis is that if the model reproduces the features of the prototype, changes in the model should predict changes to be made in the prototype providing these changes are not too drastic. This follows the philosophy of Vernon Harcourt (1889) on physical estuary modelling.

The present analysis is concerned mainly with the fundamental determination of one of the problems in hydraulic research. This is the means by which a storm surge is propagated and its interaction with the tidal regime. The study area namely the Firth of Clyde has in the past been subject to severe storm surges and yet no apparent detailed investigation of the susceptibility of the area to major storm surges appears to have been conducted. The simulation of such surge events in this area has most certainly not been attempted with the resolution undertaken in this research. Previous research concerning the British Isles has instead been focussed on the North Sea following the disasterous flood of 1953 which has been detailed by Rossiter (1954).

The most serious hazard produced by meteorological conditions of storm intensity in coastal low lands is the flooding of coastal regions by sea water through the action of a storm surge. Any increased understanding of this phenomena should contribute to the implementation of necessary coastal protection to safeguard life and property. The ultimate objective of any surge research should be to make predictions with the accuracy required for advanced warning time needed for effective disaster protection. Some protective actions cost very little relative to their protection value. For example it may be possible to protect some valuable but exposed property by providing emergency water tight bulkheads that can be installed quickly when required. In a case where the safeguarding of human life is concerned, any evacuation scheme or breakwater construction would be fully justified.

The general system of long wave equations that represent storm surges has been treated numerically with success for the past twenty-five years. In various modes these systems may model one, two or three spatial dimensions but are usually stated in terms of vertically integrated differential equations and extend in complexity to include the effect of the earth's rotation and field accelerations. These equations also describe the majority of hydraulic problems when presented

in simple or more complex form and comprise to form the basis for a numerical model. The obvious attraction of applying such a model to a specific hydraulic problem is that it is able to provide offshore information. This feature is particularly important if the situation in the offshore area is undetermined. Alternatively, such deficiencies may be overcome by employing a physical model and the use of a numerical model in the present research is not intended to undermine the physical model. Instead the numerical model should be seen not merely as a replacement of the physical model but rather as a complementary means of modelling and as a development into some areas inaccessible to physical modelling. Nevertheless the physical model is still a valuable engineering tool which in the hands of a skilled operator will continue to make substantial contributions to the solution of complex hydraulic problems. However for many applications of modelling, especially those involving wind stresses, salinity variations, effects of the Coriolis acceleration and such influences, the physical model is not a feasible approach and the mathematical model is therefore used.

Attempts have been made with promising results to develop a long wave numerical model based on the 'x-t' method of characteristics in the Department of Civil Engineering, University of Strathclyde. This method, in comparison to other numerical schemes has the advantage that computations can be performed without the use of a staggered grid such that elevation and velocities are calculated at the same grid points. Townson (1974) has extended its application to 'x-y-t' space for uniformly variable depth configurations and at a later date, Matsoukis (1980) succeeded in making the scheme operational for an irregular sea bottom. In establishing that the numerical scheme correctly integrated the partial differential equations, Matsoukis also showed that a linear interpolation scheme was most compatible with the characteristic equations. It was at a later stage that Matsoukis published his results and so to some extent his research and the present analysis have similar objectives. The area of overlap is the verification of the accuracy of the numerical scheme within which the present research is more concerned with the development of the boundary conditions. In applying the numerical scheme to simulate tidal motion in 'x-t' dimensions using simple channels in 'x-y-t' space,

some important conclusions were drawn concerning the correct form of boundary interpolation. These simulations have proved useful as a means of refining the numerical scheme. For this reason, the analytical investigations are presented as an integral part of the present research.

Ensuring that as far as possible, any numerical discrepancies have been eliminated and that the limitations of the numerical scheme have been identified is vitally important in establishing the accuracy of the model. Otherwise, as a result, the wrong conclusions would be made regarding the nature of the tide and surge processes. With this in mind, the investigation of the numerical aspects of the method of characteristics has somewhat dominated this research in relation to an examination of the physical features of tides and surges in the Firth of Clyde. Such considerations are in keeping with Abbot's opinion (1976) regarding the need for further investigation into the modelling process. It is this theme in addition to the study of the natural tide and surge processes that have determined the direction and formed the content of the present research.

CHAPTER 1

THE BASIC, PARTIAL - DIFFERENTIAL EQUATIONS FOR LONG - PERIOD GRAVITY WAVES

1.1 INTRODUCTION

This chapter reviews the classical derivation of the partial differential equations for the non-steady motion of long waves as detailed by Lamb (1932), Stoker (1957), Dronkers (1964) and many others. Such wave motion forms the basis of tidal movements and are produced by gravitational forces. In comparison with these forces, the effects associated with the viscous nature of the fluid are of secondary importance except in the immediate vicinity of solid boundaries. Consequently, the equations describing tidal propagation are derived from the Euler equations of ideal fluid flow rather than from the more general Navier-Stokes equations. However the effects of viscosity are introduced into the equations of motion, and special attention is given to the engineering practice of using empirical values. The method of deriving the 'long wave' equations is based upon the vertical integration of the equation of motion and the continuity equation for an incompressible fluid in Eulerian co-ordinates.

1.2 BASIC EQUATIONS

The basis of this research is the fluid-flow equations representing velocities and pressures relative to a fixed co-ordinate system. These equations are therefore in the Eulerian form. The Cartesian axes x and y are taken counterclockwise in a horizontal plane of the undisturbed water surface, with the z-axis vertically upward. The components of velocity are u, v and ω which are parallel to the co-ordinate axis at the point (x,y,z). For nonviscous flow the dynamic equations may be written

$$\frac{\partial u}{\partial t} + u\frac{\partial u}{\partial x} + v\frac{\partial u}{\partial y} + \omega\frac{\partial u}{\partial z} = X - \frac{1}{\rho}\frac{\partial p}{\partial x} \qquad (1.1)$$

$$\frac{\partial v}{\partial t} + u\frac{\partial v}{\partial x} + v\frac{\partial v}{\partial y} + \omega\frac{\partial v}{\partial z} = Y - \frac{1}{\rho}\frac{\partial p}{\partial y} \qquad (1.2)$$

$$\frac{\partial \omega}{\partial t} + u\frac{\partial \omega}{\partial x} + v\frac{\partial \omega}{\partial y} + \omega\frac{\partial \omega}{\partial z} = Z - \frac{1}{\rho}\frac{\partial p}{\partial z} \qquad (1.3)$$

where ρ is the density of the fluid, p is the pressure on an element

and X,Y,Z are the components of the external forces per unit mass. These forces comprise of the forces generated by the rotation of the earth, the tide generating forces and the gravity force in the z-direction.

The left hand side of each of these equations of motion represents the total derivative (defined by the operator $\frac{d}{dt}$) of the component velocity experienced by a particular fluid particle . The total rate of increase of the components of particle acceleration can be attributed to two separate effects

a) A rate of change which is independent of the state of motion of the particle and is defined by the operator $\frac{\partial}{\partial t}$

b) A rate of change which accounts for field gradients in the property of the particle at a given time. The effect is termed 'convective' and defined by the operator $u\frac{\partial}{\partial x} + v\frac{\partial}{\partial y} + \omega\frac{\partial}{\partial z}$

To complete the description of ideal fluid flow, the continuity equation for an incompressible fluid takes the following form

$$\frac{\partial u}{\partial x} + \frac{\partial v}{\partial y} + \frac{\partial \omega}{\partial z} = 0 \qquad (1.4)$$

1.3 EQUATIONS FOR LONG-PERIOD WAVE MOTION

The cartesian co-ordinate system is taken in the horizontal plane of the undisturbed water surface. The distance between this reference plane and the bottom is specified by H and the distance between this reference plane and the water surface at a specific time is given by η

Long wave motion in general implies a wave motion in a depth which is small compared with the wavelength ($H/L < 1/20$) and to some extent the wave amplitude is small compared to the length ($\eta/L < 1/100$). Forced tidal response, surge propagation and seiche action may all be considered as long wave phenomena. For such waves, the theoretical derivation neglects the vertical acceleration of the fluid particles since these accelerations are very small with respect to the acceleration of the gravity field. Also, the velocities of the water particles in the z-direction may be neglected in dealing with long waves. Thus, all terms containing ω in equations (1.1), (1.2) and (1.3) are omitted.

Since the effects of the vertical acceleration and velocity

may be neglected, equation (1.3) may be written as

$$\frac{1}{\rho} \cdot \frac{\partial p}{\partial z} = Z \tag{1.5}$$

In the vertical direction the external forces Z are the gravity force, the component of the forces induced by the earth's rotation and the tide generating forces. The latter two are very small compared to gravity and so can be neglected in the analysis giving $Z = -g$. It is assumed that the density is uniform and consequently the pressure is assumed to be hydrostatic and a linear function of depth, as follows

$$p(z) = \rho g(\eta - z) + p_a \tag{1.6}$$

where p_a is the atmospheric pressure. In tidal computations, atmospheric pressure is usually assumed to remain constant over the problem area however pressure variations are important in the generation of storm surges. The derivatives of pressure in the horizontal directions now become a function of water level and atmospheric pressure,

$$\frac{\partial p}{\partial x} = \rho \cdot g \cdot \frac{\partial \eta}{\partial x} + \frac{\partial p_a}{\partial x} \tag{1.7}$$

$$\frac{\partial p}{\partial y} = \rho \cdot g \cdot \frac{\partial \eta}{\partial y} + \frac{\partial p_a}{\partial y} \tag{1.8}$$

It has been shown by Hansen (1956) that the vertically averaged velocity components in a horizontal plane of the fluid can be defined according by

$$U = \frac{1}{(H+\eta)} \int_{-H}^{\eta} u \cdot dz \tag{1.9}$$

$$V = \frac{1}{(H+\eta)} \int_{-H}^{\eta} v \cdot dz \tag{1.10}$$

As mentioned already in section 1.2, the horizontal components of the external forces per unit mass namely X and Y include the effects of the earth's rotation and the tide generating forces. Numerical computations and estimates based upon theoretical considerations have shown that the tide generating forces can generally be omitted from actual computations. Consequently the only external force requiring consideration is that of the earth's rotation. The Coriolis acceleration components, and the associated inertia forces are induced by the

rotation of the earth with angular velocity ω and therefore depend on the latitude ψ of the body of fluid. With the co-ordinate system as previously defined, the x-axis can be considered eastwards and the y-axis northwards. The inertia forces in the positive x and y directions are $\rho.\Omega.V$ and $-\rho.\Omega.u$ respectively where $\Omega = 2.\omega.\sin\psi$. When these forces are integrated with respect to z and divided by the total depth $(H+\eta)$, the final form can be equated to the external forces as follows

$$X = 2.V.\omega.\sin\psi \qquad (1.11)$$

$$Y = -2.u.\omega.\sin\psi \qquad (1.12)$$

These are the forces on a unit mass of the fluid.

The dynamic equations (1.1) and (1.2) are integrated with respect to z from the bed to the surface of the fluid, and divided by the total depth $(H+\eta)$. By deleting the vertical velocity terms and introducing the equations (1.7) to (1.12), the integrated dynamic equations for a unit mass of fluid become

$$\frac{\partial u}{\partial t} + u\frac{\partial u}{\partial x} + V\frac{\partial u}{\partial y} + g\frac{\partial \eta}{\partial x} + \frac{1}{\rho}\frac{\partial p_a}{\partial x} - \Omega V = 0 \qquad (1.13)$$

$$\frac{\partial V}{\partial t} + u\frac{\partial V}{\partial x} + V\frac{\partial V}{\partial y} + g\frac{\partial \eta}{\partial y} + \frac{1}{\rho}\frac{\partial p_a}{\partial y} + \Omega u = 0 \qquad (1.14)$$

Up to this point in the derivation, an inviscid fluid has been considered. However expressions for the viscous shear-stress representing effects of wind at the surface and friction at the bottom can be obtained by examining the Navier - Stokes equations for turbulent flow. Such expressions can then be introduced into equations (1.13) and (1.14).

The inclusion of horizontal friction forces strictly implies consideration of viscous turbulent flow and the associated concepts of 'momentum exchange' and 'eddy viscosity'. The friction forces in the negative x and y directions can be expressed in terms of the local fluid velocity components u and v. These forces can be integrated throughout the depth and divided by the total depth $(H+\eta)$ to produce the following terms

$$e_1\left[\frac{\partial^2 u}{\partial x^2} + \frac{\partial^2 u}{\partial y^2}\right] + \frac{e_2}{H+\eta}\left[\frac{\partial u}{\partial z}\right]_{-H}^{\eta} \qquad (1.15)$$

$$e_1 \left[\frac{\partial^2 V}{\partial x^2} + \frac{\partial^2 V}{\partial y^2} \right] + \frac{e_2}{H+\eta} \left[\frac{\partial v}{\partial z} \right]_{-H}^{\eta} \qquad (1.16)$$

The velocities U and V in these equations are depth averaged and the constants e_1 and e_2 are the 'dynamic coefficients of eddy viscosity' in the horizontal and vertical planes respectively. These coefficients contain the effect of both viscosity and turbulent processes. As a result of the dimensions of the fluid flow, the eddy coefficient in the horizontal plane is usually greater than in the vertical plane. If it is assumed that the shear stresses associated with horizontal momentum transfer are small, then the friction forces remaining are those in the horizontal direction which are caused by vertical velocity gradients. In the integrated form, the horizontal shear stresses τ_x and τ_y in the negative x and y directions are prescribed as

$$\tau_x = e_2 \left[\frac{\partial u}{\partial z} \right]_{-H}^{\eta} \qquad (1.17)$$

$$\tau_y = e_2 \left[\frac{\partial v}{\partial z} \right]_{-H}^{\eta} \qquad (1.18)$$

These expressions represent the difference in shear stress between surface and bed which are undoubtedly affected by the presence of wind stresses on the water surface.

Experimental evidence indicates that shear stress at the sea bed may be expressed in terms of the well known Chezy friction coefficient C as is used in open channel flow. However it is emphasised that this approach must be regarded as a very limited means of fully describing the process of tidal dissipation even though it is used in the present analysis.

The equilibrium between gravitational and resistance forces can be expressed as

$$\tau_{rb} = \rho \cdot g \cdot (H+\eta) \cdot i \qquad (1.19)$$

where τ_{rb} is the resultant shear stress proportional to the resultant depth average velocity $(U^2+V^2)^{\frac{1}{2}}$ and i is the slope of the water surface. The resultant velocity may be deduced from De Chezy's empirical relationship namely

$$\sqrt{u^2+v^2} = C.\sqrt{i.(H+\eta)} \tag{1.20}$$

since $(H+\eta)$ corresponds to the hydraulic mean depth in a very wide channel. From the previous two equations, it follows that the resultant frictional stress at the sea bed is given by

$$\tau_{rb} = \rho.g\left[\frac{u^2+v^2}{C^2}\right] \tag{1.21}$$

Also, the components of the resultant frictional stress which oppose the fluid flow are expressed as follows

$$\tau_{xb} = \rho.g.u\frac{\sqrt{u^2+v^2}}{C^2} \tag{1.22}$$

$$\tau_{yb} = \rho.g.v\frac{\sqrt{u^2+v^2}}{C^2} \tag{1.23}$$

The frictional resistance factor C, which is used to establish these relationships between the squared velocity and the bottom stress, can be found only by observation. This coefficient depends on the roughness of the bottom, the bottom material, and the depth.

The horizontal shear force at the free surface of the fluid as a result of wind stress may be determined from an empirical approach similar to that for investigating bottom stress. The wind stress is a forcing function in the system of equations and is related to the square of the fluid flow as is bottom stress. However for wind stress the medium of flow is air not water. The components of wind stress are expressed as

$$\tau_{xs} = k.\rho_a.W.W\cos\beta \tag{1.24}$$

$$\tau_{ys} = k.\rho_a.W.W\sin\beta \tag{1.25}$$

where k is the wind stress coefficient, ρ_a is the density of air and W is the wind speed above the water surface.

Introducing the expressions for bottom stress and wind stress into the two-dimensional dynamic equations ((1.13) and (1.14)) produces the following

$$\frac{\partial u}{\partial t} + u\frac{\partial u}{\partial x} + v\frac{\partial u}{\partial y} + g\frac{\partial \eta}{\partial x} + \frac{1}{\rho}\frac{\partial p_a}{\partial x} - \Omega v = \frac{(\tau_{xs}-\tau_{xb})}{\rho(H+\eta)} \tag{1.26}$$

$$\frac{\partial v}{\partial t} + u\frac{\partial v}{\partial x} + v\frac{\partial v}{\partial y} + g\frac{\partial \eta}{\partial y} + \frac{1}{\rho}\frac{\partial p_a}{\partial y} + \Omega u = \frac{(\tau_{ys}-\tau_{yb})}{\rho(H+\eta)} \tag{1.27}$$

These equations include the forcing functions of wind stress and barometric pressure in the x and y directions respectively.

In a similar manner, the continuity equation can be integrated over the vertical and so equation (1.4) may be expressed as

$$\int_{-H}^{\eta} \left(\frac{\partial u}{\partial x} + \frac{\partial v}{\partial y} \right) dz = 0 \qquad (1.28)$$

As a result of the condition $\omega = 0$, a particule of fluid must remain on the same horizontal plane throughout its motion. Accordingly the boundary condition for the free surface is obtained from the 'chain rule'

$$\omega(\eta) = \frac{\partial \eta}{\partial t} + u \cdot \frac{\partial \eta}{\partial x} + v \cdot \frac{\partial \eta}{\partial y} \qquad (1.29)$$

Similarly at the sea bed

$$\omega(-H) + u \cdot \frac{\partial H}{\partial x} + v \cdot \frac{\partial H}{\partial y} = 0 \qquad (1.30)$$

Now equation (1.28) can be written as

$$\int_{-H}^{\eta} \frac{\partial u}{\partial x} \cdot dz + \int_{-H}^{\eta} \frac{\partial v}{\partial y} \cdot dz = 0 \qquad (1.31)$$

where $$\frac{\partial}{\partial x} \int_{-H}^{\eta} u \cdot dz = u \cdot \frac{\partial \eta}{\partial x} + u \cdot \frac{\partial H}{\partial x} + \int_{-H}^{\eta} \frac{\partial u}{\partial x} \cdot dz \qquad (1.32)$$

and $$\frac{\partial}{\partial y} \int_{-H}^{\eta} v \cdot dz = v \cdot \frac{\partial \eta}{\partial y} + v \cdot \frac{\partial H}{\partial y} + \int_{-H}^{\eta} \frac{\partial v}{\partial y} \cdot dz \qquad (1.33)$$

which are obtained from the differential theory governing the product of two variables. By adding equations (1.32) and (1.33) to obtain equation (1.31) and by taking into account the boundary conditions at the free surface and the bottom, the following equation is obtained

$$\frac{\partial}{\partial x} \int_{-H}^{\eta} u \cdot dz + \frac{\partial}{\partial y} \int_{-H}^{\eta} v \cdot dz = - \frac{\partial \eta}{\partial t} \qquad (1.34)$$

Recalling from equations (1.9) and (1.10) the respective definitions $U(H+\eta) = \int_{-H}^{\eta} u \cdot dz$ and $V(H+\eta) = \int_{-H}^{\eta} v \cdot dz$ and substituting these definitions into equation (1.34) produces

$$\frac{\partial}{\partial x} [U(H+\eta)] + \frac{\partial}{\partial y} [V(H+\eta)] + \frac{\partial \eta}{\partial t} = 0 \qquad (1.35)$$

This equation expresses the conservation of mass within an elementary column of fluid.

Equations (1.26), (1.27) and (1.35) together constitute a non-linear hyperbolic system of first order partial differential equations which mathematically define the conditions governing long wave motion in (x-y-t) space. Their solution is obtained when each of the unknowns u, v and η is related to the independent variables x,y,t. The form of the equtions is such that theoretically, a general solution applying to all circumstances does not exist and therefore approximate solutions are determined. In a tidal system the complexity of its movement usually results in a reduction to lower order systems. In this way the analytical solutions in simplified situations and the numerical analysis of more realistic cases have been developed. The analysis of these systems is detailed in chapters 4 and 7 respectively.

The advances in computational facilities and techniques have enabled mathematical solutions of the more complex systems of long wave equations to be found. In obtaining the solution surfaces, the numerical approach is very much dependent on the results from field research which indicates the extent of problems associated with a realistic situation. However given the appropriate empirical coefficients and the initial and boundary conditions, the solution is obtainable once a numerical technique has been perfected. The development of the characteristic conditions as a numerical technique is therefore the subject of the next chapter.

CHAPTER 2
THE METHOD OF CHARACTERISTICS IN (X,Y,T) SPACE

2.1 INTRODUCTION

An exact harmonic solution to the long wave equations cannot be produced from an analysis which takes into consideration all the major processes that operate within a system. More precisely, it is impossible to combine the equations of motion and continuity, which constitute a hyperbolic system, into an elliptic second order partial differential equation representing an analytical expression. When a system consists of an irregular configuration in which shallow water effects and frictional stresses are significant a numerical method is the only means of providing a solution to the hyperbolic equations.

The usual numerical technique involves the transformation of the basic equations into finite difference form to obtain a numerical solution. In achieving this solution the numerical scheme requires an integration process applicable over a series of discrete points which describe the spatial variation of the dependent variables. Generally the values of the dependent variables are computed at points on a rectangular grid in space and time. The principal feature of such a method is that the motion is propagated from given initial conditions and is depicted at successive time increments as it spreads over the problem area. The solution at a point is independent of events in the system at any other times and is formulated solely by conditions prevailing at a particular time in the domain of dependence of that point. Therefore a hyperbolic problem is, in most cases, independent of the initial conditions, a feature closely related to the meaning of hyperbolicity. If the initial values closely represent the final solution then the problem should be accurately modelled from the start. In reality however, these values are only approximate and a period of time must elapse during which it is anticipated, the final solution is approached. This philosophy is discussed by Stoker (1957). If the scheme includes a continuous external harmonic disturbance the numerical scheme should eventually produce a corresponding harmonic solution which is a reasonable indication that at least stability has been maintained. However it is necessary to ensure further that the numerical integration procedure gives a solution which converges to that of the

original differential equations. Convergence is only achieved when the numerical scheme is both consistent and stable; these conditions are discussed in section 2.4.

It should be noted that numerical techniques are not solely limited to producing harmonic solutions. Since the periodicity of the final solution is dependent on whether the boundary conditions are periodic or not; no other requirements concerning periodicity are necessary. Thus methods of the numerical step by step type are particularly suitable for the analysis of surge effects.

The most obvious and the simplest means of integrating the dependent variables over a discrete number of points is to substitute some form of finite difference approximation directly into the basic system of hyperbolic partial differential equations constituting long wave motion. Alternatively, there are some distinct advantages to be gained on applying a finite difference scheme to the characteristic equations rather than the original set of basic equations. The characteristic equations are produced through linear combinations of the original hyperbolic equations and have the property that they involve differentiation in one less direction than the original equations. For example, in one-dimensional unsteady flow, the characteristic equations become ordinary differential equations. In general, a characteristic in n independent variables is a sub-space of $n-1$ dimensions in space at which derivative discontinuities may occur. For equations (1.26), (1.27) and (1.35) the characteristic equations remain partial differential equations with the directions of differentiation contained within surfaces called 'characteristic surfaces'. Solutions to these equations then must also propagate within the characteristic surfaces. The system is hyperbolic and the associated characteristic surfaces represent the boundaries between disturbed and undisturbed regions. The characteristic surfaces can therefore be thought of as wave fronts which delineate the propagation of disturbances through the fluid. These disturbances propagate with time in the x and y directions with speeds determined by the local inclination of these surfaces in x-y-t space. Since partial derivatives of the dependent variables in the direction normal to the characteristic surfaces drop out of the characteristic equations, these allow discontinuities in the gradients of U, V and η across the characteristic surfaces. It is the very existence of derivative

discontinuities across these integral surfaces which classify the problem as being hyperbolic. In contrast, the existence of such discontinuities is imaginary in the elliptic problem which typifies the steady flow of fluid, heat or stress. For example the elliptic equations governing the ocean tides and seiche action in lakes and harbours are derived from the long wave equations through simplifying assumptions. In these problems the physical conditions require that every part of the surface solution depends on all the other parts. This implies that the solution surface and its derivatives are continuous at every point in the problem area and that characteristic surfaces marking any possible discontinuities are non-existent. In the third class of problem, that of parabolic systems, the propagation occurs only in one direction such as in diffusion and heat conduction. In these systems the characteristic paths are coincident.

The method of characteristics essentially involves tracing the propagation of waves. Using this technique, the formation of discontinuities or shock waves may be analysed without any difficulty. Since the derivatives located in the characteristic surfaces are not discontinuous then consequently a finite difference approximation may safely be applied. It should be emphasised that the existence of characteristic surfaces implies only the possibility of discontinuities across the solution surface and not a definite presence of them. Even when discontinuities are not present there are certain attractive features associated with the method of characteristic lines or surfaces. The most important attribute of this method is the analagous processes between the physical system and its characteristic representation. For example the domain of dependence and the region of influence at any point are defined rigorously by the method of characteristics and correspond to the point in the physical prototype.

It is of some importance to note that certain finite difference schemes involving central difference approximations require that the surface elevations and depth mean velocities be computed at alternate points in alternate time planes. (Dronkers and Schonfeld (1955)). This method leads to difficulty in interpreting the results especially at the boundary points. Fortunately with the finite difference scheme required to implement the characteristic conditions, the dependent

variables are computed at the same grid points at the same instants of time. The above methods are explicit since the values of the dependent variables at a certain grid point are calculated without regard to the values at the other grid points at the same time level. Alternatively, implicit schemes are available in which the values of the dependent variables at the one time level are calculated simultaneously from each other. Implicit finite difference schemes are not thought to be as physically analagous as the characteristic scheme and so are not considered any further in the present research.

Referring back to the long wave equations ((1.35), (1.26) and (1.27)), the mean depth of the fluid, H is a function of the space variables only. The analysis is somewhat simplified by introducing the total depth term Z defined as

$$Z = H + \eta \tag{2.1}$$

and the basic equations can be restated as

$$\frac{\partial Z}{\partial t} + u\frac{\partial Z}{\partial x} + v\frac{\partial Z}{\partial y} + Z\frac{\partial u}{\partial x} + Z\frac{\partial v}{\partial y} = 0 \tag{2.2}$$

$$\frac{1}{g}\frac{\partial u}{\partial t} + \frac{u}{g}\frac{\partial u}{\partial x} + \frac{v}{g}\frac{\partial u}{\partial y} + \frac{\partial Z}{\partial x} - \frac{\partial H}{\partial x} = \frac{-1}{\rho g}\frac{\partial p_a}{\partial x} + \frac{\Omega v}{g} + \frac{(\tau_{xs} - \tau_{xb})}{\rho \cdot g \cdot Z} \tag{2.3}$$

$$\frac{1}{g}\frac{\partial v}{\partial t} + \frac{u}{g}\frac{\partial v}{\partial x} + \frac{v}{g}\frac{\partial v}{\partial y} + \frac{\partial Z}{\partial y} - \frac{\partial H}{\partial y} = \frac{-1}{\rho g}\frac{\partial p_a}{\partial y} - \frac{\Omega u}{g} + \frac{(\tau_{ys} - \tau_{yb})}{\rho \cdot g \cdot Z} \tag{2.4}$$

The terms not involving partial differentials of the dependent variables have been placed on the right hand side of the equations and include the external forces and shear stress terms. Equations (1.35), (1.26) and (1.27) can also be written in matrix form as follows

$$I\frac{\partial \Lambda}{\partial t} + A\frac{\partial \Lambda}{\partial x} + B\frac{\partial \Lambda}{\partial y} = G \tag{2.5}$$

in which I is the identity matrix and

$$\Lambda = \begin{bmatrix} Z \\ u \\ v \end{bmatrix} \qquad A = \begin{bmatrix} u & Z & 0 \\ g & u & 0 \\ 0 & 0 & u \end{bmatrix} \qquad B = \begin{bmatrix} v & 0 & Z \\ 0 & v & 0 \\ g & 0 & v \end{bmatrix} \tag{2.6}$$

with

$$G = \begin{bmatrix} 0 \\ g\frac{\partial H}{\partial x} - \frac{1}{\rho}\frac{\partial p_a}{\partial x} + \Omega v + \frac{(\tau_{xs} - \tau_{xb})}{\rho Z} \\ g\frac{\partial H}{\partial y} - \frac{1}{\rho}\frac{\partial p_a}{\partial y} - \Omega u + \frac{(\tau_{ys} - \tau_{yb})}{\rho Z} \end{bmatrix} \tag{2.7}$$

These equations represent the hyperbolic system to a first order of accuracy.

The means of evaluating a system of hyperbolic partial differential equations describing fluid wave motion using the method of characteristics was first introduced by D'Alembert (1747) as a result of an investigation of air currents. Riemann (1860) generalised and expanded the basic concept of this method. Massau (1889) presented an important paper describing a semi-graphical integration method using a further development of characteristics for evaluating a system of wave equations. More recently, Daubert and Graffe (1967) have given a derivation of the method in (x-y-t) space. The analysis presented in the next section is a modified version of that given by Fox (1966) which also has been reviewed by Webster (1968).

2.2 THE CHARACTERISTIC CONDITIONS

The analysis of characteristics is achieved through a transformation of coordinates. If a cartesian coordinate system q-r-s chosen with a local inclination to the x-y-t system such that the coefficients of all partial derivatives with respect to, say, r in the transformed equations are in the same proportion in each equation, then a linear combination of the three equations will eliminate the r derivatives and so reduce the number of independent variables by one. The resulting equation will contain derivatives only in the q and s directions, which will then define locally the characteristic plane, normal to r. Since the derivatives on the characteristic surface are continuous, the derivatives with respect to q and s must be likewise. By eliminating derivatives with respect to r which may be discontinuous, the resulting system of equations may be expressed in finite difference form with complete safety.

In an arbitrarily orientated q-r-s system, equation (2.5) transforms to

$$D \frac{\partial \Delta}{\partial q} + E \frac{\partial \Delta}{\partial r} + F \frac{\partial \Delta}{\partial s} = G \qquad (2.8)$$

in which D, E and F are the transformations of the original coefficient matrices in the new coordinate system. In particular

$$E = \frac{\partial r}{\partial t} \cdot I + \frac{\partial r}{\partial x} \cdot A + \frac{\partial r}{\partial y} \cdot B \qquad (2.9)$$

in which $\partial r/\partial t$, $\partial r/\partial x$ and $\partial r/\partial y$ are the direction cosines of vectors oriented in the r direction. The elements of the matrix E are found from equations (2.6) and (2.9) to be

$$E = \begin{bmatrix} R & z\frac{\partial r}{\partial x} & z\frac{\partial r}{\partial y} \\ g\frac{\partial r}{\partial x} & R & 0 \\ g\frac{\partial r}{\partial y} & 0 & R \end{bmatrix} \qquad (2.10)$$

in which $$R = \frac{\partial r}{\partial t} + u\frac{\partial r}{\partial x} + v\frac{\partial r}{\partial y} \qquad (2.11)$$

For r to be normal to the characteristic surface, the determinant of E must equal zero.

The singularity of E implies that some linear combination of the rows will produce a zero vector. Assuming that there exists a matrix vector H such that $H.E = O$, then multiplying both sides of equation (2.8) produces

$$H.D.\frac{\partial A}{\partial q} + H.F.\frac{\partial A}{\partial s} = H.G \qquad (2.12)$$

In this equation the derivatives of the dependent variables are taken with respect to the q or s coordinate and so the equation in this form constitutes the 'characteristic condition' for the system of basic equations.

The expansion of the determinant of equation (2.10) yields the result

$$R\left\{R^2 - g.z\left[\left(\frac{\partial r}{\partial x}\right)^2 + \left(\frac{\partial r}{\partial y}\right)^2\right]\right\} = O \qquad (2.13)$$

Equation (2.13) can be satisfied either by setting R or the expression in braces equal to zero. The latter case yields the more useful result

$$r^T.J.r = O \qquad (2.14)$$

in which $$J = \begin{bmatrix} 1 & u & v \\ u & u^2 - c^2 & u.v \\ v & u.v & v^2 - c^2 \end{bmatrix} \qquad (2.15)$$

and the variable c is defined as

$$c^2 = g.Z \tag{2.16}$$

The quantity r^T is the transpose of the unit vector in the r direction and takes the form

$$r^T = \begin{bmatrix} \frac{\partial r}{\partial t} & \frac{\partial r}{\partial x} & \frac{\partial r}{\partial y} \end{bmatrix} \tag{2.17}$$

Equation (2.14) applies at every point in the flow field in x-y-t space. It can be regarded as a necessary relationship among the direction cosines of every possible orientation of a normal at a point on the characteristic surface. If a plane defined by t = 1 in some local origin is placed at this point, the intersection of this plane with the family of normals will be a plane curve whose coordinates (x,y) will be related to the direction cosines of the normals by

$$\frac{1}{\frac{\partial r}{\partial t}} = \frac{x}{\frac{\partial r}{\partial x}} = \frac{y}{\frac{\partial r}{\partial y}} \tag{2.18}$$

In view of this expression, equation (2.14) becomes

$$K^T . J . K = 0 \tag{2.19}$$

in which $K^T = [1 \quad x \quad y]$.

Expansion of equation (2.19) yields a second-degree equation in x and y which of necessity represents a conic section. Depending upon the relative values of $(u^2 + v^2)^{\frac{1}{2}}$ and $c = (gZ)^{\frac{1}{2}}$ this can either be an ellipse a parabola or a hyperbola. The family of normals passing through a given point (x,y,t) then comprise of a circular cone in x-y-t space. Lines perpendicular to these normals must be tangent to the characteristic surface there. In order to discern the nature of this characteristic surface, an expression relating the direction cosines of the family of tangent lines is required. The vector $L = J.K$ must be tangent to the characteristic surface since K and J.K are orthogonal. With some algebraic manipulations the following expression is obtained

$$L^T . J^{-1} . L = 0 \tag{2.20}$$

and reveals that the characteristic surfaces at a given point envelope a circular cone, each of whose elements is perpendicular to the cone of normals. The projections of differential elements of this charateristic cone passing through its apex are therefore related by

$$\begin{bmatrix} dt & dx & dy \end{bmatrix} \begin{bmatrix} 1 - \frac{u^2+v^2}{c^2} & \frac{u}{c^2} & \frac{v}{c^2} \\ \frac{u}{c^2} & \frac{-1}{c^2} & 0 \\ \frac{v}{c^2} & 0 & \frac{-1}{c^2} \end{bmatrix} \begin{bmatrix} dt \\ dx \\ dy \end{bmatrix} = 0 \qquad (2.21)$$

in which the square matrix is J^{-1}.

The differential consideration is introduced at this point because in general C, U and V are different in every point of x-y-t space and therefore only in a differential region about a given point is the characteristic surface a cone. If it is desired to extend the surface to finite regions, the inclination of its generators must change as it becomes successively tangent to varying differential cones. Hence in a finite region of x-y-t space the characteristic surfaces form a conoid rather than a cone. Equation (2.21) can also be written as

$$(dx - u.dt)^2 + (dy - v.dt)^2 = c^2 dt^2 \qquad (2.22)$$

The quadratic surface described by equation (2.22) is called a 'characteristic conoid' and its generators are called 'bicharacteristics'. Water waves propagate along bicharacteristics in three-dimensional space in exactly the same way as along characteristic curves in two-dimensions. The component velocities of the wave along the bicharacteristics are expressed in terms of a parametric angle θ, as follows

$$\frac{dx}{dt} = u + c.\cos\theta \qquad (2.23)$$

$$0 \leq \theta \leq 2\pi$$

$$\frac{dy}{dt} = v + c.\sin\theta \qquad (2.24)$$

and satisfy equation (2.22). The angle θ corresponds to the whole circle bearing of the bicharacteristic projected on a constant time plane and measured from the positive x - direction at the vertex of the conoid.

In order to simplify the numerical integration procedure in the present analysis it is assumed that the bicharacteristics can be represented by straight lines with θ constant. The implications of this assumption are discussed in section 2.3. It is sufficient to note at the present that the modified bicharacteristics passing through a point delineate a characeristic cone and not a conoid.

There are actually two families of characteristic surfaces and consequently two sets of normals; one family has been established by satisfying equation (2.19) while the other corresponds to $R = 0$ where $R = \frac{\partial r}{\partial t} + u \frac{\partial r}{\partial x} + v \frac{\partial r}{\partial y}$. Equations (2.19) and (2.20) are also applicable to the second family of characteristics and it is easily deduced that

$$K^T . L = L^T . K = 0 \qquad (2.25)$$

For the second family of characteristics, a further relationship similar to equation (2.25) may be derived. By introducing a vector M defined as

$$M = \begin{bmatrix} 1 \\ u \\ v \end{bmatrix} \qquad (2.26)$$

then the condition $R = 0$ can be written as

$$K^T . M = M^T . K = 0 \qquad (2.27)$$

Equation (2.27) is only satisfied when the equality $L = M$ exists and in this case the characteristic surface of the second type is defined by the line directions

$$\frac{dx}{dt} = u \qquad (2.28)$$

$$\frac{dy}{dt} = v \qquad (2.29)$$

In physical terms these latter two equations describe the motion of a fluid particle or streamline. Such a streamline defines the motion of the main body of fluid and is actually a degenerate characteristic since a true characteristic defines the motion of a water wave. In the present analysis the particle path is assumed to approximate a straight line as have the bicharacteristics previously considered.

The directions of the first family of bicharacteristics given by equations (2.23) and (2.24) suggest the form of the linear combination required in order to eliminate the partial derivatives in the r direction from the characteristic flow equations. The specific form of the ratio of the combinations is contained in the vector and is

$$H = \begin{bmatrix} 1 & c.\cos\theta & c.\sin\theta \end{bmatrix} \qquad (2.30)$$

It follows that the multiplication of this vector with the transformed

equation (2.8) will produce the fundamental characteristic equation (2.12). Since the original set of equations (2.2), (2.3) and (2.4) are exactly equivalent to the transformed equations then such a multiplication of the original equations must yield the characteristic condition. Therefore equation (2.3) is multiplied by $c.\cos\theta$ and added to equation (2.4) multiplied by $c.\sin\theta$ and added to equation (2.2). After a certain amount of algebraic manipulation the result is

$$\frac{\partial Z}{\partial t} + (u + c.\cos\theta).\frac{\partial Z}{\partial x} + (v + c\sin\theta).\frac{\partial Z}{\partial y}$$

$$+ \frac{c.\cos\theta}{g}\left[\frac{\partial u}{\partial t} + (u + c.\cos\theta).\frac{\partial u}{\partial x} + (v + c.\sin\theta).\frac{\partial u}{\partial y}\right]$$

$$+ \frac{c.\sin\theta}{g}\left[\frac{\partial v}{\partial t} + (u + c.\cos\theta).\frac{\partial v}{\partial x} + (v + c.\sin\theta).\frac{\partial v}{\partial y}\right]$$

$$= \frac{c^2\sin\theta}{g}\left[-\sin\theta.\frac{\partial u}{\partial x} + \cos\theta.\frac{\partial u}{\partial y}\right]$$

$$- c^2\frac{\cos\theta}{g}\left[-\sin\theta.\frac{\partial v}{\partial x} + \cos\theta.\frac{\partial v}{\partial y}\right]$$

$$+ c.\cos\theta.\frac{\partial H}{\partial x} + c.\sin\theta.\frac{\partial H}{\partial y}$$

$$+ c.\cos\theta.F_x + c.\sin\theta.F_y \qquad (2.31)$$

The characteristic condition given in equation (2.31) can be regarded as containing two differential operators. The first operator is a total time derivative $\frac{d}{dt}$ of the dependent variable and has the form

$$\frac{\partial}{\partial t} + (u + c.\cos\theta).\frac{\partial}{\partial x} + (v + c.\sin\theta).\frac{\partial}{\partial y}$$

along a given bicharacteristic. The second operator

$$-\sin\theta.\frac{\partial}{\partial x} + \cos\theta.\frac{\partial}{\partial y}$$

involves spatial differentiation of the dependent variable in a direction normal to the bicharacteristic. The characteristic condition can be expressed in terms of these operators producing total time derivatives of the dependent variables as follows

$$g.\frac{dz}{dt} + c.\cos\theta.\frac{du}{dt} + c.\sin\theta.\frac{dv}{dt} = f \qquad (2.32)$$

where $$f = c.g.\cos\theta.\frac{\partial H}{\partial x} + c.g.\sin\theta.\frac{\partial H}{\partial y}$$

$$- c^2\left[\sin^2\theta.\frac{\partial u}{\partial x} - \sin\theta.\cos\theta.\left(\frac{\partial u}{\partial y}+\frac{\partial v}{\partial x}\right) + \cos^2\theta.\frac{\partial v}{\partial y}\right]$$

$$+ c.g.\cos\theta.F_x + c.g.\sin\theta.F_y \qquad (2.33)$$

where F_x and F_y represent the terms on the right hand side of the equations (2.3) and (2.4) respectively.

The particle path of the fluid corresponding to the second family of bicharacteristics, is defined by the directions

$$dx = u.dt \quad , \quad dy = v.dt$$

Hence the total time derivative of surface elevation along this bicharacteristic may be written as

$$\frac{dz}{dt} = \frac{\partial z}{\partial t} + u.\frac{\partial z}{\partial x} + v\frac{\partial z}{\partial y} \qquad (2.34)$$

On inserting this total derivative into equation (2.2) the particle path relationship immediately becomes

$$g.\frac{dz}{dt} = - c^2\left[\frac{\partial u}{\partial x} + \frac{\partial v}{\partial y}\right] \qquad (2.35)$$

and is simply another form of the continuity equation.

With regard to equation (2.32), the possibility of an infinite number of values for θ suggests that there are an infinite number of characteristic conditions. This implies that there is an infinite number of sources propagating waves which is clearly not the case. Matsoukis (1980) has shown that there are, in fact, only four sources of principal waves in x-y-t space and therefore only four possible bicharacteristics along which these waves travel. The four directions occur at intervals of $\pi/2$ in the parametric angle θ and correspond to positive and negative waves travelling along the positive and negative x and y directions respectively. For example a positive wave in the positive x direction has an associated family of characteristics defined by $dx/dt = u+c$, $dy/dt = v$, and is a result of the quadratic form of equation (2.22). There are therefore only four families of characteristic surfaces which are tangential to the envelope cone along the bicharacteristics. The characteristic cone was considered by Matsoukis (1980) to represent all the possible bicharacteristics that water waves could

follow but, in fact, the waves only travel along four of them. These conclusions have an important bearing in determining the formation of the numerical scheme discussed in the next section.

2.3 THE CHARACTERISTIC NUMERICAL SCHEME

There are at present numerous characteristic methods available for the integration of the hyperbolic long wave equations in two spatial dimensions and three independent variables. Very few of these methods have been applied to computationally significant problems, with the exception of the schemes proposed by Thornhill (1948), Coburn and Dolph (1949), Hartree (1953) and Butler (1960). These characteristic schemes have been reviewed by Fox (1966) and more recently by Katepodes and Strelkoff (1979). The method originally proposed by Butler (1960) known as the inverse pentahedral network produces second order accuracy with respect to Δt and forms the basis of the numerical technique used in the present analysis. The proposed technique outlined in this section is of first order accuracy with respect to Δt.

Consider a two-dimensional orthogonal grid of points taken on some initial surface in the x-y plane with each point spaced a distance apart. The values of the dependent variables are calculated at each and every grid point and constitute a discrete series of approximate values to a continuous solution. The calculations are accomplished by introducing the characteristic conditions as operations on the values at each gridpoint and so the behaviour of the fluid at one time level is advanced to later time planes.

With regard to a general situation, consider a point with coordinates (x_o, y_o, t_o) remote from the spatial boundaries of the problem. If the values of the dependent variables are desired at this point then linear bicharacteristics are extended backwards in time until they intersect the previous solution surface in $t = t_o - \Delta t$. These bicharacteristics emanate from the vertex of the conoid at values of the parametric angle θ separated by increments of $\pi/2$. This arrangement of bicharacteristics and the particle path bicharacteristic

are as shown in figure 2.1

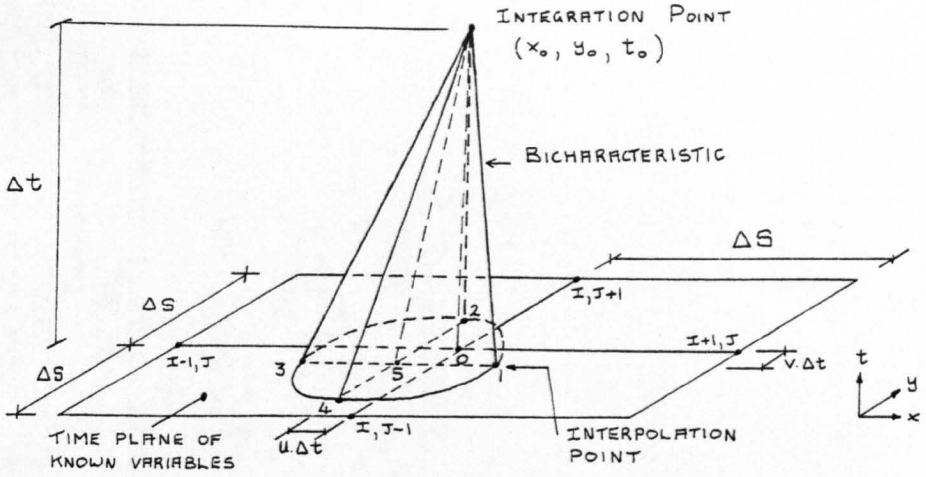

Figure 2.1

In figure 2.1 the parametric angle take the values

$$\theta_1 = \pi \quad , \quad \theta_2 = \frac{3\pi}{2}$$

$$\theta_3 = 0 \quad , \quad \theta_4 = \frac{\pi}{2} \qquad (2.36)$$

and so determine the directions of the characteristics.

In figure 2.2 a section in the x -plane taken from the time $t-\Delta t$ to $t+\Delta t$ shows that the linear bicharacteristics define two separate regions.

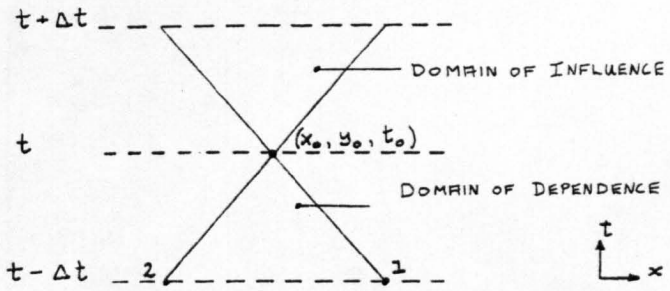

Figure 2.2

The region between t and $t+\Delta t$ is called the domain of influence since it comprises a space-time continium which is affected by water waves generated at point (x_o, y_o, t_o). In the same way the solution at the vertex of the cone at time t is dependent on the generation of water waves at time $t-\Delta t$. For this reason the region is called the

domain of dependence. It is one of the basic assumptions of a scheme of first order accuracy that the celerity of the wave is constant during any time Δt while in the domain of dependence and so the bicharacteristics are linear. The value of the celerity is obtained at the point O with coordinates $(x_o, y_o, t-\Delta t)$ to ensure an explicit form of numerical scheme.

Under circumstances of constant celerity and with the parametric angle taking the values in equation (2.36) the respective characteristic conditions derived from equation (2.32) are along bicharacteristic $\frac{dx}{dt} = u - c$, $\frac{dy}{dt} = V$

$$g \cdot \frac{dz}{dt} - c \cdot \frac{du}{dt} = - c^2 \frac{\partial V}{\partial y} - c \cdot g \cdot \frac{\partial H}{\partial x} + c \cdot g \cdot F_x$$

along bicharacteristic $\frac{dx}{dt} = u$, $\frac{dy}{dt} = V - c$

$$g \cdot \frac{dz}{dt} - c \cdot \frac{dV}{dt} = - c^2 \frac{\partial u}{\partial x} - c \cdot g \cdot \frac{\partial H}{\partial y} + c \cdot g \cdot F_y$$

along bicharacteristic $\frac{dx}{dt} = u + c$, $\frac{dy}{dt} = V$

$$g \cdot \frac{dz}{dt} + c \cdot \frac{du}{dt} = - c^2 \frac{\partial V}{\partial y} + c \cdot g \cdot \frac{\partial H}{\partial x} - c \cdot g \cdot F_x$$

along bicharacteristic $\frac{dx}{dt} = u$, $\frac{dy}{dt} = V + c$

$$g \cdot \frac{dz}{dt} + c \cdot \frac{dV}{dt} = - c^2 \frac{\partial u}{\partial x} + c \cdot g \cdot \frac{\partial H}{\partial y} - c \cdot g \cdot F_y \qquad (2.37)$$

where

$$F_x = \frac{-1}{\rho \cdot g} \cdot \frac{\partial p_a}{\partial x} + \frac{\Omega \cdot V}{g} + \frac{(\tau_{xs} - \tau_{xb})}{\rho \cdot g \cdot Z}$$

$$F_y = \frac{-1}{\rho \cdot g} \cdot \frac{\partial p_a}{\partial y} - \frac{\Omega \cdot u}{g} + \frac{(\tau_{ys} - \tau_{yb})}{\rho \cdot g \cdot Z} \qquad (2.38)$$

Together with the above characteristic conditions, there is also the particle path equation (2.35) defined along the bicharacteristic

$$\frac{dx}{dt} = u \ , \ \frac{dy}{dt} = V \ ; \quad g \frac{dz}{dt} = - c^2 \left(\frac{\partial u}{\partial x} + \frac{\partial V}{\partial y} \right) \qquad (2.39)$$

The total derivatives along the bicharacteristics in equations (2.37) and (2.39) can be replaced by forward differences in time (providing

the time increment is small) as follows

$$g \cdot \frac{Z-Z_1}{\Delta t} - c \cdot \frac{U-U_1}{\Delta t} = -c^2 \cdot \frac{\partial V}{\partial y} - c \cdot g \cdot \frac{\partial H}{\partial x} + c \cdot g \cdot F_x \qquad (2.40)$$

$$g \cdot \frac{Z-Z_2}{\Delta t} - c \cdot \frac{V-V_2}{\Delta t} = -c^2 \cdot \frac{\partial U}{\partial x} - c \cdot g \cdot \frac{\partial H}{\partial y} + c \cdot g \cdot F_y \qquad (2.41)$$

$$g \cdot \frac{Z-Z_3}{\Delta t} + c \cdot \frac{U-U_3}{\Delta t} = -c^2 \frac{\partial V}{\partial y} + c \cdot g \cdot \frac{\partial H}{\partial x} - c \cdot g \cdot F_x \qquad (2.42)$$

$$g \cdot \frac{Z-Z_4}{\Delta t} + c \cdot \frac{V-V_4}{\Delta t} = -c^2 \frac{\partial U}{\partial x} + c \cdot g \cdot \frac{\partial H}{\partial y} - c \cdot g \cdot F_y \qquad (2.43)$$

$$g \cdot \frac{Z-Z_5}{\Delta t} = -c^2 \left(\frac{\partial U}{\partial x} + \frac{\partial V}{\partial y} \right) \qquad (2.44)$$

In these characteristic conditions Z, U, V represent the integrated dependent variables at the vertex of the conoid and Z_n, U_n, V_n $(1 \leq n \leq 5)$ are interpolated values on the previous time plane $t - \Delta t$. The values of the partial derivatives of U, V and H are those at point 5. The five equations comprise a system involving five unknowns; the three dependent variables and the partial derivatives, $\frac{\partial U}{\partial x}$ and $\frac{\partial V}{\partial y}$. Either of the integrated variables Z, U, V are obtained by combining the equations (2.40) to (2.44) in such a way as to remove the partial derivatives and then substituting

$$\frac{\partial H}{\partial x} = \frac{H_1 - H_3}{2 \cdot c \cdot \Delta t} \quad , \quad \frac{\partial H}{\partial y} = \frac{H_2 - H_4}{2 \cdot c \cdot \Delta t} \qquad (2.45)$$

Hence adding equations (2.40) to (2.43) and subtracting twice equation (2.44) gives

$$Z = \tfrac{1}{2}\left(Z_1 + Z_2 + Z_3 + Z_4 - 2Z_5 \right) - \tfrac{1}{2} \frac{c}{g} \left(V_2 - V_4 + U_1 - U_3 \right) \qquad (2.46)$$

Subtracting equation (2.42) from equation (2.40) produces

$$U = \tfrac{1}{2}\left(U_1 + U_3 \right) - \tfrac{1}{2} \frac{g}{c} \left(Z_1 - H_1 - Z_3 + H_3 \right) - g \cdot F_x \cdot \Delta t \qquad (2.47)$$

Subtracting equation (2.43) from equation (2.41) produces

$$V = \tfrac{1}{2}\left(V_2 + V_4 \right) - \tfrac{1}{2} \cdot \frac{g}{c} \left(Z_2 - H_2 - Z_4 + H_4 \right) - g \cdot F_y \cdot \Delta t \qquad (2.48)$$

for a grid point remote from the boundary conditions. The equations (2.46) to (2.48) yielding the integrated dependent variables are identical to that given by Townson (1974).

It is apparent from equations (2.46) to (2.48) that computing the dependent variables involves the values at the intermediate points 1 to 5 at which the bicharacteristics intersect the time plane t-Δt. At this time level an interpolation scheme is required in order to calculate the values of Z, U, V, H at the intermediate points from the known grid point values. With reference to figure 2.1 and considering linear bicharacteristics, the coordinates of the intermediate points at which interpolation is made are;

$$x_{2,4,5} = x_o - U.\Delta t \qquad x_{1,3} = x_o - (U \mp C).\Delta t$$

$$y_{1,3,5} = y_o - V.\Delta t \qquad y_{2,4} = y_o - (V \mp C).\Delta t \qquad (2.49)$$

The most suitable interpolation scheme describing a quantity Q at various points has been shown by Matsoukis (1980) to be a first order linear polynomial such that

$$Q = Ax + By + C \qquad (2.50)$$

where

$$A = \Delta Q/\Delta x = (Q_{I+1,J} - Q_{I-1,J})/2.\Delta S$$

$$B = \Delta Q/\Delta y = (Q_{I,J+1} - Q_{I,J-1})/2.\Delta S$$

$$C = \tfrac{1}{4}(Q_{I+1,J} + Q_{I-1,J} + Q_{I,J+1} + Q_{I,J-1})$$

and ΔS is the spacing between grid points.

The actual form of the interpolation scheme is determined by the following considerations. The basic system of differential equations have been derived by applying the physical laws to a control volume of infinitesimal base dimensions 2δS along the x- and y- axes. If Q represents the dependent variables at a point (x,y) and it is assumed that the variation of the quantity Q is continuous then the value of this quantity at a point $(x+2\delta S, y+2\delta S)$ is given by Taylor's formula for two independent variables namely

$$Q(x+2\delta S, y+2\delta S) = Q(x,y) + 2.\delta S.\frac{\partial Q}{\partial x} + 2\delta S.\frac{\partial Q}{\partial y} \qquad (2.51)$$

$$+ 2\left(\delta S^2.\frac{\partial^2 Q}{\partial x^2} + 2\delta S^2.\frac{\partial^2 Q}{\partial x.\partial y} + \delta S^2.\frac{\partial^2 Q}{\partial y^2}\right) + \ldots$$

In the derivation of the differential scheme only the first three terms of Taylor's formula were considered therefore the formula was applied with first order accuracy. The corresponding control volume in the

difference scheme can be considered to be of base length $2\Delta S$ along the x- and y- axes, where $\Delta S \to \delta S \to 0$. Hence applying Taylor's formula to this control volume with first order accuracy gives

$$Q\left(x + 2.\Delta S,\ y + 2.\Delta S\right) = Q(x,y) + 2.\Delta S.\frac{\Delta Q}{\Delta x} + 2.\Delta S.\frac{\Delta Q}{\Delta y} \qquad (2.52)$$

which can be rewritten using the grid point coordinates

$$Q_{I+1,J+1} = Q_{I-1,J-1} + 2.\Delta S.\frac{\Delta Q}{\Delta x} + 2.\Delta S.\frac{\Delta Q}{\Delta y} \qquad (2.53)$$

The component of the variable Q in the x- direction can be expressed as $Q_{I+1,J} = Q_{I-1,J} + 2.\Delta S.\frac{\Delta Q}{\Delta x}$ which if rearranged produces

$$\frac{\Delta Q}{\Delta x} = \frac{Q_{I+1,J} - Q_{I-1,J}}{2.\Delta S} \qquad (2.54)$$

Similarly the component of Q in the y- direction is $Q_{I,J+1} = Q_{I,J-1} + 2.\Delta S.\frac{\Delta Q}{\Delta y}$ which rearranges to give

$$\frac{\Delta Q}{\Delta y} = \frac{Q_{I,J+1} - Q_{I,J-1}}{2.\Delta S} \qquad (2.55)$$

Firstly it is noted that in order to have equivalence between the differential and difference expressions then $\frac{\Delta Q}{\Delta x} \to \frac{\partial Q}{\partial x}$ as $\Delta x \to 0$ and $\frac{\Delta Q}{\Delta y} \to \frac{\partial Q}{\partial y}$ as $\Delta y \to 0$. Secondly, the finite difference expressions in equations (2.54) and (2.55) are equivalent to the coefficients A and B respectively of the interpolation scheme. Therefore these coefficients A and B are actually numerical approximations to the differential terms $\frac{\partial Q}{\partial x}, \frac{\partial Q}{\partial y}$ respectively at the central point. It is also apparent then that the following conditions are valid;

$$\begin{aligned}
Q_{I+1,J} &= Q_{I,J} + \Delta S.\frac{\partial Q}{\partial x} = C + A.\Delta S \\
Q_{I-1,J} &= Q_{I,J} - \Delta S.\frac{\partial Q}{\partial x} = C - A.\Delta S \\
Q_{I,J+1} &= Q_{I,J} + \Delta S.\frac{\partial Q}{\partial y} = C + B.\Delta S \\
Q_{I,J-1} &= Q_{I,J} - \Delta S.\frac{\partial Q}{\partial y} = C - B.\Delta S
\end{aligned} \qquad (2.56)$$

The constant term C of the interpolation scheme is therefore obtained by adding the four equations in (2.56) to produce

$$C = \tfrac{1}{4}\left(Q_{I+1,J} + Q_{I-1,J} + Q_{I,J+1} + Q_{I,J-1}\right)$$

Only this condition satisfies all the requirements of equation (2.56). It should be noted that the three coefficients of interpolation A, B and C are obtained from the set of four equations in (2.56), whereas actually only three equations are required for an exact solution. The use of four equations implies a plane passing through four distinct grid points which may not always be possible and in such a case the interpolating plane represents an averaged one.

With the interpolating coefficient as prescribed in equation (2.50) the values at the intermediate points may be calculated. The interpolation scheme is actually a first order version of Taylor's formula and ensures consistency between the differential scheme and the difference scheme. Therefore the finite difference expressions of equations (2.54) and (2.55) are not merely numerical approximations but necessary and sufficient conditions for equivalence between the numerical and differential processes. Furthermore a second order interpolation scheme is incompatible with the first order accuracy in which the long wave equations have been derived. Matsoukis (1980) has shown that second order interpolation schemes introduce additional terms in the difference scheme which are not present in the differential one.

The form of the numerical scheme as expressed by the characteristic equations (2.46), (2.47) and (2.48) is only a temporary one and is subsequently modified by the introduction of the interpolation scheme. The unknowns Z, U, V thus become dependent on the values of the variables at the grid points at time t-Δt and not on the intermediate points 1 to 4 on this time plane. Equations (2.46) to (2.48) become

$$\begin{aligned} Z &= Z_5 - \frac{c^2}{g} \cdot \Delta t \cdot \left(A_u + B_v \right) \\ U &= U_5 - g \cdot \Delta t \cdot A_\eta - g \cdot \Delta t \cdot F_x \\ V &= V_5 - g \cdot \Delta t \cdot B_\eta - g \cdot \Delta t \cdot F_y \end{aligned} \qquad (2.57)$$

which can be written as

$$\begin{aligned} \frac{Z - Z_5}{\Delta t} &= -\frac{c^2}{g} \cdot \frac{\Delta U}{2 \cdot \Delta s} - \frac{c^2}{g} \cdot \frac{\Delta V}{2 \cdot \Delta s} \\ \frac{U - U_5}{\Delta t} &= -g \cdot \frac{\Delta \eta}{2 \cdot \Delta s} - g \cdot \left(F_x \right)_5 \\ \frac{V - V_5}{\Delta t} &= -g \cdot \frac{\Delta \eta}{2 \cdot \Delta s} - g \cdot \left(F_y \right)_5 \end{aligned} \qquad (2.58)$$

where $\eta = Z_o - H_o$ is the elevation above mean water level at a time $t-\Delta t$ and H_o is the interpolated mean water depth at grid point O. The previous equations have a similar form to the following equations which are the initial partial differential equations of long wave motion:

$$\begin{aligned} \frac{dZ}{dt} &= -\frac{c^2}{g}\cdot\frac{\partial u}{\partial x} - \frac{c^2}{g}\cdot\frac{\partial V}{\partial y} \\ \frac{du}{dt} &= -g\cdot\frac{\partial \eta}{\partial x} - g\cdot F_x \\ \frac{dV}{dt} &= -g\cdot\frac{\partial \eta}{\partial y} - g\cdot F_y \end{aligned} \qquad (2.59)$$

In fact a comparison of equations (2.58) with (2.59) shows that the numerical scheme for an internal point based on the characteristic conditions is a numerical approximation of the governing long wave equations. Such an approximation is only produced under the conditions resulting from introducing a linear interpolation scheme. It is clear that the means of integrating the initial differential equations is along the particle path characteristic $\frac{dx}{dt} = u$, $\frac{dy}{dt} = V$. However to retain an explicit form of solution using the numerical scheme the values along the particle path are calculated at point 5 at a time $t-\Delta t$. In relation to point O, (see figure 2.1) point 5 has coordinates $(-u.\Delta t, -V.\Delta t)$ which represent convective displacements. For the case of tidal motion in which the convective terms are small, conditions at points O and 5 are very similar and there is then the possibility of constructing a linear finite difference scheme based solely on grid point values and independent of the characteristic paths. In the tide and surge simulations presented in Chapters 7, 8 and 9 the convective terms have been included where finite amplitude conditions are encountered. In these simulations the numerical scheme for an internal point is obtained from equation (2.57) by substituting the finite difference approximations found from the interpolation scheme of equation (2.50). The final system of equations take the form

$$\begin{aligned} Z &= Z_5 - \frac{c^2}{g}\cdot\Delta t\cdot\left(u_{x+1,y} - u_{x-1,y} + V_{x,y+1} - V_{x,y-1}\right)/2.\Delta s \\ u &= u_5 - g\cdot\Delta t\cdot\left(\eta_{x+1,y} - \eta_{x-1,y}\right)/2.\Delta s - g\cdot\Delta t\cdot(F_x)_5 \\ V &= V_5 - g\cdot\Delta t\cdot\left(\eta_{x,y+1} - \eta_{x,y-1}\right)/2.\Delta s - g\cdot\Delta t\,(F_y)_5 \end{aligned} \qquad (2.60)$$

where F_x from equation (2.38) becomes

$$F_x = -\frac{1}{\rho g}\frac{p_{x+1,y}-p_{x-1,y}}{2\cdot\Delta s} + \frac{2}{g}\cdot\omega\cdot\sin\psi\cdot V_5 + \frac{(u_5^2+V_5^2)^{1/2}\cdot u_5}{C^2\cdot Z_5} - k\,\frac{\rho_a\cdot W_5^2\cdot\cos\beta}{\rho_w\cdot g\cdot Z_5} \qquad (2.61)$$

and similarly F_y becomes

$$F_y = -\frac{1}{\rho g}\frac{p_{x,y+1}-p_{x,y-1}}{2\cdot\Delta s} - \frac{2}{g}\cdot\omega\cdot\sin\psi\cdot u_5 + \frac{(u_5^2+V_5^2)^{1/2}\cdot V_5}{C^2\cdot Z_5} - k\,\frac{\rho_a W_5^2\cdot\sin\beta}{\rho_w\cdot g\cdot Z_5} \qquad (2.62)$$

In the tests presented in the following chapters, the pressure gradient term was not retained in the numerical scheme. In practice the values of the external forces are computed at point O instead of at point 5, to reduce the amount of interpolation.

Application of the interpolation scheme $Q=Ax+By+C$ to the terms Z_5, u_5 and V_5 in equations (2.60) leads to the following expression stated in terms of the general dependent variable Q as

$$Q_5 = Q_o - u_{x,y}\cdot\Delta t\cdot(Q_{x+1,y}-Q_{x-1,y})/2\cdot\Delta s - V_{x,y}\cdot\Delta t\cdot(Q_{x,y+1}-Q_{x,y-1})/2\cdot\Delta s \qquad (2.63)$$

where $Q_o = \frac{1}{4}(Q_{x+1,y}+Q_{x-1,y}+Q_{x,y+1}+Q_{x,y-1})$

The analytical solutions developed in Chapter 4 are derived from linear considerations and do not include convective acceleration terms. To reproduce these solutions numerically, the numerical scheme for an internal point as shown in equation (2.60) must be suitably modified. Hence the convective terms denoted by multiples of $u_{x,y}$ and $V_{x,y}$ in equation (2.63) are excluded from the linear scheme so that $Z_5=Z_o$, $u_5=u_o$ and $V_5=V_o$. The necessity of linear conditions also requires that the celerity in the continuity equation in (2.60) be calculated from the mean water depth and not the total depth. The linearised numerical scheme for an internal point then becomes

$$\begin{aligned} Z &= Z_o - H_o\cdot\Delta t\cdot(u_{x+1,y}-u_{x-1,y}+V_{x,y+1}-V_{x,y-1})/2\cdot\Delta s \\ u &= u_o - g\cdot\Delta t\cdot(\eta_{x+1,y}-\eta_{x-1,y})/2\cdot\Delta s - g\cdot\Delta t\cdot(F_x)_o \\ V &= V_o - g\cdot\Delta t\cdot(\eta_{x,y+1}-\eta_{x,y-1})/2\cdot\Delta s - g\cdot\Delta t\cdot(F_y)_o \end{aligned} \qquad (2.64)$$

It is evident from the comparison of either equations (2.60) or (2.64) with equations (2.46) to (2.48) that the interpolation scheme becomes an integral component of the numerical scheme and is bound to have a critical effect on the stability and consistency of that scheme. With this viewpoint an understanding of the fundamental properties of convergence consistency and stability is required before any practical application of the scheme can be made.

2.4 CONVERGENCE

The term convergence has in the past been somewhat loosely regarded as the process in which the numerical scheme achieves a periodic final solution from an arbitrary initial surface. This periodicity does not necessarily ensure convergence and is merely the result of an induced harmonic disturbance in the system and only implies that the numerical scheme is stable. Therefore there is no guarantee that the periodic solution obtained is equivalent to that attributed to the system of partial differential equations. However it is exactly this equivalence between the numerical and physical processes that defines convergence of a numerical scheme. In a strict mathematical sense, a numerical scheme is considered to be convergent when the solution of the difference equations tends to the solution of the differential equations as the space and time increments tend to zero.

A rigorous mathematical analysis of convergence is still not entirely satisfactory for non-linear finite difference schemes. Alternatively a numerical approach could be used in which the results from repeated tests with decreasing space and time increments are compared with an analytical solution or observed data. The sequence of solutions could then be examined for convergence. This approach is unfortunately impractical owing to the demands on machine time when using small values of space and time increments. Another more logical means of conducting the analysis of convergence is to consider the consistency and stability of the numerical scheme. Consistency examines the limit of the difference equations themselves as the space and time increments tend to zero instead of examining the numerical solution of these equations. A stability analysis can be performed to investigate the error in the solution of linearised difference equations with finite values of the space and time increments as the number of computations tends to

infinity. Obviously if the numerical scheme is either inconsistent or unstable then convergence is not achieved. Hence both consistency and stability are necessary and sufficient conditions for convergence of a linearised scheme.

2.4.1 Consistency

A consistency analysis is required since the incorporation of an interpolation scheme into the numerical scheme modifies the characteristic conditions. It has already been shown in section 2.3 that the interpolation scheme $Q = Ax + By + C$ is essentially consistent with Taylor's expansion to first order accuracy and so did not introduce spurious terms into the characteristic conditions. This is evident from the numerical equations (2.58) incorporating the interpolation scheme on comparison with the original partial differential equations (2.59). It now remains to show that the numerical scheme is consistent in that as the space and time increments tend to zero, the difference equations become identical to the original differential equations.

The technique used in the consistency analysis is to express each dependent variable with local coordinates (δx, δy, δt) relative to a central grid point O using Taylor's expansion. With Q representing the dependent variable, Taylor's expansion to a first order approximation becomes

$$Q\left(\delta x, \delta y, \delta t\right) = Q_o + \delta x \cdot \frac{\partial Q_o}{\partial x} + \delta y \cdot \frac{\partial Q_o}{\partial y} + \delta t \cdot \frac{\partial Q_o}{\partial t} \qquad (2.65)$$

This expression is applied in turn to the characteristic equations (2.46) to (2.48) while neglecting the external forces and stress terms which have no effect on the generality of the consistency analysis. Consider first, equation (2.46) namely

$$Z = \tfrac{1}{2}\left(Z_1 + Z_2 + Z_3 + Z_4 - 2Z_5\right) - \tfrac{1}{2}\frac{c}{g}\left(V_2 - V_4 + U_1 - U_3\right)$$

The introduction of Taylor's formula which may be regarded as an interpolation scheme transforms equation (2.46) into

$$Z_o + \delta t \frac{\partial Z_o}{\partial t} = \tfrac{1}{2}\left[2Z_o - 2U_o \cdot \delta t \cdot \frac{\partial Z_o}{\partial x} - 2V_o \cdot \delta t \frac{\partial Z_o}{\partial y} \right]$$
$$- \frac{c_o}{2g}\left[2 \cdot c_o \cdot \delta t \cdot \frac{\partial U_o}{\partial x} \right]$$
$$- \frac{c_o}{2g}\left[2 \cdot c_o \cdot \delta t \cdot \frac{\partial V_o}{\partial y} \right]$$

which can be further reduced to a form comparable with the original

continuity equation (2.2) and is

$$\frac{\partial Z_o}{\partial t} + u_o \frac{\partial Z_o}{\partial x} + V_o \frac{\partial Z_o}{\partial y} + \frac{c_o^2}{g} \cdot \frac{\partial u_o}{\partial x} + \frac{c_o^2}{g} \cdot \frac{\partial V_o}{\partial y} = 0 \qquad (2.66)$$

A similar transformation of the dynamic characteristic condition (equation (2.47)) may be obtained as follows

$$u = \tfrac{1}{2}(u_1 + u_3) - \tfrac{1}{2}\frac{g}{c}(\eta_1 - \eta_3)$$

becomes

$$u_o + \delta t \frac{\partial u_o}{\partial t} = \tfrac{1}{2}\left[2u_o - 2u_o \delta t . \frac{\partial u_o}{\partial x} - 2.V_o . \delta t \frac{\partial u_o}{\partial y} \right]$$

$$- \frac{g}{2c_o}\left[2.c_o . \delta t . \frac{\partial \eta_o}{\partial x} \right]$$

which simplifies to

$$\frac{\partial u_o}{\partial t} + u_o \frac{\partial u_o}{\partial x} + V_o \frac{\partial u_o}{\partial y} + g \frac{\partial \eta_o}{\partial x} = 0 \qquad (2.67)$$

which is equivalent to the left hand side of equation (2.3). Similarly equation (2.48) which is

$$V = \tfrac{1}{2}(V_2 + V_4) - \tfrac{1}{2}\frac{g}{c}(\eta_2 - \eta_4)$$

is tranformed to

$$V_o + \delta t . \frac{\partial V_o}{\partial t} = \tfrac{1}{2}\left[2V_o - 2u_o . \delta t . \frac{\partial V_o}{\partial x} - 2.V_o . \delta t . \frac{\partial V_o}{\partial y} \right]$$

$$- \frac{g}{2c_o}\left[2.c_o . \delta t . \frac{\partial \eta_o}{\partial y} \right]$$

which simplifies to

$$\frac{\partial V_o}{\partial t} + u_o \frac{\partial V_o}{\partial x} + V_o \frac{\partial V_o}{\partial y} + g . \frac{\partial \eta_o}{\partial y} = 0 \qquad (2.68)$$

and is equivalent to the left hand side of equation (2.3).

It is apparent from equations (2.66) to (2.68) that the consistency conditions are satisfied for an internal point. In the same way it is easily shown that the boundary conditions are also consistent and so the physical consistency of the proposed numerical method may be established.

2.4.2 Stability

A system of difference equations constituting a numerical scheme

can be regarded as being stable if the growth of rounding and discretisation errors is bounded as the number of computations tend to infinity. In the case of a harmonic solution the scheme is stable if this solution is a close approximation to the solution of the original partial differential equations. In other words the stability of a consistent difference scheme implies its convergence, a feature noted by Lax and Richtmyer (1956).

The absolute magnitude of the bound of the error is obviously related to the accuracy of the numerical scheme and the values of the space and time increments. A stability analysis will therefore require to establish restrictions on the size of the space and time increments which when imposed on the difference equations will prevent errors from being amplified to an unacceptable extent. According to Richtmyer and Morton (1967) instability is not a result of rounding errors but is clearly a property of the difference scheme. Also Courant, Friedrichs and Lewy (1928) have remarked that instability is accelerated by reducing the spatial representation of the numerical grid while retaining the same timestep. This finding suggests that an upper bound to the size restriction of the grid may not be sufficient and that a lower bound is required.

Consider the general form of a system of hyperbolic partial differential equations defined as

$$\frac{\partial Q}{\partial t} = \sum_{k=1}^{m} A_k \cdot \frac{\partial Q}{\partial x_k}$$

where m is the number of spatial variables, Q represents the matrix of dependent variables and A_k the corresponding real coefficient matrices. The above quasilinear system describes the propagation of long waves for which the numerical scheme has been developed. The simulation of this motion is classed as an initial and boundary value problem for which a stability analysis is unfortunately not at present available. The normal approach is to treat the problem as an initial value one and test the stability of finite difference equations by applying a Fourier analysis to a linearised difference scheme with constant coefficients. It may be applied also with caution to non-linear difference schemes with variable coefficients. However Strang (1964) has shown that the

stability of a non-linear system depends on the stability of the linearised difference equations providing the solution has a sufficient number of continuous derivatives. This requirement has been rigorously proved by Stetter (1961) to be fulfilled when the difference equations are derived from the characteristic conditions since derivative discontinuities cannot occur along the bicharacteristics. Hence for a non-linear system the stability analysis may be applied to the linearised characteristic scheme and confidently assumed to apply equally to the non-linear system.

The necessary condition for convergence of a difference scheme derived from a system of linear partial differential equations with constant coefficients was established by Courant, Friedrichs and Lewy (1928) and is termed the CFL condition. It requires that the domain of dependence of the difference scheme must contain the domain of dependence of the differential equations. The differential domain of dependence is defined as the base of the characteristic cone at time $t-\Delta t$ and is shown in figure 2.3.

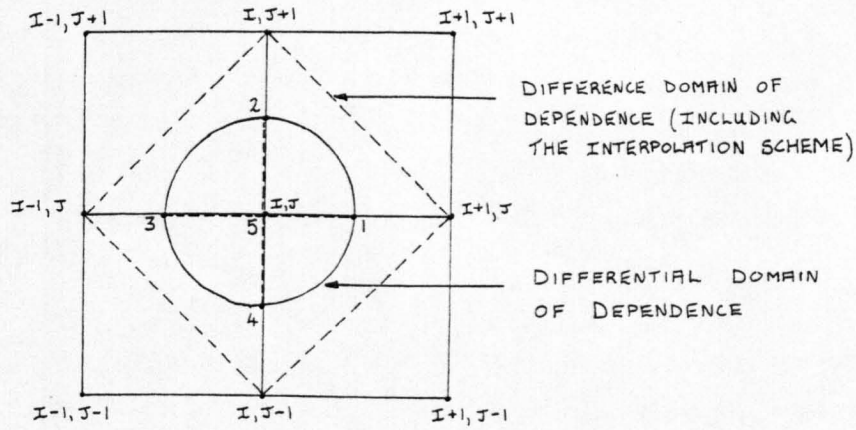

Figure 2.3

For the difference scheme represented by equations (2.64) the values of the dependent variables at point $O_{I,J}$ at time t are obtained by considering the known values of the variables at grid points $(I-1,J)$, $(I,J-1)$, $(I+1,J)$ and $(I,J+1)$ at time $t-\Delta t$. Therefore the domain of dependence of the difference scheme is the convex hull of base points defined by the boundary of the union of all triangles formed by joining all pairs of points by straight lines. The difference domain of dependence is also shown in figure 2.3 and it is apparent that the CFL condition only takes

into account the location of those base points which are vertices of the convex hull. As a result of this limitation and the fact that the difference scheme is non-simplicial it remains to be determined whether the CFL condition is a sufficient stability criterion or merely a necessary one.

It is worth emphasising that the numerical scheme is explicit and that the approximate solution at a grid point at time level t is calculated using the known values at a certain number of grid points at time $t-\Delta t$. If the number of grid points used is $L + 1$ where L is the number of space variables then the numerical scheme may be regarded as simplicial. The proposed numerical scheme is clearly non-simplicial since four grid points on the initial value surface are considered rather than three which is the simplicial requirement.

With regard to the general influence of the CFL criterion on the stability of a numerical scheme Hahn (1958) extended the work of Lax (1958) to demonstrate that the CFL criterion is a sufficient condition for stability for all simplicial networks. Hahn also showed that the CFL criterion is sufficient for non-simplicial networks providing the space increment is the same size in both the x and y directions. Since this requirement is fulfilled in all the tests in the present research it is concluded that the CFL criterion is both a necessary and sufficient condition to ensure stability of the numerical scheme.

The implication of the CFL stability criterion can be fully realised on considering the equivalence theorem of Lax. The theorem amounts to the fact that given a properly posed initial value problem and a consistent linearised finite difference approximation with constant coefficients then the stability of the numerical scheme is a necessary and sufficient condition for convergence. As a consequence of Lax's theorem, satisfaction of the CFL condition ensures both stability and convergence of the numerical scheme.

Ignoring for a moment Hahn's conclusion regarding the sufficiency of the CFL criterion for non-simplicial networks, the same conclusion can be verified in another way by applying the von Neumann stability criterion to the present numerical scheme. In this way it can be shown that both criteria impose the same restrictions on the value

of the time increment in order to maintain stability. The von Neumann condition, presented in detail by Lax and Richtmyer (1956) is a necessary condition for the stability of linear finite difference equations with constant coefficients. With regard to the works of Strang and Stretter which justified the application of the CFL criterion to the present numerical scheme, the same argument applies to the von Neumann criterion. Furthermore, Lax (1958) has shown that this criterion is both a necessary and sufficient condition for stability, providing that the initial data is infinitely differentiable. The doubt concerning the sufficiency of the von Neumann criterion for arbitrary initial data can be removed by realising that this data can be closely approximated by infinitely differentiable data. By investigating a number of difference schemes, Richtmyer (1957) also came to the same conclusion as Lax concerning the sufficiency of the von Neumann criterion.

The basic difference between the CFL and the von Neumann criteria is that the former condition only considers the location of those base points which are vertices of the convex hull. The von Neumann condition considers both the location of all the base points and the means by which the solution at a point is calculated from the dependent variables at the base points. For this reason the von Neumann criterion is regarded as a stronger necessary condition for stability of non-simplicial networks and is equivalent to the CFL condition for simplicial networks.

The von Neumann stability analysis gives an insight into what happens during computation by following a Fourier expansion of a line of errors as time progresses. Stability in this sense refers to the Fourier transformation of a linearised difference scheme to a form

$$\xi^{t+\Delta t} = A \cdot \xi^{t} \qquad (2.69)$$

where the elements of the vector ξ^t are the Fourier coefficients of the dependent variables at time t and A is the so called 'amplification matrix'. In quasi-linear equations the dependent variables appearing in A are supposed to be 'locally constant', an assumption which becomes invalidated when these variables change rapidly from one grid point to another. The von Neumann necessary condition for stability states that all eigenvalues λ_i of this amplification matrix must be less than or equal

to unity in absolute value. The condition $\lambda_i \leq 1 + O(\Delta t)$ is usually strengthened by one or another sufficient conditions as described by Richtmyer and Morton (1967).

The eigenvalues of the amplification matrix are obtained from the determinant of the 'characteristic equation' $A-\lambda I=0$ where I is the unit matrix. Following the analysis presented by Matsoukis (1980) the determinant may be expressed as

$$\begin{vmatrix} A-\lambda & A_{12} & A_{13} \\ A_{21} & A-\lambda & 0 \\ A_{31} & 0 & A-\lambda \end{vmatrix} = 0 \qquad (2.70)$$

which becomes

$$(A-\lambda)\left[(A-\lambda)^2 - A_{12}\cdot A_{21} - A_{13}\cdot A_{31}\right] = 0 \qquad (2.71)$$

For the case $A-\lambda=0$ the root λ_1 is equal to $A = \frac{1}{2}\cos\left(\frac{2\pi m}{L_x}\cdot\Delta s\right) + \frac{1}{2}\cos\left(\frac{2\pi n}{L_y}\cdot\Delta s\right)$ and for any pair of grid points (m,n) the condition $|\lambda_1|\leq 1$ is satisfied. The other two eigenvalues λ_2, λ_3 are calculated from the quadratic expression in equation (2.71) as

$$\lambda_{2,3} = \frac{1}{2}\left[\cos\left(\frac{2\pi m}{L_x}\cdot\Delta s\right) + \cos\left(\frac{2\pi n}{L_y}\cdot\Delta s\right)\right] \mp \frac{c\cdot\Delta t}{\Delta s}\sqrt{\left(\sin^2\left(\frac{2\pi m}{L_x}\cdot\Delta s\right) + \sin^2\left(\frac{2\pi n}{L_y}\cdot\Delta s\right)\right)} \qquad (2.72)$$

The von Neumann condition requires $|\lambda_{2,3}|\leq 1$ which is ensured for any grid points (m,n), with associated wavelengths (L_x, L_y), when

$$\Delta t \leq \frac{\sqrt{2}}{2}\cdot\frac{\Delta s}{c} \qquad (2.73)$$

It is important to compare the restriction in timestep given by equation (2.73) with the condition imposed by the CFL condition. At the maximum limiting timestep the characteristic cone representing the domain of dependence of the differential scheme is as shown in figure 2.4 .

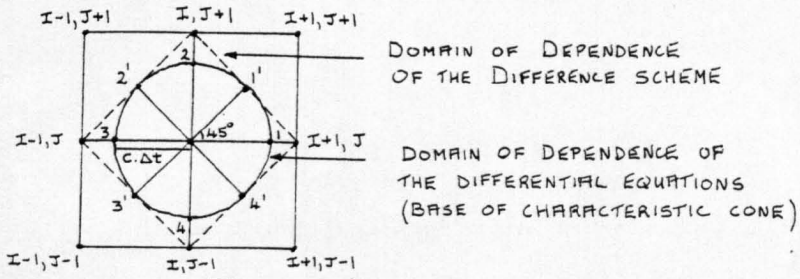

Figure 2.4

It is apparent from figure 2.4 that at this limiting condition the characteristic cone is tangential to the convex hull of the difference equations. This geometrical condition has been noted by Mitchell (1969) from which it is obvious that $C \cdot \Delta t = \frac{\sqrt{2}}{2} \cdot \Delta S$. Hence the CFL stability requirement in (x-y-t) space may be expressed by the inequality

$$\Delta t \leq \frac{\sqrt{2}}{2} \cdot \frac{\Delta S}{C} \qquad (2.74)$$

which is identical to that derived from the von Neumann stability analysis. It has therefore been shown that at least for the method of characteristics, the CFL condition is both a necessary and sufficient criterion for stability and hence for convergence of the difference equations.

The stability considerations presented in this section have been orientated towards assessing the degree of influence of the CFL criterion on the finite difference scheme based on characteristic equations. Establishing this influence is important since the CFL condition is more than just a relationship between time and space increments, it represents a significant fundamental relationship between the physical celerity C and the numerical celerity $\frac{\Delta S}{\Delta t}$ in the numerical scheme. Obviously in an accurate simulation the numerical celerity must propagate through the space-time grid as close as possible to the physical celerity with which principal waves propagate in reality. In this respect the CFL condition maintains stability as a numerical requirement for the simulation of physical conditions. Conversely, certain tests presented in Chapter 4 suggest that numerical discrepancies occur when deviations from the physical conditions controlled by the CFL criterion take place.

One important consequence of the CFL condition at the limiting timestep is that along certain curves namely the bicharacteristics, the domain of dependence of the difference equations is tangential to the differential cone. Referring back to figure 2.4 which depicts the system at time $t-\Delta t$, the four tangent points $1'$, $2'$, $3'$, and $4'$ evidently occur at the base of the bicharacteristics considered over a period Δt. The important feature highlighted by considering the CFL criterion is that the bicharacteristics occur at 90° increments of

the parametric angle θ orientated at 45° angles to the x-axis. This orientation suggests that the characteristic equations derived from equation (2.32) should be formulated with values of the parametric angle taken in turn as

$$\theta_{1'} = \frac{5\pi}{4} \qquad \theta_{2'} = \frac{7\pi}{4}$$
$$\theta_{3'} = \frac{\pi}{4} \qquad \theta_{4'} = \frac{3\pi}{4} \tag{2.74}$$

instead of the values taken along the axes directions given in equation (2.36). The two respective methods are henceforth denoted as 45° characteristics and 90° characteristics and a comparison of their results and an assessment of their accuracy in simulating tidal flow is presented in chapters 4 and 7. At present it suffices to say that a non-linear finite difference scheme for an internal point based on 45° characteristics and the proposed interpolation scheme may be shown to be identical to equations (2.60) which is the non-linear finite difference scheme obtained from 90° characteristic considerations. However the finite difference expressions at the boundary points developed using 45° and 90° characteristics are found on comparison to be slightly dissimilar from each other. Attention is given to these boundary conditions which are examined in the next chapter.

CHAPTER 3

NUMERICAL ASPECTS AND DEVELOPMENTS

3.1 INTRODUCTION

Consideration must first be given to the development of finite difference expressions which describe numerically the long wave motion at boundary points. The general situation at a particular boundary point is as for an internal point in that the values of the dependent variables Z,U,V are known on a time plane $t = t_o - \Delta t$ and are required at a grid point with coordinates (x_o , y_o , t_o). Once again the characteristic conditions of equations (2.40) to (2.44) associated with the bicharacteristics have to be combined so as to produce the required solution. However at a boundary point the presence of the boundary will prevent the establishment of at least one of the bicharacteristics in the problem area and the solution must be formulated from the remaining bicharacteristics. At the same time the situation is somewhat simplified since the imposed boundary condition at a point reduces the number of unknown variables by at least one.

An irregular coastline may be approximated by an orthogonal mesh of grid points. It is usual practice to identify each particular boundary point by assigning to it a configuration number which characterises that particular boundary configuration. The allocation of these numbers for a typical coastline is shown in figure 3.1.

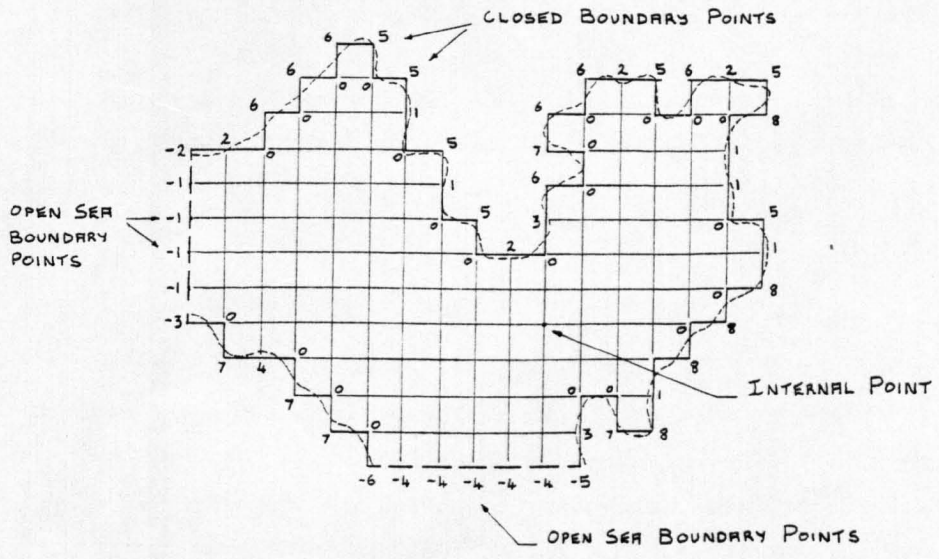

Figure 3.1

It should be noted from this figure that certain outlying points along the coastline may be assigned the configuration number 0 and are regarded as having identical conditions as those for an internal point.

With reference to figure 3.1 two types of boundary points may be distinguished in the following way:

a) Open boundary points;

These points delineate an interface between the area under examination and the open sea through which tide and surge waves are propagated. This interface or open boundary is distinguished by the occurrence of flow with a component normal to the orientation of the open boundary.

Open boundary points are denoted by negative configuration numbers and the associated boundary conditions may be stated as follows;

$$\begin{aligned} &\text{Points } -1, -4 : \quad u \neq 0 \;, \quad v \neq 0 \\ &\text{Points } -2, -3 : \quad u \neq 0 \;, \quad v = 0 \\ &\text{Points } -5, -6 : \quad u = 0 \;, \quad v \neq 0 \end{aligned} \tag{3.1}$$

The zero velocities at some of these points are a result of the assumption that no flow occurs normal to the coastline.

If the problem area is an estuary it is assumed that the open boundary is sufficiently removed from the immediate influence of the estuary so that the effect of the oceanic tides can be represented as harmonic variations in surface displacements. This variation is established by referring to measurements obtained from tide recorders or by using Tide Tables.

b) Closed boundary points;

The series of points forming a closed boundary can be considered to represent a fixed vertical wall with a variation in height which corresponds to the total depth of water $(H+\eta)$ along the particular coastline. It is assumed that the component of velocity normal to this

boundary 'wall' is zero and so for points with the following configuration numbers, the boundary conditions are;

$$\begin{aligned} &\text{Points } 1,3: && u = 0 \;,\; V \neq 0 \\ &\text{Points } 2,4: && u \neq 0 \;,\; V = 0 \\ &\text{Points } 5,6,7,8: && u = 0 \;,\; V = 0 \end{aligned} \qquad (3.2)$$

Whereas with open boundary points only the required velocity components are computed from the finite difference scheme obtained from the characteristic conditions, both elevation and any non-zero velocity are computed at a closed boundary point.

3.2 BOUNDARY EQUATIONS BASED ON 90° CHARACTERISTICS

The values of the dependent variables at the boundary points may be obtained by considering the bicharacteristic directions proposed by Butler (1960), namely $\theta = \pi, \frac{3\pi}{2}, 0, \frac{\pi}{2}$. The derivation uses as a basis the characteristic conditions given by Townson (1974). These conditions have been stated as equations (2.40) to (2.44) and correspond to the four bicharacteristic directions and the particle path streamline. It is worth restating these conditions as follows;

$$g.\frac{z-z_1}{\Delta t} - c.\frac{u-u_1}{\Delta t} = -c^2.\frac{\partial V}{\partial y} - c.g.\frac{\partial H}{\partial x} + c.g.F_x \qquad (3.3)$$

$$g.\frac{z-z_2}{\Delta t} - c.\frac{V-V_2}{\Delta t} = -c^2.\frac{\partial u}{\partial x} - c.g.\frac{\partial H}{\partial y} + c.g.F_y \qquad (3.4)$$

$$g.\frac{z-z_3}{\Delta t} + c.\frac{u-u_3}{\Delta t} = -c^2.\frac{\partial V}{\partial y} + c.g.\frac{\partial H}{\partial x} - c.g.F_x \qquad (3.5)$$

$$g.\frac{z-z_4}{\Delta t} + c.\frac{V-V_4}{\Delta t} = -c^2.\frac{\partial u}{\partial x} + c.g.\frac{\partial H}{\partial y} - c.g.F_y \qquad (3.6)$$

$$g.\frac{z-z_5}{\Delta t} = -c^2.\left(\frac{\partial u}{\partial x} + \frac{\partial V}{\partial y}\right) \qquad (3.7)$$

Consider now the group of closed boundary points with configuration numbers 1, 2, 3, or 4 confining the analysis to boundary point number 1 which may be considered typical of these points.

At this boundary point not all the bicharacteristics intersect the initial value surface and so the spatial domain of dependence is reduced. As shown in figure 3.2 the domain corresponds to that portion of the base of the characteristic cone which is situated within the problem area and is determined by the geometric shape of the boundary.

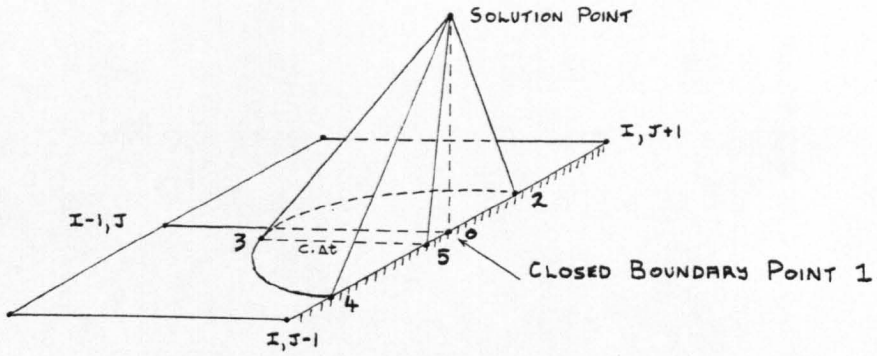

Figure 3.2

The solution for Z is formulated along the bicharacteristic paths 2, 3, 4 and 5 by combining the corresponding characteristic conditions. In this way the two unknowns $\frac{\partial u}{\partial x}$ and $\frac{\partial V}{\partial y}$ are eliminated from the problem and the solution is

$$Z = Z_3 + \tfrac{1}{2}(Z_2 + Z_4) - Z_5 - \tfrac{1}{2}\frac{c}{g}(V_2 - V_4 - 2.u_3) + c.\frac{\partial H_5}{\partial x}.\Delta t - c.F_x.\Delta t \qquad (3.8)$$

Since the boundary condition is $u = 0$, the term F_x is also zero valued.

Similarly by considering the bicharacteristics 2 and 4 and hence subtracting equation (3.6) from (3.4), the expression for velocity V is obtained as follows;

$$V = \tfrac{1}{2}(V_2 + V_4) - \tfrac{1}{2}\frac{g}{c}(Z_2 - Z_4) + g.\frac{\partial H_5}{\partial y}.\Delta t - g.F_y.\Delta t \qquad (3.9)$$

This equation is identical to that for an internal point.

A linear interpolation scheme $Q = Ax + By + C$ which is similar to that for an internal point is introduced to define a plane passing through the points $(I,J+1)$, $(I,J-1)$ and $(I-1,J)$. The coefficients have the form

$$A = \left[\tfrac{1}{2}\left(Q_{I,J+1} + Q_{I,J-1}\right) - Q_{I-1,J} \right] / \Delta S$$

$$B = \left(Q_{I,J+1} - Q_{I,J-1} \right) / 2.\Delta S$$

$$C = \tfrac{1}{2}\left(Q_{I,J+1} + Q_{I,J-1} \right) \qquad (3.10)$$

The coordinates of the bicharacteristic base points are

$$x_{2,4,5} = x_0 \quad , \quad x_3 = x_0 - c.\Delta t$$

$$y_{3,5} = y_0 - V.\Delta t \quad , \quad y_{2,4} = y_0 - (V \mp c).\Delta t$$

Hence with (x_0, y_0) as the origin of the local coordinate system

$$Z_2 = Z_5 + c.\Delta t.B_Z$$

$$Z_4 = Z_5 - c.\Delta t.B_Z$$

therefore $\frac{1}{2}(Z_2 + Z_4) = Z_5$ in equation (3.8). Similar substitutions for Z, U, V and H using this interpolation scheme transforms equations (3.8)and (3.9) to finite difference equations expressed in terms of the grid points. From the point of view of clarity, the essential form of these expressions is more apparent on considering the particular case $\frac{\partial H}{\partial x} = 0$. With this condition the boundary equations (3.8) and (3.9) become

$$Z = Z_3 - \frac{c^2}{g}.\Delta t.\left[\tfrac{1}{2}\left(U_{I,J+1} + U_{I,J-1}\right) - U_{I-1,J} \right] / \Delta S$$

$$- \frac{c^2}{g}.\Delta t.\left[V_{I,J+1} - V_{I,J-1} \right] / 2.\Delta S$$

$$V = V_5 - g.\Delta t.\left[\eta_{I,J+1} - \eta_{I,J-1}\right] / 2.\Delta S - g.F_y.\Delta t \qquad (3.11)$$

for a boundary point with a configuration number equal to 1. The values of Z_3 and V_5 are obtained from the interpolation scheme; for example

$$Z_3 = Z_5 - c.\Delta t.A_Z - V.\Delta t.B_Z$$

$$V_5 = V_0 - V.\Delta t.B_V \qquad \left(V_0 = \tfrac{1}{2}\left(V_{I,J+1} + V_{I,J-1}\right)\right)$$

The second type of closed boundary point is the 'corner' point which is represented by the configuration number 5, 6, 7 or 8. Point 5 is representative of such points and is now examined for the derivation of its boundary equations. With regard to figure 3.3 the only bicharacteristic paths inside the problem area are those with characteristic conditions given by equations (3.5), (3.6) and (3.7).

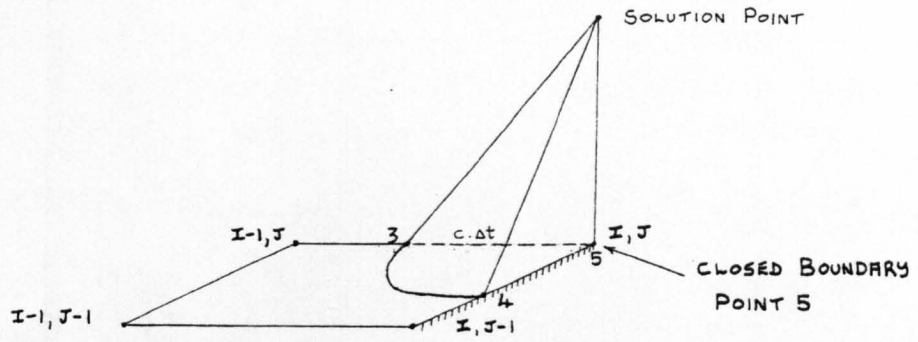

Figure 3.3

From these equations, expressions are required for the three unknown variables, the total depth Z and the partial derivatives $\frac{\partial U}{\partial x}$ and $\frac{\partial V}{\partial y}$ at point I,J. The velocities at this point are determined by the boundary condition U = V = 0. The solution for Z is obtained by adding equations (3.5) and (3.6) and subtracting equation (3.7), and is

$$Z = Z_3 + Z_4 - Z_5 + \frac{c}{g}\left(U_3 + V_4\right) + c.\Delta t\left(\frac{\partial H_5}{\partial x} + \frac{\partial H_5}{\partial y}\right) \qquad (3.12)$$

The partial derivatives of mean water depth may be expressed as

$$\frac{\partial H}{\partial x} = \frac{H_5 - H_3}{c.\Delta t} \quad , \quad \frac{\partial H}{\partial y} = \frac{H_5 - H_4}{c.\Delta t} \qquad (3.13)$$

and these substitutions in equation (3.12) produces

$$\eta = \eta_3 + \eta_4 - \eta_5 + \frac{c}{g}\left(U_3 + V_4\right) \qquad (3.14)$$

which is the expression for surface elevation above mean water level.

An interpolation scheme of the form $Q = Ax + By + C$ is introduced so as to produce a plane passing through the three points $(I-1,J)$, (I,J) and $(I,J-1)$. The interpolating coefficients may be expressed as

$$A = \frac{Q_{I,J} - Q_{I-1,J}}{\Delta S} \quad , \quad B = \frac{Q_{I,J} - Q_{I,J-1}}{\Delta S} \quad , \quad C = Q_{I,J} \qquad (3.15)$$

and are consistent with the expressions in equation (3.13). Introducing the interpolation scheme into equation (3.12) produces

$$Z = Z_3 + Z_4 - Z_5 - \frac{c^2}{g}.\Delta t\left(\frac{U_{I,J} - U_{I-1,J} + V_{I,J} - V_{I,J-1}}{\Delta S}\right) \qquad (3.16)$$

in which the finite difference expressions for $\frac{\partial H}{\partial x}$ and $\frac{\partial H}{\partial y}$ have been omitted to simplify the presentation.

An alternative derivation for the solution of Z is to assume that the terms $\frac{\partial u}{\partial x}$ and $\frac{\partial v}{\partial y}$ are not unknowns and can be represented by their finite difference approximations. Hence the solution is obtained by combining only equations (3.5) and (3.6) and neglecting the particle path equation. The characteristic solution for Z is therefore

$$Z = \tfrac{1}{2}(Z_3 + Z_4) + \tfrac{1}{2}\frac{c}{g}(u_3 + v_4) - \tfrac{1}{2}\frac{c}{g}\left(\frac{\partial u}{\partial x} + \frac{\partial v}{\partial y}\right)\cdot\Delta t + \tfrac{1}{2}\cdot c\cdot\left(\frac{\partial H}{\partial x} + \frac{\partial H}{\partial y}\right)\cdot\Delta t \quad (3.17)$$

Introducing the interpolation scheme transforms this equation into

$$Z = \tfrac{1}{2}(Z_3 + Z_4) - \frac{c^2}{g}\cdot\Delta t\cdot\left(\frac{u_{x,y} - u_{x-1,y} + v_{x,y} - v_{x,y-1}}{\Delta S}\right) \quad (3.18)$$

which is equivalent to the finite difference expression given by equation (3.16) provided $Z_5 = \frac{1}{2}(Z_3 + Z_4)$. This equation suggests that, at least for boundary point 5, the quantities $\frac{\partial u}{\partial x}$ and $\frac{\partial v}{\partial y}$ can indeed be approximated by means of their finite difference expressions $(u_{x,y} - u_{x-1,y})/\Delta S$ and $(v_{x,y} - v_{x,y-1})/\Delta S$ respectively.

At boundary points 6, 7 and 8 the solutions may be derived in a similar manner and have a form comparable to equation (3.18).

Open sea boundary points are responsible for generating tidal waves (and surge waves if required) into the area of the model. In the tidal problem such points ultimately establish harmonic conditions throughout the model. At this type of point the harmonic displacement of the sea surface is specified while the velocity components U or V or both remain as unknown dependent variables.

Considering a point with the configuration number-1 as typical of such open boundary points, the system of bicharaceristics is as shown in figure 3.4.

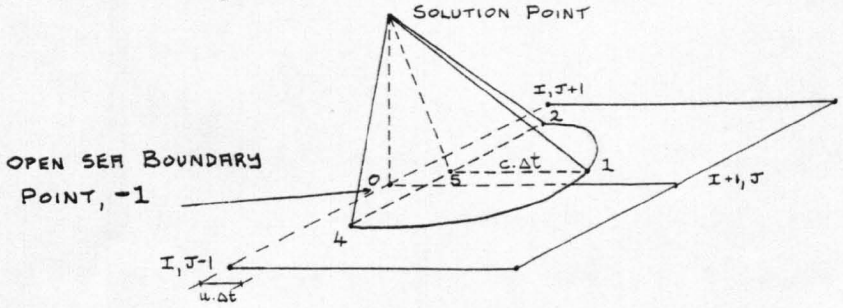

Figure 3.4

The system consists of all the bicharacteristics except number 3 and so equation (3.5) is not included in the characteristic conditions.

The remaining four conditions may be combined to provide a solution for the unknowns U and V whilst eliminating the unknowns $\frac{\partial U}{\partial x}$ and $\frac{\partial V}{\partial y}$ from the conditions themselves. As a result the solution becomes

$$U = U_1 + \frac{g}{c}(Z - Z_1) + \tfrac{1}{2}(V_2 - V_4) + g \cdot \frac{\partial H_s}{\partial x} \cdot \Delta t - g \cdot F_x \cdot \Delta t$$

$$V = \tfrac{1}{2}(V_2 + V_4) - \tfrac{1}{2}\frac{g}{c} \cdot (Z_2 - Z_4) + g \cdot \frac{\partial H_s}{\partial y} \cdot \Delta t - g \cdot F_y \cdot \Delta t$$

with

$$Z = a \cdot \cos(\sigma t) + H_o \qquad (3.19)$$

The derivation of the velocity component V is identical to that given for boundary point 1.

The interpolation scheme $Q = Ax + By + C$ with the values of the coefficients given by equation (3.10) applied to boundary point 1 is also applicable to the present case. Incorporating this interpolation scheme into the velocity equations in (3.19) produces

$$U = U_1 + \frac{g}{c} \cdot (Z - Z_1) + c \cdot \Delta t \cdot \frac{(V_{x,y+1} - V_{x,y-1})}{2 \cdot \Delta s} + g \frac{\partial H_s}{\partial x} \cdot \Delta t - g \cdot F_x \cdot \Delta t \qquad (3.20)$$

$$V = V_5 - g \cdot \Delta t \cdot \frac{(\eta_{x,y+1} - \eta_{x,y-1})}{2 \cdot \Delta s} - g \cdot F_y \cdot \Delta t$$

In the previous equations the components of friction incorporated in the terms F_x and F_y (in dimensionless form) are neglected at the open boundary points since the tidal elevation whether measured or taken from tables implicitly includes this effect. The velocities are therefore computed from these 'frictionalised' elevations and so explicit friction terms need not be present.

In equations (3.20) the values of U_1 and Z_1 are interpolated from the grid point values as follows (using Q as the general dependent variable)

$$Q_1 = Q_5 - c \cdot \Delta t \cdot \left(Q_{x+1,y} - \tfrac{1}{2}\left(Q_{x,y+1} + Q_{x,y-1} \right) \right) / \Delta s \qquad (3.21)$$

where $Q_5 = \tfrac{1}{2}(Q_{x,y+1} + Q_{x,y-1}) - U \cdot \Delta t (Q_{x+1,y} - \tfrac{1}{2}(Q_{x,y+1} + Q_{x,y-1}) / \Delta s$

$$- V \cdot \Delta t \left(Q_{x,y+1} - Q_{x,y-1} \right) / 2 \cdot \Delta s \qquad (3.22)$$

It is apparent then that the particle path point 5 has coordinates $(-U \cdot \Delta t, -V \cdot \Delta t)$ relative to the boundary point under discussion. If this boundary point is situated in deep sea the values of the particle velocities will be very small compared to the wave celerity therefore

the particle point 5 will lie very close to the boundary point. On the flood tide ($u>0$) the convective displacement $x_5 = -u.\Delta t$ will be negative and so the particle path point will lie outside the area of the model. The situation is more satisfactory on the ebb tide since $u<0$ and the particle path lies inside the model. Hence equation (3.22) is only strictly appropriate for an ebb tide situation. Ideally the central difference expression $u.\Delta t(Q_{I+1,J} - Q_{I-1,J})/2.\Delta S$ is required in equations (3.21) and (3.22) however the data at point $Q_{I-1,J}$ is unavailable and so a forward difference is used instead. As a result of the position of the particle path on the flow tide this forward difference is strictly not applicable and so an extrapolation is required. If it is assumed that the value $(\frac{\partial Q}{\partial x})_5$ outside the model is equivalent to the value $(\frac{\partial Q}{\partial x})_5$ inside the model then the respective backward and forward differences may be equated

$$\frac{\frac{1}{2}\left(Q_{I,J+1} + Q_{I,J-1}\right) - Q_{I-1,J}}{\Delta S} = \frac{Q_{I+1,J} - \frac{1}{2}\left(Q_{I,J+1} + Q_{I,J-1}\right)}{\Delta S} \qquad (3.23)$$

This assumption appears to be reasonable provided, as already mentioned, the particle path point is positioned close to the boundary point. Only then can equation (3.22) be considered a good approximation to the exact interpolation of the particle path point on the flood tide. In contrast, if the open boundary was positioned in shallow water where the fluid velocities U and V were of substantial magnitude compared to the wave celerity then a more accurate extrapolation scheme would have to be devised.

The final type of boundary point to be examined results from the junction between a closed and open sea boundary. A typical example of such a point is shown in figure 3.5 and has the configuration number -2.

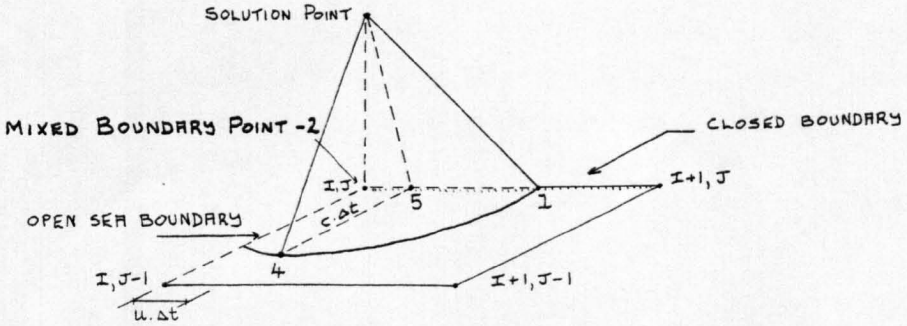

Figure 3.5

The boundary condition at this point is V=0 and since the total elevation is a known harmonic function then the three unknown variables are u, $\frac{\partial u}{\partial x}$ and $\frac{\partial v}{\partial y}$. There are three bicharacteristics 1, 4 and 5 with associated characteristic conditions namely equations (3.3), (3.6) and (3.7). Combining these equations so as to eliminate the terms $\frac{\partial u}{\partial x}$ and $\frac{\partial v}{\partial y}$ gives a solution of the form

$$u = u_1 - v_4 + \frac{g}{c}\left(z - z_1 - z_4 + z_5\right) + g\left(\frac{\partial H_5}{\partial x} + \frac{\partial H_5}{\partial y}\right).\Delta t - g.F_x.\Delta t$$

with $v = 0$

$$z = a.\cos(\sigma t) + H_0 \qquad (3.24)$$

Using the interpolation scheme $Q = Ax + By + C$ and taking the values of the coefficients as those for a 'corner' point given in equation (3.15), the interpolation of the intermediate points in the above equation is straightforward. The final expression for the velocity component u may be expressed in terms of η by assuming the term $(H_5 - H_0)$ is negligible. Hence

$$u = u_1 + \frac{g}{c}\left(\eta - \eta_1 - \eta_4 + \eta_5\right) - c.\Delta t.\left(\frac{V_{I,J} - V_{I,J-1}}{\Delta S}\right) - g.F_x.\Delta t$$

with (3.25)

$$u_1 = u_{I,J} + c.\Delta t.\left(\frac{u_{I+1,J} - u_{I,J}}{\Delta S}\right)$$

$$\eta_4 = \eta_{I,J} - c.\Delta t\left(\frac{\eta_{I,J} - \eta_{I,J-1}}{\Delta S}\right)$$

$$\eta_5 = \eta_{I,J} - u.\Delta t.\left(\frac{\eta_{I+1,J} - \eta_{I,J}}{\Delta S}\right)$$

The position of particle path point 5 on the flood tide has the same convective displacement $-u.\Delta t$ in the x direction as that of boundary point -1. Hence the same assumptions regarding extrapolation have been made for boundary point -2.

An analysis of boundary points -3, -5, -6 follows the same principles governing the derivation of equation (3.24) and the final form is also similar. For example the solution at boundary point -3 is

$$u = u_1 + v_2 + \frac{g}{c}\left(z - z_1 - z_2 + z_5\right) + g\left(\frac{\partial H_5}{\partial x} + \frac{\partial H_5}{\partial y}\right) - g.F_x.\Delta t$$

$$v = 0 \qquad (3.26)$$

$$z = a.\cos(\sigma t) + H_0$$

With the boundary conditions formulated the next logical step would be to examine their stability. However a stability analysis at the boundary points is extremely difficult. One possible means of analysis is to consider the Ryandiki - Godunov criterion although Richtmyer and Morton (1967) have commented that it is 'fearfully complicated'. Unfortunately the condition is only a necessary one and may not be sufficient for ensuring complete stability. The von Neumann stability analysis is reasonably straightforward in its application but does not account for the various boundary conditions and therefore is not completely rigorous. It is notable that the C.F.L. condition, by virtue of being applicable to any specific point, gives requirements for boundary points in the same manner as for an internal point.

In practice simple numerical tests have been used to establish stability and consistency of the internal point. Once this has been verified, any signs of instability on further application of the scheme can only be assumed to originate from the boundary conditions. For example in section 4.3.1 the internal point and boundary conditions were stable in test 7. The same numerical scheme for the internal points was used in test 8. Since the results from test 8 showed signs of instability then this can only be attributed to changing the boundary conditions from those in test 7.

Specific tests in Chapter 4 are aimed at establishing the accuracy of the 90° characteristic numerical scheme by simulating idealised motion and comparing results with the governing analytical solution. In these tests consistency of the numerical scheme with the simplifying assumptions used to derive the analytical solution requires that at all grid points numerical celerity be calculated from mean water depth and that convective terms be removed from the prescribed characteristic equations.

As an example of the accuracy of the 90° characteristic scheme, the simulation of a two-dimensional seiche in test 41 (section 4.4.2) gave results very close to those from the analytical solution. However in test 39 a numerical scheme based on 45° characteristics reproduces exactly the motion presribed by the analytical solution. The difference in results obtained from the two schemes lies in the differing boundary equations. Hence the 45° characteristic boundary equations are presented

in the next section so that the significance of their difference from the 90° characteristic boundary equations may be better understood.

3.3 BOUNDARY EQUATIONS BASED ON 45° CHARACTERISTICS

The 45° characteristic equations as developed by Matsoukis (1980) were shown by him to be theoretically superior and slightly more accurate in practice than the 90° characteristic scheme. It is emphasised that both schemes have identical form at an internal point and differ only at the boundary points. To formulate the boundary equations, the 45° characteristic conditions must first be considered. These conditions are obtained from equation (2.32) by taking values of the parametric angle as

$$\theta_{1'} = \frac{5\pi}{4} \quad , \quad \theta_{2'} = \frac{7\pi}{4} \qquad \theta_{3'} = \frac{\pi}{4} \quad , \quad \theta_{4'} = \frac{3\pi}{4} \tag{3.27}$$

which correspond to the bicharacteristics shown in figure 3.6

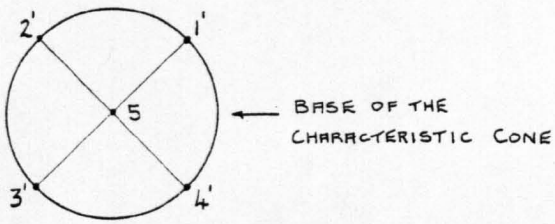

Figure 3.6

The characteristic conditions have the form

$$g\left(\frac{z-z_{1'}}{\Delta t}\right) - \frac{\sqrt{2}}{2}\cdot c\cdot\left(\frac{u-u_{1'}}{\Delta t}\right) - \frac{\sqrt{2}}{2}\cdot c\cdot\left(\frac{v-v_{1'}}{\Delta t}\right) = -c\cdot g\cdot\frac{\sqrt{2}}{2}\left(\frac{\partial H}{\partial x}+\frac{\partial H}{\partial y}\right)$$
$$-\frac{c^2}{2}\left(\frac{\partial u}{\partial x}-\frac{\partial u}{\partial y}-\frac{\partial v}{\partial x}+\frac{\partial v}{\partial y}\right) - \frac{\sqrt{2}}{2}\cdot c\cdot g\cdot\left(-F_x - F_y\right) \tag{3.28}$$

$$g\cdot\left(\frac{z-z_{2'}}{\Delta t}\right) + \frac{\sqrt{2}}{2}\cdot c\cdot\left(\frac{u-u_{2'}}{\Delta t}\right) - \frac{\sqrt{2}}{2}\cdot c\cdot\left(\frac{v-v_{2'}}{\Delta t}\right) = -c\cdot g\cdot\frac{\sqrt{2}}{2}\left(-\frac{\partial H}{\partial x}+\frac{\partial H}{\partial y}\right)$$
$$-\frac{c^2}{2}\left(\frac{\partial u}{\partial x}+\frac{\partial u}{\partial y}+\frac{\partial v}{\partial x}+\frac{\partial v}{\partial y}\right) - \frac{\sqrt{2}}{2}\cdot c\cdot g\cdot\left(F_x - F_y\right) \tag{3.29}$$

$$g\cdot\left(\frac{z-z_{3'}}{\Delta t}\right) + \frac{\sqrt{2}}{2}\cdot c\cdot\left(\frac{u-u_{3'}}{\Delta t}\right) + \frac{\sqrt{2}}{2}\cdot c\cdot\left(\frac{v-v_{3'}}{\Delta t}\right) = c\cdot g\cdot\frac{\sqrt{2}}{2}\left(\frac{\partial H}{\partial x}+\frac{\partial H}{\partial y}\right)$$
$$-\frac{c^2}{2}\left(\frac{\partial u}{\partial x}-\frac{\partial u}{\partial y}-\frac{\partial v}{\partial x}+\frac{\partial v}{\partial y}\right) - \frac{\sqrt{2}}{2}\cdot c\cdot g\cdot\left(F_x + F_y\right) \tag{3.30}$$

$$g(z-z_{4'}) - \frac{\sqrt{2}}{2}\cdot c\cdot(u-u_{4'}) + \frac{\sqrt{2}}{2}\cdot c\cdot(v-v_{4'}) = c\cdot g\cdot\frac{\sqrt{2}}{2}\left(-\frac{\partial H}{\partial x}+\frac{\partial H}{\partial y}\right)$$
$$-\frac{c^2}{2}\left(\frac{\partial u}{\partial x}+\frac{\partial u}{\partial y}+\frac{\partial v}{\partial x}+\frac{\partial v}{\partial y}\right) - \frac{\sqrt{2}}{2}\cdot c\cdot g\cdot(-F_x+F_y) \quad (3.31)$$

and the particle path equation is

$$g\left(\frac{z-z_5}{\Delta t}\right) = -c^2\left(\frac{\partial u}{\partial x}+\frac{\partial v}{\partial y}\right) \quad (3.32)$$

The derivation of the 45° boundary equations is similar to that for 90° characteristics. However in the former case the partial derivatives are this time treated as known variables. This assumes that the interpolating coefficients A and B are close approximations to the partial derivatives which is reasonable provided the grid size is sufficiently small.

Consider again boundary point 1 with the boundary condition U = 0 and the 45° bicharacteristics as shown in figure 3.7

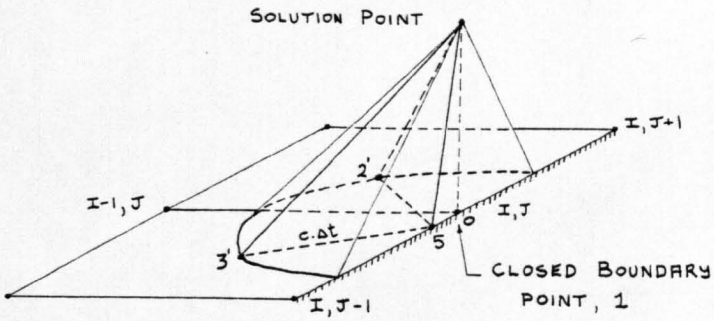

Figure 3.7

There are two bicharacteristics available (since the particle path is not really a bicharacteristic) and two unknown variables Z and V. Hence by adding and subtracting equations (3.29) and (3.30) the respective solutions for Z and V are as follows

$$z = \tfrac{1}{2}(z_{2'}+z_{3'}) + \frac{\sqrt{2}}{4}\frac{c}{g}(u_{2'}+u_{3'}) + \frac{\sqrt{2}}{4}(v_{3'}-v_{2'})$$
$$-\tfrac{1}{2}\frac{c^2}{g}\left(\frac{\partial u}{\partial x}+\frac{\partial v}{\partial y}\right)\cdot\Delta t + \frac{\sqrt{2}}{2}\cdot c\cdot\Delta t\cdot\frac{\partial H}{\partial x} \quad (3.33)$$

$$v = \tfrac{1}{2}(v_{2'}+v_{3'}) - \tfrac{1}{2}(u_{2'}-u_{3'}) + \frac{\sqrt{2}}{2}\cdot\frac{g}{c}\cdot(z_{3'}-z_{2'})$$
$$+\frac{\sqrt{2}}{2}\cdot c\cdot\Delta t\left(\frac{\partial u}{\partial y}+\frac{\partial v}{\partial x}\right) + g\cdot\Delta t\cdot\frac{\partial H}{\partial y} - g\cdot\Delta t\cdot F_y \quad (3.34)$$

These solutions have been obtained without the involvement of the particle

path equation.

With the interpolation scheme $Q = Ax + By + C$ and the coefficients given in equation (3.10) (where A and B are approximations to $\frac{\partial Q}{\partial x}$ and $\frac{\partial Q}{\partial y}$ respectively) the following expressions are obtained

$$u_{3'} = -c.\frac{\sqrt{2}}{2}.\Delta t.\frac{\partial u}{\partial x} - c.\frac{\sqrt{2}}{2}.\Delta t.\frac{\partial u}{\partial y} + u_5$$

$$u_{2'} = -c.\frac{\sqrt{2}}{2}.\Delta t.\frac{\partial u}{\partial x} + c.\frac{\sqrt{2}}{2}.\Delta t.\frac{\partial u}{\partial y} + u_5 \quad (u_5 = 0)$$

hence $$\frac{\sqrt{2}}{4}.\frac{c}{g}\left(u_{2'} + u_{3'}\right) = -\tfrac{1}{2}\frac{c^2}{g}.\frac{\partial u}{\partial x}.\Delta t$$

similarly $$\frac{\sqrt{2}}{4}.\frac{c}{g}\left(v_{3'} - v_{2'}\right) = -\tfrac{1}{2}\frac{c^2}{g}.\frac{\partial v}{\partial y}.\Delta t$$

With these substitutions in equation (3.33) and taking $\frac{\partial H}{\partial x} = 0$ for convenience of presentation the solution for Z is

$$z = \tfrac{1}{2}\left(z_{2'} + z_{3'}\right) - \frac{c^2}{g}.\Delta t.\frac{\partial u}{\partial x} - \frac{c^2}{g}.\Delta t.\frac{\partial v}{\partial y}$$

which may be written as

$$z = \tfrac{1}{2}\left(z_{2'} + z_{3'}\right) - \frac{c^2}{g}.\Delta t.\left[\tfrac{1}{2}\left(u_{x,y+1} + u_{x,y-1}\right) - u_{x-1,y}\right]/\Delta s$$
$$- \frac{c^2}{g}.\Delta t\left[v_{x,y+1} - v_{x,y-1}\right]/2.\Delta s \qquad (3.35)$$

and has a form similar to its 90° characteristic alternative (equation (3.11)).

Equation (3.34) may be expressed in terms of η as

$$v = \tfrac{1}{2}\left(v_{2'} + v_{3'}\right) - \tfrac{1}{2}\left(u_{2'} - u_{3'}\right) + \frac{\sqrt{2}}{2}.\frac{g}{c}.\left(\eta_{3'} - \eta_{2'}\right)$$
$$+ \frac{\sqrt{2}}{2}.c.\Delta t.\left(\frac{\partial u}{\partial y} + \frac{\partial v}{\partial x}\right) - g.\Delta t.F_y \qquad (3.36)$$

The interpolation scheme gives

$$v_{2'} = v_5 - \frac{\sqrt{2}}{2}.c.\Delta t.\frac{\partial v}{\partial x} + \frac{\sqrt{2}}{2}.c.\Delta t.\frac{\partial v}{\partial y}$$

$$v_{3'} = v_5 - \frac{\sqrt{2}}{2}.c.\Delta t.\frac{\partial v}{\partial x} - \frac{\sqrt{2}}{2}.c.\Delta t.\frac{\partial v}{\partial y}$$

hence $$\tfrac{1}{2}\left(v_{2'} + v_{3'}\right) = v_5 - \frac{\sqrt{2}}{2}.c.\Delta t.\frac{\partial v}{\partial x}$$

and similarly $$\tfrac{1}{2}\left(u_{2'} - u_{3'}\right) = \frac{\sqrt{2}}{2}.c.\Delta t.\frac{\partial u}{\partial y}$$

Substituting these terms in equation (3.36) gives

$$V = V_5 - g \cdot \Delta t \left[\eta_{I,J+1} - \eta_{I,J-1} \right] / 2 \cdot \Delta s - g \cdot \Delta t \cdot F_y \qquad (3.37)$$

which is equivalent to the velocity expression for an internal point and also to that derived using 90° characteristics.

Both 90° and 45° characteristics yield solutions at the boundary points where the absence of certain bicharacteristics causes the solution for total elevation to be formulated in terms of the characteristic path points. This contrasts with the solution for an internal point where the form of the equations indicates that the solution propagates along the particle path. It is therefore at the boundary points that the characteristic conditions have their most important role and hence the importance of establishing a method which considers the correct position of the bicharacteristics.

The boundary point with a configuration number of 5 is typical of a 'corner' point which has as boundary conditions U=0,V=0. In figure 3.8 the single bicharacteristic is depicted and its characteristic condition (equation (3.30)) provides the solution directly for Z.

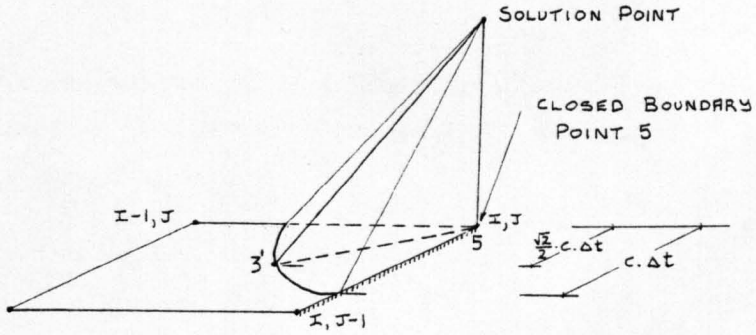

Figure 3.8

Hence

$$Z = Z_{3'} + \frac{\sqrt{2}}{2} \cdot \frac{c}{g} \left(U_{3'} + V_{3'} \right) + \frac{\sqrt{2}}{2} \cdot c \cdot \left(\frac{\partial H}{\partial x} + \frac{\partial H}{\partial y} \right) \cdot \Delta t$$
$$- \tfrac{1}{2} \cdot \frac{c^2}{g} \left(\frac{\partial U}{\partial x} + \frac{\partial V}{\partial y} \right) \cdot \Delta t + \tfrac{1}{2} \cdot \frac{c^2}{g} \left(\frac{\partial U}{\partial y} + \frac{\partial V}{\partial x} \right) \qquad (3.38)$$

Interpolating for point 3' using the equation $Q = Ax + By + C$ produces

$$U_{3'} \approx U_5 - \frac{\sqrt{2}}{2} \cdot c \cdot \Delta t \cdot \frac{\partial U}{\partial x} - \frac{\sqrt{2}}{2} \cdot c \cdot \Delta t \cdot \frac{\partial U}{\partial y} \qquad (U_5 = 0)$$

$$V_{3'} = V_5 - \frac{\sqrt{2}}{2} \cdot c \cdot \Delta t \cdot \frac{\partial V}{\partial x} - \frac{\sqrt{2}}{2} \cdot c \cdot \Delta t \cdot \frac{\partial V}{\partial y} \qquad (V_5 = 0)$$

which combines to give

$$\frac{\sqrt{2}}{2} \cdot \frac{c}{g} \cdot \left(u_{3'} + v_{3'} \right) = -\frac{1}{2} \cdot \frac{c}{g} \cdot \Delta t \left(\frac{\partial u}{\partial x} + \frac{\partial u}{\partial y} + \frac{\partial v}{\partial x} + \frac{\partial v}{\partial y} \right)$$

Substituting this expression into equation (3.38) and expressing

$$\frac{\sqrt{2}}{2} \cdot c \cdot \Delta t \cdot \left(\frac{\partial H}{\partial x} + \frac{\partial H}{\partial y} \right) = H_5 - H_{3'}$$

results in

$$\eta = \eta_{3'} - \frac{c^2}{g} \left(\frac{\partial u}{\partial x} + \frac{\partial v}{\partial y} \right) \cdot \Delta t$$

With the coefficients of the interpolation scheme taking the values given in equation (3.15) the solution takes the final form

$$\eta = \eta_{3'} - \frac{c^2}{g} \cdot \Delta t \left(\frac{u_{I,J} - u_{I-1,J} + v_{I,J} - v_{I,J-1}}{\Delta S} \right) \qquad (3.39)$$

where $c^2/g = Z_{I,J}$

In equation (3.39) the form of the difference expressions is identical to equation (3.16) however the latter equation was derived using the approach whereby the partial derivative terms were considered to be unknown. The equivalence between the finite difference expressions in both equations using two different approaches suggests an equivalence between the partial derivatives and their finite difference representations.

Consider now the set of open boundary points represented by configuration number -1 with its bicharacteristics as shown in figure 3.9.

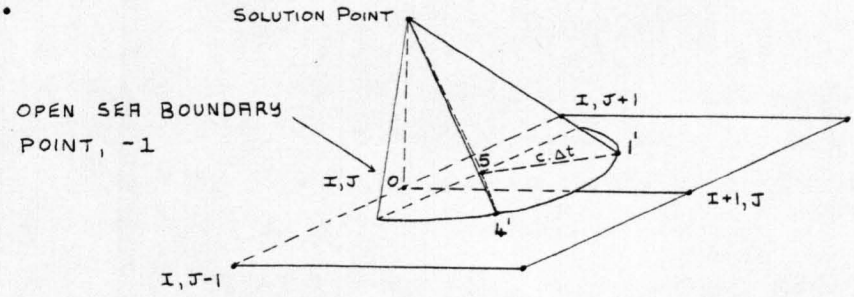

Figure 3.9

Since the surface displacement Z is a known harmonic function the characteristic conditions along the two bicharacteristics may be combined to give solutions for the unknowns U and V. The solution for the V component of velocity is formulated by subtracting equation (3.29) from (3.31) to give

$$V = \tfrac{1}{2}(V_{1'} + V_{4'}) + \tfrac{1}{2}(U_{1'} - U_{4'}) - \frac{\sqrt{2}}{2}\cdot\frac{g}{c}(\eta_{1'} - \eta_{4'}) - \frac{\sqrt{2}}{2}\cdot c.\Delta t\left(\frac{\partial U}{\partial x} + \frac{\partial V}{\partial y}\right) \quad (3.40)$$

By introducing the interpolation scheme $Q = Ax + By + C$ with coefficients given by equation (3.10), the solution for V becomes

$$V = V_5 - g.\Delta t.(\eta_{x,y+1} - \eta_{x,y-1})/2.\Delta s \quad (3.41)$$

This expression is identical to that obtained by considering 90° characteristics.

In the same way equations (3.29) and (3.31) may be added to produce the solution for U namely

$$U = \tfrac{1}{2}(U_{1'} + U_{4'}) + \tfrac{1}{2}(V_{1'} - V_{4'}) + \frac{\sqrt{2}}{2}\cdot\frac{g}{c}(2Z - Z_{1'} - Z_{4'}) + g\cdot\Delta t.\frac{\partial H}{\partial x} + \frac{\sqrt{2}}{2}\cdot c.\Delta t.\left(\frac{\partial U}{\partial x} + \frac{\partial V}{\partial y}\right) \quad (3.42)$$

A further development is to incorporate the particle path equation (3.32) to give

$$U = \tfrac{1}{2}(U_{1'} + U_{4'}) + \tfrac{1}{2}(V_{1'} - V_{4'}) + \frac{\sqrt{2}}{2}\cdot\frac{g}{c}\cdot(Z + Z_5 - Z_{1'} - Z_{4'}) + g\Delta t.\frac{\partial H}{\partial x} \quad (3.43)$$

The values at the intermediate points 1 to 5 may be expressed in terms of the grid point values using the interpolation scheme as follows

$$\begin{aligned} \tfrac{1}{2}(U_{1'} + U_{4'}) &= U_5 + \frac{\sqrt{2}}{2}\cdot c.\Delta t.\frac{\partial U}{\partial x} \\ \tfrac{1}{2}(V_{1'} - V_{4'}) &= \frac{\sqrt{2}}{2}\cdot c.\Delta t.\frac{\partial V}{\partial y} \\ \tfrac{1}{2}(Z_{1'} + Z_{4'}) &= Z_5 + \frac{\sqrt{2}}{2}\cdot c.\Delta t.\frac{\partial Z}{\partial x} \end{aligned} \quad (3.44)$$

As with the 90° characteristic scheme at this boundary point, the intermediate point 5 will lie outside the model during the flow tide. The assumptions mentioned previously regarding the extrapolation procedure are also applicable to 45° characteristics.

Finally, the boundary point -2 is examined since it represents a mixed open and closed boundary system. The boundary conditions are

$$\begin{aligned} Z &= a.\cos(\sigma t) + H_o \\ V &= 0 \end{aligned}$$

so the only unknown is the velocity component U. Its solution is obtained from the characteristic condition (equation (3.31)) directly by considering the bicharacteristic shown in figure 3.10.

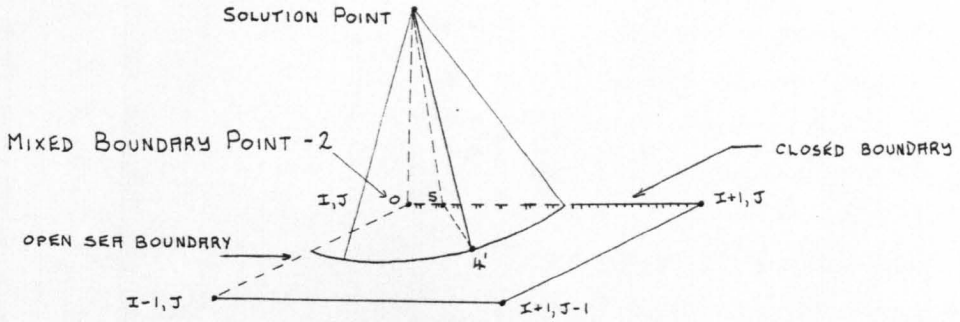

Figure 3.10

The solution for U is therefore

$$u = u_{4'} - V_{4'} + \frac{\sqrt{2}g}{c}(\eta - \eta_{4'}) + \frac{\sqrt{2}g}{c}(H - H_5) + \frac{\sqrt{2}}{2}c.\Delta t.\left(\frac{\partial u}{\partial x} + \frac{\partial u}{\partial y} + \frac{\partial V}{\partial x} + \frac{\partial V}{\partial y}\right) \quad (3.45)$$

With the interpolation scheme $Q = Ax + By + C$ and the coefficients given in equation (3.15) the values at the intermediate points may be expressed as

$$u_{4'} = u_5 + \frac{\sqrt{2}}{2}\cdot c.\Delta t.\frac{\partial u}{\partial x} - \frac{\sqrt{2}}{2}\cdot c.\Delta t.\frac{\partial u}{\partial y}$$

$$V_{4'} = V_5 + \frac{\sqrt{2}}{2}\cdot c.\Delta t.\frac{\partial V}{\partial x} - \frac{\sqrt{2}}{2}\cdot c.\Delta t.\frac{\partial V}{\partial y} \qquad (V_5 = 0)$$

Hence $$(u_{4'} - V_{4'}) = u_5 - V_5 + \frac{\sqrt{2}}{2}\cdot c.\Delta t.\left(\frac{\partial u}{\partial x} - \frac{\partial u}{\partial y} - \frac{\partial V}{\partial x} + \frac{\partial V}{\partial y}\right)$$

If the term $(H-H_5)$ is neglected then the interpolations transform equation (3.45) into

$$u = u_5 + \frac{\sqrt{2}.g}{c}(\eta - \eta_{4'}) + \sqrt{2}.c.\Delta t.\left(\frac{\partial u}{\partial x} + \frac{\partial V}{\partial y}\right)$$

which may be written as

$$u = u_5 + \frac{\sqrt{2}.g}{c}(\eta - \eta_{4'}) + \sqrt{2}.c.\Delta t.\left(\frac{u_{I+1,J} - u_{I,J} + V_{I,J} - V_{I,J-1}}{\Delta s}\right) \quad (3.46)$$

The essential feature in deriving this and the other solutions at the boundary points is that terms such as $\frac{\partial u}{\partial y}, \frac{\partial V}{\partial x}$ appear in the characteristic form of the solution which subsequently cancel with the terms in the interpolated expressions for the intermediate points. Hence the final form only contains terms such as $\frac{\partial u}{\partial x}$ and $\frac{\partial V}{\partial y}$ which may be expressed in terms of the grid points.

3.4 CONSTANT DEPTH CONSIDERATIONS

The simulation of a two-dimensional seiche in a frictionless basin of constant depth provides a good illustration of the success or otherwise of the integration and interpolation procedures based on either 90° or 45° characteristics. The results of the tests using both numerical schemes are presented in section 4.4.2 and suggest that the 45° characteristic scheme is the only one which can successfully reproduce the analytical motion. The greater accuracy produced using a 45° characteristic scheme compared with a 90° characteristic one can only be attributed to the boundary equations since only at these points do the numerical schemes differ.

The analytical solution is only produced when the numerical scheme is linearised and when boundary point 1 has the following equations

$$Z = Z_o - H_o.\Delta t.\left[\tfrac{1}{2}\left(U_{x,y+1} - U_{x,y-1}\right) - U_{x-1,y}\right]/\Delta s$$
$$- H_o.\Delta t.\left[V_{x,y+1} - V_{x,y-1}\right]/2.\Delta s$$

$$V = V_o - g.\Delta t.\left(\eta_{x,y+1} - \eta_{x,y-1}\right)/2.\Delta s \qquad (3.47)$$

$$U = 0$$

where $$Z_o = \tfrac{1}{4}\left(Z_{x,y+1} + Z_{x,y-1} + 2.Z_{x-1,y}\right) \qquad (3.48)$$

$$V_o = \tfrac{1}{4}\left(V_{x,y+1} + V_{x,y-1} + 2.V_{x-1,y}\right) \qquad (3.49)$$

and when boundary point 5 has the following conditions

$$Z = Z_o - H_o.\Delta t.\left(U_{x+1,y} - U_{x,y} + V_{x,y} - V_{x,y-1}\right)/\Delta s \qquad (3.50)$$

$$U = V = 0$$

where $$Z_o = \tfrac{1}{2}\left(Z_{x-1,y} + Z_{x,y-1}\right) \qquad (3.51)$$

It remains now to show that these boundary equations can only be derived from 45° characteristics and not from 90° characteristics.

It has already been mentioned that the CFL criterion is not merely a stability condition but at its limit gives the relationship between numerical and physical celerity. In x-y-t space this relationship is $c = \frac{\sqrt{2}}{2}.\frac{\Delta s}{\Delta t}$ and it is essential that this condition is maintained

so as to ensure an equivalence between the numerical and physical celerities. Therefore to accurately simulate two-dimensional seiche action the numerical timestep must be calculated as $\Delta t = \frac{\sqrt{2}}{2} \cdot \frac{\Delta s}{c}$.

Consider now the base of the characteristic cone at boundary point 1 obtained from 45° and 90° characteristics in figures 3.11(a) and 3.11(b) respectively

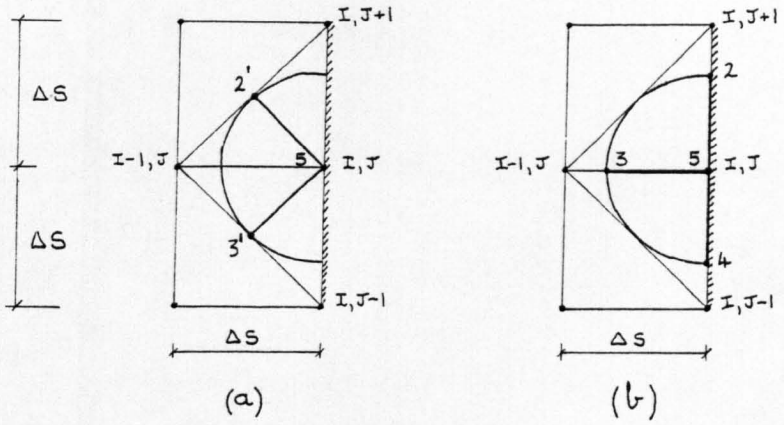

Figure 3.11

By observing the CFL criterion the domain of dependence of the differential scheme (the cone) is, at the limit, tangential to the domain of dependence of the difference scheme (the rhombus shown in figure 3.11). However only in the case of 45° characteristics do the base of the bicharacteristics lie at the tangent points.

The 45° characteristic solution for surface elevation (equation (3.35)) has been derived as

$$Z = \tfrac{1}{2}\left(Z_{2'} + Z_{3'}\right) - \frac{c^2}{g} \cdot \Delta t \cdot \left(\tfrac{1}{2}\left(u_{I,J+1} + u_{I,J-1}\right) - u_{I-1,J}\right) / \Delta s$$
$$- \frac{c^2}{g} \cdot \Delta t \cdot \left(V_{I,J+1} - V_{I,J-1}\right) / 2.\Delta s$$

This equation is in fact identical to equation (3.47) providing

$$Z_o = \tfrac{1}{2}\left(Z_{2'} + Z_{3'}\right)$$

Now by interpolating

$$Z_{2'} = Z_5 - \frac{\sqrt{2}}{2} \cdot c \cdot \Delta t \cdot \frac{\partial Z}{\partial x} + \frac{\sqrt{2}}{2} \cdot c \cdot \Delta t \cdot \frac{\partial Z}{\partial y}$$

$$Z_{3'} = Z_5 - \frac{\sqrt{2}}{2} \cdot c \cdot \Delta t \cdot \frac{\partial Z}{\partial x} - \frac{\sqrt{2}}{2} \cdot c \cdot \Delta t \cdot \frac{\partial Z}{\partial y}$$

and $Z_5 = C_z$ under linear considerations.

Hence $$\tfrac{1}{2}\left(Z_{2'} + Z_{3'}\right) = Z_5 - \frac{\sqrt{2}}{2} \cdot c.\Delta t \cdot \frac{\partial Z}{\partial x}$$

Since the CFL limiting timestep is used

$$\frac{\sqrt{2}}{2} \cdot c.\Delta t = \frac{\Delta s}{2}$$

and from the interpolating coefficients

$$Z_5 = \tfrac{1}{2}\left(Z_{x,y+1} + Z_{x,y-1}\right)$$

$$\frac{\partial Z}{\partial x} = \left(\tfrac{1}{2}\left(Z_{x,y+1} + Z_{x,y-1}\right) - Z_{x-1,y}\right)/\Delta s$$

Therefore

$$Z_5 - \frac{\sqrt{2}}{2} \cdot c.\Delta t \cdot \frac{\partial Z}{\partial x} = \tfrac{1}{2}\left(Z_{x,y+1} + Z_{x,y-1}\right) - \tfrac{1}{2}\left(\tfrac{1}{2}\left(Z_{x,y+1} + Z_{x,y-1}\right) - Z_{x-1,y}\right)$$

and so

$$\tfrac{1}{2}\left(Z_{2'} + Z_{3'}\right) = \tfrac{1}{4}\left(Z_{x,y+1} + Z_{x,y-1} + 2.Z_{x-1,y}\right)$$

as required.

Starting from equation (3.36) which is the characteristic solution for V and assuming that $(U_{2'} - U_{3'})$ is negligible at boundary point 1 and also that the motion is irrotational so that $\frac{\partial u}{\partial y} - \frac{\partial v}{\partial x} = 0$ then it is easily shown that

$$\tfrac{1}{2}\left(V_{2'} + V_{3'}\right) = \tfrac{1}{4}\left(V_{x,y+1} + V_{x,y-1} + 2.V_{x-1,y}\right)$$

and the solution for V in equation (3.47) is obtained.

It is now shown that the 90° characteristic scheme cannot form the required numerical scheme given in equation (3.47) for boundary point 1. Starting from the term Z_3 in equation (3.11), the interpolation scheme gives

$$Z_3 = Z_5 - c.\Delta t \cdot \frac{\partial Z}{\partial x}$$

which may be written in terms of the grid points as

$$Z_3 = \tfrac{1}{2}\left(Z_{x,y+1} + Z_{x,y-1}\right) - \frac{\sqrt{2}}{2}\left(\tfrac{1}{2}\left(Z_{x,y+1} + Z_{x,y-1}\right) - Z_{x-1,y}\right)$$

With $c.\Delta t = \frac{\sqrt{2}}{2}.\Delta s$ from the CFL condition the final form is

$$Z_3 = \tfrac{1}{4}\left((2-\sqrt{2})\left(Z_{x,y+1} + Z_{x,y-1}\right) + 2.\sqrt{2}.Z_{x-1,y}\right)$$

which is different from that in equation (3.48). It is precisely this term Z_3 that causes the 90° characteristic scheme to differ in construction from the 45° characteristic scheme.

A similar analysis is now performed at the corner boundary point 5 by considering the bicharacteristics as shown in figure 3.12.

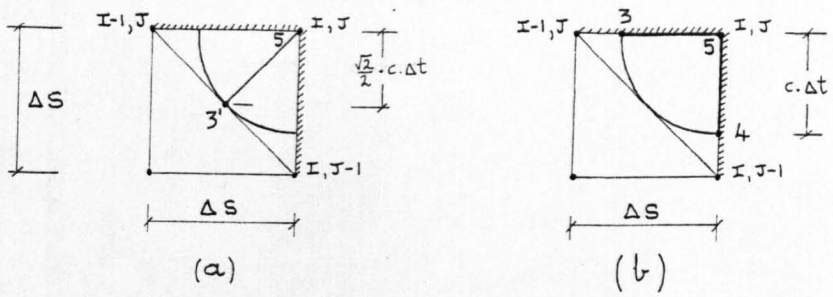

Figure 3.12

Again only the 45° characteristic coincides with the point where the difference and differential schemes are tangent and where a solution is possible (figure 3.12(a)). The 45° characteristic solution for surface elevation at the corner point has been shown to be

$$Z = Z_{3'} - \frac{c^2}{g} \cdot \Delta t \cdot \left(u_{I,J} - u_{I-1,J} + V_{I,J} - V_{I-1,J} \right) / \Delta S$$

which is equivalent to equation (3.50) providing $Z_{3'} = Z_o$

Now $Z_{3'} = Z_5 - \frac{\sqrt{2}}{2} \cdot c \cdot \Delta t \cdot \frac{\partial Z}{\partial x} - \frac{\sqrt{2}}{2} \cdot c \cdot \Delta t \cdot \frac{\partial Z}{\partial y}$

obtained from the interpolation scheme. Inserting the interpolating coefficients gives

$$Z_{3'} = Z_{I,J} - \frac{\sqrt{2}}{2} \cdot c \cdot \Delta t \cdot \left(Z_{I,J} - Z_{I-1,J} \right) / \Delta S - \frac{\sqrt{2}}{2} \cdot c \cdot \Delta t \cdot \left(Z_{I,J} - Z_{I,J-1} \right) / \Delta S$$

Since the CFL limiting timestep is used $\frac{\sqrt{2}}{2} \cdot c \cdot \Delta t = \frac{\Delta S}{2}$ and so

$$Z_{3'} = \tfrac{1}{2} \cdot \left(Z_{I-1,J} + Z_{I,J-1} \right)$$

as required by equation (3.51).

Similar considerations given to the 90° characteristic solution (equation (3.16)) namely

$$Z = Z_3 + Z_4 - Z_5 + \frac{c^2}{g} \cdot \Delta t \cdot \left(u_{I,J} - u_{I-1,J} + V_{I,J} - V_{I,J-1} \right) / \Delta S$$

shows that

$$Z_3 + Z_4 - Z_5 = 2 \cdot Z_5 - c \cdot \Delta t \cdot \frac{\partial Z}{\partial x} - c \cdot \Delta t \cdot \frac{\partial Z}{\partial y} - Z_5$$

Inserting the interpolating coefficients yields

$$Z_3 + Z_4 - Z_5 = Z_{I,J} - c \cdot \Delta t \cdot \left(Z_{I,J} - Z_{I-1,J} + Z_{I,J} - Z_{I,J-1} \right) / \Delta S$$

Since $c \cdot \Delta t = \frac{\sqrt{2}}{2} \cdot \Delta S$ from the CFL condition then the previous expression

gives something quite different from equation (3.51).

It is apparent then that at the boundary points the form of the solution depends on whether 90° or 45° characteristic equations are used. To reproduce exactly the analytical motion for the two-dimensional seiche the CFL condition must be adhered to in determining the numerical timestep. Additionally the correct solution is only obtained by taking characteristics at 45° angles.

It is worth considering at this stage the effect of the interpolation scheme in modifying the characteristic equations at the boundary points 1, 2, 3 and 4. Until now only one linear interpolation scheme has been used to derive the final form of the boundary equations at boundary point 1. The interpolation scheme (known as interpolation scheme 3) is of the form $Q = Ax + By + C$ and has the following coefficients

$$A = \left(\tfrac{1}{2}\left(Q_{x,y+1} + Q_{x,y-1}\right) - Q_{x-1,y}\right)/\Delta s$$

$$B = \left(Q_{x,y+1} - Q_{x,y-1}\right)/2.\Delta s$$

$$C = \tfrac{1}{2}\left(Q_{x,y+1} + Q_{x,y-1}\right)$$

From this interpolation scheme, equation (3.37) was derived at boundary point 1 which under linear, frictionless constant depth conditions becomes

$$V = V_o - g.\Delta t.\left(\eta_{x,y+1} - \eta_{x,y-1}\right)/2.\Delta s \qquad (3.52)$$

where

$$V_o = \tfrac{1}{2}\left(V_{x,y+1} + V_{x,y-1}\right) \qquad (3.53)$$

It has been shown that interpolation scheme 3 applied to the characteristic velocity equation (3.36) under the same conditions also produces equation (3.52) however V_o takes the form

$$V_o = \tfrac{1}{4}\left(V_{x,y+1} + V_{x,y-1} + 2.V_{x,y-1}\right) \qquad (3.54)$$

There are therefore two different forms of the solution for V_o and hence for V. It is found that in the case of an 'x-t' seiche in a basin of constant depth that the analytical motion is produced only when V_o has the form given in equation (3.54). This also means that at boundary points 2 and 4 the correct form for U_o in the equation

$$U = U_o - g.\Delta t.\left(\eta_{x+1,y} - \eta_{x-1,y}\right)/2.\Delta s \qquad (3.55)$$

must be

$$U_o = \tfrac{1}{4}.\left(U_{x+1,y} + U_{x-1,y} + 2.U_{x,y\mp1}\right) \qquad (3.56)$$

Under constant depth considerations at boundary point 1 the correct form for V_o (equation (3.54)) suggests an interpolation scheme $Q = Ax + By + C$ with coefficients

$$A = 0 \quad , \quad B = 0 \quad , \quad C = \tfrac{1}{4} \cdot \left(Q_{x,y+1} + Q_{x,y-1} + 2 \cdot Q_{x-1,y} \right)$$

where Q represents the dependent variables Z, U and V. This interpolation scheme which is only applicable in constant depth configurations (with the numerical timestep calculated from the CFL condition) is known as interpolation scheme 1. Its incorporation into boundary point 1 and its corresponding form incorporated into boundary points 2, 3 and 4 represents one necessary requirement for the successful simulation of the one and two-dimensional seiche motion in a basin of constant depth.

For the general case of an irregularly varying sea bed and under non-convective flow conditions the solution for the velocity components U and V at an internal point has been shown to be

$$U = U_o - g \cdot \Delta t \cdot \left(U_{x+1,y} - U_{x-1,y} \right) / 2 \cdot \Delta S$$

where $U_o = \tfrac{1}{4} \left(U_{x+1,y} + U_{x-1,y} + U_{x,y+1} + U_{x,y-1} \right)$,

$$V = V_o - g \cdot \Delta t \cdot \left(V_{x,y+1} - V_{x,y-1} \right) / 2 \cdot \Delta S$$

where $V_o = \tfrac{1}{4} \left(V_{x+1,y} + V_{x-1,y} + V_{x,y+1} + V_{x,y-1} \right)$

On comparing this scheme with those derived using interpolation scheme 1 it is apparent that at boundary point 1 (or 3) the boundary conditions given in equations (3.52) and (3.54) are consistent with the V - component of flow at an internal point. Similarly at boundary point 2 (or 4) the boundary equations (3.55) and (3.56) are consistent with the U - component of flow at the internal point. This suggests that the boundary conditions given by equations (3.52), (3.54), (3.55) and (3.56) are the correct form for flow in channels of variable depth as well as for constant depth.

Interpolation scheme 1 may be viewed as providing expressions only at the particle path point (U_o, V_o). It does not provide a means of interpolating at the intermediate points where the bicharacteristics lie. However the solution for the total depth at boundary point 1 is given by equation (3.35) in terms of the bicharacteristic points. In such a case it is perfectly correct to use interpolation scheme 3 since

for elevation this interpolation scheme is the general form of interpolation scheme 1, and gives an equivalent solution for elevation as interpolation scheme 1 for channels of constant depth.

To summarise then, the solution in a channel which is not of constant depth is obtained by using equations (3.52), (3.54), (3.55) and (3.56) for the velocity components which are based on interpolation scheme 1 while the total depth equation must be incorporated with interpolation scheme 3. This arrangement is termed interpolation scheme 4 and is shown in test 26 (section 4.3.3) to produce the most favourable results of all the tests used to simulate a forced oscillation in a channel of linearly varying mean depth.

The remaining linear interpolation scheme that is considered in the present investigation has at boundary point 1 for example, coefficients of the form

$$A = \left(Q_{x,y} - Q_{x-1,y} \right) / \Delta s$$

$$B = \left(Q_{x,y+1} - Q_{x,y-1} \right) / 2.\Delta s$$

$$C = Q_{x,y}$$

It is shown in Chapter 7 that this interpolation scheme (interpolation scheme 2) is preferable to the other schemes when the coastline is very irregular. A possible explanation for the success of interpolation scheme 2 and the limitations of the others in a real situation is suggested in section 7.3.2. Interpolation scheme 2 may be viewed as a scheme constructed out of the necessity for results close to the physical prototype with less regard for its mathematical verification. In contrast both these requirements are fulfilled when using boundary interpolation scheme 1 for constant depth channels and also when using boundary interpolation scheme 4 in channels of linearly varying mean depth.

3.5 THE METHOD OF SUBDIVISIONS

Any improvement of the characteristic numerical scheme must first involve an understanding of the fundamental mechanism by which simulated waves are propagated through the grid along the bicharacteristics. Only then will any limitations in the scheme become apparent for further examination and rectification. With this concept in mind, the simple case of a unimodel seiche in a closed basin of constant depth

in x-t space is now considered.

It has been shown in Chapter 2 that to maintain stability a timestep must be selected that is less than or equal to that prescribed by the CFL criterion. It is now shown that consistency considerations between the numerical and physical processes require that the timestep be the maximum permissible value obeying the CFL condition. Furthermore a timestep less than this does not improve the accuracy of the simulation, in fact it reduces it. Consider the characteristic paths in figure 3.13 representing wave fronts in a one-dimensional seiche in a channel of constant depth and hence constant celerity

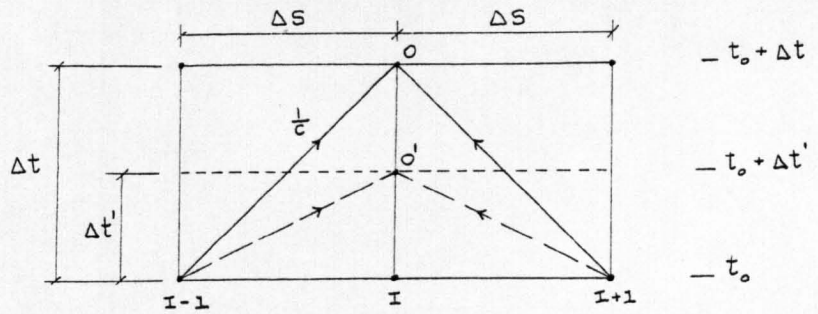

Figure 3.13

The solution at point O is formulated from the superimposition of two waves of celerity C travelling in opposite directions along the x-axis and meeting at point O. In numerical terms the solution at point O at time $t + \Delta t$ is obtained from the two characteristic paths originating at points I-1 and I+1 and travelling with a numerical celerity $\frac{\Delta s}{\Delta t}$. The numerical scheme must therefore be constructed so that tidal waves propagate with celerity $\frac{\Delta s}{\Delta t}$ and this should be as close as possible to the physical celerity c to maintain an equivalence between the numerical and physical processes. This relationship is precisely that given by the CFL condition at the limiting timestep ie $\Delta t = \frac{\Delta s}{c}$. If a timestep $\Delta t'$ is selected such that it is half the value of the maximum timestep then the solution will be required at O' as shown in figure 3.13. This implies that the characteristics originating from I+1 and I-1 propagate with computed celerity $\frac{\Delta s}{\Delta t'}$ which is twice the physical celerity. In this case physical consistency is not maintained. In section 4.4.1, the simulation of a one dimensional seiche in x-y-t space using tests 35 and 37 verify that the analytical motion is only achieved when the timestep is obtained from the CFL criterion at its limiting condition.

The results in this section suggest a decreasing performance on reducing the timestep in each test. The conclusion is obvious, once the spacestep has been selected there is only one value of timestep Δt appropriate to the problem. A greater value than Δt causes instability, a lesser value leads to inaccuracy. This conclusion applies in any number of space dimensions.

Now consider the previous seiche motion in x-t space only now the bed slope varies linearly. To preserve the stability requirements the computational grid must be based on the maximum depth in the channel. Hence having selected a suitable spacestep, the timestep is obtained from the CFL criterion $\Delta t = \Delta s / c_{MAX}$ where $c_{MAX} = (gH_{MAX})^{\frac{1}{2}}$. At a point along the channel where $H < H_{MAX}$ the arrangement of characteristics is as shown in figure 3.14

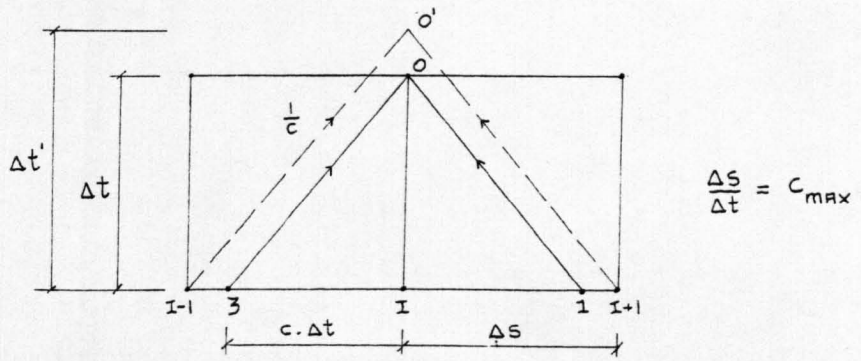

Figure 3.14

The solution at point O' can be expressed directly in terms of the characteristics originating from grid points I-1 and I+1. The solution is as follows

$$Z = \tfrac{1}{2}\left(Z_{I-1} + Z_{I+1}\right) - \frac{c^2}{g}\cdot\Delta t'\left(u_{I+1} - u_{I-1}\right)/2.\Delta s \qquad (3.57)$$

$$u = \tfrac{1}{2}\left(u_{I-1} + u_{I+1}\right) - g.\Delta t'\left(Z_{I+1} - Z_{I-1}\right)/2.\Delta s \qquad (3.58)$$

However the constraints of a regular grid require that the solution be obtained at point O. At such a point the characteristics are assumed to emanate from the intermediate points 1 and 3 and not from the grid points I+1, I-1 as in the previous case. To obtain a solution at point O the values of the dependent variables at points 1 and 3 must be obtained by interpolating between the known values at the grid points. The solution at point O is

$$Z = \tfrac{1}{2}\left(Z_1 + Z_3\right) - \tfrac{1}{2}\cdot\frac{c}{g}\cdot\left(u_1 - u_3\right) \qquad (3.59)$$

$$u = \tfrac{1}{2}\left(u_1 + u_3\right) - \tfrac{1}{2}\cdot\frac{g}{c}\left(\eta_1 - \eta_3\right) \qquad (3.60)$$

and a linear interpolation scheme $Q = Ax + C$ with

$$A = \left(Q_{x+1} - Q_{x-1}\right)/2.\Delta s \quad , \qquad C = \tfrac{1}{2}\left(Q_{x+1} + Q_{x-1}\right)$$

transforms the characteristic equations into

$$z = \tfrac{1}{2}\left(z_{x+1} + z_{x-1}\right) - \tfrac{1}{2}\,\frac{c}{g}\left(\frac{c.\Delta t}{\Delta s}\left(u_{x+1} - u_{x-1}\right)\right) \qquad (3.61)$$

$$u = \tfrac{1}{2}\left(u_{x+1} + u_{x-1}\right) - \tfrac{1}{2}\,\frac{g}{c}\left(\frac{c.\Delta t}{\Delta s}\left(\eta_{x+1} - \eta_{x-1}\right)\right) \qquad (3.62)$$

A comparison of these equations with equations (3.57) and (3.58) shows that the only difference is the value of the timestep, nevertheless the solutions are different. In equations (3.61) and (3.62) the term $\frac{c.\Delta t}{\Delta s}$ denoted as δ is known as the 'courant number' and represents the ratio of celerity at point O to the maximum celerity. The expression $(1-\delta)$ provides a measure of the degree to which interpolation is required at each point. It is apparent from the geometry of the characteristics shown in figure 3.14 that the characteristics at point O arrive ahead of the characteristics at point O' by $(1-\delta).\Delta s/c$ time units too soon and as already mentioned the solutions at both points are not equivalent.

The extent to which an interpolation scheme poses problems in the case of variable celerity may be better understood on considering the propagation of characteristics in x-t space over several time increments as shown in figure 3.15.

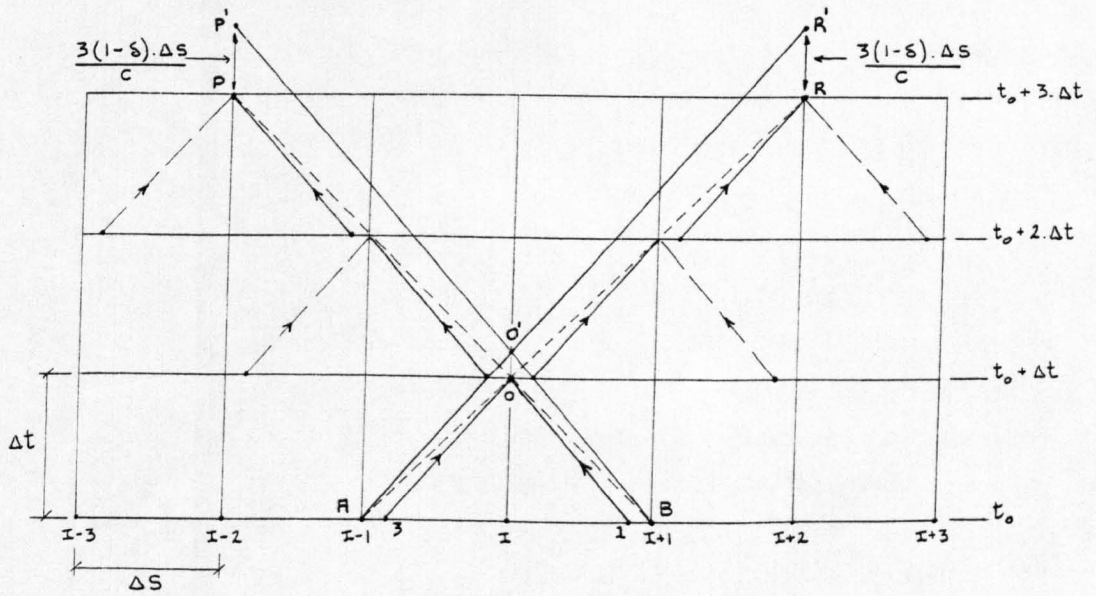

Figure 3.15

Consider a true disturbance, travelling with a celerity c and represented by a negative characteristic at point B which arrives at point P'. In numerical terms the disturbance at point B is transmitted to point P through the series of 'broken-line' characteristics which employ the interpolation scheme. After three successive time increments the interpolated characteristic arrives $3(1-\delta).\Delta s/c$ time units too soon in front of the true physical disturbance. The numerical wave front represented by the broken-line characteristics has in fact been generated at a celerity determined by the grid parameters (which is the maximum celerity in the channel) and is not equivalent to the celerity at point I. From the symmetry of the figure it is also apparent that a similar argument is valid for positive characteristics.

The problems associated with a regular mesh of grid points applied to the case of variable celerity as a result of linearly varying mean depth manifest themselves in the form of numerical attenuation. The tests in section 4.4.3 provide ample evidence of this attenuation. However it is notable that the method of characteristics indicates how attenuation might occur by showing that disturbances may be wrongly propagated through the grid. These erroneous disturbances or 'ghost characteristics' are shown as dotted lines in figure 3.15. The generality of this figure also implies that reducing both grid parameters will not improve the simulation.

Numerical attenuation was also found by Wiggert and Sundquist (1977) when simulating free wave motion of variable celerity using the method of characteristics with linear interpolations and a regular grid. Their error analysis suggested that a measure of the propagation error may be expressed as

$$\frac{C_{max}}{C} = \frac{n}{n-(1-\delta)} \qquad (3.63)$$

where n is the number of subdivisions of the spacestep. (Note that $n=1$ for the grid shown in figure 3.15). The term δ can be regarded as a shifting operator brought about by the need for interpolation. Its affect on the total error can be reduced according to equation (3.63) by increasing the value of n. The emphasis is only on reducing the error since n would require to be very large to remove the error completely. A large number of points over the spatial domain is impractical with the present computer facilities.

The ideal computational grid would be one with a flexible spacestep which could adjust to ensure that at each point the domain of dependence of the difference and differential schemes were tangential to one another along the characteristics. At present this situation only occurs in cases of constant depth where there is one fixed celerity. The method of subdivisions attempts to approximate the ideal state in channels of variable depth whilst retaining the advantages of a regular grid for example the convenience of having results at equidistant points. The method aims at ensuring that the characteristic paths are positioned in the immediate vicinity of the grid points so that the error associated with interpolating $(1-\delta)$ is reduced. By considering once again a channel of linearly varying mean depth in 'x-t' space with emphasis on the movement of wave fronts as depicted by the characteristics, the advantages of the method of subdivisions in comparison to former methods become apparent. Consider the characteristics at an internal point in a channel where the spacestep ΔS is divided into three equal parts as shown in figure 3.16.

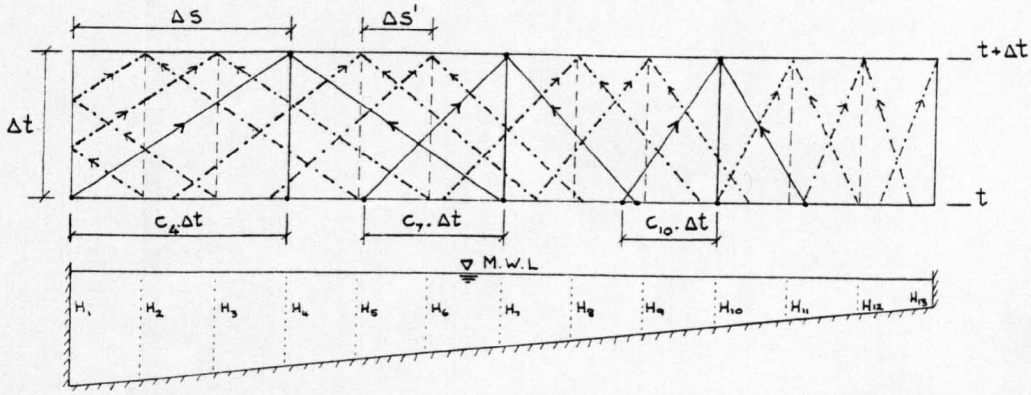

Figure 3.16

It is obvious that in subdividing the spacestep and so increasing the number of grid points, the feet of the characteristics will be closer to these points than before. The error in interpolating from these points $(1-\delta)$ is now reduced from $1-\frac{c.\Delta t}{\Delta s}$ to $1-\frac{c.\Delta t}{m.\Delta s'}$, where m is the minimum number of subdivisions required to form the domain of dependence of the difference scheme at a given point. Another advantage of this scheme is that since the characteristic paths are close to the grid points, the characteristics at one time level will follow on closely from those at the previous time level. Thus by using a method such as

this, the characteristics are more continuous and therefore there is less possibility that 'ghost characteristics' are being generated. However it would not be expected by using only three subdivisions of the spacestep to entirely remove this unwanted process.

In considering the method of subdivisions in 'x-t' space the CFL criterion $\Delta t = \Delta s/c_{max}$ is still valid and may be written as

$$\Delta t = \frac{n.\Delta s'}{c_{max}} \qquad (3.64)$$

It is an interesting sideline of the method of subdivisions that if $\Delta s'$ is given the value of Δs, and if $n = 3$ then equation (3.64) produces a value of timestep, three times larger than that given by $\Delta t = \Delta s/c$. In such a case the timestep has been amplified instead of subdividing the spacestep yet no violation of the CFL criterion has occurred. The possibility therefore exists of performing computations using a larger timestep than that required with a regular grid without subdivisions. This feature is examined in section 5.6.3 for wind surge propagation on a shelf with linearly varying mean depth. Again the advantage of more continuous characteristics using subdivisions is evident from figure 3.17

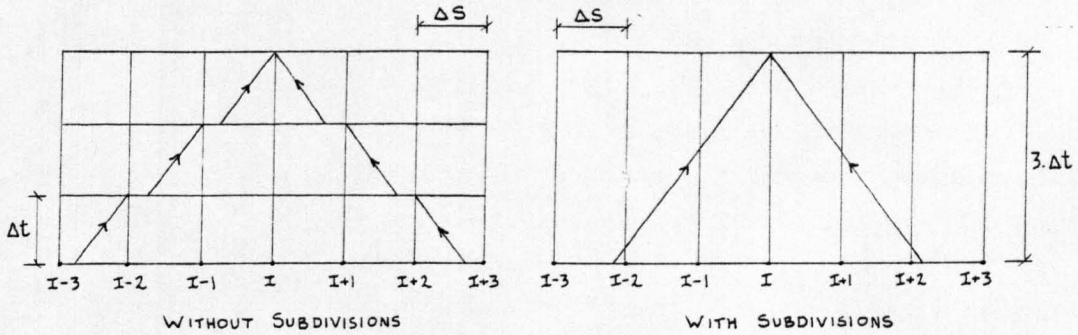

Figure 3.17

The method of subdivisions outlined so far seems an attractive proposition, however near the boundary points its implementation is rather more difficult. This is especially true as the number of space dimensions increases and this author has found no publications regarding this problem in x-y-t space although Vardy (1977) has presented details in 'x-t' space. Consider now a typical boundary point in 'x-t' space with three subdivisions of the spacegrid as shown in figure 3.18.

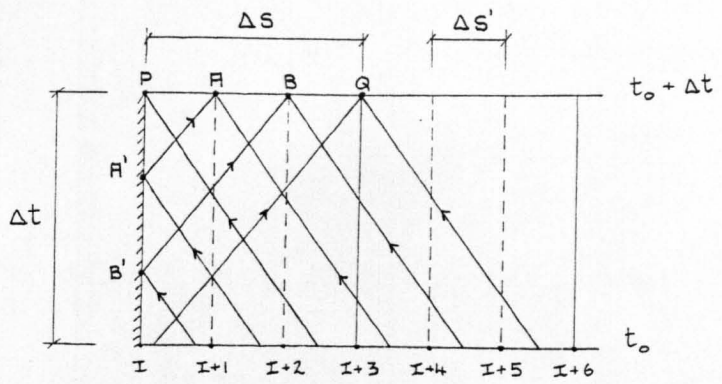

Figure 3.18

At the boundary point I the solution can be obtained directly from backward characteristic in the usual manner however at grid points I+1,I+2 the forward characteristics intersect the boundary along its time axis. At these points the characteristic equations (3.61) and (3.62) are not applicable since they are derived from forward and backward characteristics originating at one time level. Considering point A, one possible means of obtaining a solution there would be first to obtain the values at point A' by interpolating from the known values at the boundary point at times t_o and $t_o+\Delta t$. The position of point A' can be obtained by assuming that the forward characteristic has a celerity given by the average celerity between points I+1 and I at time t_o. The characteristic equations would then have to be revised to include characteristics generated at different time levels within a given timestep. This method is extremely complicated in x-y-t space and so was not attempted. Instead as an initial investigation of the method of subdivisions a simple linear interpolation applied between the points P and Q was used to obtain the values at A and B.

The interpolation scheme incorporated into the numerical scheme for two space-dimensions is now outlined. Essentially it consists of assigning at each grid point, an interpolation number in accordance with the particular way in which a bicharacteristic intersects a boundary point. If there is no intersection then the solution at the vertex of the bicharacteristics is calculated in the usual manner and the grid point given the interpolation number 0. Each point is examined at any given time level to establish the grid points required to form the

domain of dependence of the difference scheme that encloses the differential one. The limiting condition is obtained from the CFL criterion namely

$$\Delta t = \frac{\frac{\sqrt{2}}{2} \cdot n \cdot \Delta s'}{c_{max}}$$

and is depicted in figure 3.19 for three subdivisions

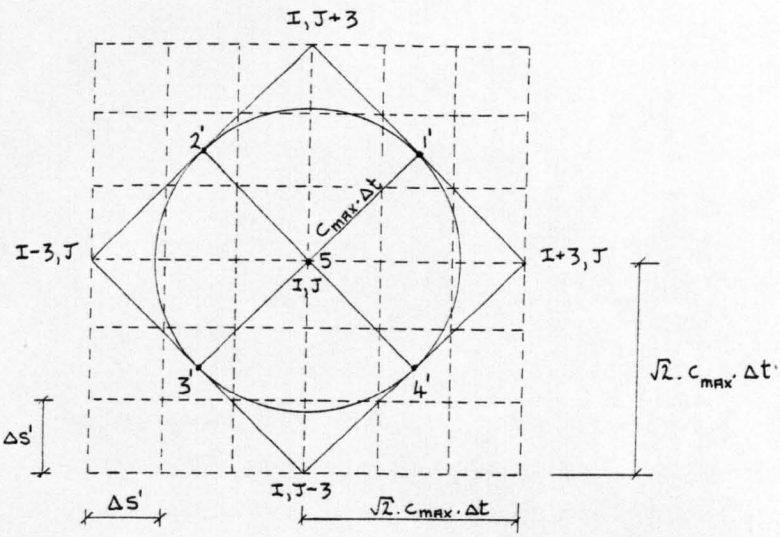

Figure 3.19

At any point in general the difference domain will require to extend a distance $\sqrt{2}.c.\Delta t$ along the x and y- directions. The length of this path in relation to one subdivision is therefore $\sqrt{2}.c.\Delta t./\Delta s'$ and the nearest integer m greater than this value indicates the number of spacesteps of size $\Delta s'$ required to form the difference domain of dependence. The number of spacesteps incorporated into the difference domain varies at each grid point according to value of celerity and takes values of 1, 2 or 3 measured from the centre of the domain. At each grid point and from the knowledge of required number of spacesteps m to form the difference domain, conditions may be written to establish if the spacesteps lie within the model. If the spacesteps are not available the grid point is assigned an interpolation number and the next point considered. A typical example of a number of grid points with their allocated interpolation numbers is shown in figure 3.20 and represents portions of the channel

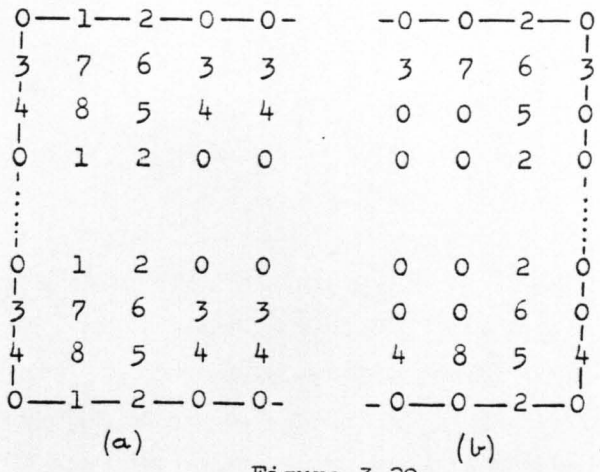

Figure 3.20

Figure 3.20(a) represents the situation near the boundaries in deep water and the non-zero interpolation numbers show that at most points the bicharacteristics intersect at least one of the boundaries and the complete difference domain cannot be formed. In figure 3.20(b) the boundaries are situated in shallower water and so only at the grid points very close to the boundaries, do the bicharacteristics intersect one of the boundaries. Having found solutions at all points with interpolation number 0 at a given time level the non-zero points may be returned to for the interpolation. The form of the interpolation is indicated by the interpolation number itself. For example at interpolation point 2 the interpolation is

$$Q_{x,y} = \tfrac{2}{3} \cdot Q_{x+1,y} + \tfrac{1}{3} \cdot Q_{x-2,y}$$

and at interpolation point 6 it is

$$Q_{x,y} = \tfrac{2}{3} \cdot Q_{x+1,y+1} + \tfrac{1}{3} \cdot Q_{x-2,y-2}$$

and so on. The interpolations in this form are somewhat imprecise, theoretically, and were only constructed because time did not allow the formation of a more satisfactory solution near the boundaries. In its application, care was taken to ensure that the grid spacing was small in relation to the problem so that the interpolations are not applied over too great a distance. In this way the method of subdivisions in its present form was found to reproduce the analytical solution for an 'x-t' seiche in 'x-y-t' space. The method is also shown in section 4.4.3 to have some success in simulating the same phenomenon in a channel of linearly varying mean depth. In this case however the method of subdivisions can

only reduce the error in interpolation, not completely remove it and as a result attenuation still occurs. This error may be more precisely defined in x-y-t space as an inability to form a domain of dependence of the difference scheme that encloses exactly the domain of dependence of the differential one throughout all points in the channel. Initially the numerical schemes which were programmed in Algol - 60 were run using a George 3 teletype system linked to an ICL 1904S computer housed at the University of Strathclyde. The programs were written in a general manner to allow their application to simple and more complex schematisations. The individuality of each problem was maintained by keeping the particular information of each case on separate data files. For the more complex configurations (presented in Chapter 7) involving a large number of grid points, the program required over twenty minutes computational time to complete one tidal cycle. Since the computer department operated a batch mode system giving priority to shorter programs, this inevitably led to a slow turnover of these programs during periods of peak demand. However by March 1979 it was possible to access the more powerful IBM 2980 computer at the Bush Estate, Edinburgh. To improve the program's efficiency it was rewritten in Fortran, the information being relayed from punched cards. As a result the computational time for subsequent programs was reduced by about one-tenth of that using the 1904S. It had been hoped that the factor would be about one-fortieth but this was not so because of the difficulty in outputing results using Fortran. A format of results which printed surface elevation and velocity components to coincide with the position of the respective grid point had been used simply and effectively in the Algol programs. In Fortran, two dimensional arrays of results cannot be printed using only one control statement, consequently the array must be printed row by row using a do loop. Also to obtain a format which represented the arrangement of grid points, meant describing the elements of the format statement and combining these elements in an array according to the configuration number. This involved long lines of programming and so increased the computational time.

The VME/B system used on the IBM 2980 also operated a batch mode system which even on this computer became overloaded with users' demands for machine time. The situation was drastically improved by

January 1980 when an on-line VDU system became generally available to all users. From then onwards a significant increase in the turnover of programs was produced.

CHAPTER FOUR

THE SIMULATION OF LONG WAVE MOTION IN CHANNELS OF SIMPLE GEOMETRIC SHAPE

4.1 INTRODUCTION

To establish that the proposed numerical schemes derived in Chapter 3 are capable of providing reliable information, two fundamental issues concerning the accuracy of these schemes must be resolved. Firstly, one must show that the numerical integration scheme can successfully solve the differential equations and secondly that the difference equations combined with the initial and boundary conditions can define the physical phenomenon. Only then is an equivalence between the physical process and the numerical model established. Testing the ability of the model to integrate the differential equations is mathematically related to the concepts of convergence, consistency and stability. For example, one of the requirements of the integration of the difference scheme is that it is equivalent to the solution of the differential one as both space and time increments tend to zero. In practice this requirement becomes difficult to implement as a result of increased computational time with successive decreases in the spacestep and timestep.

Application of the numerical model directly to an idealised or real situation and comparing the model's results to theoretical formulae or recorded data is the commonest form of testing a numerical model. By selecting a channel in which the geometry is easily defined, the boundary conditions can be accurately represented in the numerical scheme. By simplifying the boundary problem the effect of the integration and interpolation schemes can be investigated more confidently than for a complex schematisation. Unfortunately an assessment of the effect of the integration scheme cannot be made separately from that of the interpolation scheme in a direct way but it can be achieved by comparing the effects produced by changing either scheme. The distinct advantage of simulating the motion

produced in a simple channel is that the analytical expression, if known, provides the elevations and velocities at every position in the channel at all time levels. This information is useful when comparing it with results from the model. The analytical models may not be totally representative of the real conditions but are nevertheless valuable as a method of verifying that the numerical model is competent in solving the differential equations. Only after this has been established can the same equations in the numerical model be applied with confidence to real situations in which the testing of initial and boundary conditions will be more rigorous. If this step is successful the model is then capable of reproducing the physical process and an equivalence exists between the numerical and physical operations.

4.2 THE ANALYTICAL SOLUTIONS

The derivations of the analytical solutions are presented in this chapter in order to emphasise the correspondence between the simplifying assumptions used in producing these equations and the requirements of the numerical scheme when simulating x-t flow. These relationships are stated later in this section and are better understood once the analytical solutions are derived.

Consider a narrow channel of variable rectangular cross section of width B and depth H, the x - axis is taken along the length of the channel with its origin at the head. The propagation of a long wave along this channel is defined by the surface elevation ϵ and the depth mean velocity U which are functions of x and t. In the absence of bed friction and Coriolis forces and assuming that ϵ is small in relation to depth H, then the equation of motion is defined as

$$\frac{\partial U}{\partial t} + g \frac{\partial \epsilon}{\partial x} = 0 \qquad (4.1)$$

and the continuity equation has the form

$$B \frac{\partial \epsilon}{\partial t} + \frac{\partial}{\partial x}(B.H.U) = 0 \qquad (4.2)$$

By eliminating the velocity U from the above equations the second - order differential equation is obtained

$$\frac{\partial^2 \epsilon}{\partial t^2} = \frac{g}{B} \frac{\partial}{\partial x}\left[B.H. \frac{\partial \epsilon}{\partial x} \right] \qquad (4.3)$$

This equation is hyperbolic and becomes elliptic under the following assumption that surface elevation is harmonic

$$\epsilon = \eta \exp(i\sigma t) \qquad (4.4)$$

The general elliptic equation is therefore

$$\frac{g}{B} \frac{d}{dx}\left[B.H. \frac{d\eta}{dx} \right] + \sigma^2 \eta = 0 \qquad (4.5)$$

The case of a channel closed at one end with the other end open to the sea (in harmonic oscillation with it) was considered by Lamb (1932) who derived simple analytical solutions for numerous channels with different configurations. The following examples are of interest

a) Constant breadth and depth
b) Constant depth and linearly varying breadth
c) Constant breadth and linearly varying depth

With the origin of the x axis located at the closed end of the channel of length a and by representing conditions at the seaward end by the symbols $\bar{\eta}$, $\bar{\epsilon}$, $\bar{H}$, $\bar{B}$ the problem is completely specified. The

tidal oscillation at the seaward end is denoted by

$$\bar{\epsilon} = \bar{\eta} \cos(\sigma t) \tag{4.6}$$

For each of the above cases Lamb solved the general equation (4.5). The results obtained by Lamb are now listed

a) Breadth $H(x) = \bar{H}$
Depth $B(x) = \bar{B}$
equation (4.5) becomes

$$g\bar{H}\frac{d^2\eta}{dx^2} + \sigma^2\eta = 0 \tag{4.7}$$

taking $k = \sigma/\sqrt{g\bar{H}}$
the solution is given by

$$\eta = \bar{\eta}\frac{\cos(kx)}{\cos(ka)} \cdot \cos(\sigma t + \phi) \tag{4.8}$$

on restoring the time factor.

b) Breadth $B(x) = \bar{B}\, x/a$
Depth $H(x) = \bar{H}$
equation (4.5) becomes

$$\frac{d^2\eta}{dx^2} + \frac{1}{x}\frac{d\eta}{dx} + k^2\eta = 0 \tag{4.9}$$

with k as previously defined, and the solution is found to be on restoring the time factor

$$\eta = \bar{\eta}\frac{J_0(kx)}{J_0(ka)} \cdot \cos(\sigma t + \phi) \tag{4.10}$$

$J_o(kx)$ is the Bessel function of zero order given by

$$J_o(x) = 1 - \frac{x^2}{2^2} + \frac{x^4}{2^2.4^2} - \frac{x^6}{2^2.4^2.6^2} + \cdots\cdots$$

or more generally by

$$J_n(x) = \sum_{r=0}^{\infty} \frac{(-1)^r \cdot (\tfrac{1}{2}x)^{n+2r}}{r!\ (n+r)!} \qquad (4.11)$$

c) Breadth $B(x) = \bar{B}$

Depth $H(x) = \bar{H}\, x/a$

The general equation (4.5) becomes

$$x \cdot \frac{d^2\eta}{dx^2} + \frac{d\eta}{dx} + k^2 a \eta = 0 \qquad (4.12)$$

with k as defined previously, and the solution is given as follows on restoring the time factor

$$\eta = \bar{\eta}\, \frac{J_o(2k\sqrt{ax})}{J_o(2ka)} \cdot \cos(\sigma t + \phi) \qquad (4.13)$$

The natural period of the lowest mode occurs when a node exists at x = a such that $\eta = 0$ and the root of the Bessel function has the value 0.7655π

Therefore $2ka = 0.7655\pi$

and on substituting for k produces

$$T = 1.306 \cdot \frac{4a}{(g\bar{H})^{1/2}} \qquad (4.14)$$

where T is the period which is equivalent to 1.306 times that of an equivalent rectangular channel of constant depth $\bar{H}$.

One of Lamb's basic assumptions is that the free surface elevations are small relative to the mean water depth. However in case c) where the channel profile is triangular this assumption will not be valid at the head of the channel. Furthermore this condition of zero mean water level cannot be applied in the numerical scheme because it requires the condition

$$\eta < H \tag{4.15}$$

so that the celerity calculated from the following equation

$$c = \left[g (H + \eta) \right]^{\frac{1}{2}} \tag{4.16}$$

is the root of a positive expression. It therefore becomes more advantageous to perform the simulations in a channel of trapezoidal profile. Firstly, though, the analytical solution for this channel is required, and the relevant hydrodynamic theory was first presented by Chrystal (1904). The derivation is as follows;

If the origin of the x - axis is taken at a point where the depth is $\overline{H}$ then the law of depth will be

$$H(x) = \overline{H}(1 - x/a) \tag{4.17}$$

where a is the length of the channel shown in figure 4.1 in its untruncated state.

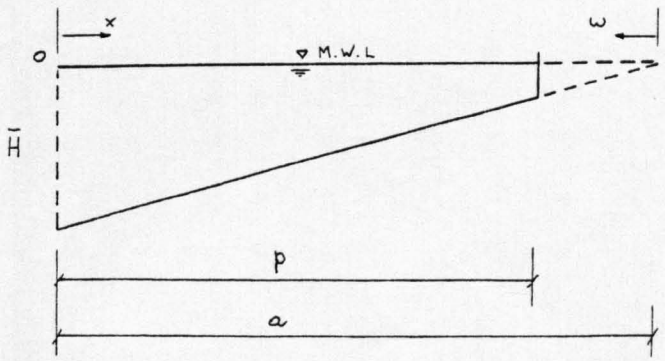

Figure 4.1

The harmonic variation of velocity at the mouth is defined as

$$U = P \cos(\sigma t + \phi) = \xi \bar{H} (1 - x/a) \qquad (4.18)$$

where ξ is the horizontal displacement and P is determined by

$$\frac{d^2 P}{dx^2} + \frac{\sigma^2 P}{g \bar{H} (1 - x/a)} = 0 \qquad (4.19)$$

The elevation of the water surface relative to mean water level is defined as

$$\eta = -\frac{\partial U}{\partial x} \qquad (4.20)$$

Equation (4.19) is transformed into

$$\frac{d^2 R}{dw^2} + \frac{1}{w} \frac{dR}{dw} + \left(1 - \frac{1}{w^2}\right) R = 0 \qquad (4.21)$$

by putting $P = Rw$ (4.22)

and $$w = \frac{2\sigma a \sqrt{(1 - x/a)}}{\sqrt{(g \bar{H})}} \qquad (4.23)$$

so that equation (4.21) is a particular case of the Bessel equation. If $J_1(w)$ and $Y_1(w)$ denote the Bessel and Neumann functions of first and second kind respectively, the general solution of (4.21) is

$$R = A . J_1(w) + B . Y_1(w) \qquad (4.24)$$

Hence with slight adaptation of the constants A and B the equation for elevation is found

$$\eta = \frac{2a}{\bar{H}} \left\{ \frac{A}{\omega} \frac{d}{d\omega} \left(\omega . J_1(\omega) \right) + \frac{B}{\omega} \frac{d}{d\omega} \left(\omega \, Y_1(\omega) \right) \right\} \qquad (4.25)$$

and also

$$\xi_\omega = \left(A \, J_1(\omega) + B \, Y_1(\omega) \right) \cos(\sigma t + \phi) \qquad (4.26)$$

One of the fundamental properties of $J_1(\omega)$ and $Y_1(\omega)$ is that

$$\frac{1}{\omega} \frac{d}{d\omega} \left(\omega \, J_1(\omega) \right) = J_0(\omega), \quad \frac{1}{\omega} \frac{d}{d\omega} \left(\omega \, Y_1(\omega) \right) = Y_0(\omega) \qquad (4.27)$$

Hence equation (4.25) becomes

$$\eta = \frac{2a}{\bar{H}} \left\{ A \, J_0(\omega) + B \, Y_0(\omega) \right\} \cos(\sigma t + \phi) \qquad (4.28)$$

on restoring the time factor. Denoting $\alpha = 2a / \sqrt{(g\bar{H})}$ (4.29)

obtained from equation (4.23) with $x = 0$ and in a similar way

$$\beta = 2a \sqrt{(1 - p/a)} \Big/ \sqrt{(g\bar{H})} \qquad (4.30)$$

corresponds to $x = p$.

The boundary condition for $\omega = \sigma\beta$ is

$$\xi = 0 \qquad (4.31)$$

Hence from equation (4.26)

$$\left(A J_1(\sigma\beta) + B Y_1(\sigma\beta) \right) \cdot \cos(\sigma t + \phi) = 0 \qquad (4.32)$$

which yields the following solution for B namely

$$B = - \frac{A J_1(\sigma\beta)}{Y_1(\sigma\beta)} \qquad (4.33)$$

and substituting into equation (4.26) gives

$$\zeta_\omega = A' \left(Y_1(\sigma\beta) \cdot J_1(\omega) - J_1(\sigma\beta) Y_1(\omega) \right) \cos(\sigma t + \phi) \qquad (4.34)$$

and in equation (4.25) gives

$$\eta = \frac{2a A'}{\bar{H}} \left[Y_1(\sigma\beta) \cdot J_0(\omega) - J_1(\sigma\beta) \cdot Y_0(\omega) \right] \cos(\sigma t + \phi) \qquad (4.35)$$

The equations (4.34),(4.35) define the movement and displacement of the free surface of this channel which is equivalent to considering one half of a symmetrical truncated lake. The lowest mode of frequency of the channel therefore corresponds to the case of odd nodality in the symmetrical truncated lake. With the boundary condition defined as

$$\eta = 0 \qquad \text{at} \qquad \omega = \sigma\alpha \qquad (4.36)$$

applied to equation (4.35) the following equation is obtained

$$Y_1(\sigma\beta) \cdot J_0(\sigma\alpha) - J_1(\sigma\beta) \cdot Y_0(\sigma\alpha) = 0 \qquad (4.37)$$

From this expression the period of the channel or lake can be found.

For the special case where p = a such the channel profile is triangular, equation (4.35) reduces to the equation (4.13) derived by Lamb. To prove this, rewrite equation (4.35) in the form

$$\eta = \frac{2a A'}{\bar{H}} \left\{ J_0(\omega) - \frac{J_1(\sigma\beta)\, Y_0(\omega)}{Y_1(\sigma\beta)} \right\} \cos(\sigma t + \phi) \qquad (4.38)$$

With p = a the boundary condition $\beta = 0$ produces

$$\lim_{\omega \to 0} \frac{J_1(\omega)}{Y_1(\omega)} = 0 \qquad (4.39)$$

so that equation (4.38) reduces to

$$\eta = \frac{2a A'}{\bar{H}} J_0(\omega) \cos(\sigma t + \phi) \qquad (4.40)$$

With the origin of the x axis at the head of the channel

$$\omega = 2\sigma a \frac{\sqrt{x/a}}{\sqrt{g\bar{H}}} \qquad (4.41)$$

and with $k = \sigma / \sqrt{g\bar{H}}$ (4.42)

yields on substitution

$$\omega = 2k\sqrt{ax} \qquad (4.43)$$

which is the argument in Lamb's expression. Finally, the constant A' in equation (4.40) can be chosen so that

$$\frac{2a A'}{\bar{H}} = \frac{\bar{\eta}}{J_0(2ka)} \qquad (4.44)$$

and the equation (4.13) is obtained namely

$$\eta = \bar{\eta} \frac{J_o(2k\sqrt{ax})}{J_o(2ka)} \cos(\sigma t + \phi)$$

A point of practical programming importance is that both the Bessel and Neumann functions are defined by infinite series, the Neumann function being a Bessel function of the second kind and can be expressed as

$$Y_n(x) = J_n(x)\left(\ln(x) - S_n\right) - \sum_{m=0}^{n-1} \frac{2^{n-m-1}\, n!\, J_n(x)}{(n-m)\cdot m!\, x^{n-m}}$$

$$+ \sum_{m=1}^{\infty} \frac{(-1)^{m-1}(n+2m)}{m(n+m)} J_{n+2m}(x) \qquad (4.45)$$

where n is the order and $S_n = 1 + \frac{1}{2} + \frac{1}{3} + \ldots \frac{1}{n}$ and $S_o = 0$

In the program only the first 12 terms of these functions were included but as a check on their ability to accurately represent these functions a comparison was made with the tabulated values of these functions. Tabulated values of Neumann's functions were not readily available, however those of Weber's Bessel function of the second kind were; Watson (1923). Weber's function of the second kind of order n is as follows

$$Y_n(x) = \frac{2}{\pi}\left(0.5772 + \ln(\tfrac{1}{2}x)\right) J_n(x) - \frac{1}{\pi}\sum_{r=0}^{n-1} \frac{(n-r-1)!}{r!}\left(\frac{2}{x}\right)^{n-2r}$$

$$- \frac{1}{\pi}\sum_{r=0}^{\infty} \frac{(-1)^r (\tfrac{1}{2}x)^{2r+n}}{r!\,(n+r)!} \left\{ 1 + \tfrac{1}{2} + \tfrac{1}{3} + \ldots + \tfrac{1}{r} + 1 + \tfrac{1}{2} + \ldots + \frac{1}{n+r} \right\} \qquad (4.46)$$

It was this function that was specified in the program and it can

also replace Neumann's function in the analytical equations (4.34) and (4.35) because equation (4.24) used in their derivation can be replaced by the following

$$R = A_1 J_1(\omega) + B_1 Y_1(\omega) \qquad (4.47)$$

This equation will produce the analytical equations identical to those of (4.34) and (4.35) except that the constant A' will take a different value.

The free surface across the channel corresponding to the four different configurations and defined by the respective equations (4.8), (4.10), (4.13), (4.35) are shown in figure 4.2. Since the tidal frequency σ and the acceleration of gravity, g, are essentially fixed, the critical parameter governing the amplitude of the free surface is the ratio $a/\sqrt{A}$. For each channel the value of this ratio is 17,500 which is close to the ratio for the channels simulated in section 4.3. The curves depicted in figure 4.2 illustrate that a contraction of depth or width, which modifies the channel shape from that of case a), causes a corresponding increase or decrease in the amplitude of the standing wave over the length of the channel. It is also possible to show that for all values of the ratio $a/\sqrt{A}$ the order of the maximum amplitude with $a/2T = 1/8$ is as shown in figure 4.2, with the largest amplitude produced in the channel of triangular profile. However if the waves were progressive, Green's theorem (Lamb p.274-5) in which $\eta \propto B^{-1/2} H^{-1/4}$, shows that a decrease in width or depth of the channel produces an increase in amplitude compared to that of case a).

In deriving the analytical solutions the problem has been reduced from a hyperbolic to an elliptic level. This reduction was accomplished by combining the partial differential equations of motion into a single second order ordinary differential equation by assuming a harmonic solution is possible. The appropriate equations are shown in (4.5) for Lamb's solutions and (4.21) for Chrystal's solution. The full extent to which classical solutions of the two-dimensional equations are possible was given by Vantroys (1959).

High (and low) water curves for flow in frictionless channels derived from analytical solutions.

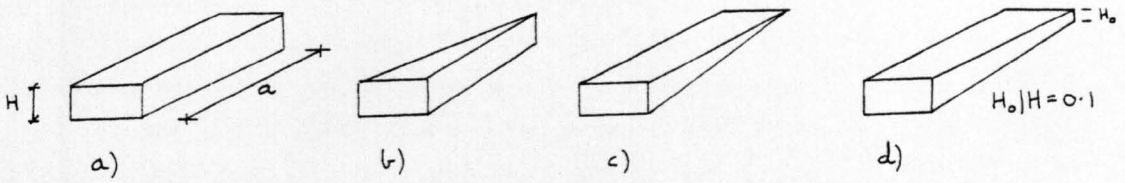

IN ALL CASES $a/CT = 1/8$ $(c = \sqrt{gH})$

AND $a/\sqrt{H} = 17{,}500$ $(a = 70{,}000m,\ H = 16m)$

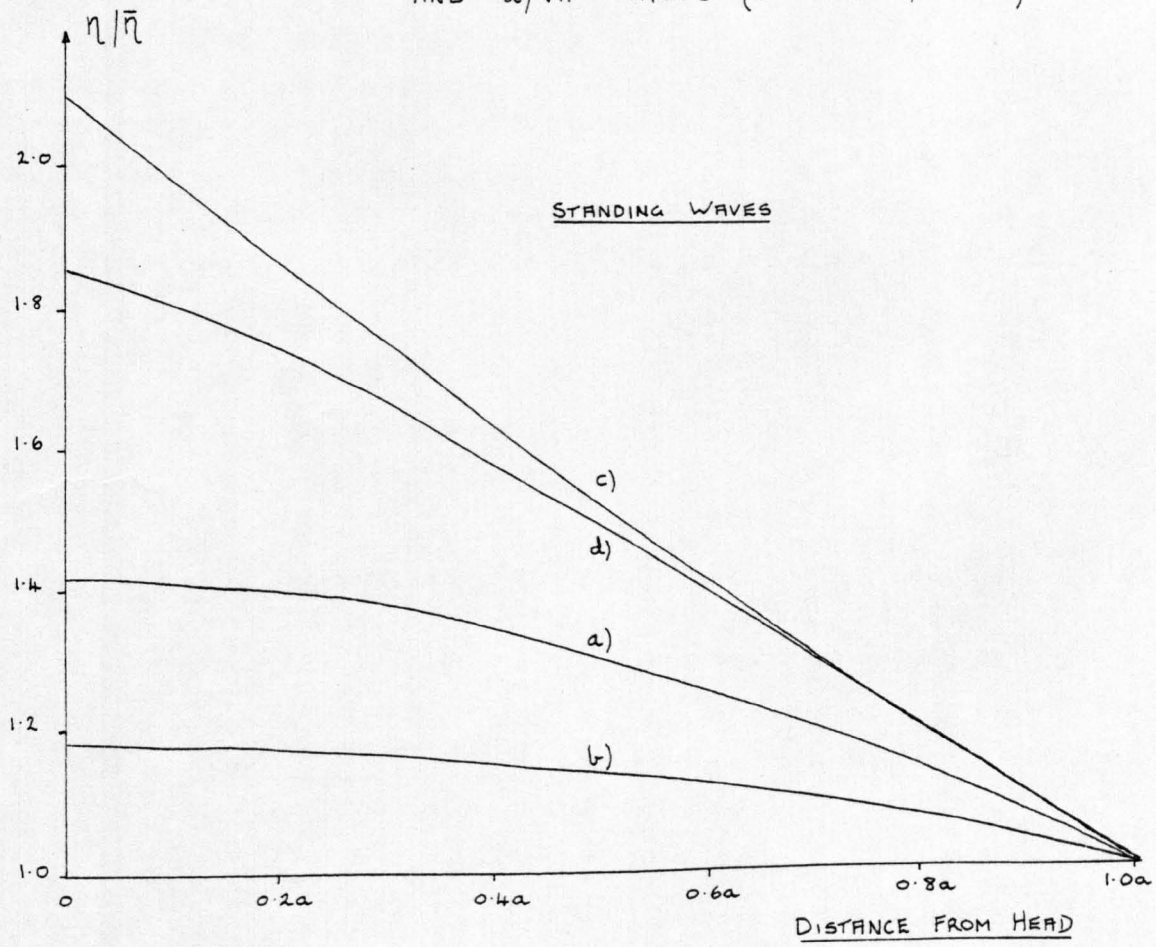

Figure 4.2

In his paper the relationship between the hyperbolic and elliptic aspects of the problem were rigorously established.

The correct approach in simulating the long wave motion in geometrically simple channels is closely related to whether the problem is elliptic or hyperbolic. The analytical solutions for 'x - t' flow were produced by removing the non-linear terms in the governing equations of motion. It is only when these terms are disregarded that the problem becomes elliptic and for the model to reproduce this solution it too must be linear. In simulating a problem of the elliptic type the final solution is not independent of the initial conditions and the starting point for the numerical calculations cannot be an arbitrary free surface but the correct free surface. A rigorous derivation of these conditions was provided by Stoker (1957). The verification of the model is that the starting free surface is reproduced at the end of each tidal cycle. This supports the idea of periodicity of the final solution and any lack of periodicity is a result of the shortcomings of the model. The importance of the starting conditions in the model was noted by Matsoukis (1980) and the numerical philosophy was summarised by him as follows:-

1. The response of a channel to a periodic excitation at the open sea boundary must be periodic.

   (a) If the solution is elliptic then it is also dependent on the initial conditions.

   (b) If the solution is hyperbolic, periodicity is achieved through the actions of friction and Coriolis forces introduced through the momentum equation and the non-linear terms in the continuity equation.

2. If the response of the channel is not periodic then the model is not functioning properly.

The reduction of a problem to the elliptic level through the assumption of small amplitude and the absence of non-linear terms effectively limits the analytical solutions either to the ocean tides

or to seiche action in closed basins. These configurations are considered in sections 4.3 and 4.4. In conclusion it should be noted that analytical formulae have been produced which account for the frictional forces albeit in a linearised form, Lorentz (1926). Proudman (1955) extended this method to include the effects of quadratic bed friction, and presented a formal solution for the case of an estuary with variable cross-section. This solution was also developed for application to uniform estuaries.

4.3 TIDAL SIMULATION IN FRICTIONLESS OPEN CHANNELS

In establishing the success or otherwise of the numerical schemes it seemed appropriate to begin by using the analytical models determined by Lamb and Chrystal described in section 4.2. In each configuration the harmonic condition of equation (4.6) was applied at its open boundary. The period of the boundary condition was chosen to be larger than the natural period of 'x - t' flow in the channel. The resulting motion was therefore a force oscillation as distinct from the natural oscillation of free waves studied in section 4.4. In assessing the accuracy of the numerical schemes in simulating 'x - t' flow using x - y - t dimensions, certain specific objectives were thought to be important. These may be summarised as follows:

a) To apply the numerical model to differing configurations. Three differing channel shapes were studied to show the effect of variable breadth and depth on the numerical scheme's performance.

b) To compare the results from the 45° and 90° characteristic schemes with the analytical solutions.

c) To investigate the influence of different linear interpolation schemes at the boundary positions by observing their effect on the final solution.

d) To show that the correct approach in simulating 'x - t' flow in frictionless channels is obtained from elliptic considerations.

e) To assess the effect of timestep on the final solution. Davies (1979) has shown that the choice of timestep is important from the point of view of numerical dissipation.

f) To investigate the effect of non-linear terms on the final solution and to test the simulation of finite amplitude waves. * SEE NOTE ON PAGE 130.

4.3.1 The rectangular channel of constant depth.

A synopsis of the investigations for the case of a frictionless rectangular channel of constant depth is presented in Table 4.2. From the information in this table the starting conditions, the boundary interpolation schemes and the geometric parameters of the channel are apparent. The parameters controlling the wave motion are also displayed together with an assessment of the results from the model. The simulations were conducted on two different channels; tests 1 to 4 correspond to a timestep 0.943 times that obtained from equation (4.51), tests 5 to 12 correspond to a timestep equal to the maximum timestep. The geometric and wave parameters for the channel used in tests 5 to 12 is calculated from the following expression,

$$C = \frac{L}{T} = \frac{0.707\ DS}{DT} \qquad (4.48)$$

for linear conditions with L equal to the wavelength and T equal to the period of the forced oscillation. The wavelength L can be expressed as

$$L = X \cdot (M-1) \cdot DS \qquad (4.49)$$

with $\chi = L/a = 8$, where a is the length of the channel and is given by

$$a = (M-1) \cdot DS \qquad (4.50)$$

where M is the number of grid points along the length of the channel. Making the necessary substitutions produces

$$DT = 0.707 \cdot T \,/\, (M-1) \cdot \chi \qquad (4.51)$$

which relates the timestep to the waveform and the computational grid. These parameters are selected in such a way that the timestep is an integer. With the timestep calculated, and the spacestep selected, the C.F.L. condition yields C and hence $\bar{H}$.

The large number of tests presented in this section requires a system which describes the important features of each numerical scheme used in these tests. Therefore a symbolic system as shown in table 4.1 is used which clarifies the presentation of the tests in the tables and graphs of this section and other sections in this chapter.

SYMBOL	DESCRIPTION OF THE NUMERICAL SCHEME
×	Boundary interpolation scheme 1 (I.S.1)
+	Boundary interpolation scheme 2 (I.S.2)
△	Boundary interpolation scheme 3 (I.S.3)
▲	Boundary interpolation scheme 4 (I.S.4)
o	Non-linear depth and convective terms present
9	Subscript represents a 90^{o} characteristic scheme

Table 4.1

The different interpolation schemes have been fully detailed in section 3.4. In some of the tests which follow the numerical scheme may contain more than one of the pertinent features shown in table 4.1. For these cases the symbols are grouped together.

The analytical solution applied to the channels with the dimensions given in table 4.2 produces a free surface and horizontal velocities as depicted in table A.1. The results from tests 1 to 12 are also presented in tables A.2 to A.5. These tables show the elevations and velocities at each tidal cycle corresponding to the grid points along the centre of the channel and also at the two corner points at the head of the channel. If the results are not periodic then they are presented for a time equal to the end of the fifth tidal cycle. The tabulated results only represent the tidal motion at high and low water in order to reduce the bulk of the results. In some cases, where the low water displacements are not included, it can be assumed that they are equal in modulus to the value of high water at the same grid point. For each test involving small amplitude, the successive high and low waters are depicted in figure 4.4 which clearly shows the tests with results favourable to the analytical solution. A similar type of graph shown in figure 4.5 shows the numerical results for the second channel used in tests 5 to 11.

By comparing one test to another in a method that highlights the effect on results of changing a particular condition and by comparing the results to those obtained from the analytical solution defined by equation (4.8), some important conclusions can be drawn.

a) It was found that in both tests 4 and 5 the results shown in tables A.2 and A.3 were identical to those of the respective analytical solutions shown in table A.1 at all positions in the channel at any time level. In both tests the numerical schemes used linear 45° characteristics. The analytical free surface corresponding to high water and zero velocities was the initial condition. The boundary interpolation scheme derived from the theory of 45° characteristics, namely I.S.1, was also used. In test 4

the numerical data corresponded to the situation where $DT < DT_{MAX}$ whereas in test 5 the use of equation (4.51) ensured that $DT = DT_{MAX}$. This was the only significant difference between the two tests and it appears that this factor is not important in simulating the motion of forced waves. It is shown later that in the case of free waves the analytical motion can only be produced using the condition $DT = DT_{MAX}$ for a channel of constant depth.

b) The numerical scheme and data of test 5 were applied to the case of a finite amplitude wave motion. The results corresponding to test 12 are shown in table A.5. Allowing for the scale factor in amplitude, the results from this test were similar to those from test 5 showing that the simulation of finite amplitude waves can be performed without becoming unstable. Since the numerical scheme was linear, the results from test 12 did not exhibit any non-linear effects associated with finite amplitude waves.

c) In test 1 the effect on the results of using open sea boundaries at the northern and southern side of the channel, where the three unknown variables were calculated, was assessed by comparison to the results of test 2. The figure 4.3 shown illustrates the boundary conditions used in both tests. Since the results from tests 1 and 2, as presented in the table A.2,

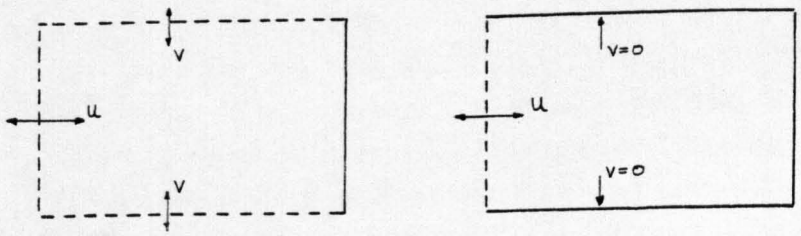

Test 1 Test 2

Figure 4.3

were identical it showed that no spurious transverse velocities were produced across these open boundaries. This is an important first step in assessing the performance of this type of boundary which is used in the shelf surge model discussed further in Chapter 9.

d) The results of test 3 on comparison with test 4 showed that the interpolation scheme used at the boundaries in test 3, namely I.S.2, had the effect of producing a harmonic solution not equal to the analytical solution. This test was conducted with $DT < DT_{MAX}$

e) A comparison of results from tests 7 and 8 in which the interpolation schemes I.S.3 and I.S.2 were investigated showed that the interpolation scheme I.S.2 was unstable when the condition $DT = DT_{MAX}$ was met. This effect is noted also in other configurations where conditions of constant depth exist and is in fact a general finding of this research. The instability of this interpolation scheme is clearly evident on the appropriate curves shown in figure 4.5 as a rapid increase in the modulus of the elevation at high and low waters.

f) The results from tests 5 and 6 on comparison showed that the interpolation scheme used in test 6 was inadequate in properly representing the conditions at the boundaries. This interpolation scheme, namely I.S.3 is stable but since the free surface elevations at high water are less than those from the analytical solution, it appears that the scheme produces numerical dissipation. This is closely related to the fact that the boundary interpolation for the velocity calculation only considers two grid points instead of three and so is inconsistent with the scheme used for internal points. This is also true for test 7 which uses the interpolation scheme of test 6.

g) It is concluded from the results of tests 4 and 5 that the elliptic approach is a successful method of simulating the

x - t motion in the frictionless channel. Other investigators, for example, Webster (1968), have treated the simulation as a hyperbolic problem by introducing friction into the scheme. In his tests this non-linear term produced convergence from the arbitrary free surface to the final solution. It was then assumed that the effect of friction on the final solution was small enough to allow a comparison with Lamb's analytical solution for a frictionless channel. In theory this method of comparison is incorrect but it was tested using the numerical scheme and data as for test 5. The results for test 11 showed that with the value of Chezy's co-efficient equal to 150, convergence to a final solution had not been obtained, however the results would indicate that convergence is slow. A lower friction parameter would accelerate the convergence but may also produce a solution that would differ from the linearised analytical solution.

h) It was concluded from tests 1 and 2, which include the non-linear and convective terms in the numerical scheme, that these terms were responsible for the final solution not being periodic, see figure 4.4. The result of successively increasing high waters would have eventually created an unstable situation through the violation of the C.F.L. condition. This would occur because $C = \sqrt{g(H+\eta)}$ and with celerity increasing the maximum timestep obtained from

$$DT_{max} = \frac{0.707DS}{C}$$

would eventually become less than the computational timestep. This was exactly the mechanism for instability for the non-linear scheme used in test 9. The results of this test from table A.4 when plotted in figure 4.5 show that the non-linear terms produce successive increases in high and low water until the third tidal cycle. At this time the C.F.L. condition is violated and its effect is shown by the increased rate of growth of the high waters and the increase in modulus of the low waters. Furthermore a comparison of test 9 with

1-D FORCED OSCILLATION

COMPUTATIONAL PARAMETERS FOR A FRICTIONLESS RECTANGULAR CHANNEL OF CONSTANT DEPTH

Test	Initial Surface	Numerical Scheme	M	N	H	$\eta_{I=1}$	T	DS	DT	DT_{max}	Final Solution
					m	m	sec	m	sec	sec	
1	Analytical	⊕	19	13	26.42	0.2	44712	5000	207	218.7	Not Harmonic
2	Analytical	⊕	19	13	26.42	0.2	44712	5000	207	218.7	Not Harmonic
3	Analytical	+	19	13	26.42	0.2	44712	5000	207	218.7	Harmonic Soln ≒ Analytical
4	Analytical	×	19	13	26.42	0.2	44712	5000	207	218.7	As Analytical
5	Analytical	×	20	13	29.45	0.2	44712	5000	207	207	As Analytical
6	Analytical	Δ	20	13	29.45	0.2	44712	5000	207	207	Harmonic Soln ≒ Analytical
7	Analytical	Δ_q	20	13	29.45	0.2	44712	5000	207	207	Harmonic Soln ≒ Analytical
8	Analytical	Δ_q	20	13	29.45	0.2	44712	5000	207	207	Unstable
9	Analytical	⊗	20	13	29.45	0.2	44712	5000	207	207	Slowly Unstable
10	Analytical	⊗	20	13	29.45	0.2	44712	5000	207	207	Harmonic Soln ≒ Analytical
11	Linear c=150	×	20	13	29.45	0.2	44712	5000	207	207	Slow Convergence
12	Analytical		20	13	29.45	2.0	44712	5000	207	207	As Analytical

Table 4.2

Envelope curves of successive high and low waters at the head of a frictionless rectangular channel ofconstant depth.

(DT < DTmax, M = 19)

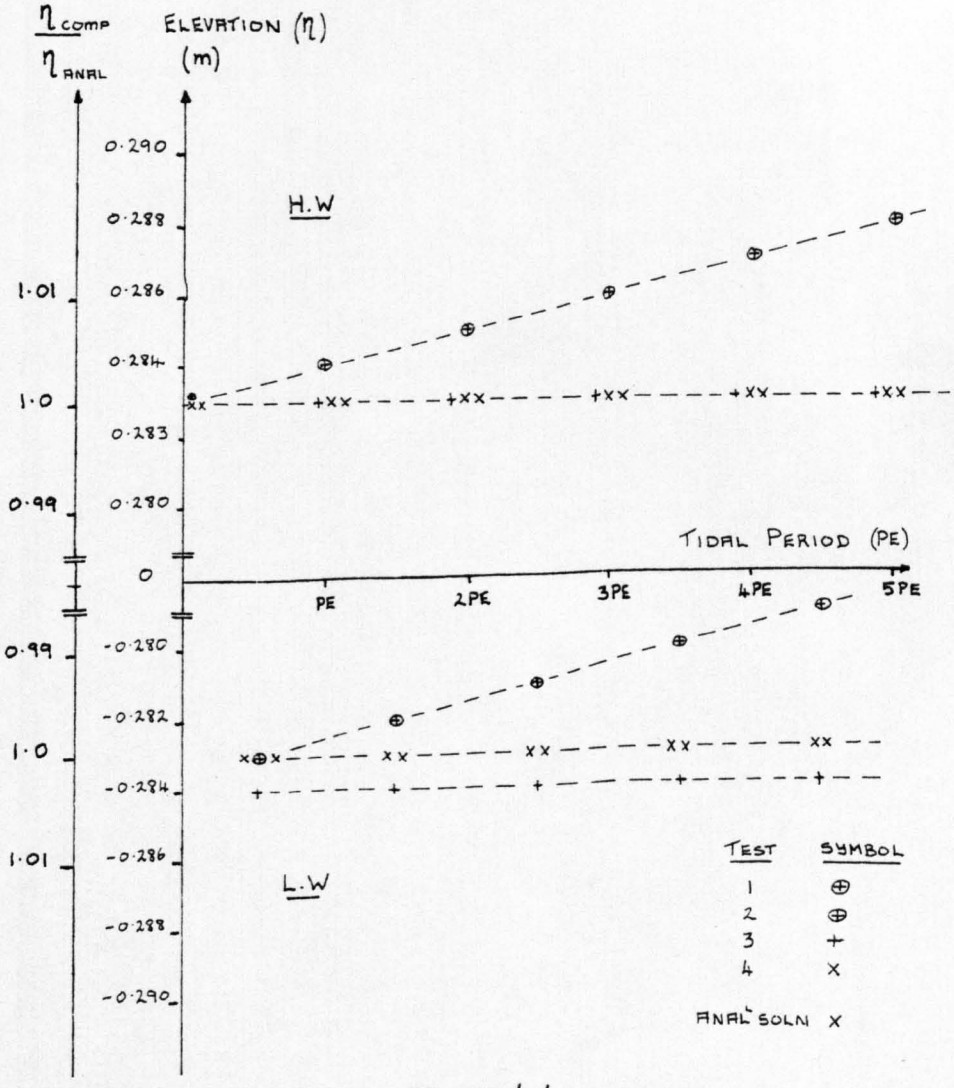

Figure 4.4

Envelope curves of successive high and low waters at the head of a frictionless rectangular channel of constant depth. (DT = DTmax, M = 20)

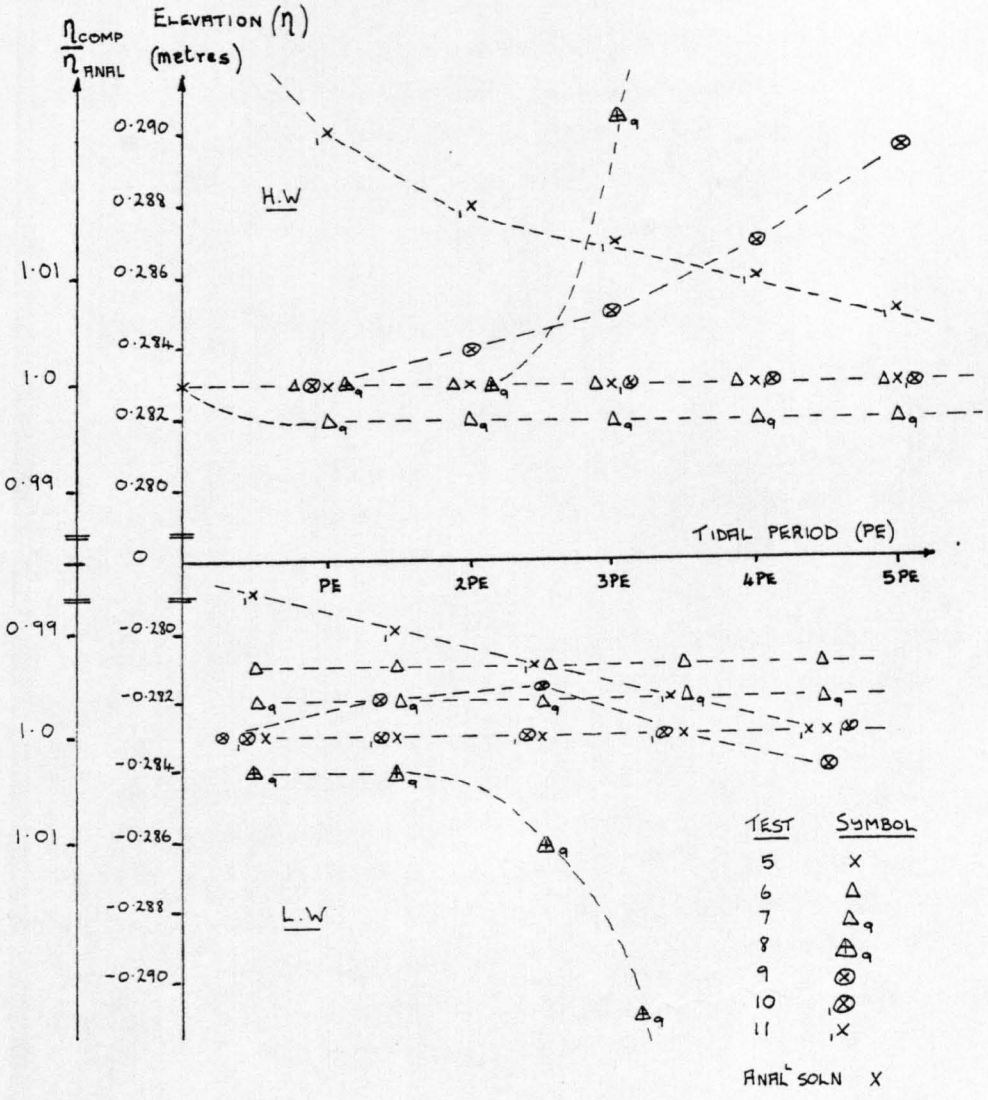

Figure 4.5

test 10, in which test 10 used a linear convective scheme, showed that the non-periodicity was directly related to the non-linear calculation of celerity from the total depth. Evidently the amplitude of the wave is not sufficiently small for the non-linear effect to be negligible. The only justifiable reason for the non-linear term to affect the periodicity is that since the channel is relatively short, then non-linear terms should not be present in the first place. By their inclusion in the interior of the channel a non-linear response is generated but at the open boundary the cosine function controlling the boundary elevation is based on linear conditions. The inconsistency between the events at the boundary and the interior of the channel may upset the periodicity of the oscillations.

4.3.2 The converging channel of constant depth.

For a channel of uniformly varying breadth the analytical solution was given in equation (4.10). In deriving this solution, Lamb made the simplifying assumption that the transverse velocities were zero and the flow was strictly in x - t dimensions. Therefore when simulating this motion in (x - y - t) space and comparing the results to Lamb's solution, the velocities in the y-direction must also be zero. In reality the same linear scheme and tidal characteristics at the entrance create two-dimensional tidal flow by virtue of the converging coastline which evidently reflects tidal waves and introduces values for the transverse velocity V. By simulating these conditions in which the transverse velocity is allowed to propagate across the channel it is shown that a periodic solution is produced from hyperbolic considerations. A comparison with the simulations of motion in the rectangular channel in section 4.3.1 shows that the hyperbolic approach is justified in the situation of a converging coastline which propagates tidal waves in the y-direction and flow is two dimensional.

From the point of view of numerical schematisation the converging coastline was replaced by a polygonal set of horizontal and vertical lines and so it provided an opportunity to study the general effect of

replacing a continuous coastline with an irregular one.

The objectives a) to f) stated in section 4.3 are applicable to the convergent channel and so the presentation of computations is similar to those of section 4.3.1. For each test the numerical scheme and the computational parameters are listed in table 4.3 together with the percentage variation of the final solution from the analytical solution based on elevations at the head of the channel. In the tables A.6 to A.9 the results from the analytical solution given by equation (4.10) and from the computations of each test corresponding to the high and low water elevations are shown. It is also of importance in these tests to consider the effect of the numerical scheme in simulating a truly standing wave therefore the mean high water interval M.H.W.I. for each test is shown. All results are representative of conditions along the centre line of the channel. By comparing the computed results with those derived from the analytical solution and by comparing individual tests to one another some useful conclusions were made. These conclusions were deduced as follows:

a) The computations from test 13 together with the results obtained from the analytical solution are presented for comparison in table A.6. The free surface in both cases corresponded to $L/a = 8.037$ which was used in equation (4.51) to calculate the timestep. The numerical scheme used in test 13 was identical to that of test 5 which was successful in simulating the tidal motion in the rectangular channel of constant depth. However in test 13 the transverse velocities were not computed, to comply with Lamb's assumption. The computations of test 13 showed that a periodic solution was established which was similar to the analytical solution. Considering that the closed boundaries were discontinuous this result was most satisfactory.

b) In test 13 an elliptic approach was used in simulating the tidal motion and for comparison the tests 14 to 16 used a hyperbolic method since transverse velocities were allowed

to propagate in the model. In all these tests the amplitudes were small and the numerical schemes linear. The results from tests 14 to 16 are shown in the respective tables A.6 and A.7 which indicate that the arbitrary initial condition is that of mean water level and zero velocities and that the final solution becomes independent of the initial conditions and is periodic after the completion of two tidal cycles. The effect of convergence for these tests 14, 15, 16 is illustrated in figure 4.6. Also shown are the results from test 13 and the analytical free surface, for successive high waters at the head of the channel. Since the numerical schemes were linear, |high water| = |low water| and so the low water elevations were not presented in the tables or graphs. A comparison of tests 13 and 16 showed that although the transverse velocity V was important in causing convergence, in test 16 it did not significantly change the final solution. Indeed this solution as shown in figure 4.6 is very close to that of test 13 and to the analytical solution. Also shown in figure 4.6 is a comparison between the results from tests 15 and 16 and again the elevations at the head of the channel are very similar. The number of grid points in the y direction N, in test 16 was ten whereas in test 15 it was eleven and it was concluded that the representation of the head of the channel by either N=2 or 3 grid points does not significantly affect the numerical computations. The results from test 14, which uses the 90° characteristic scheme and interpolation scheme 3 (I.S.3), are also shown in figure 4.6 and this scheme gives a reasonably accurate harmonic free surface solution.

c) In test 17 a finite amplitude wave of 1m amplitude at the open boundary was simulated and the results are shown in table A.8 together with the analytical solution for linear conditions. The numerical scheme however was non-linear and its effect is shown in the results where the high water elevations are greater than the low waters. The final

solution was established using 90^{o} characteristics and I.S.2 which is conditionally stable for $DT < DT_{MAX}$. The results were in good agreement with those of the analytical solution suggesting that the channel was too short for the non-linear terms to have an appreciable effect.

d) In simulating the tidal motion in the converging channel Matsoukis (1980) produced results of very high accuracy for small amplitude waves. His channel parameters are listed in table 4.3 under tests 18 and 19. These tests indeed prove that a high degree of accuracy can be obtained and the results are presented in table A.9. These results however became less significant when it was noted that Matsoukis had not maintained a linear variation in the breadth of the channel which violated one of Lamb's assumptions. The channel is shown in figure 4.7 together with a channel in which the breadth is a linear function of its length. There seems no obvious reason why Matsoukis compared the results from his channel with Lamb's analytical solution.

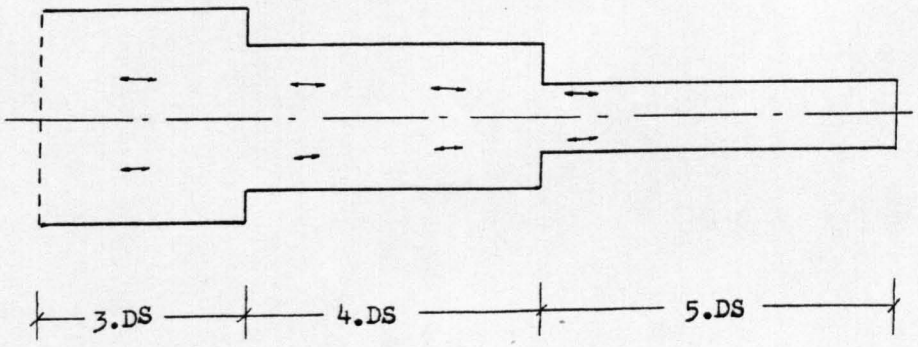

The Matsoukis Channel

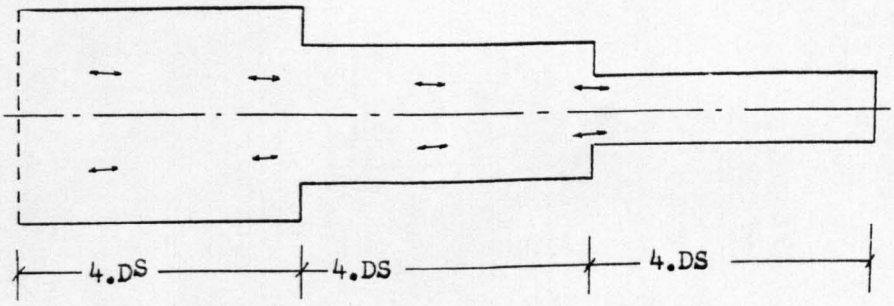

The Linear Breadth Schematisation

Figure 4.7

1-D FORCED OSCILLATION

COMPUTATIONAL PARAMETERS FOR A FRICTIONLESS CONVERGENT CHANNEL OF CONSTANT DEPTH

Test	Initial Surface	Numerical Scheme	M	N	H	$\eta_{I=1}$	T	DS	DT	DT_{max}	Final Solution. % Difference from Analytical,
					m	m	secs	m	sec	sec	
13	Analytical	$_1\times$	20	10	11.464	0.2	43200	3000	200	200	4.2
14	M.W.L.	Δ_9	20	11	11.464	0.2	43200	3000	200	200	4.2
15	M.W.L.	$_2\times$	20	11	11.464	0.2	43200	3000	200	200	7.2
16	M.W.L.	$_3\times$	20	10	11.464	0.2	43200	3000	200	200	4.7
17	Analytical	$\textcircled{A}_9$	20	11	10	1.0	43200	3000	200	214	2.5
18	M.W.L.	Δ_9	13	7	30	1.0	44712	3930	162	162	0.67
19	M.W.L.	$\times$	13	7	30	1.0	44712	3930	162	162	0.48

Table 4.3

NOTE: Prefix to symbols is a graphical aid.

Frictionless convergent channel of constant depth.

Successive high and low waters at the head

of the channel. $|H.W| = |L.W|$

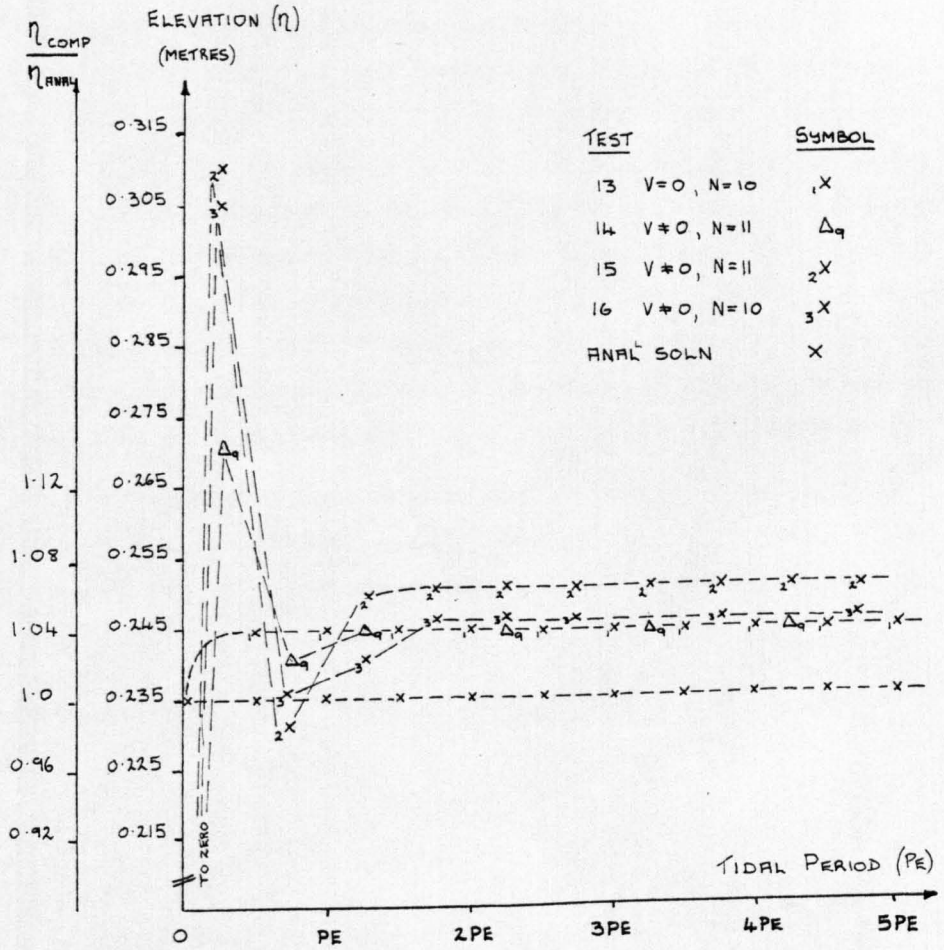

Figure 4.6

4.3.3 The rectangular channel of linearly varying mean depth.

Previous investigations of forced wave simulation presented in sections 4.3.1 and 4.3.2 have been concerned with channels of constant depth. For these configurations the successful numerical scheme used 45° characteristics which were linearised. This linearisation was in accordance with the linear assumptions governing the derivation of the analytical solutions in section 4.1. In simulating the tidal motion in a channel of linearly varying mean depth the above-mentioned linear scheme was applied without any changes. The use of a linear scheme required that the initial conditions were those of the analytical free surface for a successful simulation. This method constituted an elliptic approach to the problem. However further tests with the channel of linearly varying mean depth showed that convergence to the analytical solution could be achieved using arbitrary starting conditions. It was concluded from the latter result that a non-linear process had occurred in the model using this configuration which originated from the terms involving celerity. More precisely, the terms involving the celerity in the numerical scheme have a non-linear effect since the celerity itself is not constant throughout the length of the channel.

The natural oscillation of the channel shown in figure 4.8 was derived by Chrystal and presented in section 4.2. This solution for the vertical displacement of the free surface applies to

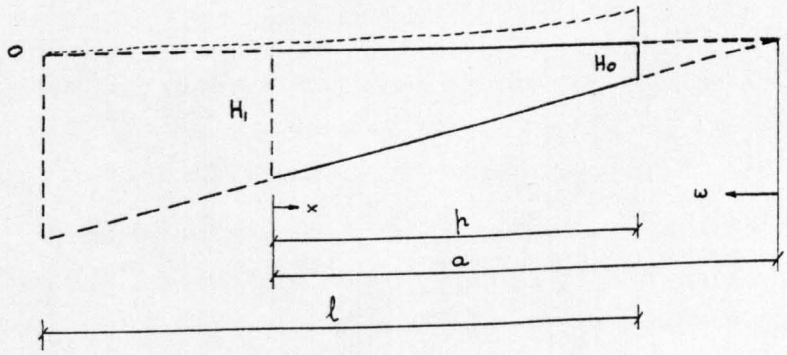

Figure 4.8

the free wave condition but can be applied to the forced wave condition with the period of the forced wave greater than the natural period of the channel. With this condition the node will be outside the channel and so the equation (4.35) defines the free surface of the channel of length l which, with the larger period, is also the surface of the forced oscillation for the channel of length a. With equations (4.23), (4,29) and (4.30) restated as

$$\omega = \sigma\alpha \left(1 - x/a\right)^{1/2} \tag{4.52}$$

$$\sigma\alpha = \frac{2\pi a}{c_1} \cdot \frac{2}{T} \tag{4.53}$$

$$\sigma\beta = \sigma\alpha \left(1 - p/a\right)^{1/2} \tag{4.54}$$

and the dimensions of the channel given in table 4.4 produces $\omega = 1.645$ corresponding to $H = H_1$ obtained from equations (4.52), (4.53) and $\omega = 0.520$ at $H = H_0$ obtained from equations (4.53) and (4.54). With the constant **A'** in equation (4.35) taken as 1.803 to produce a maximum amplitude of 1.3m corresponding to the depth H_1, the analytical surface for the forced oscillation using Weber's function in (4.35) becomes

$$\eta = 1.803 \left(1.423\ J_0(\omega) + 0.2513\ Y_0(\omega)\right) \tag{4.55}$$

for the high water displacements along the channel. This surface is compared with the figures obtained using Lamb's equation (4.13), for a channel of length a and a triangular profile in table A.10.

The numerical schemes constituting tests 20 to 27 are classified according to the starting conditions and the interpolation schemes, in table 4.4. Also shown, as an assessment of the accuracy of each test, is the percentage variation of elevation, at the head of the channel, from that of the analytical solution, taken at the end of the fifth tidal cycle. In some of the tests the periodicity of the simulated elevations was subject to small fluctuations and to

show this feature the results from each test corresponding to high and low water are shown in tables A.11 to A.18. This fluctuation is better observed in figures 4.9 and 4.10 which show the results in the tables A.11 to A.18 in graphical form for successive high and low water displacements at the head of the channel. This position in the channel was chosen since it represents the maximum disagreement with Chrystal's analytical solution.

In conducting the tests 20 to 23 the initial conditions were not those of the analytical solution. The effect of arbitrary initial conditions on the periodicity and accuracy of the final solution is illustrated in figure 4.9 and the following observations were made from the results of these tests:

a) In test 23 the initial condition was that of mean water level and zero velocities along the channel. The convergence to a final solution had not occurred even after 5 tidal cycles. This indicated a very slow rate of convergence. In test 22 the rate of convergence was quicker when the initial conditions were closer to Chrystal's analytical solution and indeed the final solution in this test was very close to the analytical. For this test the initial surface was the high water level given by Lamb's equation (4.13). In both tests interpolation scheme 3 was used which was shown in test 6 to be reasonably accurate. The numerical schemes in both tests 22 and 23 were identical and based on linear 45° characteristics.

b) The conditions of test 21 were identical to those of test 22 except that in the former test the numerical scheme contained the non-linear depth term $(H+\eta)$ and the convective terms. A comparison of results from both tests showed that the non-linear shallow water effect was produced, namely an increase in positive elevation and a decrease in negative elevation resulting in an increase in mean water level. This effect is a consequence of two factors, firstly the wave is of finite amplitude and secondly the effect of decreasing depth towards the shore. Time did not permit a quantitative assessment of the accuracy with which the numerical scheme reproduces this

phenomenum. Obviously since the results of test 21 include the non-linear effect they are not in exact agreement with the results from Chrystal's solution. The results from test 21 are very close to those of test 20 and this agreement corresponds to the similarity in both numerical schemes. However the numerical scheme of test 20 (and also test 25) are only applicable to constant depth configurations and although the results are favourable they are not obtained using the correct scheme.

Tests 24 to 27 were conducted to show that the simulation can be performed using an elliptic method which essentially means that the numerical schemes were linear and so required the analytical condition as an initial condition. The elevations for successive high waters are shown in figure 4.10 and the following comments are applicable:

a) Of the tests 24, 25 and 26 the results from test 26 are the most satisfactory and are shown in table A.17. These results also show that no variation of phase occurs along the channel and that the final solution is a standing wave. The interpolation scheme I.S.4 was constructed in accordance with consistency requirements and is theoretically superior to the interpolation schemes of tests 24 and 25. For example in test 24 the boundary interpolations for velocity are not consistent with the velocity interpolations at internal points. For reference this scheme is interpolation scheme 3. In test 25 the interpolation scheme I.S.1, although in the same form as that in test 26, is only applicable for constant depth configurations.

b) The results shown in figure 4.10 suggest that a small disturbance is present which slightly affects the periodicity. After three tidal cycles the disturbance is negligible in tests 24 and 26. The disturbance is not a result of simulating finite amplitude waves because the same disturbance was observed using small amplitude waves in test 27. The results for this test are shown in table A.18.

1-D FORCED OSCILLATION

COMPUTATIONAL PARAMETERS FOR A FRICTIONLESS RECTANGULAR CHANNEL OF LINEARLY VARYING MEAN DEPTH

Test	Initial Surface	Numerical Scheme	M	N	H	$\eta_{I=1}$	T	DS	DT	DT_{max}	Final Solution % Diff From Analytical I=19 t=5T
					m	m	secs	m	secs	secs	
20	Lamb's	⊗	19	11	160:16	1.3	44712	11,600	207	208	2.7
21	Lamb's	Ⓐ	19	11	160:16	1.3	44712	11,600	207	208	1.8
22	Lamb's	,△	19	11	160:16	1.3	44712	11,600	207	208	0.45
23	M.W.L.	△	19	11	160:16	1.3	44712	11,600	207	208	7.7
24	Chrystal's	△	19	11	160:16	1.3	44712	11,600	207	208	0.45
25	Chrystal's	,×	19	11	160:16	1.3	44712	11,600	207	208	0.90
26	Chrystal's	▲	19	11	160:16	1.3	44712	11,600	207	208	0.35
27	Chrystal's	△	19	11	160:16	0.1	44712	11,600	207	208	0.59

Table 4.4

Envelope curves for successive high and low waters at the head of a frictionless rectangular channel with linearly varying mean depth.

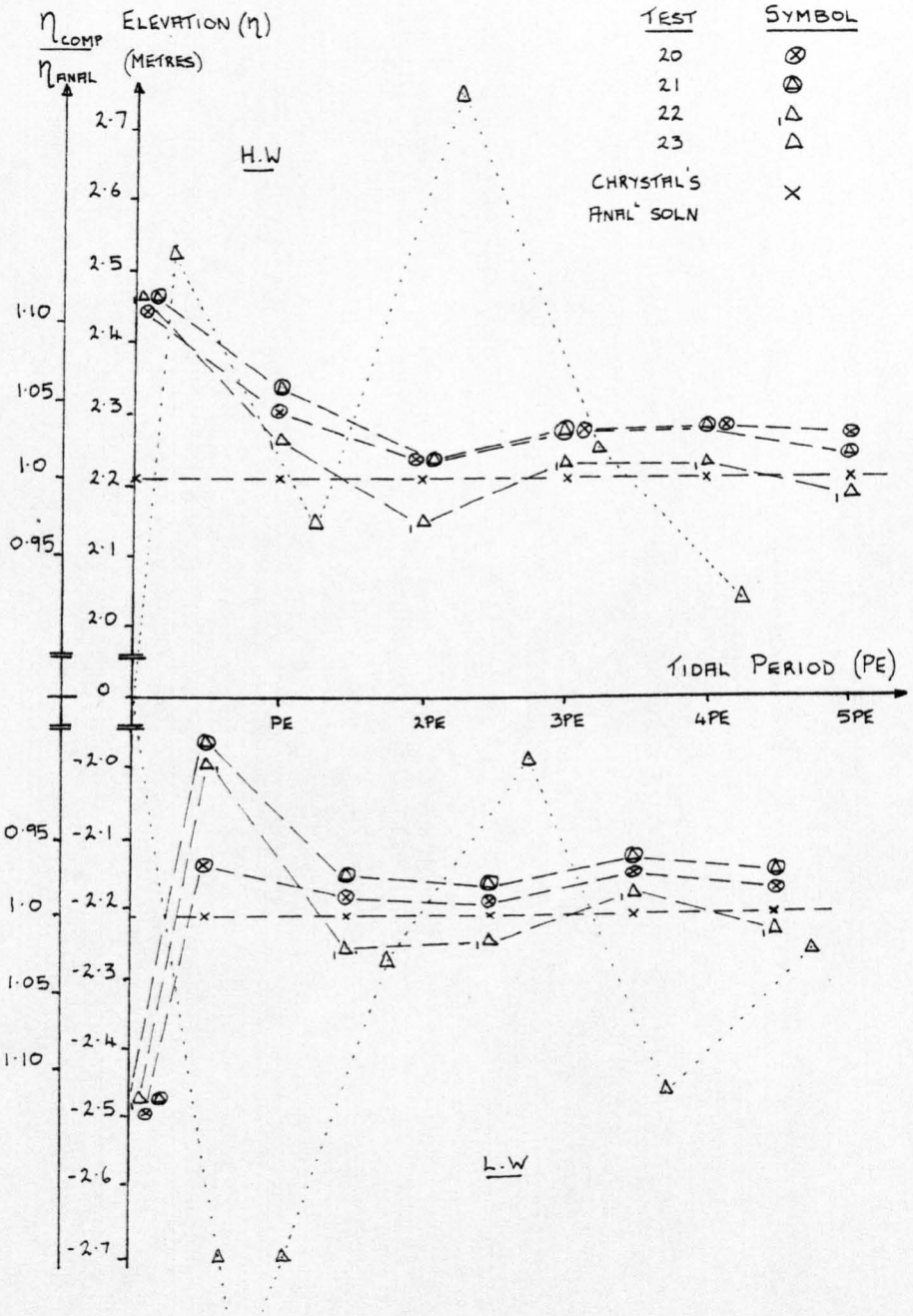

Figure 4.9

Envelope curves of successive high and low waters at the head of a frictionless rectangular channel with linearly varying mean depth.

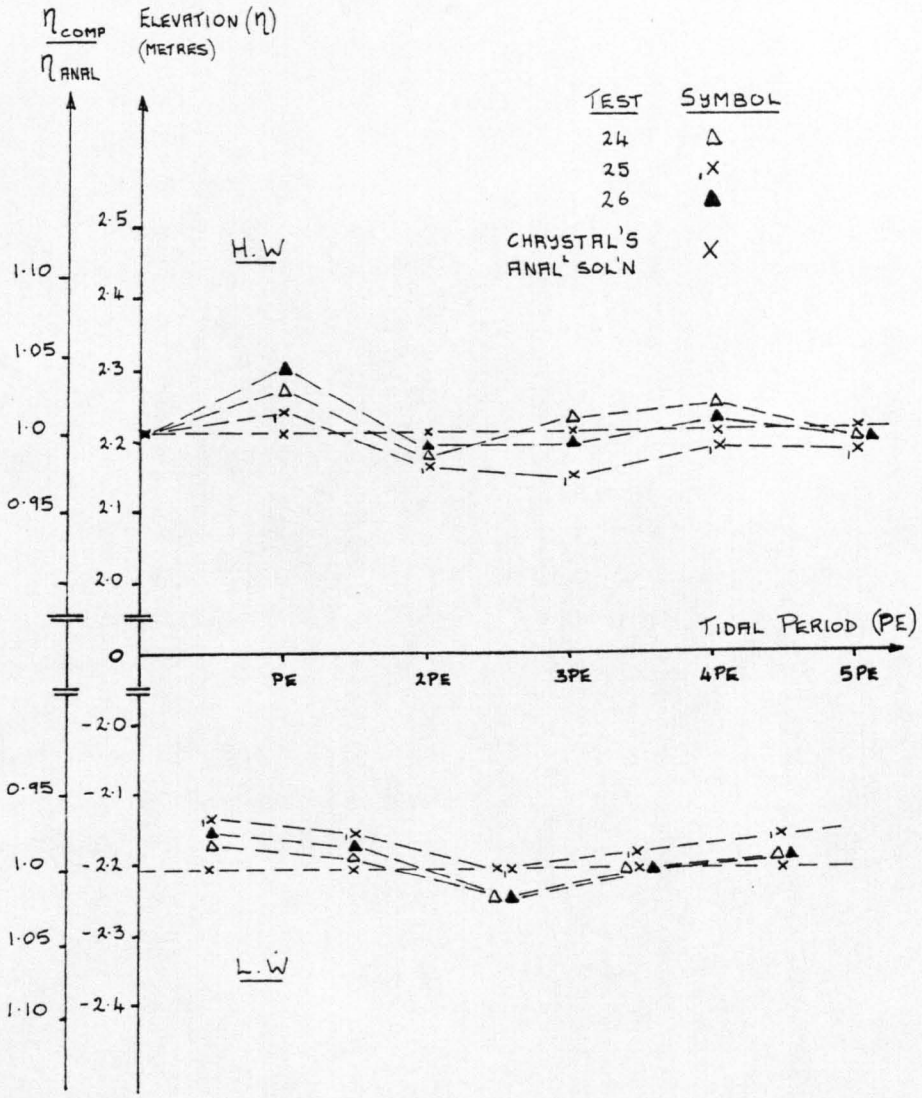

Figure 4.10

c) From the results of tests 24 to 27 the most successful simulation was that of test 26 which used linear 45° characteristics and interpolation scheme 4. In sections 4.3.1 and 4.3.2 the most satisfactory interpolation scheme was interpolation scheme 1. There is no reason why one interpolation scheme should be more suitable for one channel and not for another and indeed interpolation scheme 1 is obtained from interpolation scheme 4 from the simplification produced when considering constant depth. The equivalence between interpolation schemes 1 and 4 has been shown in section 3.4. These interpolations were tested using an elliptic approach, with success, and in addition, by considering any special nature of the flow, as described also in section 4.3.2 the hyperbolic method of simulation is another alternative.

4.4 SEICHE SIMULATION IN CLOSED BASINS

The occurrence of seiches in nature is invariably associated with the oscillations of a relatively small body of water, such as in a lake or harbour. These oscillations normally occur at a natural frequency which is higher than those of tidal movements therefore tidal resonance is unlikely to become a problem. With the assumptions of small amplitude waves, the absence of bed friction and Coriolis forces, and constant equilibrium depth the long wave equations can be combined to give the following elliptic equation,

$$\frac{\partial^2 \eta}{\partial x^2} + \frac{\partial^2 \eta}{\partial y^2} + \frac{\sigma^2}{g\bar{H}} \eta = 0 \qquad (4.56)$$

This equation is the two-dimensional form of equation (4.7) derived by Lamb in section 4.2 and describes the free oscillation of a body of water. An analytical solution of equation (4.56) may be found for the free oscillating modes for a rectangular basin with length L in the x direction and width B in the y direction. This solution is as

follows

$$\eta = A \cos\left(m\pi\frac{x}{L}\right) \cdot \cos\left(n\pi\frac{y}{B}\right) \cdot \cos(\sigma t)$$

$$u = A\frac{\sqrt{2}}{2}\frac{c}{H} \sin\left(m\pi\frac{x}{L}\right) \cdot \cos\left(n\pi\frac{y}{B}\right) \cdot \sin(\sigma t)$$

$$v = A\frac{\sqrt{2}}{2}\frac{c}{H} \cos\left(m\pi\frac{x}{L}\right) \cdot \sin\left(n\pi\frac{y}{B}\right) \cdot \sin(\sigma t) \qquad (4.57)$$

where A is the maximum amplitude at the boundaries and m and n are the number of nodes in the x and y direction respectively, which identify the particular mode of oscillation. The natural frequency is determined by

$$\sigma = \pi\sqrt{g\bar{H}} \cdot \sqrt{\left(\frac{m}{L}\right)^2 + \left(\frac{n}{B}\right)^2} \qquad (4.58)$$

and is a function of the dimensions of the basin.

For the particular case of an x - t seiche of lowest mode, $m=1$, $n=0$ the equations of (4.57) become

$$\eta = A \cos\left(\pi\frac{x}{L}\right) \cdot \cos(\sigma t)$$

$$u = A\frac{c}{H} \sin\left(\pi\frac{x}{L}\right) \cdot \sin(\sigma t) \qquad (4.59)$$

$$v = 0$$

The period for this case is obtained from equation (4.58) and is

$$T = \frac{2L}{C} \qquad (4.60)$$

where $C = \sqrt{g\bar{H}}$

Consideration of the free oscillations in closed basins, for the purpose of simulation, closely follows the objectives pursued in the simulation of forced waves. For consistency the period chosen for free wave simulation is the same as that for the forced wave condition and is of tidal magnitude. An important consequence of considering closed basins is that in the absence of any external forcing functions such as a boundary condition the numerical scheme can be tested to establish if it is conservative. For example, in the constant depth case it is shown that only the numerical timestep corresponding to the limiting timestep obtained from the C.F.L. condition will produce the free oscillations prescribed by the analytical solution. This is assuming that the correct starting conditions and boundary interpolations have been applied. If not, or if another timestep is used the numerical scheme produces a motion that either becomes unstable or attenuates numerically.

4.4.1 The x - t seiche in a rectangular basin of constant depth.

A synopsis of the tests 28 to 37 is presented in table 4.6 showing the computational parameters in simulating x - t oscillations. Since the variation of the free surface from the analytical one is a measure of the inaccuracy of the numerical scheme, the last column in table 4.6 shows the extent of this variation. A measure of this variation is the attenuation of elevation at the boundaries during each tidal oscillation and is calculated from $1 - \eta_{k+1} | \eta_k$ where k is the number of free oscillations. The tests can be divided into three distinct sets according to the ratio of DT/DTmax and only in test 35 with this ratio equal to unity is the analytical solution achieved. A comparison of all these tests for successive high waters at the boundaries of the basin is shown in figure 4.11. The curves on this graph show clearly the attenuation which is proportional to the gradient of the curve, and is associated with most of the tests.

The pertinent information extracted from an examination of each test is listed in tables A.19 to A.22. An account of each test together with its conclusion is provided as follows:

a) All the tests had as their starting condition the analytical free surface corresponding to high water and zero velocities throughout the basin. One exception was test 34 which used a linearly sloping free surface and failed to reproduce the analytical scheme. This test confirms once more that a hyperbolic approach cannot be used in an elliptic problem, for configurations of constant depth.

b) The results from test 35 reproduced exactly the motion given by the analytical solution, throughout all time levels. The timestep was found from equation (4.51) with X = 2. The numerical scheme required DT = DTmax and interpolation scheme 1 and used linear 45° characteristics. This scheme was used in the successful simulation in previous configurations.

c) Using the scheme of test 35 with values of timestep less than the maximum timestep showed that the attenuation per tidal cycle increased as DT/DTmax decreased. This phenomenumis shown in table 4.5.

Test	DT/DTmax	% Attenuation/cycle
33	0.995	0.5
31	0.943	4.6
37	0.500	43.7

Table 4.5

The mechanism for attenuation has been discussed in section 3.5 and is basically the result of the difference between the numerical and physical celerities. The timestep is related to the physical celerity through the C.F.L. condition, $DT_{max} = 0.707\ DS/C_{max}$. If another value of DT is chosen then the numerical celerity C will not be equal to the physical celerity since C = 0.707 DS/DT.

1-D FREE OSCILLATION

COMPUTATIONAL PARAMETERS FOR THE FRICTIONLESS RECTANGULAR BASIN OF CONSTANT DEPTH

Test	Initial Surface	Numerical Scheme	M	N	H m	$\eta_{I=1}$ m	T secs	DS m	DT sec	DT_{max} sec	Final Solution % Attenuation/Period
28	Analytical	⊗	19	13	26.42	0.2	44712	20,000	828	878	5.4
29	Analytical	⊕	19	13	26.42	0.2	44712	20,000	828	878	2.1
30	Analytical	+	19	13	26.42	0.2	44712	20,000	828	878	1.8
31	Analytical	₀×	19	13	26.42	0.2	44712	20,000	828	878	4.6
32	Analytical	₁+	20	13	29.45	0.2	44712	20,000	828	832	Unstable
33	Analytical	₁×	20	13	29.45	0.2	44712	20,000	828	832	0.5
34	Linear	₁Δ	20	13	29.45	0.2	44712	20,000	828	832	7.08
35	Analytical	×	19	13	26.56	0.2	44676	20,000	876	876	0.
36	Analytical	Δ	19	13	26.56	0.2	44676	20,000	876	876	4.4
37	Analytical	₂×	19	13	26.56	0.2	44676	20,000	438	876	43.7

Table 4.6

NOTE: Prefix to symbols is a graphical aid.

Envelope curves of successive high water elevations at the boundary of a frictionless closed basin of constant depth. $|H.W| = |L.W|$

TEST	SYMBOL	TEST	SYMBOL	TEST	SYMBOL
28	⊗	32	$_1+$	35	× (ANAL SOLN)
29	⊕	33	$_1\times$	36	Δ
30	+	34	$_1\Delta$	37	$_2\times$
31	$_\circ\times$				

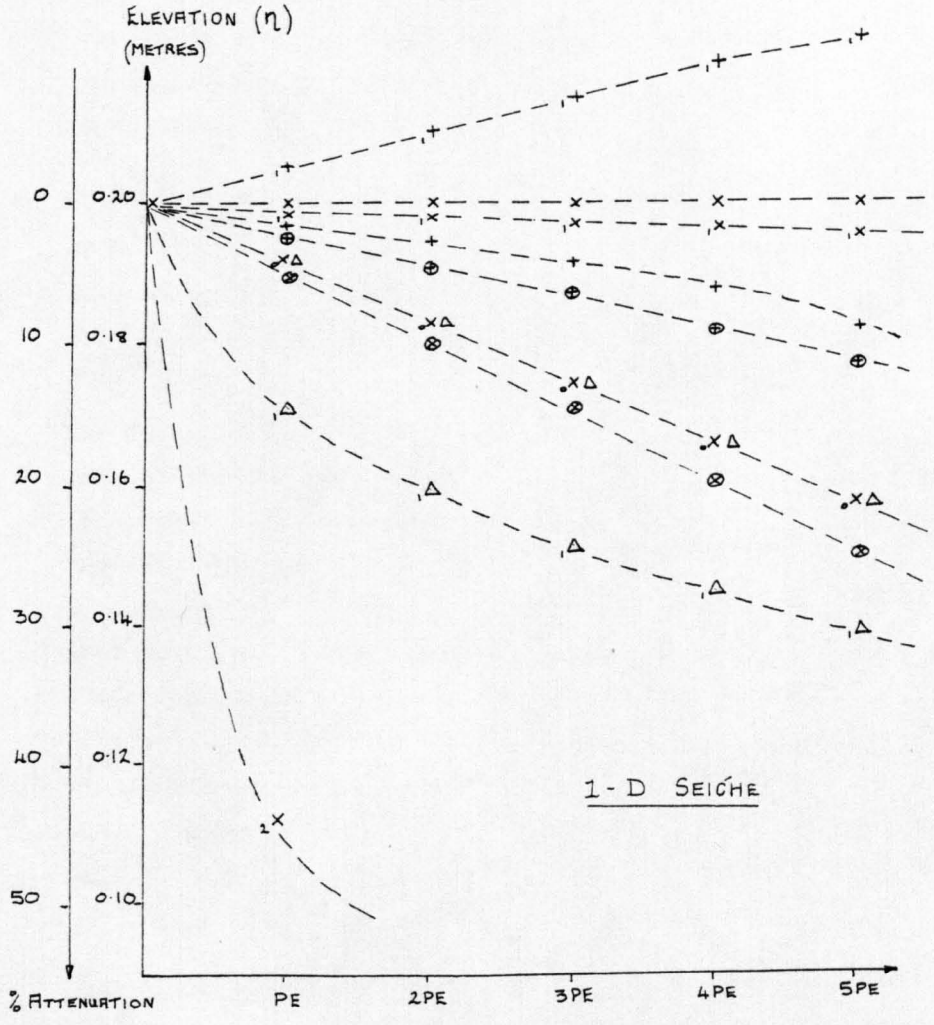

Figure 4.11

d) The results of tests 29 and 30 are shown in table A.20. Since test 30 used a linear numerical scheme and test 29 a non-linear one, a comparison between the results of both tests showed that the effect of the non-linear terms was very small. In both tests attenuation occurred since the condition DT = DTmax was not fulfilled and the attenuation was found to be greater when the numerical scheme contained non-linear terms.

e) The results of test 36 showed that attenuation had taken place. The data was identical to that for test 35 but the interpolation scheme was not the same. In test 36 interpolation scheme 3 was used and it differs from interpolation scheme 1 in the construction of the velocity equation at the boundary points. The failure of interpolation scheme 3 to produce the analytical motion was also observed in tests 6 and 7 for the rectangular channel of constant depth.

f) The interpolation scheme 2 used in test 30 was also found to be dissipative since the energy loss resulted in elevations smaller than those of the analytical solution. In this test DT = 0.943 DT_{max}. For the same numerical scheme applied in test 32 with DT = 0.995 DT_{max} the results were unstable. This instability is shown in figure 4.11 as a curve with a positive gradient. The conclusion from these two tests is that interpolation scheme 2 becomes unstable when the timestep is very close to that determined from the C.F.L. condition. It is precisely this interpolation scheme that is applied successfully to the simulation of tides and surges in Chapters 7 and 8 and an explanation for its inclusion in the numerical scheme is provided in section 7.3. At this stage it is only important to note that the analytical motion is produced with interpolation scheme 1 using the method of linear 45° characteristics with DT = DT_{max} for configurations with free oscillations.

4.4.2 The x - y - t seiche in a square basin of constant depth

The simulation of the x - y - t seiche action provides an opportunity of testing the models under circumstances of truly two

dimensional flow in which a comparison of the computations can be made with those from the analytical solution. Before the simulation can begin the channel geometry must be calculated whilst ensuring that the equality $DT = DT_{max}$ is satisfied. This condition ensures that there is an equivalence between the numerical and physical celerities. The simulation was performed using the lowest mode of oscillation therefore m = n = 1 and equation (4.58) reduces to

$$\sigma = \frac{1}{\sqrt{2}} \cdot \frac{2\pi}{L} \cdot C \qquad (4.61)$$

Rearranging this equation produces

$$\frac{C.T}{L} = \sqrt{2} \qquad (4.62)$$

This expression is the wavelength divided by the channel length (since L = B) and has been defined as x in equation (4.51). This equation with $X = \sqrt{2}$ yields

$$DT = T/2.(M-1) \qquad (4.63)$$

With T = 44712 secs, M = 19 gives DT = 1242 secs and with DS = 20,000m the celerity obtained from the C.F.L. condition is 11.385 m/s. The depth H from C^2/g is therefore 13.212m. This data is shown in table 4.7 and was used in tests 38 to 41. The information on this table shows that in tests 38 and 39 the tidal oscillations were simulated in exact agreement with the motion determined by equations (4.57) shown in table A.23. The exact reproduction of the analytical motion by this model is verification that for channels and basins of constant depth the method of characteristics is conservative. Matsoukis (1980) considered the simulation of the x - y - t seiche as a very stringent test and showed that some well known finite difference models did not successfully produce this motion.

2-D FREE OSCILLATION

COMPUTATIONAL PARAMETERS FOR THE FRICTIONLESS SQUARE BASIN OF CONSTANT DEPTH

Test	Initial Surface	Numerical Scheme	M	N	H	$\eta_{I=1}$	T	DS	DT	DT_{max}	Final Solution
					m	m	secs	m	sec	sec	
38	Analytical	×	19	19	13.212	0.2	44712	20,000	1242	1242	As Anal Soln
39	Analytical	△	19	19	13.212	0.2	44712	20,000	1242	1242	As Anal Soln
40	Analytical	⊗	19	19	13.212	0.2	44712	20,000	1242	1242	Not Periodic
41	Analytical	$\triangle_9$	19	19	13.212	0.2	44712	20,000	1242	1242	Periodic and very close to Anal Solution

Table 4.7

It is again emphasised that only one numerical scheme used in the tests of free and forced waves has produced the analytical tidal motion in each configuration. This scheme uses interpolation scheme 1 and linearised 45° characteristics. To evaluate the accuracy of simulating with a numerical scheme using 90° characteristics, test 41 was conducted and the results compared to those from test 39. The results from test 41 are presented in table A.24 for successive high water displacements corresponding to grid points positioned along the diagonal of the basin. The elevations at any time level in test 41 were found to be very close but not exactly equal to those from test 39. The maximum difference in elevation between both tests occurred at high water or low water at the closed boundary points. The elevation there was 0.201m in test 41 whereas in test 39 and for the analytical solution it was 0.200m. Nevertheless the method of characteristics derived from bicharacteristics taken at 90° angles gives reasonably accurate results. This is not surprising since this method only differs in its construction from that using 45° characteristics when considering a boundary point. Both schemes are identical for the determination of the unknown variables at an internal point.

In test 40 the numerical scheme of test 38 was re-run with non-linear and convective terms included. The computations are shown in table A.24 and show that high and low waters are increasing positively with each oscillation. The conclusion from this test is the same as for that of test 9 which also included non-linear terms in the system. This conclusion is that the periodicity of the numerical results is disturbed by the introduction of non-linear terms and that their inclusion is not justified since the problem is essentially linear by virtue of starting condition. In being linear the problem is therefore elliptic and so requires the correct starting conditions; this is provided by the analytical solution which is also linear.

4.4.3 The x - t seiche in a basin of linearly varying mean depth.

It has already been established in section 4.2 from equations (4.15) and (4.16) that the simulation of motion in a channel of triangular profile is impractical for the numerical schemes developed in Chapter 3. It is more convenient to consider a channel of

trapezoidal profile and this configuration was tested in section 4.3.3 by comparing to Chrystal's analytical solutions derived in section 4.2. This channel was again investigated but with both ends closed to determine whether the numerical scheme can accurately simulate the free wave oscillations. The dimensions of the basin are shown in figure 4.12.

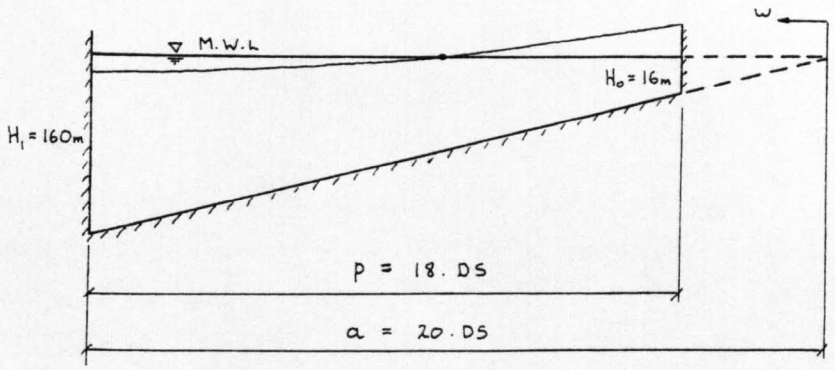

Figure 4.12

The lowest mode of oscillation in this basin corresponds to the second mode of the equivalent open channel. The period equation is obtained from equation (4.34) with the boundary condition $\xi = 0$ at $\omega = \sigma\alpha$ and is

$$Y_1(\sigma\alpha) \cdot J_1(\sigma\beta) - J_1(\sigma\alpha) \cdot Y_1(\sigma\beta) = 0 \qquad (4.64)$$

From equation (4.30) and the dimensions of the basin

$$\sigma\beta = 0.3162\,\sigma\alpha \qquad (4.65)$$

Using trial values for $\sigma\beta$ and $\sigma\alpha$ to satisfy equation (4.64) gives $\sigma\alpha = 4.8$ and $\sigma\beta = 1.517$. From equation (4.29)

$$\sigma\alpha = \frac{2\pi}{T} \cdot \frac{2a}{c_1} \qquad (4.66)$$

gives T = 15328 sec.

The timestep DT corresponding to DT_{max} is obtained from the C.F.L. condition namely

$$DT = \frac{0.707DS}{C}$$

The free surface is determined from equation (4.35) so that

$$\eta = A' \left(Y_1(\sigma\alpha) \cdot J_0(\omega) - J_1(\sigma\alpha) \cdot Y_0(\omega) \right) \cdot \cos(\sigma t + \phi) \quad (4.67)$$

The constant A' was taken as 0.7446 in the simulation to produce a maximum of 0.1m amplitude at the left hand side of the basin. The free surface along the x axis of the basin corresponding to high water conditions at one end is shown in table A.25.

The dimensions of the basin together with the set of parameters used to identify the tests 42 to 45 are shown in table 4.8. A description of each test highlighting its significant features and a comment on its results is as follows

a) Tests 42 and 43 used the same data, however the interpolation scheme in test 43 is only applicable to constant depth cases. The results produced in table A.26 can therefore be ignored. In both tests the analytical solution was not produced, instead numerical attenuation of the elevations and velocities occurred. The attenuation produced in each oscillation was found to be constant and was not unlike that produced in basins of constant depth simulated in section 4.4.1. In the latter case the attenuation occurred in some cases because DT < DTmax which was shown to mean an inequality between the numerical and physical celerities.

b) The problems of simulating free waves using a fixed size of computational grid, which implies a fixed numerical celerity, applied to a situation of variable physical celerity have been discussed in section 3.5. For such a case, a heavy dependence is placed on the interpolation scheme and it was shown that a

more accurate method would be to subdivide the spacestep whilst retaining the original timestep. Such a scheme was devised and the details presented in Chapter 3 and it was applied in test 44 with the data as shown in table 4.8. The results along the centre line of the channel in the direction of motion are shown for high and low waters in table A.27. These results show that subdividing the spacestep used in test 42, by a factor of 3 does not entirely remove the attenuation but succeeds in reducing it from 45% per oscillation to 21% per oscillation.

An alternative method, investigated in test 45 was merely to reduce the space and time steps of test 42 by a factor of 3. The numerical data is shown in table 4.8 and the results for high and low water are presented in table A.27. From these results the attenuation per cycle was also found to be 21%. In both tests 44 and 45 the spacestep was one-third of that in test 42 and to maintain the length of the basin constant for all tests, the number of grid points in the x direction in tests 44 and 45 was fifty-five. Although the results from tests 44 and 45 were very similar the computational time for test 44 using the method of subdivisions only required one-third of the computational time for test 45.

A theoretical explanation of the simulation of results other than those of the analytical solution for free wave motion has been presented in section 3.5. In that section the disadvantages of numerical interpolation as a result of using a regular grid were noted whilst the advantages of using the method of subdivisions were also highlighted. With the results from tests 42, 44 and 45 the following conclusion is made regarding <u>free</u> wave oscillations in a basin of <u>variable</u> depth. For this case the energy loss cannot be entirely removed when the numerical scheme uses either a regular grid method or the method of subdivisions (although the latter scheme is more favourable). The features causing the energy loss are as follows:

a) The presence of ghost characteristics as a result of interpolation.

b) The application of an interpolation scheme which uses grid points that lie outside the domain of dependence of the difference scheme.

1-D FREE OSCILLATION

COMPUTATIONAL PARAMETERS FOR THE FRICTIONLESS RECTANGULAR BASIN

WITH LINEARLY VARYING MEAN DEPTH

Test	Initial Surface	Numerical Scheme	M	N	H m	T secs	DS m	DT secs	DT_{max} secs	Final Solution % Attenuation/Period
42	Analytical	▲	19	11	160 to 16	15318	11600	207	207	45
43	Analytical	x	19	11	160 to 16	15318	11600	207	207	34
44	Analytical	▲	55	11	160 to 16	15318	3867	207	69	21
45	Analytical	▲	55	11	160 to 16	15318	3867	69	69	21

Table 4.8

c) The method of subdivisions implies more than one numerical celerity for which the interpolation scheme is theoretically accurate. However, in reality, the variable depth basin has an infinite number of celerities corresponding to the variation in mean depth.

The method of subdivisions is therefore an improvement on the regular grid method but requires further development.

Note on finite amplitude

Any reference in this thesis to a finite amplitude wave is made only with respect to mean water depth H such that $\eta > H/10$. For these waves, the non-linear processes in their propagation are important and so have been investigated. In general the wave forms studied are all of small amplitude by conventional definition (since $\eta < L/100$) although non-linear according to the Ursell parameter in which $\eta L^2/H^3 \gg 1$.

CHAPTER 5

THE SIMULATION OF WIND DRIVEN SURGES IN CHANNELS OF SIMPLE GEOMETRY

5.1 INTRODUCTION

The verification, that a numerical model accurately represents the dynamics of the study region by comparing it with field observations, is of limited value. The limitations of this approach are partly the results of using inadequate data together with an incomplete understanding of the behaviour of the numerical procedure. Certain features should be highlighted:

a) There is still a general lack of sufficient records of water depth and velocity throughout temporal and spatial domains of interest especially offshore and in the open sea. This position is steadily improving, however, for example field study data is published in the M.I.A.S. reports.

b) Accurate vertically averaged velocities are particularly scarce.

c) The overall effect of using an irregularly shaped schematisation of the original configuration is important yet can be difficult to estimate in view of point (a).

These various sources of error and uncertainty in verification are eliminated when the numerical solutions are compared with the analytical solutions for surge development given later in this chapter. A rather systematic assessment of the performance of the numerical scheme may be based on the philosophy of Chapter 4. By necessity the shallow water equations have been linearised and likewise the numerical scheme constituting the model. In both situations wind stress and variable bathymetry have been incorporated in the solutions of the shallow water equations.

The simple geometric configurations employed in the successful testing of the model for tidal propagation may also form the basis of the analytical solutions describing the free surface produced by the

wind field. A comparison of numerical results with these analytical solutions is conducted for uniform and non-uniform, steady and unsteady wind fields. This also bears upon the use of a wind drag coefficient as, for example, by Heaps (1969).

5.2 WIND FIELDS AND WIND STRESS

One of the largest components of a storm wave is supplied by the wind stress on the water surface. A full account of the wind wave interaction is most involved and outwith the direction of this research but it should be noted that at the present, the energy transfer mechanism from wind to water waves and the resulting wave growth is not fully understood. All wave forecasting relationships are adjusted by actual wave data. Such forecasts are obtained from semi-theoretical or semi-empirical theories, the latter approach encompasses the significant wave method and the wave spectrum method.

Wave theories for wave generation have been proposed concerning the critical wind speed at which the fluid flow at the interface changes from hydrodynamically smooth to rough turbulent. Most theories presume that the stress developed will vary with the duration and fetch of the wind. Of particular importance is Munk's theoretical analysis (1955) which shows clearly the importance of the high frequency components of the wave motion which contribute largely to the form drag. According to Munk's theory the drag on the sea surface should not vary greatly with the fetch of the wind over the water surface, as the high frequency wave motion reaches the value for a fully developed sea much more rapidly than the low-frequency components. A similar conclusion was found by Francis (1951) during the measurement of the drag coefficient of a water surface in wind tunnel experiments. He concluded from his measurements that the mechanism for drag is not controlled by the large waves but largely by the tiny wind ripples. Therefore it is the smaller elements of roughness from the water's surface which provide the traction for the wind on the sea. This can be likened to the sand grain roughness, rather than the bed dunes, providing roughness resistance to water flow in channels.

The mathematical expression defining the shear stress at the

air-water interface is obtained in an empirical manner and is given by Hellstrom (1941)

$$\tau = k \rho_a W_y^2 \tag{5.1}$$

where k is the wind drag coefficient,

ρ_a is the density of air

and W_y is the shear velocity of the wind at a height y above the water surface. In most wind measurements, the values of wind speed are recorded at the 10m height and in storm surge calculations it is more appropriate to express equation (5.1) using ρ_ω, the density of water. Therefore

$$\tau = K \rho_\omega W_{10}^2 \tag{5.2}$$

An upper bound of $K = 3.3 \times 10^{-6}$ for the wind drag coefficient is generally applied to limited bodies of water when $W_{10} \geq 15 m/s$ and for the open ocean $K = 3 \times 10^{-6}$ is appropriate. By comparing equations (5.1) and (5.2) the following expression is produced

$$K = k \rho_a / \rho_\omega \tag{5.3}$$

With the values of $\rho_a = 1.25 kg/m^3$ and $\rho_\omega = 1025 kg/m^3$ equation (5.3) produces the relationship

$$K = k / 820 \tag{5.4}$$

In the present numerical scheme the wind resistance coefficient k was specified as 2.513×10^{-3} for $W_{10} > 19.2$ m/s. These values were first suggested by Charnock and Crease (1957) and seem to be generally accepted as being representative of the drag coefficient on the sea surface.

The analytical solutions derived in the next section have been developed by other authors using equation (5.2) and so are expressed in terms of K. When comparing the numerical results to those from the analytical solution an equivalence between k and K must be maintained. This is accomplished using equation (5.4) and so $k = 2.513 \times 10^{-3}$ in the model is equivalent to $K = 3.06 \times 10^{-6}$ in the analytical solutions.

5.3 THE ANALYTICAL SOLUTIONS FOR STEADY STATE WIND FIELDS /

5.3 THE ANALYTICAL SOLUTIONS FOR STEADY STATE WIND FIELDS

The wind field exerts a tractive force on the water resulting in the water being dragged in the direction of the wind. The equilibrium surface slope maintained by the action of a steady wind field blowing over shallow water has been theoretically derived by Hellstrom. Although the mechanism represents a gross simplification, it may be expressed as

$$\frac{dS}{dx} = \frac{n\,T}{\rho_w\, g\, H} \qquad (5.5)$$

where dS/dx is the surface gradient as a result of wind stress and n is a constant dependent on frictional conditions at the sea bottom. For frictionless conditions $n=1$ and generally takes a value from 1 to 1.5. Substituting for T (equation 5.2) into equation (5.5) produces

$$\frac{dS}{dx} = \frac{K\,W_{10}^2}{g\,H} \qquad (5.6)$$

for the frictionless case.

Considering the case of a steady uniform wind field directed along the axis of a channel of constant depth, the hydrostatic pressure is expressed as

$$P = \rho_w\, g\,(H+S) \qquad (5.7)$$

and a more accurate version of equation (5.5) is therefore

$$\frac{dS}{dx} = \frac{K\,W_{10}^2}{g\,(H+S)} \qquad (5.8)$$

which includes the hydrostatic effect of the surge in the term $(H+S)$. Integration yields an expression for the surge height S; the proof is presented by Ippen (1966) and is as follows

$$g\,(H+S).dS = K.W^2\,dx$$

$$g\int H.dS + g\int S.dS = K.W^2\int dx$$

Since H is constant

$$g.H.S + \tfrac{1}{2}\,g\,S^2 = K.W^2 L$$

where L is the length of the channel. Hence

$$S = \frac{K W^2 L}{g(H + S/2)} \tag{5.9}$$

Equation (5.9) is quadratic and it is easily proved that the positive root is given by

$$S = H\left[\sqrt{\frac{2KW^2L}{gH^2} + 1} - 1\right] \tag{5.10}$$

For the case of the closed basin shown in figure 5.1

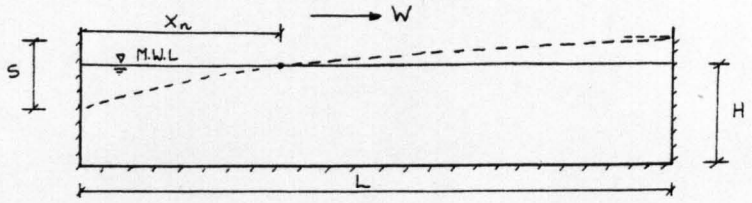

Figure 5.1

the surge S is not measured from mean water level but from the lowest water level. Equation (5.10) applies equally to an open channel of constant depth since this case is merely a segment of the closed basin. In both configurations it is more convenient to calculate the surge height from mean water level S' and one way is to assume that S' = S/2. This condition is only an approximation and a more accurate method arises from considering the position of the nodal point. Assuming that the node is not necessarily at the centre of the basin, its position is expressed as

$$\frac{X_n}{L} = 1 - \frac{S_{max}^2 + 2S_{max}H}{2KW^2L/g} \tag{5.11}$$

where $S = S_{max}$ at $X = L$ and Xn is as shown in figure 5.1. From equations (5.10) and (5.11) the following expressions can be derived

$$+S_{M.W.L} = H\left[\sqrt{\frac{2KW^2L(1 - X_n/L) + 1}{gH^2}} - 1\right] \tag{5.12}$$

$$-S_{M.W.L} = H\left[\sqrt{\frac{-2KW^2L(X_n/L) + 1}{gH^2}} - 1\right] \tag{5.13}$$

With $X_n/L = 0.5$ these equations show in fact that $|+S_{M.W.L}| \neq |-S_{M.W.L}|$. When the surge is small in relation to the depth it is reasonable to assume that the node is at the centre of the basin.

A similar method is used to derive the analytical solution for a steady uniform wind field applied to a channel of linearly varying mean depth. Considering the channel shown in figure 5.2 the

analytical solution is obtained by integrating equation (5.6).

$$\int dS = \frac{KW^2}{g}\int_{x_o}^{x_1}\frac{dx}{H} = \frac{KW^2}{g}\cdot\frac{1}{m}\int_{H_o}^{H_1}\frac{dy}{H}$$

since $dy = m.dx$. Therefore

$$S = \frac{KW^2}{gm}\left(\log_e H_1 - \log_e H_o\right)$$

$$S = \frac{KW^2}{gm}\log_e\left(\frac{H_1}{H_o}\right) \qquad (5.14)$$

where m is the bed slope.

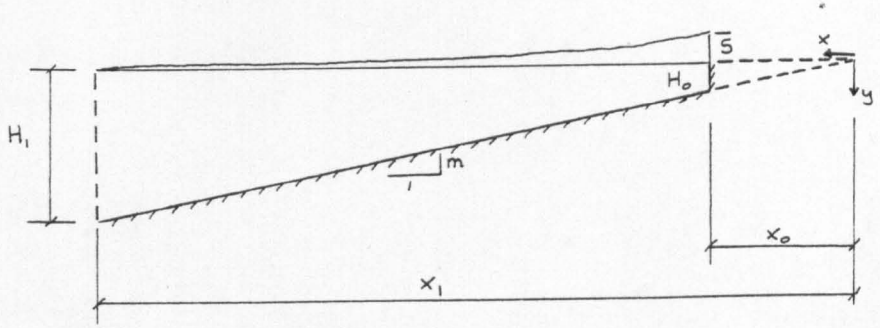

Figure 5.2

The surge height obtained from equation (5.14) is accurate for $H_o > 10m$ and if the surge height is large in comparison to H_o then the following expression should be used.

$$S = \frac{KW^2}{gm}\log_e\frac{H_1}{(H_o + S)} \qquad (5.15)$$

Equation (5.14) can only be realistically applied to channels of trapezoidal as opposed to triangular longitudinal profiles. For the latter configuration this analytical solution would predict an infinite surge height, since $H_o = 0$.

A comprehensive derivation of the analytical solution for a uniform steady wind field applied to open channels of variable bathymetry was given by Lynch and Gray (1978). They provided an analytical solution for channels which have their depths represented by

$$H = c.x^n \qquad (5.16)$$

where c is a constant and n is not necessarily an integer and may assume any real value. The analytical solution is not confined to a

wind field directed along the axis of the channel, as shown in figure 5.3.

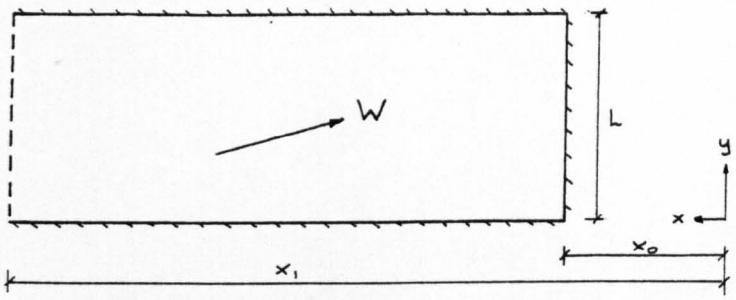

Figure 5.3

The boundary conditions for this problem are as follows at

$$x = x_o : \quad \frac{\partial S}{\partial x} + \frac{T_x}{\rho_w g c x^n} = 0 \qquad (5.17)$$

$$\text{at} \quad x = x_1 : \quad S(x, y) = 0 \qquad (5.18)$$

$$\text{at} \quad y = 0, L : \quad \frac{\partial S}{\partial y} + \frac{T_y}{\rho_w g c x^n} = 0 \qquad (5.19)$$

The complete steady state response to an arbitrary wind stress thus obtained by superposition of x and y components is

$$S(x,y) = T_x \left(a - b x^{1-n} \right) + T_y \left\{ x^h \sum_{J=1}^{\infty} Z_h \left(\frac{\gamma_J x}{x_o} \right) \left[f_J \cosh \left(\frac{\gamma_J y}{x_o} \right) + e_J \sinh \left(\frac{\gamma_J y}{x_o} \right) \right] \right\} \qquad (5.20)$$

in which Tx and Ty are the x and y components of wind stress respectively. This equation is valid for $n \neq 1$ and

$$a = x_1^{1-n} / \rho_w (1-n) \cdot g \cdot c \;, \quad b = 1 / \rho_w (1-n) \cdot g \cdot c \qquad (5.21)$$

For the case $n = 1$ the first term in equation (5.20) is replaced by $T_x (a - b \log_e x)$ and the constants a and b are calculated from the boundary conditions (5.17) and (5.18). The values are

$$a = \log_e x_1 / \rho_w \cdot g \cdot c \;, \quad b = 1 / \rho_w \cdot g \cdot c \qquad (5.22)$$

In the special case where Ty = 0 and $n = 1$, equation (5.20) reduces to the analytical solution given by equation (5.14). The variables in the

second part of equation (5.20) are expressed as follows

$$h = (1 - n)/2 \tag{5.23}$$

$$e_J = \frac{x_o G_J}{\gamma_J g^c \rho_w} \tag{5.24}$$

$$f_J = e_J \left[1 - \cosh\left(\frac{\gamma_J L}{x_o}\right)\right] \Big/ \sinh\left(\frac{\gamma_J L}{x_o}\right) \tag{5.25}$$

$$G_J = \frac{\int_{x_o}^{x_1} x^h \cdot Z_h\left(\frac{\gamma_J x}{x_o}\right) dx}{\int_{x_o}^{x_1} x \left[Z_h\left(\frac{\gamma_J x}{x_o}\right)\right]^2 dx} \tag{5.26}$$

where $Z_h(x) = J_h(x) \cdot Y_h(x_1) - J_h(x_1) \cdot Y_h(x)$ (5.27)

and γ_J is the Jth zero of Z_{h-1}.

Equation (5.20) is impractical for readily producing results for comparison with the simulated results. The actual simulation was therefore not performed although it poses no difficulties. However the configurations corresponding to equations (5.12) and (5.14) were simulated.

5.4 APPLICATION OF THE WIND STRESS TO THE NUMERICAL SCHEME

Having derived analytical solutions suitable for comparison with the results from the numerical scheme the next step was to represent the wind stress effect in the scheme using the appropriate algorithms. This was accomplished in several steps which are outlined in the flow charts shown in figures 5.4, 5.5 and 5.6. Firstly the wind field is specified using an expression that defines its position relative to the channel or basin. This is shown in block 1 of figure 5.4, as is also the incorporation of the wind stress coefficient into the calculation of wind stress at each grid point. Each grid point was defined by a configuration number and for each point the wind stress was applied as an external force to the characteristic equations governing velocity. This latter step is shown in block 2 of figure 5.4.

The flow diagram which represents steady uniform wind conditions may easily be modified to account for a non-uniform or non-steady wind field. In the case of a progressive wind field with

a triangular wind stress distribution the unsteady movement was achieved in two steps. These steps are shown in figures 5.5, 5.6 and can be summarised as follows:

a) The wind stress distribution is mathematically defined as a continuous function of length and breadth of the channel. Block 1 in figure 5.5 therefore replaces block 1 in figure 5.4.

b) The transient nature of the wind field was achieved by advancing the wind field one grid step at prescribed regular intervals of time. Providing these gridsteps are not too large, the wind field maintains a continuous motion over the channel. The steps involved in this stage are shown in the flow chart of figure 5.6 which modifies that of figure 5.5.

The definitions of the symbols shown in figure 5.4 are as follows:

WC, WK : Wind stress coefficient and wind speed in M.P.H. respectively.

BK : Wind direction measured clockwise from true north,

LF, LB : Each is an integer multiple of the spacestep DS, measured from the edge of the shelf defining the position of the front and back of the fetch respectively.

W(I,J), B(I,J) : Wind speed and direction respectively at each grid point.

WX(I,J), WY(I,J): Wind stress in the respective X and Y direction at each grid point.

UF(I,J), VF(I,J): Depth averaged velocities in the respective X and Y direction at each grid point.

A : The celerity of the wave.

EF(I,J), H(I,J), ZF(I,J): The respective elevation above M.W.L, the depth below M.W.L and the total depth at each point.

D : Density of sea water.

ST : Time at which the wind field is first applied.

IN : Principally for moving wind fields, it is the time interval in which the wind field moves across one spacestep.

KT, KTMAX : KT is a counter that stores the number of discrete movements of the wind field and KTMAX is the maximum number of required movements.

Application of wind stress to program.

Steady, uniform wind stress.

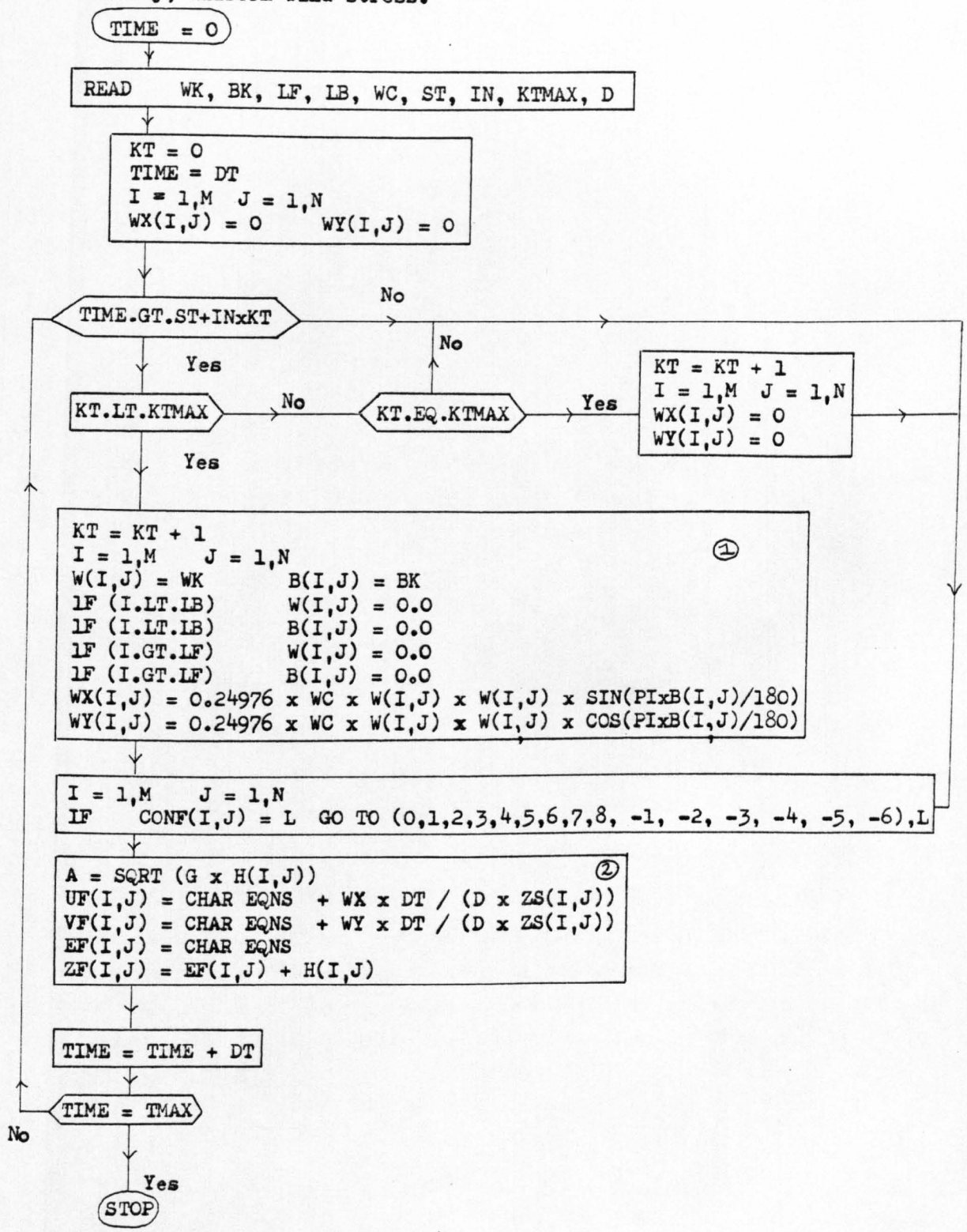

Figure 5.4

For a steady, triangular wind stress field block 1 in figure 5.4 now becomes as shown in figure 5.5

```
TK = WK x WK                                                    (1)
LW = LF - LB
 I = 1,M
 J = 1,N
IF  (I.LE.(0.5xLW+LB))                    TS = TKx2x(I-LB)/LW
IF  (I.GT(0.5xLW+LB))                     TS = TKx2x(LF-I)/LW
 B(I,J) = BK
IF (I.LT.LB)   TS = 0.0
IF (I.LT.LB)   B(I,J) = 0.0
IF (I.GT.LF)   TS = 0.0
IF (I.GT.LF)   B(I,J) = 0.0
W(I,J) = SQRT (TS)
WX(I,J) = 0.24976xWCxW(I,J)xW(I,J)xSIN(PIxB(I,J)/180)
WY(I,J) = 0.24976xWCxW(I,J)xW(I,J)xCOS(PIxB(I,J)/180)
```

Figure 5.5

with the symbols defined as follows;

LW : Length of the fetch as an integer multiple of the spacestep DS.

TK : Obtained by squaring the maximum wind speed and proportional to the maximum wind stress.

TS : A parameter proportional to the wind stress at a position I along the shelf.

The value of wind stress at each grid point is calculated from the geometry of the stress field defined by the parameters LF, LB, LW as shown. If the triangular wind stress field is unsteady, then figure 5.5 is adapted by inserting two extra lines of computation as shown in figure 5.6.

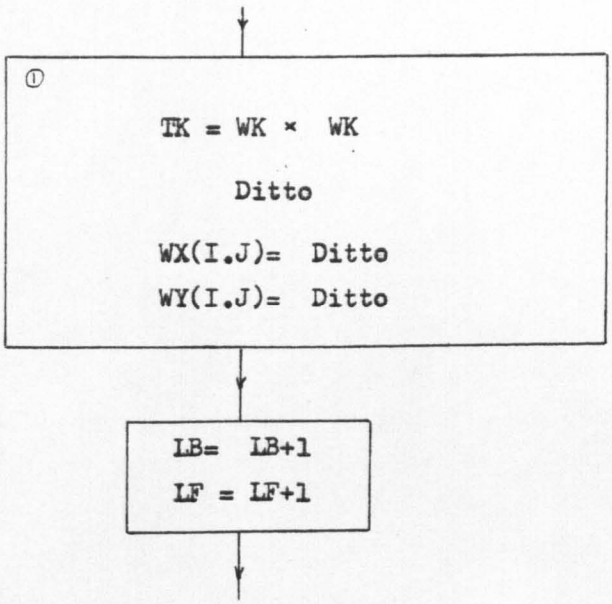

Figure 5.6

Hence after a time interval IN the values of the integers LB and LF which control the position of the fetch relative to the shelf are increased by one. This corresponds to a movement of a distance DS such that the speed of propagation of the storm V_w is equivalent to the ratio DS/IN. As mentioned previously it is important that the spacestep is not too large or the accuracy of the simulation is affected. This point is referred to again in section 5.6.2 with the computational results provided in table 5.5.

5.5 STEADY STATE ANALYTICAL SURGE SIMULATION

5.5.1 Channels and Basins of Constant Depth.

Equation (5.12) was compared with the numerical scheme using the configuration geometry of tests 4 and 31, corresponding to the open channel and closed basin respectively. The initial conditions were that of mean water level and zero velocities. In applying a steady uniform wind field over these constant depth configurations it was important to determine the accuracy of the simulation. In this respect the model's response is related to the particular value of wind stress coefficient. This coefficient was determined from the value of uniform wind speed in the following way

$$W \leq 11 : \quad k = 0.554 \times 10^{-3}$$

$$11 < W < 43 : \quad k = -0.12 + 0.06124\, W \times 10^{-3}$$

$$W \geq 43 : \quad k = 2.513 \times 10^{-3} \qquad (5.38)$$

with W in M.P.H. These coefficients were first presented by Heaps (1969) and their origins are discussed in Chapter 8. In each test a different value of wind speed was used and its effect on the surge height noted. The corresponding analytical surge was calculated for comparison, using equation (5.12) and the convertion equation (5.4).

In each test the results of the simulated surge showed that a steady state condition was not achieved. These tests were conducted firstly on the closed basin of constant depth. Instead of an equilibrium water surface, the simulation produced free oscillations in the basin. As a result of $DT \neq DT_{max}$ some attenuation was present and its effect on the oscillations is shown in figure 5.7. The curve was derived from the surge elevations at the boundary of the basin for W = 30 M.P.H. It was noted that in each test the average of the maximum and minimum oscillations was found to be very close to the value for the analytical surge. This was also true for subsequent oscillations in the channel. The maximum, minimum and average computed surge heights are presented in table 5.1 together with the analytical surge for the basin of constant depth.

To decide whether or not the surge oscillations were produced solely as a result of the channel acting as a closed system, the same wind fields were applied to an open channel of constant depth. The results for each test showed that surge oscillations occurred corresponding to the natural period of the channel. For one such test which used W = 50 M.P.H. the surge oscillations are shown in figure 5.8. As for the closed basin, the average of the maximum and minimum surges at the head of the open channel are very close to the analytical steady state surge height. The computed and analytical surges are shown in table 5.2 for four values of wind speed.

In both channels, which were frictionless, the simulated motion was that of a free wave oscillation superimposed on the steady state surge. The oscillations slowly diminished in amplitude as a result of numerical attenuation present in the model since $DT \neq DT_{max}$.

Surge histories at a landward boundary point produced by a uniform wind field.

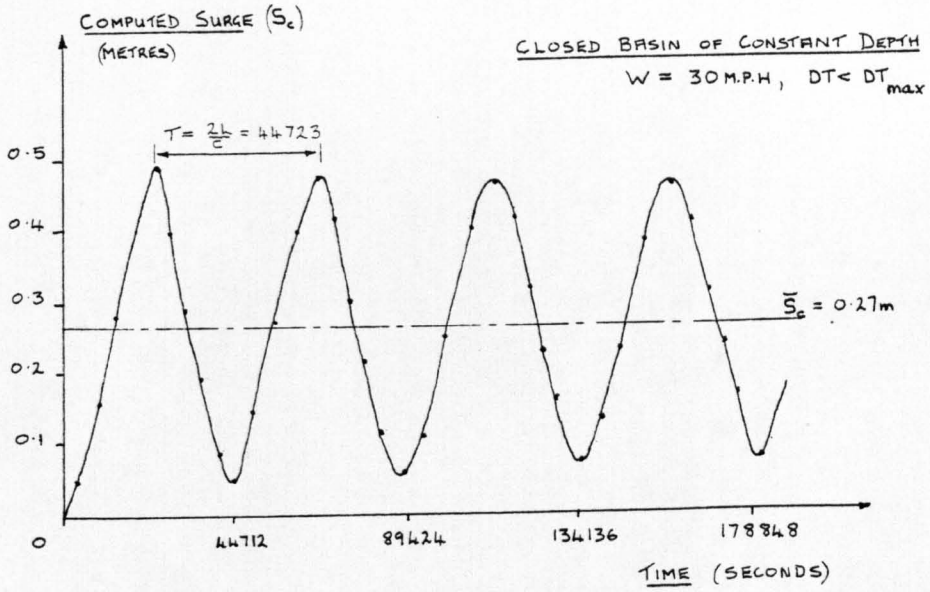

Figure 5.7

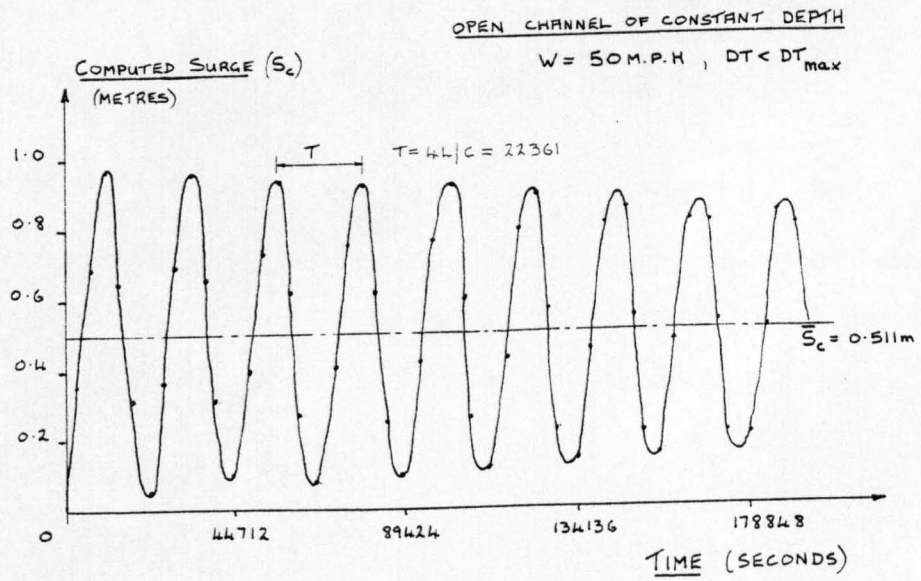

Figure 5.8

The Response of a Closed Basin of Constant Depth to a Steady Uniform Wind Field

Comparison of Analytical and Computed Surges

Wind Speed	Computed			Average Surge $\bar{S}_c$	Analytical Surge S_o	$\frac{\bar{S}_c}{S_o}$
	Wind Drag Coeff k	Max Surge	Min Surge			
M.P.H.	$\times 10^{-3}$	m	m	m	m	
10	0.55	0.03	-0.01	0.01	0.0093	1.07
20	1.10	0.13	0.01	0.075	0.075	1.01
30	1.71	0.47	0.07	0.27	0.27	1.00
40	2.33	1.16	0.10	0.63	0.62	1.02
50	2.51	1.97	0.16	1.06	1.04	1.02
60	2.51	2.78	0.26	1.52	1.49	1.02
70	2.51	3.76	0.36	2.06	2.00	1.03

Table 5.1

The Response of an Open Channel of Constant Depth.

10	0.55	0.0138	-0.0048	0.0045	0.0046	0.978
30	1.71	0.225	0.029	0.127	0.129	0.984
50	2.51	0.958	0.064	0.511	0.525	0.973
70	2.51	1.828	0.152	0.990	1.020	0.970

Table 5.2

The failure of the model to produce a steady state free surface was not a result of any limitations or inadequacy of the numerical scheme. It became clear in retrospect that the oscillations were produced as a result of the method of initialising the wind field over the channel or basin. Since the wind field was impressed suddenly over the surface of the model a dynamic effect was introduced which was responsible for generating the oscillations. To remove this effect one might, intuitively seek to specify a slowly increasing wind field such that the maximum value of the uniform wind is reached as $t \rightarrow \infty$. This method however was found to be impractical and an alternative is demonstrated in section 5.6.3.

5.5.2 Rectangular channel with linearly varying mean depth.

Further tests involving the simulation of steady state surges were conducted. Both uniform and non-uniform steady wind fields were applied separately to a frictionless shelf of linearly varying mean depth. The shelf dimensions shown in figure 5.9 are identical to those from test 45 except that the spacestep has been changed from 3867m to 4,000m. With this change the length of the channel corresponds to the breadth of the continental shelf of the west coast of central Scotland. This shelf is discussed in greater detail in Chapter 9.

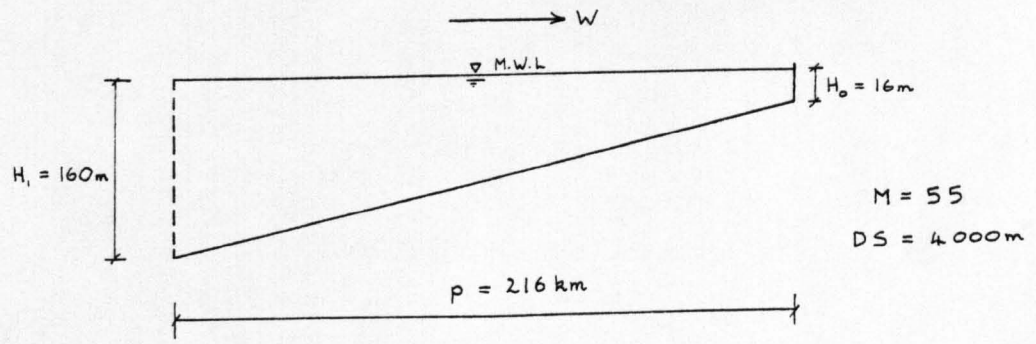

Figure 5.9

A uniform wind field with a wind speed of 50 M.P.H. and a wind stress coefficient obtained from the conditions in equation (5.28) determined the external forces in the model. The initial conditions were once again those of mean water level and zero velocities which applies to all non-tidal surge tests. Computations of the surge produced at the shore of the rectangular shelf, corresponding to H_o

are shown in figure 5.10. Also shown is the steady state surge S_o obtained from the analytical solution stated previously as equation (5.14). The computed surge was once again subject to dynamic effects which appear as free oscillations across the shelf. The oscillations at the shore, as shown in figure 5.10, have exactly the natural period of the channel corresponding to the lowest mode of oscillation as determined from Chrystal's equation (4.37). The slow attenuation in amplitude with successive oscillations has been described in Chapter 3 and shown in the tests of Section 4.4. It is the effect on free waves as a result of an inability to maintain DT = DTmax throughout a channel of variable depth. The results from section 4.3.3 showed that no apparent attenuation was produced when simulating forced waves. The results from figure 5.10 also verify that no energy loss has occurred in simulating the forced part of the surge because the average surge obtained from the maximum and minimum oscillations is exactly equal to the analytical steady state surge.

An identical conclusion can be made from the results of simulating a steady, non-uniform wind field across the shelf. Details are given in figure 5.11 for this test which shows that the average computed surge is equal to the analytical surge. The spatial variation of wind stress was triangular and the position of the stress and wind field relative to the channel is shown in figure 5.12. The analytical solution for this type of trapezoidal channel and wind stress

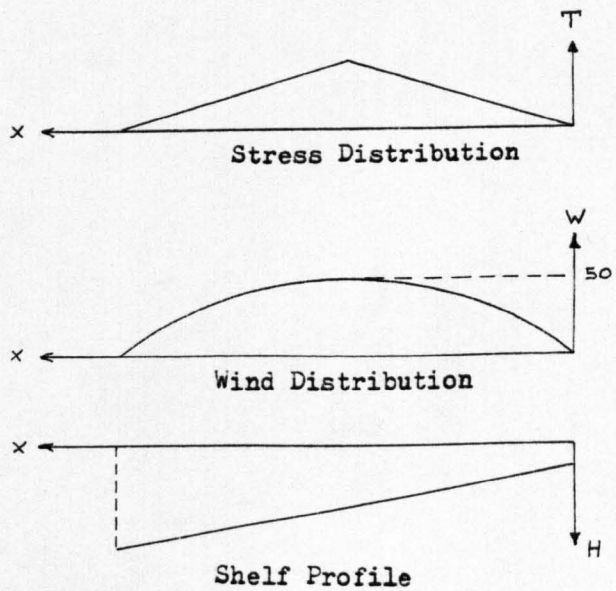

Figure 5.12

Surge histories at a coastal point of a rectangular shelf of linearly varying mean depth. (M=55, DS=4km)

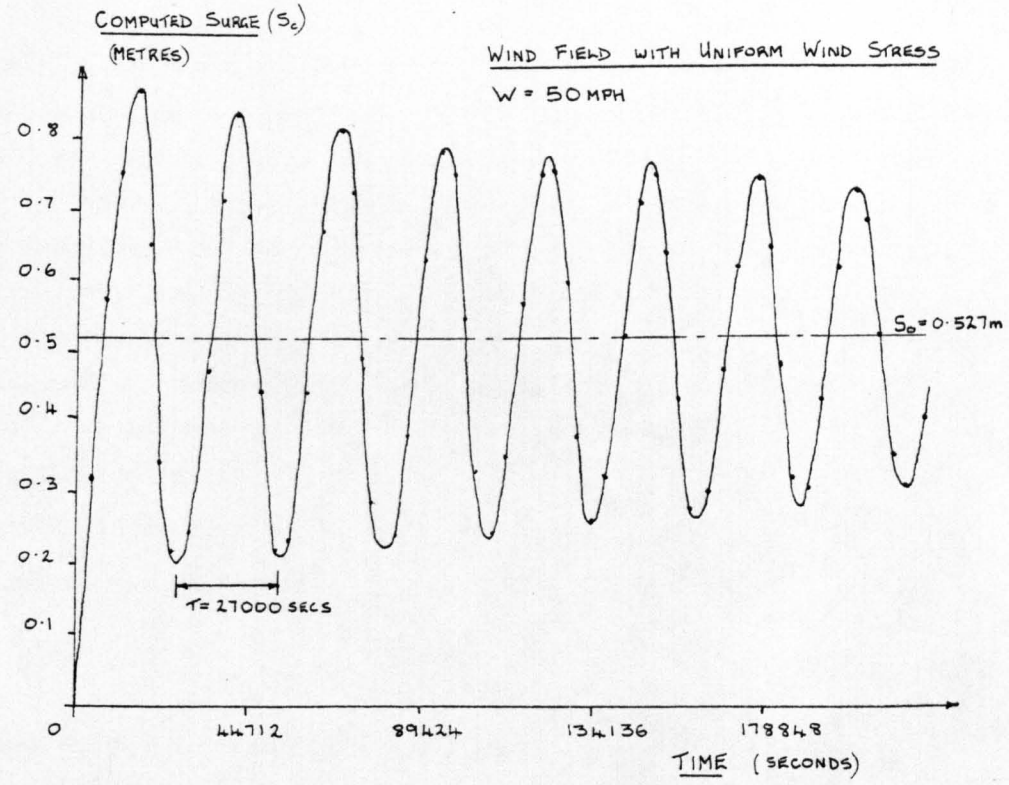

Figure 5.10

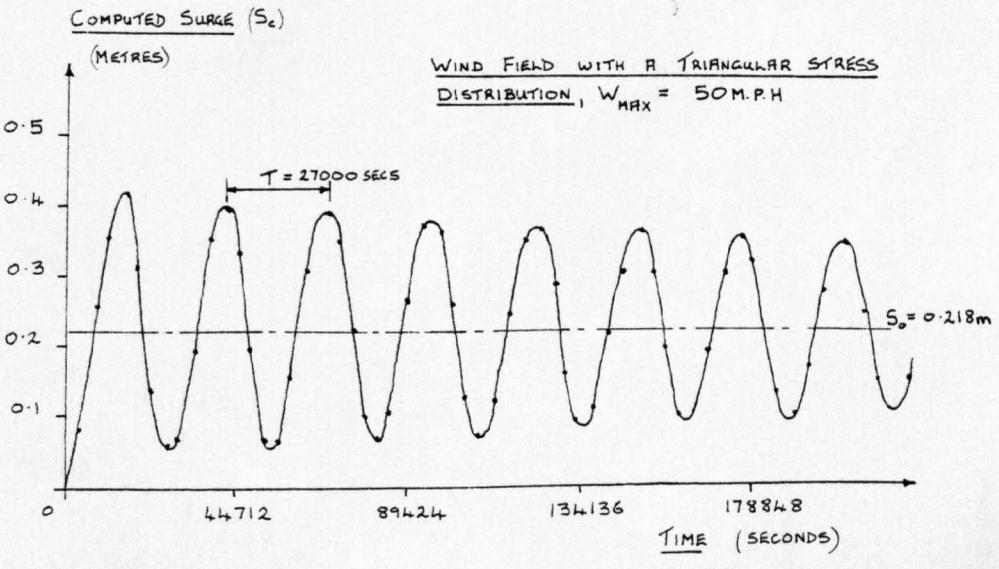

Figure 5.11

arrangement was first stated (without proof) by Reid (1956) and is expressed as

$$S = \frac{K W^2}{c_1} T_f \left(\frac{H_1}{H_0} \right)^{1/4} Z \qquad (5.29)$$

where T_f is the travel time of a free wave across the channel and c_1 is the maximum celerity corresponding to the open end of the channel. Reid has termed Z as a dynamic response factor dependent on the length of the fetch. In his paper he calculated the maximum response factor at the shore for each fetch, found by numerical integration for different trial positions of the fetch. Unfortunately Reid does not give details of the position of the fetch corresponding to each response factor but only for the maximum response factors. The arrangement shown in figure 5.12 does not correspond to a maximum response case by virtue of the position of the fetch relative to the shelf. Therefore the response factor at the shore is determined from first principles as follows.

Consider the wind stress in dimensionless form given by

$$f = \frac{K \rho_w W^2}{K \rho_w W_m^2} = \left(\frac{W}{W_m} \right)^2 \qquad (5.30)$$

where W_m is the maximum wind speed in the fetch. The function f shown in figure 5.13 is discontinuous and its integration is performed in two parts, A and B

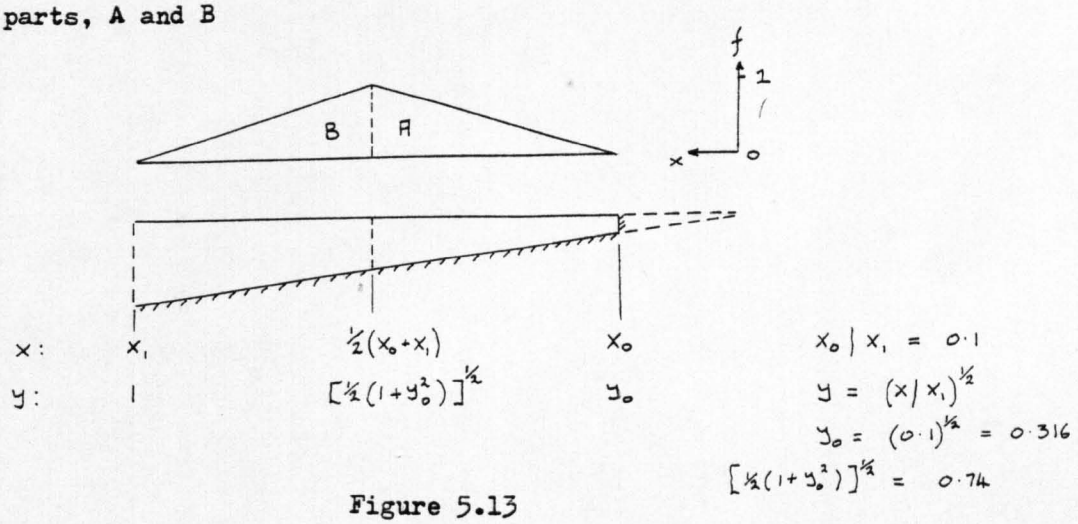

Figure 5.13

For part A:

$$x = x_0 : \quad f = 0$$

$$x = \tfrac{1}{2}(x_1 + x_0) : \quad f = 1$$

produces $$f_A = \frac{x_o - x}{x_o - \frac{1}{2}(x_1 + x_o)} \tag{5.31}$$

With $y = (x/x_1)^{\frac{1}{2}}$ and dividing the top and bottom of equation (5.31) by x_1 gives

$$f_A = \frac{y^2 - y_o^2}{\frac{1}{2}(1 - y_o^2)} \tag{5.32}$$

For part B $\quad x = x_1 : \quad f = 0$

$$x = \tfrac{1}{2}(x_1 + x_o) : \quad f = 1$$

gives $$f_B = \frac{x_1 - x}{x_1 - \frac{1}{2}(x_1 + x_o)} \tag{5.33}$$

Transforming this equation by dividing the numerator and denominator by x_1 gives

$$f_B = \frac{1 - y^2}{\frac{1}{2}(1 - y_o^2)} \tag{5.34}$$

Reid has shown that the exact integral of the response factor at the shore is expressed as

$$Z_o = \frac{y_o^{\frac{1}{2}}}{\gamma} \int_{y_o}^{1} y^{-1} \cdot f \cdot dy \tag{5.35}$$

where $\gamma = 1 - y_o$ and for this channel where $x_o/x_1 = 0.1$, $\gamma = 0.684$.

Expressing equation (5.35) in terms of f_A and f_B produces

$$Z_o = \frac{y_o^{\frac{1}{2}}}{\gamma} \left[\int_{y_o}^{[\frac{1}{2}(1+y_o^2)]^{\frac{1}{2}}} \frac{1}{y} \cdot f_A \cdot dy + \int_{[\frac{1}{2}(1+y_o^2)]^{\frac{1}{2}}}^{1} \frac{1}{y} \cdot f_B \cdot dy \right] \tag{5.36}$$

Substituting equations (5.32), (5.34) into equation (5.36) gives

$$Z_o = \frac{y_o^{\frac{1}{2}}}{\gamma} \left[\int_{0.316}^{0.74} \frac{1}{y} \frac{(y^2 - y_o^2)}{\frac{1}{2}(1 - y_o^2)} \cdot dy + \int_{0.74}^{1} \frac{1}{y} \frac{(1 - y^2)}{\frac{1}{2}(1 - y_o^2)} \cdot dy \right] \tag{5.37}$$

which simplifies to

$$Z_o = \frac{y_o^{\frac{1}{2}} \cdot \gamma^{-1}}{\frac{1}{2}(1 - y_o^2)} \left[\int_{0.316}^{0.74} \left(y - \frac{y_o^2}{y} \right) dy + \int_{0.74}^{1} \left(\frac{1}{y} - y \right) \cdot dy \right] \tag{5.38}$$

Integrating this equation produces

$$Z_o = 1.826 \left[\left(\tfrac{1}{2} y^2 - y_o^2 \log_e y \right) \Big|_{0.316}^{0.74} + \left(\log_e y - \tfrac{1}{2} y^2 \right) \Big|_{0.74}^{1} \right] \tag{5.39}$$

Inserting the numerical values into equation (5.39) gives $Z_o = 0.392$.

With the channel dimensions inserted into equation (5.29) and the value of $K = 3 \times 10^{-6}$ suggested by Reid, the following equation is produced

$$S_o = 0 \cdot 557 \, Z_o \qquad (5.40)$$

Equation (5.40) gives $S_o = 0.218$m as the steady state surge for a triangular wind stress distribution, where the fetch length is equal to the breadth of the shelf. This surge height at the shore is shown in figure 5.11 and is very close to the average computed surge obtained from the maximum and minimum surges.

5.6 UNSTEADY STATE; ANALYTICAL SURGE SIMULATION

As mentioned in Section 5.1 the analytical solutions are an important means of verifying the accuracy of the model under simplifying conditions. However if the assumptions used in the analytical derivation lack any physical meaning then the analytical solutions are of little value. For example the steady state analytical solutions apparently do not consider the complete dynamic process by which such a surface is produced. By contrast the numerical model, which does not ignore the dynamic considerations, thus cannot produce a steady state surge. By considering for simulation purposes the case of an unsteady wind field, there is the advantage of studying an important natural phenomena namely the transient effect of a wind field. Before actually conducting any numerical tests it is necessary to have a theoretical method as a comparison, that accounts for the dynamic effect of a transient wind field. For this purpose the semi-analytical method devised by Reid (1956) is appropriate.

Reid succeeded in obtaining the water response using a method whereby all the factors defining the shape, size and duration of the surge were included without making the method impractical. The method was based on the simplified linear one-dimensional equations of motion, utilizing the method of characteristics to obtain the solution. A simple graphical integration procedure was devised which accounted for the bottom slope of the shelf and it was capable of dealing with almost any distribution of onshore components of wind speed. He only considered wind-driven surges and to facilitate interpretation of the results, the wind stress distribution was the same in all cases.

However, different combinations of the fetch length and speed of propagation of the storm were examined. Wind intensity was accounted for by employing a dimensionless parameter.

The limitations of Reid's method are that two-dimensional effects associated with finite storm width, longshore winds, and variations of bottom topography parallel to the shore were not considered. Furthermore, bottom friction and non-linearity associated with large water level changes were not included. This compromise was necessary because exact solutions of the hydrodynamic equations were (and still are) so complicated that a complete mathematical solution capable of dealing with any storm condition was outside the realm of practicability. At that time also, computer technology was inadequate for the application of a comprehensive yet flexible numerical scheme. However, for storms of large width parallel to the shore and for conditions where the surge is smaller than the mean water depth, Reid's method leads to reasonably realistic results.

5.6.1 Derivation of a semi-analytical surge solution on a shelf of linearly varying mean depth.

Although Reid's particular area of interest was Narragansett Bay in New England the results from his calculations are applicable to any shelf region. This is a direct consequence of Reid generalising the problem by employing the concept of dimensionless variables. The only restriction in applying his results to any other shelf area is that the depth ratio is as follows

$$H_o / H_1 = 0 \cdot 1 \qquad (5.41)$$

This condition was applied to the channel used in the tests of section 5.5.2 and the channel has been the basis for further tests presented later. The dimensionless variables define any triangular storm stress distribution and any rectangular shelf with a linearly varying mean depth.

One important dimensionless variable, namely dimensionless time is defined at this point, as follows

$$t' = t / T_f \qquad (5.42)$$

because it is commonly used in subsequent presentations of results. The variable T_f which is the travel time for a free wave to cross the shelf is defined as

$$T_f = L / \bar{C} \tag{5.43}$$

where $\bar{C}$ is the average celerity across the shelf given by

$$\bar{C} = \tfrac{1}{2} (C_1 + C_o) \tag{5.44}$$

Equations (5.43) was considered by Reid to be indicative of the natural period of the shelf therefore it is important to understand the steps leading to its derivation. Starting with the Green-Du Boys theorem (Defant (1961))

$$T_f = \int_{x_o}^{x_1} \frac{1}{(g H)^{1/2}} \cdot dx \tag{5.45}$$

which is applied to the shelf shown in figure 5.14

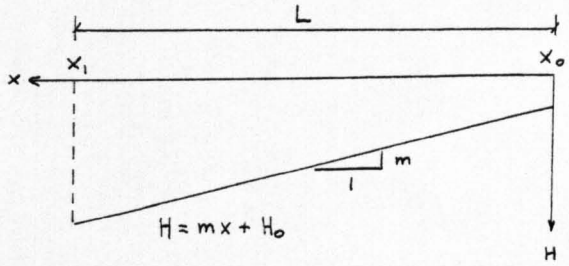

$x_1 - x_o = 216$ km

$m = 1/1500$

Figure 5.14

the following equation is obtained

$$T_f = \frac{1}{g^{1/2}} \int_{x_o}^{x_1} (m x + H_o)^{-1/2} \cdot dx \tag{5.46}$$

and on integrating yields

$$T_f = \frac{1}{g^{1/2} m} \left[2 (H_1^{1/2} - H_o^{1/2}) \right] \tag{5.47}$$

Multiplying the numeration and denominator by $(H_1^{\frac{1}{2}} + H_o^{\frac{1}{2}})$ produces

$$T_f = \frac{2}{g^{1/2} m} \frac{(H_1 - H_o)}{(H_1^{1/2} + H_o^{1/2})} \tag{5.48}$$

and with $C_1 = (gH_1)^{\frac{1}{2}}$, $Co = (gH_o)^{\frac{1}{2}}$ and $(H_1 - H_o)/m = L$ equation (5.48) becomes

$$T_f = \frac{L}{\tfrac{1}{2} (C_o + C_1)} \tag{5.49}$$

which is equivalent to the combination of equations (5.43) and (5.44). Hence the Green-Du Boys integral provides an expression for T_f based on the average celerity of the shelf. Using equation (5.49) and the dimensions of the channel shown in figure 5.14 a travel time of 8284 secs is obtained.

The basic linearised differential equations of motion and continuity for the simplified one-dimensional water level problem are respectively

$$\frac{\partial Q}{\partial t} + g H \frac{\partial \eta}{\partial x} = \frac{T}{\rho_w} \tag{5.50}$$

$$\frac{\partial \eta}{\partial t} + \frac{\partial Q}{\partial x} = 0 \tag{5.51}$$

for Reid's case. He transformed these equations into the following equations.

$$\frac{\partial Y}{\partial t'} + \gamma \left[\frac{\partial Z}{\partial y} - \tfrac{1}{2} \frac{Z}{y} \right] = - y^{-\frac{1}{2}} f \tag{5.52}$$

$$\frac{\partial Z}{\partial t'} + \gamma \left[\frac{\partial Y}{\partial y} + \tfrac{1}{2} \frac{Y}{y} \right] = 0 \tag{5.53}$$

by using the following dimensionless variables

$$y = (x / x_1)^{\frac{1}{2}} \tag{5.54}$$

$$Z = \eta \frac{c_1 y^{\frac{1}{2}}}{K W^2 T_f} \tag{5.55}$$

$$Y = \frac{Q}{K W^2 T_f y^{\frac{1}{2}}} \tag{5.56}$$

$$f = \frac{T}{K \rho_w W_m^2} \tag{5.57}$$

$$\gamma = 1 - (x_0 / x_1)^{\frac{1}{2}} \tag{5.58}$$

As a first step Reid considered the special case of steady state. The boundary conditions for this and any other problem was taken to be

$$x = x_1 : \quad Z = 0 \tag{5.59}$$

$$x = x_o : \qquad Y = 0 \tag{5.60}$$

The boundary equation (5.60) modifies the equation (5.52) into the form

$$\gamma \left[\frac{\partial Z}{\partial y} - \tfrac{1}{2} \frac{Z}{y} \right] = - y^{-\frac{1}{2}} f \tag{5.61}$$

which can be rearranged in the form

$$\gamma \frac{\partial}{\partial y} \left(y^{-\frac{1}{2}} \cdot Z \right) = - y^{-1} f \tag{5.62}$$

The solution of this differential equation is

$$Z_o = \frac{y_o^{\frac{1}{2}}}{\gamma} \int_{y_o}^{1} y^{-1} \cdot f \cdot dy \tag{5.63}$$

which is the analytical form, and Z_o is the value of Z at the shore. For the limiting case of a large fetch the forcing function f can be considered uniform ($f = 1$) and equation (5.63) yields

$$Z_r = \tfrac{1}{\gamma} y_o^{\frac{1}{2}} \log_e \left(\tfrac{1}{y_o} \right) \tag{5.64}$$

where Z_r is Reid's exact value of the dynamic response factor at the shore in the steady state. By substituting in equation (5.64) the relationships (5.54), (5.55), (5.57) and (5.58) the more common form of equation (5.14) is produced. Equation (5.64) also shows that the maximum dynamic response for a uniform wind field in steady state is $Z_r = 0.945$ with the condition that $(H_o/H_1) = 0.1$. In deriving equation (5.64) the condition (5.55) was used which if rearranged produces

$$\eta = \frac{K W^2 T_f}{c_1} \left(\frac{H_1}{H_o} \right)^{\frac{1}{4}} Z \tag{5.65}$$

This is Reid's steady state surge equation for a triangular wind stress distribution which is the general case from which the analytical solution for a uniform wind surge has just been derived.

In order to simplify the graphical procedure, Reid assumed that the terms Z/y and Y/y in the equations (5.52) and (5.53) respectively were small compared to the terms $\partial Z/\partial y$ and $\partial Y/\partial y$, and so could be neglected. This approximation is reasonable provided that y_o is sufficiently large so that the quantity $(H_o \cdot H_1)^{\frac{1}{2}}$ is not too small. After applying these approximations to equation (5.52) and then considering the steady state and boundary conditions (5.59) and (5.60) the following expression is

produced

$$\gamma \frac{dz}{dy} = -y^{-\frac{1}{2}} \cdot f \qquad (5.66)$$

and the solution at the shore is

$$z'_o = \frac{1}{\gamma} \int_{y_o}^{1} y^{-\frac{1}{2}} \cdot f \cdot dy \qquad (5.67)$$

This integral is slightly different in form from the exact integral expressed in equation (5.63). Using equation (5.67) Reid calculated the values of z'_o for different positions of the fetch by numerical integration for different values of fetch length. The maximum value of z'_o for each fetch denoted by z_m found from these calculations are shown in figure 5.24 together with the exact maximum steady state values z_r obtained from equation (5.63). The variation between the two curves is represented by a factor r such that

$$z_r = r \cdot z_m \qquad (5.68)$$

The values of this correction factor r are provided in the table 5.3 as shown.

F/L	0	0.2	0.5	1.0	2.0	4.0	8.0	∞
r	1.00	0.905	0.817	0.795	0.755	0.751	0.746	0.739

Table 5.3

The case of steady state therefore served as a useful method of calibration for Reid's graphical process since the factor r related this scheme to the analytical solution. He assumed that r was only dependent on the fetch length and as a result he applied the correction factors to the maximum dynamic response z_m obtained from the same wind stress in the unsteady state. Therefore by using the graphical process the maximum response factor z_m at the shore was found for the unsteady state and suitably corrected using the appropriate correction factor. This method led Reid to investigate a large number of moving wind fields of triangular stress distribution. From these results he plotted a response diagram as shown in figure 5.15. The response diagram gives the estimated maximum dynamic response z_r associated with a particular storm speed and size. Coupled

with a knowledge of the shelf dimensions, the approximate maximum water level at the shore is accordingly provided from the equation (5.65) with $\eta = S_r$ and $\bar{z} = \bar{z}_r$

In performing the calculations Reid assumed that the wind drag coefficient was constant for wind speeds of storm intensity. This assumption evidently simplified the calculations since the dimensionless intensity of the wind stress factor f defined previously as

$$f = \frac{K \rho_w W^2}{K \rho_w W_m^2} = \left(\frac{W}{W_m}\right)^2 \qquad (5.30)$$

becomes only a function of wind speed. Therefore f and $\bar{z}_o$ from equation (5.67) are only functions of distance x providing K is constant. The dynamic response factor $\bar{z}_o$ can therefore be calculated solely from the shelf dimensions and the wind stress function. This would not be the case if the wind drag coefficient was a function of wind speed such that

$$f = \frac{K W^2}{K_m W_m^2} \qquad (5.69)$$

and $\bar{z}_o$ would then be dependent on the value of the wind drag coefficient. The validity of assuming the wind drag constant throughout the wind distribution is investigated in the next section.

5.6.2 Simulation of Unsteady Wind Fields

In order to verify the accuracy of the model by comparing its surge heights with those of Reid's, it was necessary to use a constant wind stress coefficient in the model. This was in keeping with Reid's method and the wind stress coefficient used in the model was

$$k = 2.513 \times 10^{-3} \quad \text{for} \quad W > 0 \qquad (5.70)$$

Before presenting the simulations it was thought important to investigate the effect, on the computed surge, of using either a variable or a constant wind stress coefficient. It seemed appropriate to make a comparison of both methods since the model can function with equal ease in both cases. For the simulations with the variable coefficients, these coefficients were taken as those presented in equation (5.28). In both cases the wind stress field had a triangular distribution with a maximum wind speed of 50 M.P.H. The configuration was that used in section 5.5.2, and shown in figure 5.9.

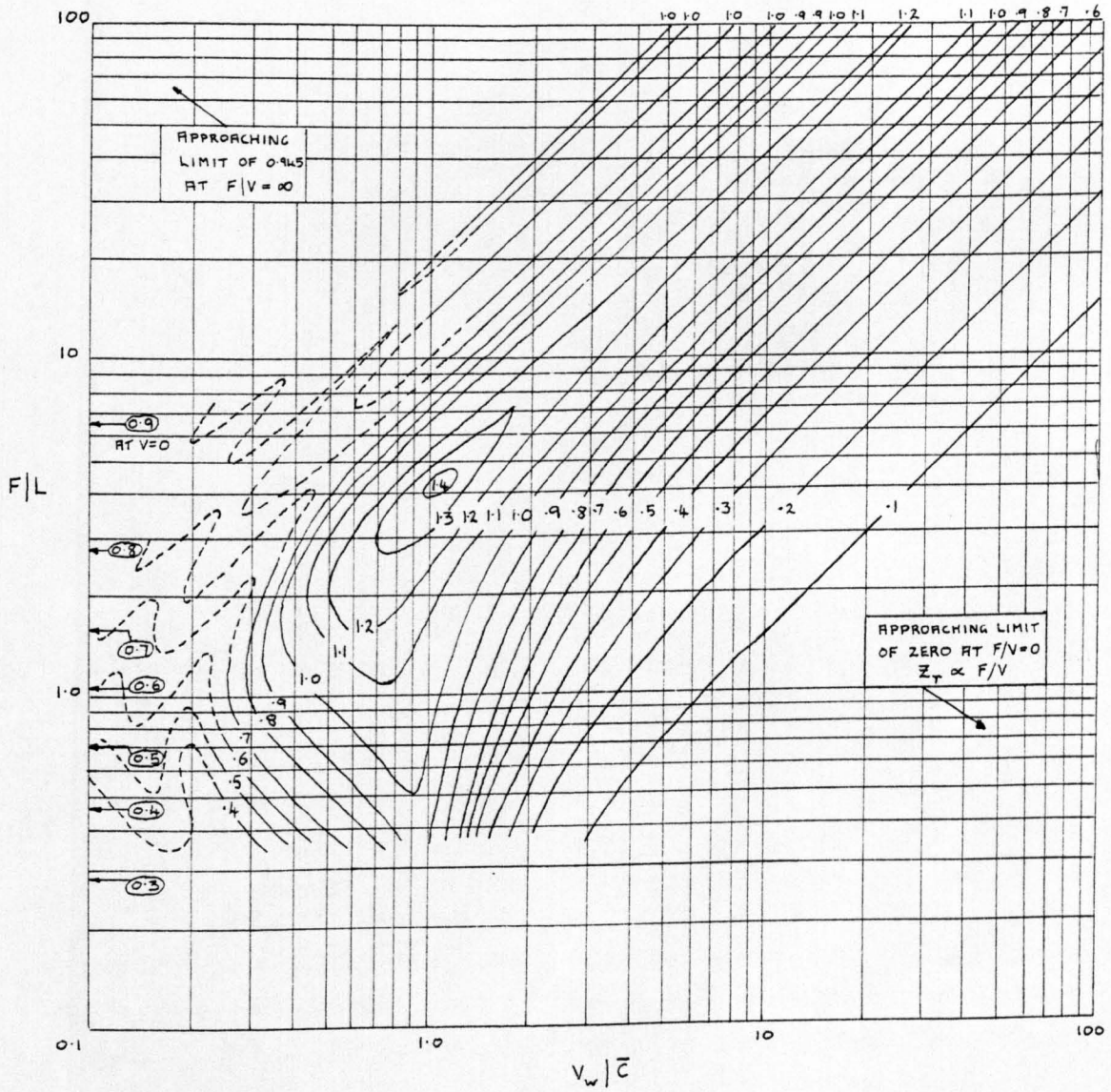

Reid's response diagram; Isolines of Z_T versus F/L and $V_w/\bar{c}$

Figure 5.15

The computed maximum surge at the shore for a constant wind drag coefficient S and for a variable wind drag coefficient S_k are shown in table 5.4 for a number of tests.

F/L	$V_w/\sqrt{c}$	S_k m	S m	S_k/S	$\frac{F/L}{V_w/\sqrt{c}}$
1	2	0.245	0.29	0.85	0.5
1	1	0.495	0.55	0.90	1
4	2	0.59	0.62	0.95	2
2	1	0.605	0.63	0.96	2
4	1	0.68	0.69	0.98	4
4	0.5	0.515	0.51	1.01	8
8	1	0.54	0.53	1.02	8

Table 5.4

The parameter F/L is the dimensionless fetch length which is the ratio of fetch length to the length of the shelf. The parameter $V_w/\sqrt{c}$ is the dimensionless storm speed which is the ratio of the speed of the storm to the average speed of a free wave across the shelf. A graphical representation of the ratio of surge heights S_k/S for both methods plotted against the storm parameter $F/V_w/\sqrt{c}$ is shown in figure 5.17. From the results a curve has been drawn as shown which indicates that the ratio S_k/S is only significantly less than one for small fast moving wind fields. For large slow moving fetches, the surges, produced, using either a variable or a constant wind drag coefficient, are very similar and the ratio S_k/S tends to unity as $\frac{F/L}{V_w/\sqrt{c}} \to \infty$. These results suggest that the central portion of the wind field has the most significant effect in surge production in comparison with the ends of the fetch. In figure 5.16 the hatched area under the wind distribution represents the length of the fetch in which the wind stress is the same using either a variable or constant drag coefficient.

Figure 5.16

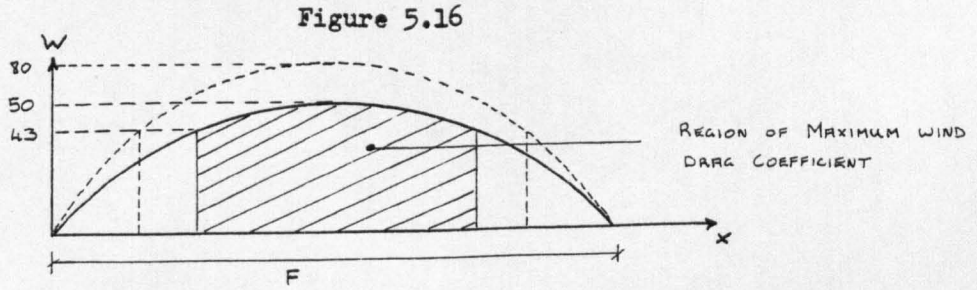

Wind surge ratio obtained from computations using a variable and a constant wind stress coefficient, plotted against a dimensionless wind field parameter.

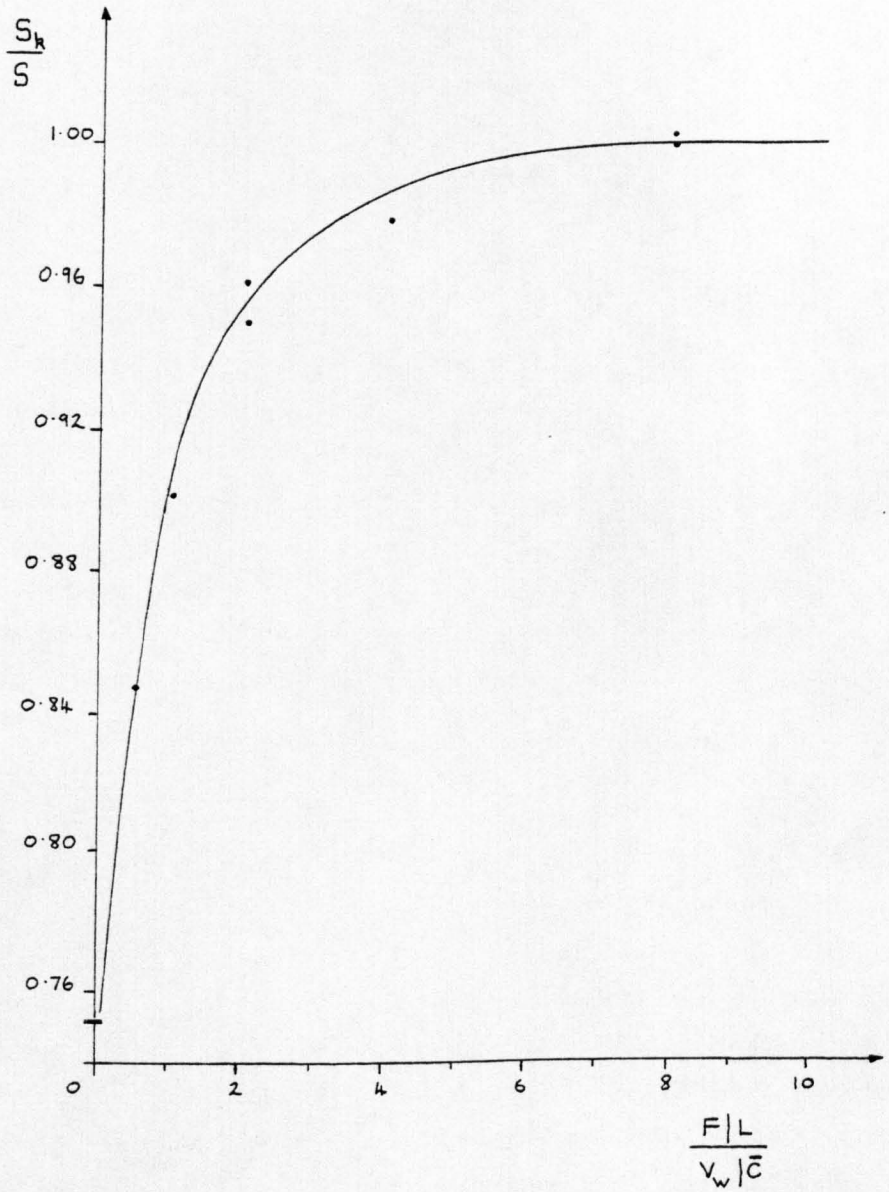

Figure 5.17

As the fetch length increases, the hatched area becomes a greater percentage of the total area and the variable wind stress coefficient's effect approaches that of a constant wind stress coefficient's effect. It is also reasonable to assume that had W_m = 80 M.P.H. in each test the curve shown in figure 5.17 would have approached unity even quicker than is shown, because the maximum wind stress coefficient would be dominant in the variable wind drag coefficient case. Reid considered actual storm events with maximum wind speeds of approximately 80 M.P.H. It therefore became reasonable to simplify the problem by assuming a constant wind drag coefficient.

Before obtaining Reid's paper, reference was made to Silvester (1974) for equations and tables governing unsteady wind fields. Silvester refers to Reid's equation namely equation (5.29) but does not

$$S = \frac{K W_m^2 \tau_f}{c_1} \cdot \left(\frac{H_1}{H_0} \right)^{1/4} \mathcal{Z}$$

mention that it is basically a steady state equation. Furthermore he uses the misleading term 'triangular wind distribution' which may be taken to imply a different function entirely from the correct expression which is a 'triangular wind stress distribution'. The difference lies in the fact that wind stress is proportional to the square of wind speed. It was only after obtaining Reid's paper and after many computations using the triangular wind field, that the correct form for the wind stress was realised. The computations are therefore not presented, except for the steady state curve shown in figure 5.24, since they are unrealistic.

The correct triangular wind stress distribution was incorporated in the model using a constant wind stress coefficient of 0.002513. The wind stress was applied over the shelf shown in figure 5.9 with a space-step of 12000 metres and 19 grid points along the length of the shelf. In each test the storm parameters F/L and $V_w/\sqrt{c}$ were given suitable values and the surge history was computed at every grid point. The maximum surge elevation at the shore S_{mc} corresponding to the storm parameters is shown in table 5.5. Also shown is the computed dynamic response factor $\mathcal{Z}_{mc}$ obtained from equation (5.40), together with Reid's response factor $\mathcal{Z}_r$ for comparison. In all these tests the computed response was less than that of Reid's, which suggested a deficiency in the method

of simulation. The computed responses were also found to be in poorer agreement with Reid's responses for the smaller values of F/L and the larger values of $V_w/\overline{C}$. This fact indicated that the discrepancy in the model was one of poor schematisation of the distribution and propagation of the wind field. Further evidence of poor schematisation of the wind field was noticed when simulating slow moving wind fields. The computed surge showed small peturbations which corresponded to the sudden movement of the wind field from one grid point to another. The peturbations are the dynamic effect associated with each movement across the grid. In order to decrease the effect of the sudden 'jumps' the grid size was reduced by one-third so that fifty-five grid points were necessary to define the shelf. Simulations on this grid were not subject to perturbation effects however it appears that to simulate accurately the surge effect of a progressive wind field the grid parameters have to be smaller than is required for tidal motion.

In figure 5.18 the curves illustrate the generation of the surge from the edge of the shelf to the shore. The simulated surge responses are shown at intervals of 1242 seconds. The storm parameters were F/L = 1 and $V_w/\overline{C}$ = 1 and the latter parameter caused the maximum surge at the shore to arrive at nearly the same time as the maximum wind passes over the shore. The respective dimensionless times were t'_m = 1.65 and t'_w = 1.50. The wind field did not produce a large free surface response except for in the relatively shallower area near or at the shore. At t'=1.80 the maximum wind speed passed over the shore and the curve at that time shows that a smaller secondary resurgence is being propagated towards the shore.

The surge histories at the shore are presented in figure 5.19 drawn from the results from several simulations. For each test the fetch length was constant such that F/L = 1 however the storm speed V_w varied. The maximum surge indicated by these curves occurs when the dimensionless storm speed $V_w/\overline{C}$ is approximately 0.75. The curves also show that the quicker moving storms produce earlier surge responses at the coast.

In figure 5.20 the curve drawn from the results of a simulation using the storm parameters F/L = 2 $V_w/\overline{C}$ = 1, shows the resurgence at the shore. This resurgence occurs after the passage of the wind field over the shelf and its period corresponds to that of the lowest mode of a free wave oscillation given by Chrystal's equation (4.37). The

parameter which indicates the dimensionless time at which the maximum wind speed passes over the shore is given by

$$t'_w = \frac{\bar{C}}{V_w}\left(1 + \frac{F}{2L}\right) \tag{5.71}$$

and the dimensionless time for the back of the fetch to cross the shore is similarly

$$t'_e = \frac{\bar{C}}{V_w}\left(1 + \frac{F}{L}\right) \tag{5.72}$$

The parameter t'_e for the case $F/L = 2$ and $V_w/\bar{C} = 1$ is shown in figure 5.20. For all the cases examined, the computed resurgences which followed the first wind driven surge produced smaller peak responses than the first peak.

From the simulation of several storms with the parameter $V_w/\bar{C} = 1$ the surge history at the shore has been drawn for each test and shown in figure 5.21. Each test corresponds to a different value of fetch length and the curves show that the maximum surge response occurs later for the storms of longer fetch. From these curves it is clear that the overall maximum surge would occur with a dimensionless fetch length ratio F/L, between three and four.

5.6.3 Comparison of Simulated and Semi-analytical Maximum Surges.

For a triangular distribution of wind stress over a shelf of linearly varying mean depth a total of twenty-nine separate surge tests were conducted. In each test the maximum surge at the shore S_{mc} and the dynamic response factor Z_{mc} obtained from equation (5.40) was noted. These results are presented in table 5.6 corresponding to the wind fetch speed and size. Reid's maximum dynamic response factors Z_r are also shown and their comparison with the computed response factors is in good agreement. In two of the tests namely with $F/L = 1$, $V_w/\bar{C} = 0.5$ and $F/L = 1$, $V_w/\bar{C} = 2$ the regular grid method of simulation and the method of subdivisions were compared. Both methods give very similar results for the maximum surge with the surges from the latter method being slightly larger. To reduce computational time the method of subdivisions (discussed in Chapter 3) has been used in obtaining the results in table 5.6.

The same tests also provided information concerning the arrival

time of the maximum surge at the shore t'_m. These results are presented in table 5.7 together with the dimensionless time for the maximum wind speed at the shore obtained from equation (5.71). The parameter $\Delta t'$ is obtained from

$$\Delta t' = t'_m - t'_\omega \qquad (5.73)$$

and denotes the time lag between the maximum surge and the maximum wind at the shore. These values together with Reid's values $\Delta t'_r$ are also shown in table 5.7. A graphical representation of the results from table 5.7 is presented in figure 5.22. The curves in this figure indicate that, irrespective of fetch length, for fast moving storms the maximum wind reaches the shore before the maximum surge and so $\Delta t'$ is positive. Conversely for slow moving storms the maximum surge reaches the shore ahead of the maximum wind and so $\Delta t'$ is negative.

From the results presented in table 5.6 a composite plot of the maximum dynamic responses against the storm parameters has been drawn and is shown in figure 5.23. Each curve represents the computed response for a particular value of the parameter F/L and for comparison the maximum dynamic responses obtained by Reid are also shown. At all values of $V_\omega/\bar{c}$ and F/L the comparison is shown to be very good. In both cases the ultimate maximum dynamic response occurs for a finite fetch length of approximately F/L = 4 and $V_\omega/\bar{c} = 1$

It has been mentioned already in section 5.5.2 that difficulty arises in simulating a steady state problem because of the dynamic effects produced. An alternative method of finding the simulated steady state surge for a particular fetch length is simply to extrapolate the appropriate curve in figure 5.23 to the ordinate axis to obtain the maximum steady state response factor. By using this response and equation (5.40) the maximum steady state surge at the shore can be found. It was by means of this extrapolation technique that the maximum steady state response factors in table 5.6 were obtained. However it was possible to simulate the surge response for storm speeds as small as $V_\omega/\bar{c} = 0.05$.

Reid found that his graphical process for finding the maximum dynamic response at the shore for the case of small storm speed gave results which showed an oscillatory character. This effect is shown in figure 5.23 for his curve with F/L = 0.5. When he presented

his curves he chose to represent the oscillations by an upper envelope curve. The computed surges produced using slow moving wind fields did not suffer from the production of this oscillatory mode. However, when plotting the results and extrapolating to the steady state situation ($V_w = 0$) the curves follow those of Reid's curves to assist in the extrapolation. As a result a comparison can be made between Reid's steady state responses and the computed steady state responses. This comparison can be made from curves 2 and 3 shown in figure 5.24. Curve 2 represents the steady state response obtained by Reid using equation (5.63) and represent exact analytical maximum dynamic responses. The steady state responses extrapolated from the computed maximum dynamic responses in figure 5.23 are represented in figure 5.24 as curve 3. The comparison between curves 2 and 3 is very good and shows that the steady state responses obtained using the numerical model are superior to those from Reid's approximation equation (5.67). The results from this approximate solution are shown as curve 1.

Curves 4 and 5 represent the triangular wind stress case and the triangular wind field case respectively. In both cases the number of grid points along the shelf was nineteen and their inclusion in figure 5.24 highlights the effect of using an insufficient number of grid points in the simulation.

Each curve shows that an increase in fetch length produces a corresponding increase in the dynamic response factor. As the fetch length becomes infinite the response factor tends to a limiting finite value, which is the response for uniform steady wind stress. For curve 2 this limit is 0.945 and with this value inserted in equation (5.65) this equation produces the same surge elevation as equation (5.14), therefore with $\bar{z}_r = 0.945$

$$S = \frac{K W^2 T_f}{C_1}\left(\frac{H_1}{H_0}\right)^{1/4} \bar{z} = \frac{K W^2}{g m}\log_e\left(\frac{H_1}{H_0}\right) \qquad (5.74)$$

The dynamic response diagram shown in figure 5.25 has been drawn from the computational results in table 5.6. The scales of F/L and $V_w/\sqrt{C}$ are logarithmic so that the limiting cases of uniform wind fields appear as straight isolines of $\bar{z}$ with unit slope. An important feature of this figure (and Reid's response diagram shown in figure 5.15) is that the ultimate maximum response $\bar{z}_{mc}$ which determines the

water level at the shore, occurs at a finite fetch length and storm speed.

Overall, figure 5.15 should be more accurate in comparison to figure 5.25 since Reid performed more tests than did the numerical model. However in the region of the ultimate maximum response, Reid's tests were insufficient in number to establish exactly the fetch length ratio which produces the ultimate maximum response. He has taken this ratio to be $F/L = 4$ and with $V_w/\sqrt{C} = 1$ is equivalent to a forcing stress function of period $4L/\sqrt{C}$. The assumption that $4L/\sqrt{C}$ is the resonant condition of the shelf is implicit in his reasoning. Reid has therefore assumed that the natural period of the shelf T can be expressed as

$$T = 4\,T_f \tag{5.75}$$

where T_f is the time for a free wave to cross the shelf determined from Equation (5.45) namely the Green-Du Boys expression. Chrystal has shown that the natural period of such a channel using the Green-Du Boys equation is too large. From Chrystal's Equation (4.37) the natural period has been found to be $3.26\ L/\sqrt{C}$ therefore

$$T = 3.26\,T_f \tag{5.76}$$

The period expressed by this equation was also confirmed by the results from the numerical model, and has been shown for the resurgences in figure 5.20. Furthermore in figure 5.21 the maximum surge has been shown to occur for a fetch length ratio between three and four. There is no doubt therefore that for this shelf or any other shelf satisfying equation (5.41) that the ultimate maximum response occurs for the storm parameters $F/L = 3.26$ and $V_w/\sqrt{C} = 1$.

Defant (1961) refers to the work of Thorade (1926) who investigated the behaviour of a long wave over a shelf of variable depth. Thorade has shown the inaccuracy of the Green-Du Boys equation when the wavelength is longer than the length of the channel. The inaccuracy increases as the wavelength increases. The Green-Du Boys theorem is only appropriate under certain circumstances which Green acknowledged yet its application has been made outwith its limits, see Groen and Groves (1962).

Surge Parameters for a Triangular Wind Stress Distribution With M = 19

$V_w/\sqrt{C}$		F/L = 0.5	F/L = 1	F/L = 2	F/L = 4	F/L = 8
0	S_{mc}		0.27		0.45	0.46
	t'_m		-		-	-
	t'_w		∞		∞	∞
	$\Delta t'$		$-\infty$		$-\infty$	$-\infty$
	Z_{mc}		0.49		0.82	0.83
	Z_r		0.56		0.83	0.91
0.05	S_{mc}		0.28		0.46	0.47
	t'_m		26.5		35.3	95
	t'_w		30.0		60.0	100
	$\Delta t'$		-3.5		-4.7	-5.0
	Z_{mc}		0.50		0.83	0.84
	Z_r		0.56		0.84	0.92
0.5	S_{mc}	0.29	0.44	0.51	0.46	
	t'_m	2.40	2.85	3.8	5.83	
	t'_w	2.50	3.0	4.0	6.0	
	$\Delta t'$	-0.10	-0.15	-0.20	-0.17	
	Z_{mc}	0.52	0.79	0.91	0.83	
	Z_r	0.76	1.02	1.18	0.95	
1.0	S_{mc}	0.29	0.42	0.50	0.60	0.52
	t'_m	1.37	1.63	2.15	3.13	5.1
	t'_w	1.25	1.50	2.0	3.0	5.0
	$\Delta t'$	0.12	0.13	0.15	0.13	0.1
	Z_{mc}	0.52	0.75	0.90	1.08	0.93
	Z_r	0.98	1.06	1.13	1.38	0.97

Table 5.5

Progression of a wind stress field across the shelf.

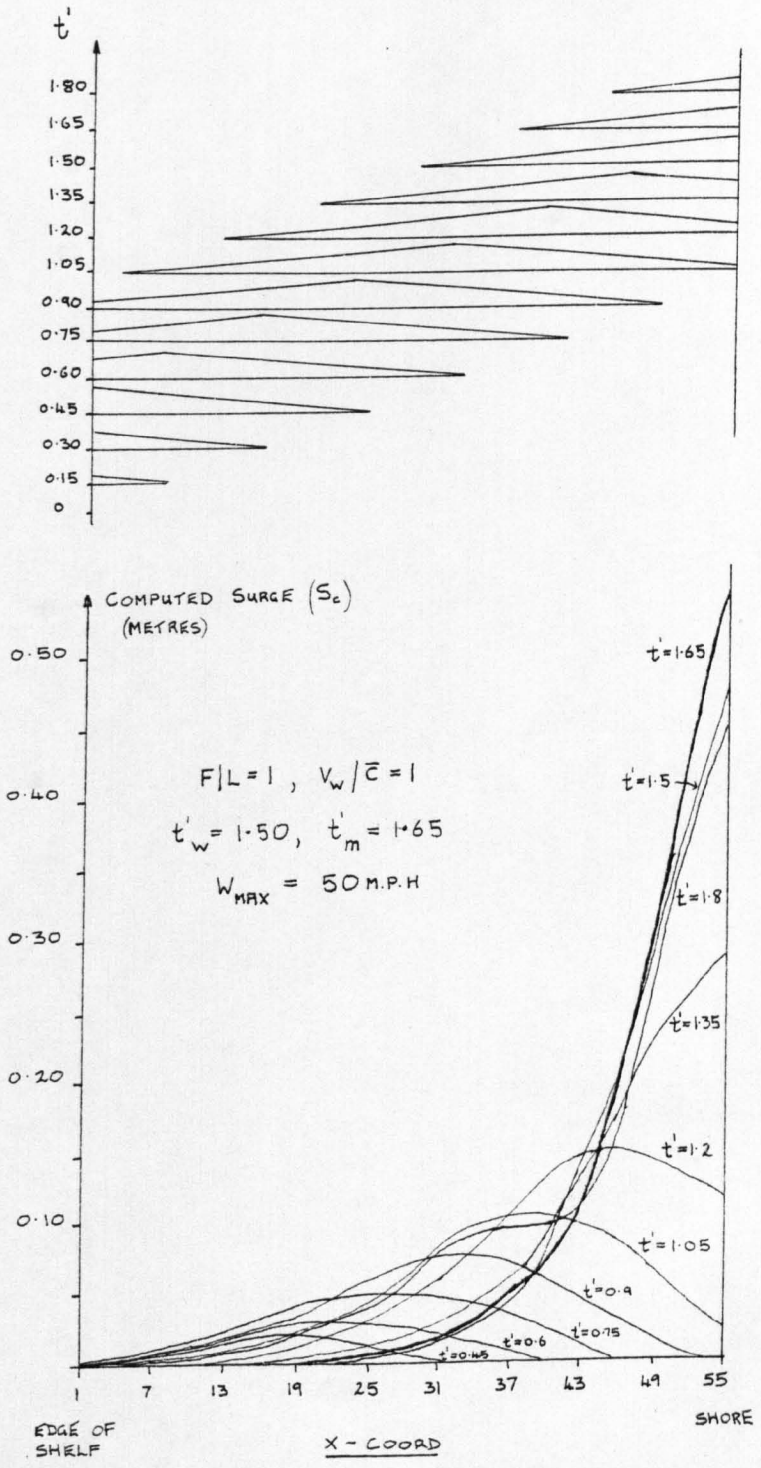

Figure 5.18

Computed surges at the shore plotted against dimensionless time.

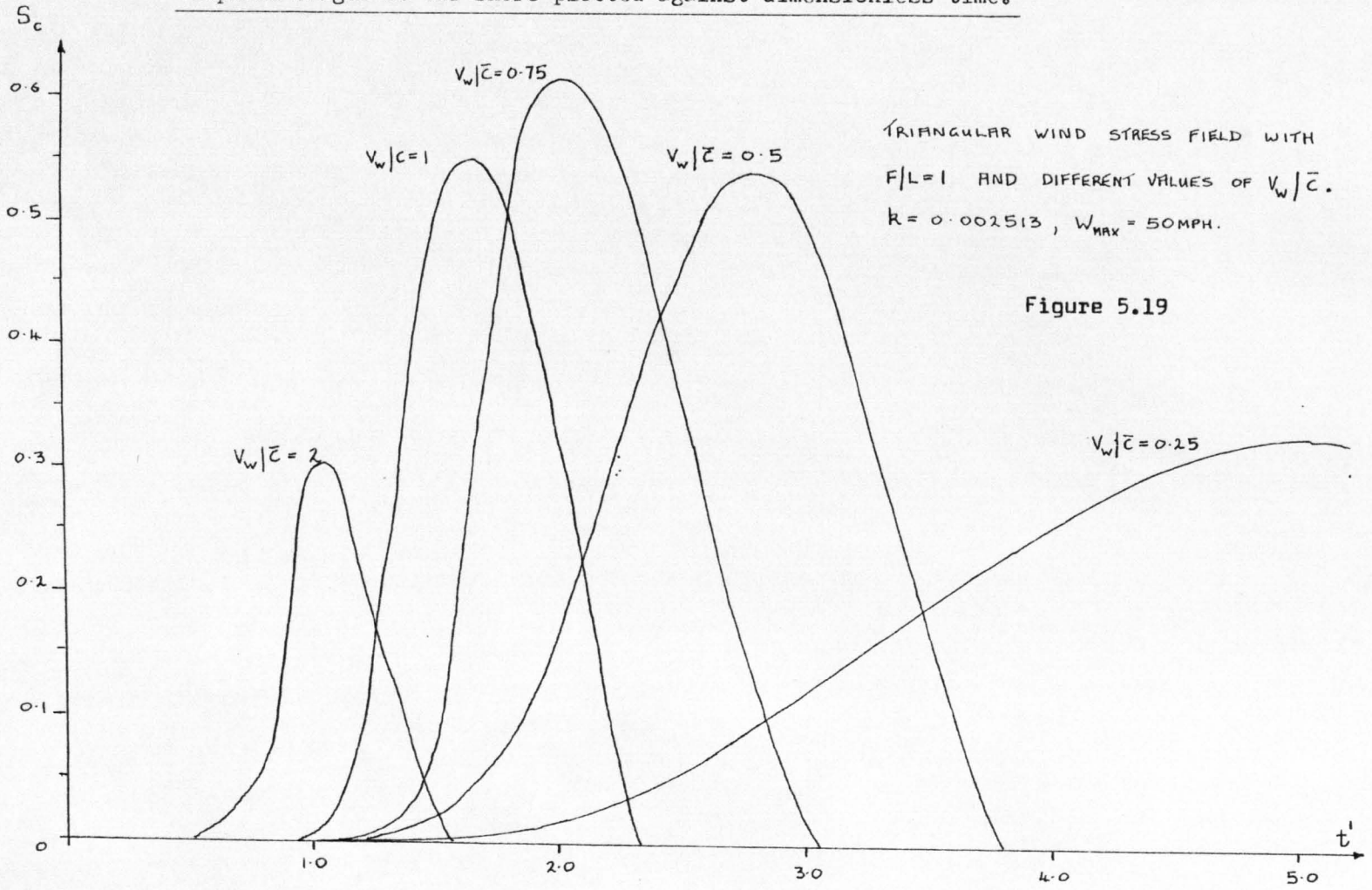

TRIANGULAR WIND STRESS FIELD WITH F/L = 1 AND DIFFERENT VALUES OF $V_w/\bar{C}$. $k = 0.002513$, $W_{MAX} = 50$MPH.

Figure 5.19

Surge history at the shore produced by the passage of a triangular wind stress distribution across the shelf (showing first free oscillation).

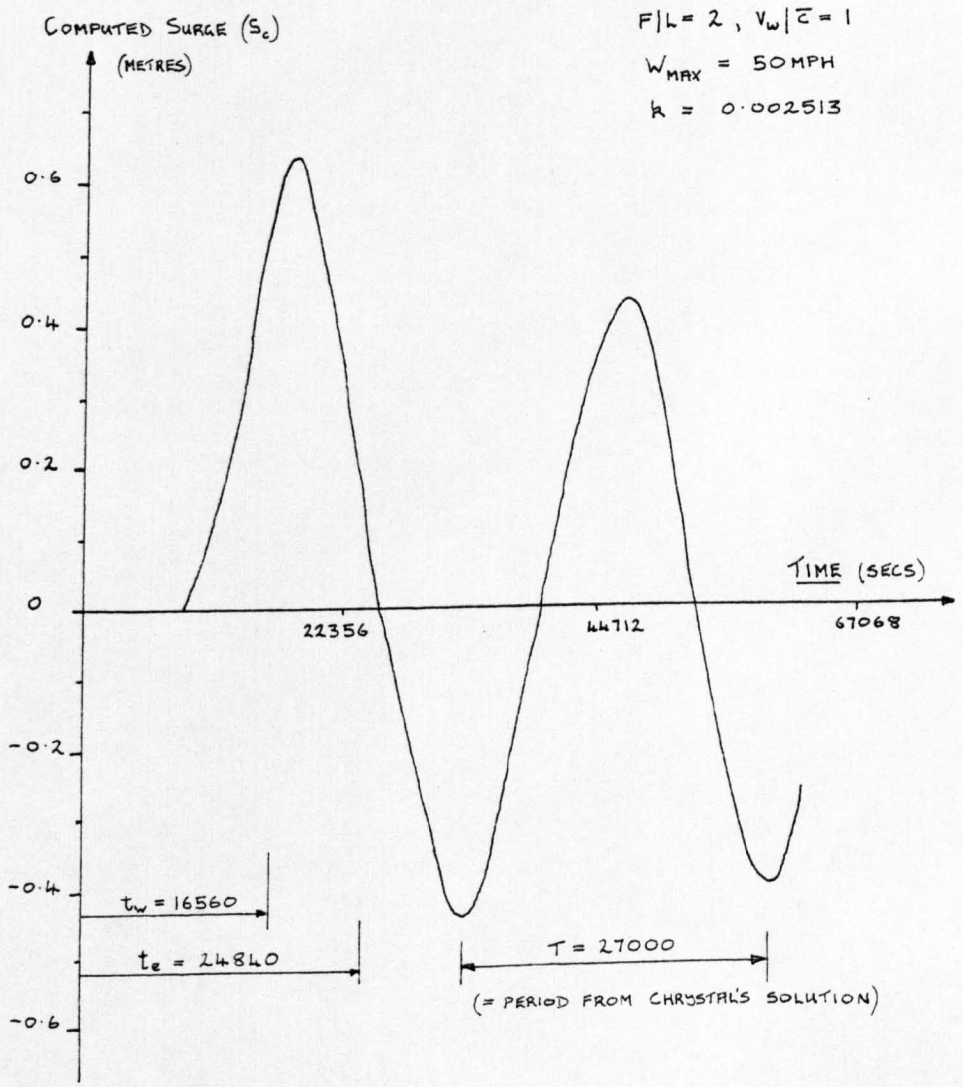

Figure 5.20

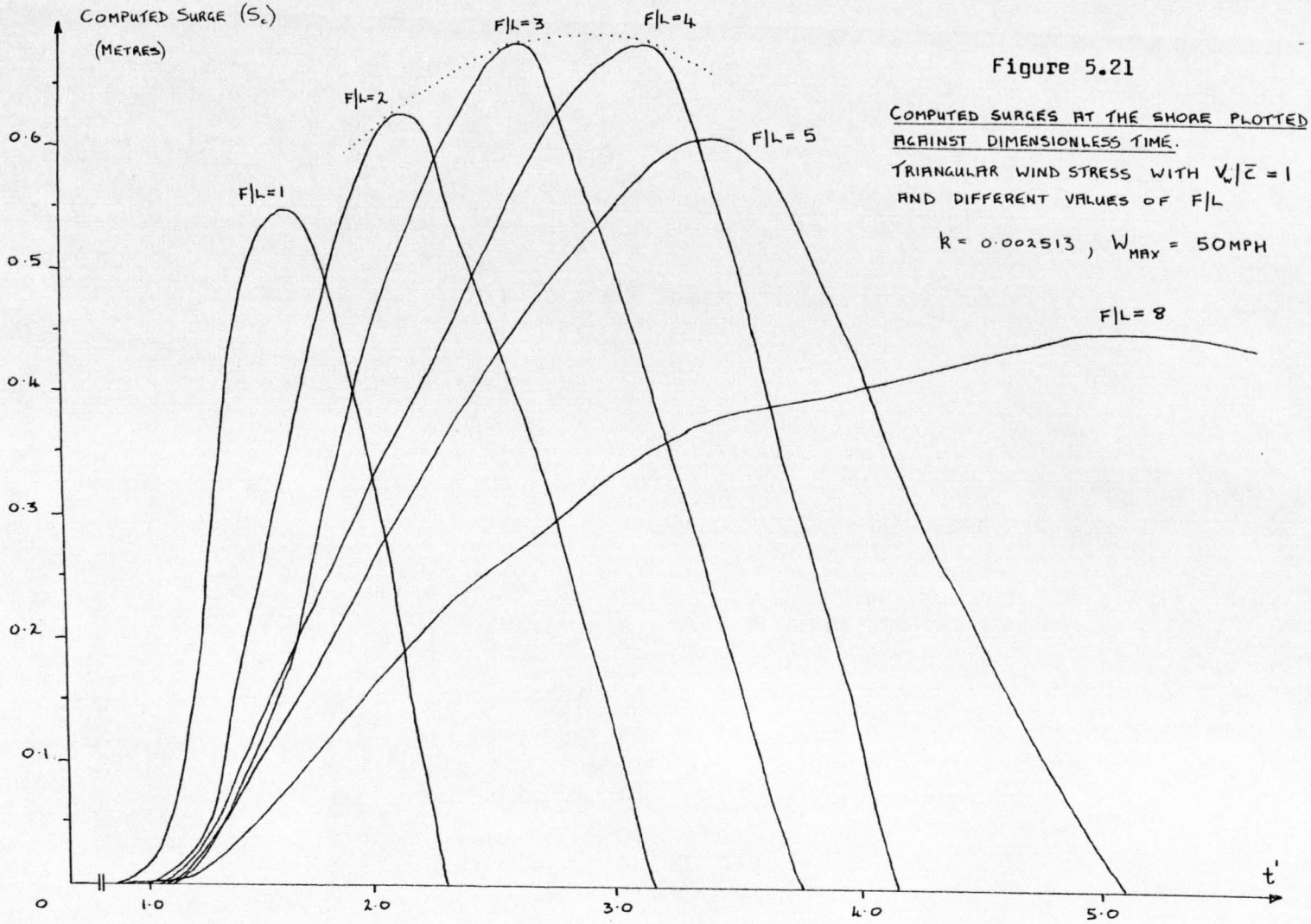

Figure 5.21

COMPUTED SURGES AT THE SHORE PLOTTED AGAINST DIMENSIONLESS TIME.

TRIANGULAR WIND STRESS WITH $V_w/\bar{C} = 1$ AND DIFFERENT VALUES OF F/L

$k = 0.002513$, $W_{MAX} = 50$MPH

Comparison of Computed and Analytical Maximum Response Factors for a Triangular Wind Stress Distribution over a Shelf of Linearly Varying Mean Depth, (M = 55)

Table 5.6

$V_w/\bar{C}$		F/L							
		0.5	1	2	3	4	5	8	16
0	S_{mc}	0.20	0.30	0.39		0.46		0.49	0.50
	Z_{mc}	0.37	0.55	0.71		0.82		0.88	0.90
	Z_r	0.38	0.56	0.72		0.83		0.91	0.93
0.05	S_{mc}	0.21	0.31	0.40					
	Z_{mc}	0.38	0.56	0.72					
	Z_r	-	-	-					
0.10	S_{mc}					0.46		0.49	0.50
	Z_{mc}					0.83		0.88	0.90
	Z_r					-		-	-
0.25	S_{mc}		0.33						
	Z_{mc}		0.59						
	Z_r		0.73						
0.50			x						
	S_{mc}	0.42	(0.55) (0.54)	0.58		0.51		0.50	
	Z_{mc}	0.75	0.99	1.04		0.92		0.90	
	Z_r	0.76	1.02	1.18		0.95		0.92	
0.75	S_{mc}	0.51	0.62	0.68		0.56		0.53	
	Z_{mc}	0.92	1.11	1.22		1.01		0.96	
	Z_r	0.94	1.07	1.22		1.21		0.97	
1.0	S_{mc}	0.49	0.55	0.63	0.69	0.69	0.60	0.53	
	Z_{mc}	0.88	0.99	1.13	1.24	1.24	1.08	0.95	
	Z_r	0.98	1.06	1.13	1.28	1.38	1.24	0.97	
2.0			x						
	S_{mc}	0.15	(0.30) (0.29)	0.41		0.62		0.68	
	Z_{mc}	0.27	0.52	0.74		1.11		1.22	
	Z_r	0.29	0.51	0.77		1.04		1.32	

(See also figure 5.25)

x Both methods used and compared.

Computed Relative Time Parameters for a Triangular Wind Stress Distribution on a Shelf of Linearly Varying Mean Depth and M = 55

Table 5.7

$V_w/\sqrt{C}$		F/L							
		0.5	1	2	3	4	5	8	16
0.0	t'_m		$< \infty$						
	t'_ω		∞						
	$\Delta t'$		$-\infty$						
	$\Delta t'_r$		$-\infty$						
0.05	t'_m	22.8	26.1	35.4					
	t'_ω	25.0	30.0	40.0					
	$\Delta t'$	-2.2	-4.9	-4.6					
	$\Delta t'_r$	-	-	-					
0.10	t'_m					27.7		48.8	89.0
	t'_ω					30.0		50.0	90.0
	$\Delta t'$					-2.3		-1.2	-1.0
	$\Delta t'_r$					-		-	-
0.25	t'_m		5.00						
	t'_ω		6.00						
	$\Delta t'$		-1.00						
	$\Delta t'_r$		-1.20						
0.50	t'_m	2.40	2.85	3.70		5.87		9.90	
	t'_ω	2.50	3.00	4.00		6.00		10.00	
	$\Delta t'$	-0.10	-0.15	-0.3		-0.13		-0.10	
	$\Delta t'_r$	-0.10	-0.20	-0.20		-0.40		-	
0.75	t'_m	1.75	2.05	2.70		3.83		6.60	
	t'_ω	1.66	2.00	2.66		4.00		6.66	
	$\Delta t'$	0.09	0.05	0.06		-0.17		-0.06	
	$\Delta t'_r$	-0.04	0.06	0.00		-0.01		-	
1.0	t'_m	1.37	1.65	2.14	2.64	3.08	3.52	5.15	
	t'_ω	1.25	1.50	2.00	2.50	3.00	3.50	5.00	
	$\Delta t'$	0.12	0.15	0.14	0.14	0.08	0.02	0.15	
	$\Delta t'_r$	0.00	0.10	0.10	-	0.10	-	0.00	
2.0	t'_m	0.90	1.00	1.30		1.85		2.70	
	t'_ω	0.62	0.75	1.00		1.50		2.50	
	$\Delta t'$	0.28	0.25	0.30		0.35		0.20	
	$\Delta t'_r$	0.43	0.30	0.30		0.35		0.40	

Figure 5.22

PLOT OF DIMENSIONLESS TIMES OF MAXIMUM SURGE, t'_m AND MAXIMUM WIND, t'_w TO REACH SHORE VERSUS DIMENSIONLESS STORM SPEED FOR DIFFERENT VALUES OF F/L. (SEE ALSO TABLE 5·7)

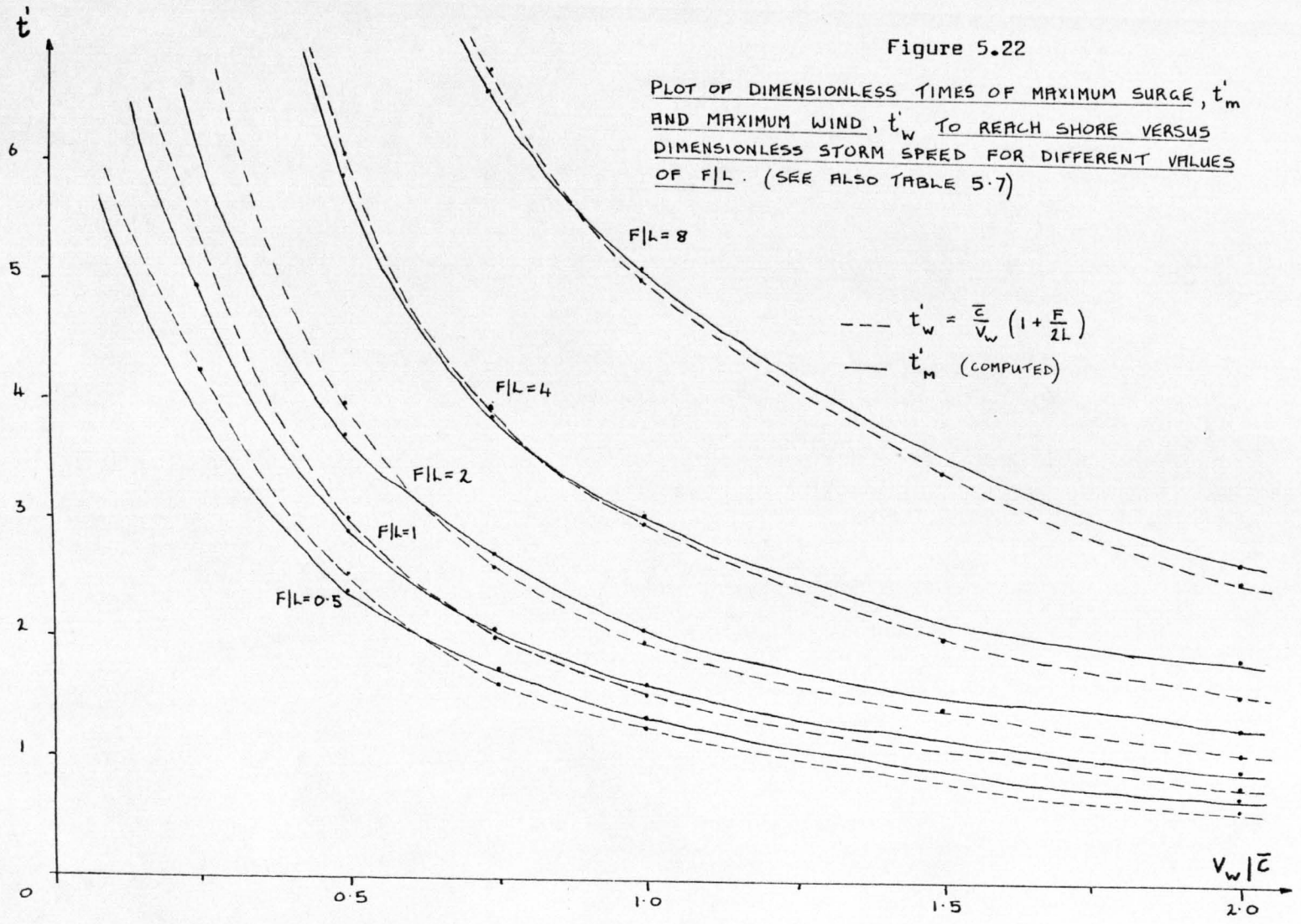

Figure 5.23

Comparison of computed and analytical maximum response factors for a triangular wind stress distribution plotted against the dimensionless storm parameter (see also Table 5.6).

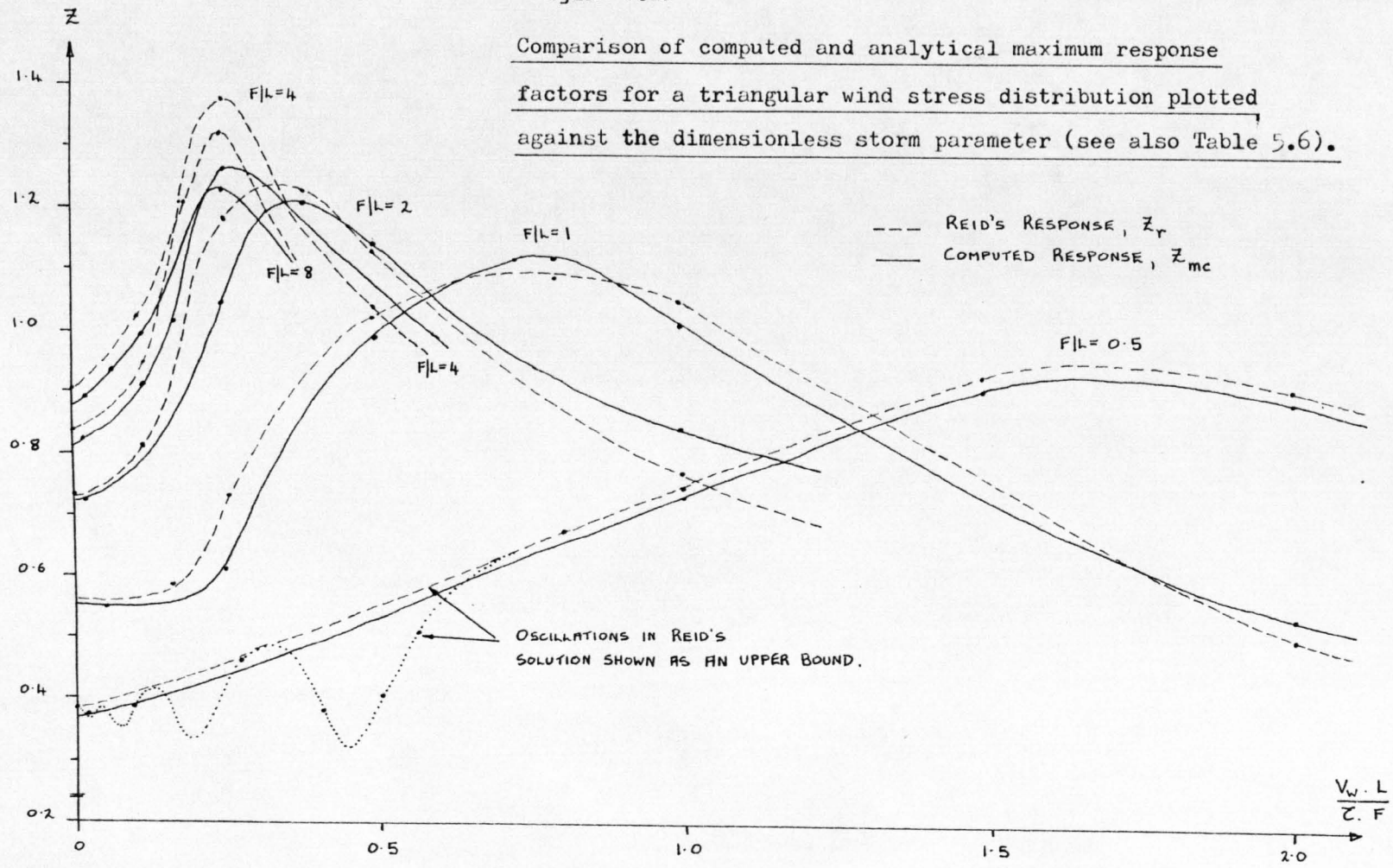

Steady state dynamic response factors at the shore of a frictionless shelf plotted against the fetch length parameter.

1 REID'S FIRST APPROXIMATION USING GRAPHICAL METHOD Z_m
2 REID'S ANALYTICAL FORMULA WITH $K = 3 \cdot 10^{-6}$ Z_r
3 TRIANGULAR WIND STRESS, M = 55 Z_{mc}
4 TRIANGULAR WIND STRESS, M = 19
5 TRIANGULAR WIND FIELD, M = 19

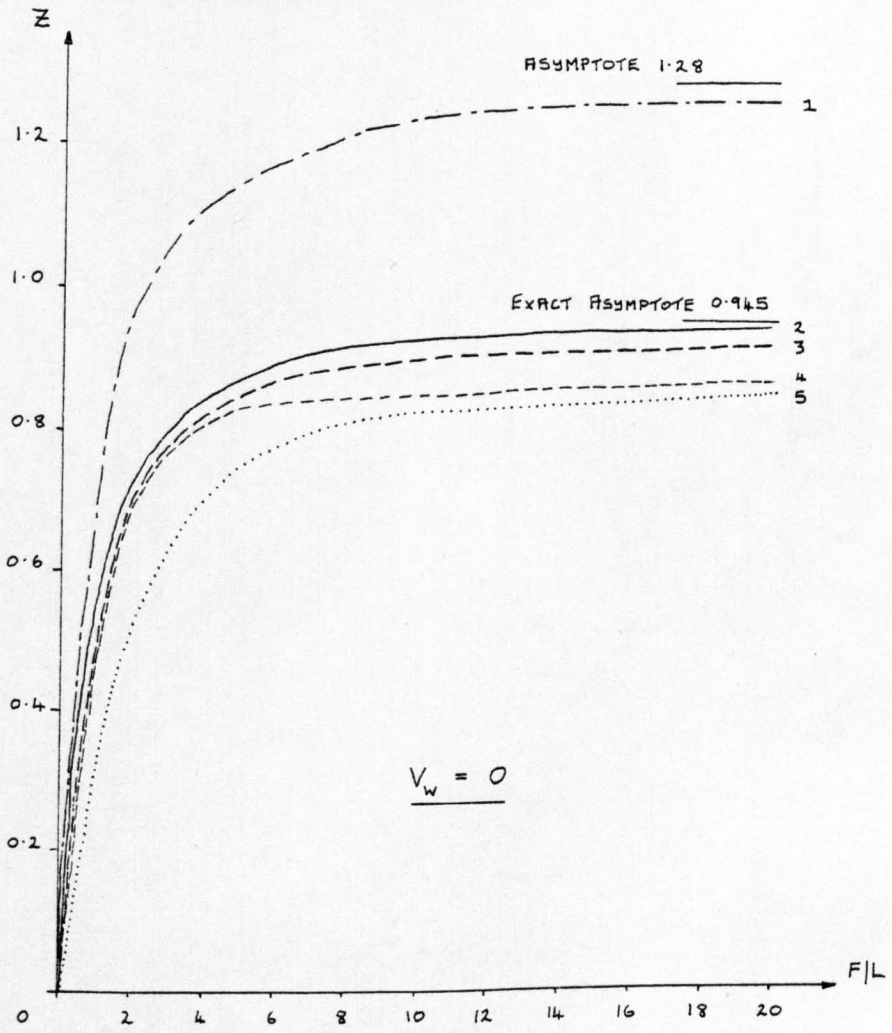

Figure 5.24

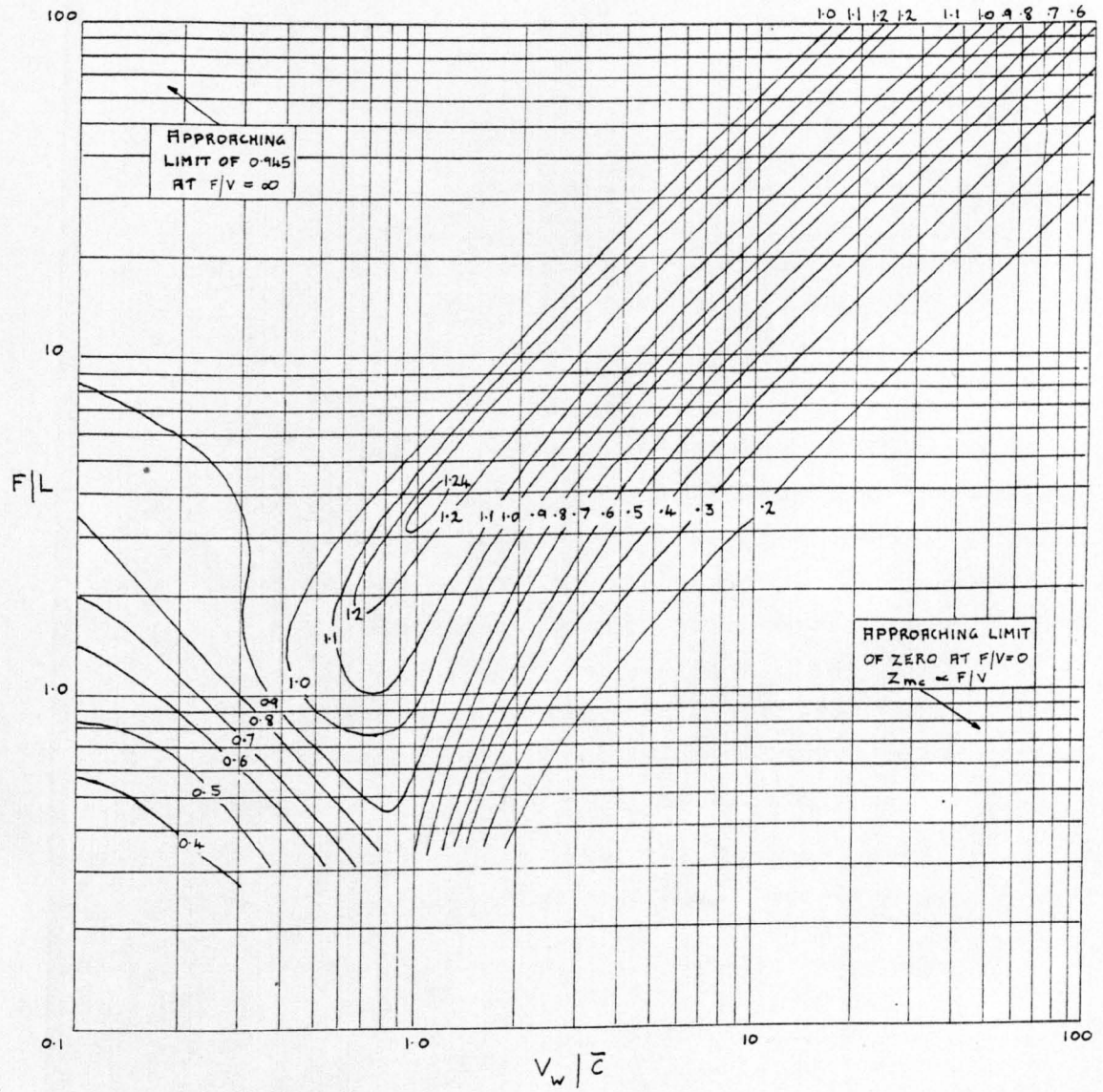

Computed response diagram; Isolines of Z_{mc} versus F/L and $V_w/\bar{c}$

Figure 5.25

For a particular occurrence of a storm, figure 5.25 can be used to find the corresponding maximum dynamic response factor. The approximate maximum surge at the shore can then be obtained by applying in equation (5.65). Two such particular surge events occurring on the west coast of Scotland have been considered for this method. The storm conditions and the wind surge obtained from equation (5.65) are shown in table 5.8.

Storm	W_m	K	F/L	V_w	$V_w/\bar{C}$	$\bar{Z}_{mc}$	S_{mc}
	MPH	$\times 10^{-6}$		Knots			m
Dec 1972	45	3.0	2	40	0.79	1.22	0.55
Mar 1979	38	2.69	2	27	0.54	1.04	0.30

Table 5.8

For the surge of December 1972 the only suitable available record of the surge was at Malin. The wind surge had a maximum value there of 0.43m obtained by removing the pressure effect from the recorded surge. The effect of pressure is discussed in Chapter 8. The shelf dimensions define a coastline that passes through Crinan, Port Ellen and Ballycastle Bay. Measurements of the 1979 surge at these ports (shown in Chapter 8) were recorded using tide gauges. The wind surge was found by adjusting the measurements for the pressure effect, and the maximum surges are as shown in table 5.9.

Port	Total Surge	Pressure Surge	Wind Surge
	m	m	m
Crinan	0.62	0.32	0.30
Port Ellen	0.56	0.30	0.26
Ballycastle Bay	0.51	0.29	0.22

Table 5.9

For both surge events the wind surge level calculated from the response diagram was larger than the maximum observed wind surge.

The following conditions were responsible for the differences just mentioned.

a) The dynamic response diagram and the analytical equation apply only to a frictionless shelf.

b) The calculated wind surge assumed that the wind distribution had a triangular stress variation and that its progression was normal to the shore.

c) It is conceivable that the recorded wind surge was reduced in height because of its interaction with the tides. The wind surge obtained from the response diagram did not consider this tidal effect.

Despite these factors the calculated and recorded wind surges are in reasonably good agreement. Actually the limitations of the computed results are in fact the limitations of the theory to which the model has been applied. Nevertheless the theory has proved useful in showing that the model has performed most satisfactorily, judging from the comparison of computed and analytical wind surges shown in this chapter. The simulations of storm surges which are not restricted by points a), b) and c) and which are therefore closer to the true physical conditions are investigated in Chapter 8.

CHAPTER 6
THE TIDAL SURVEY

6.1 INTRODUCTION

The sea area of particular interest in this research included, in addition to the Firth of Clyde, the adjacent waters of the Sound of Jura, and the North Channel approaches to both areas. For numerical modelling purposes, the definition of the sea area is partially determined from the position of a suitable sea boundary or boundaries. Since these boundaries provide a means of inputing data into the model, it is essential that they are positioned in sea areas where existing tidal information is available. For the model subsequently used, it was necessary to have three such sea boundaries in order to define adequately the boundary conditions. The locations of these boundaries are shown in figure 6.1.

At the southern sea boundary, which extended from Larne to Portpatrick, tidal information from recording gauges was available from both ports. This data in effect provided the tide and surge information for that boundary. For the entire sea area at coastal locations, tidal information was abstracted from the Admiralty Tide Tables Volume I (1972),(1979). For offshore areas the Admiralty chart No 5058 provided co-phase and co-range information for average spring tide conditions. These tables and the chart were the only available sources of tidal information at the western and northern sea boundaries. The western sea boundary was chosen so that its extremities occurred at Ballycastle Bay in County Antrim, and Port Ellen on the coast of Islay. The absence of tide recording gauges at both these ports meant that no surge information was available at this boundary. Similarly, no surge records existed at Crinan which was taken as representative of the smaller northern sea boundary. The lack of surge data alone would have justified the need to install tide gauges at Crinan, Port Ellen and Ballycastle Bay. However there was another reason. The tidal phases at Crinan, Port Ellen, (and any other port in the Sound of Jura) obtained from the Tide Tables (1979) were in disagreement with those from the co-phase chart. As an attempt to resolve this problem and establish which set of data was correct, a small tidal survey was undertaken.

The Clyde sea area represented by the waters enclosed by the three open sea boundaries of Model 1.

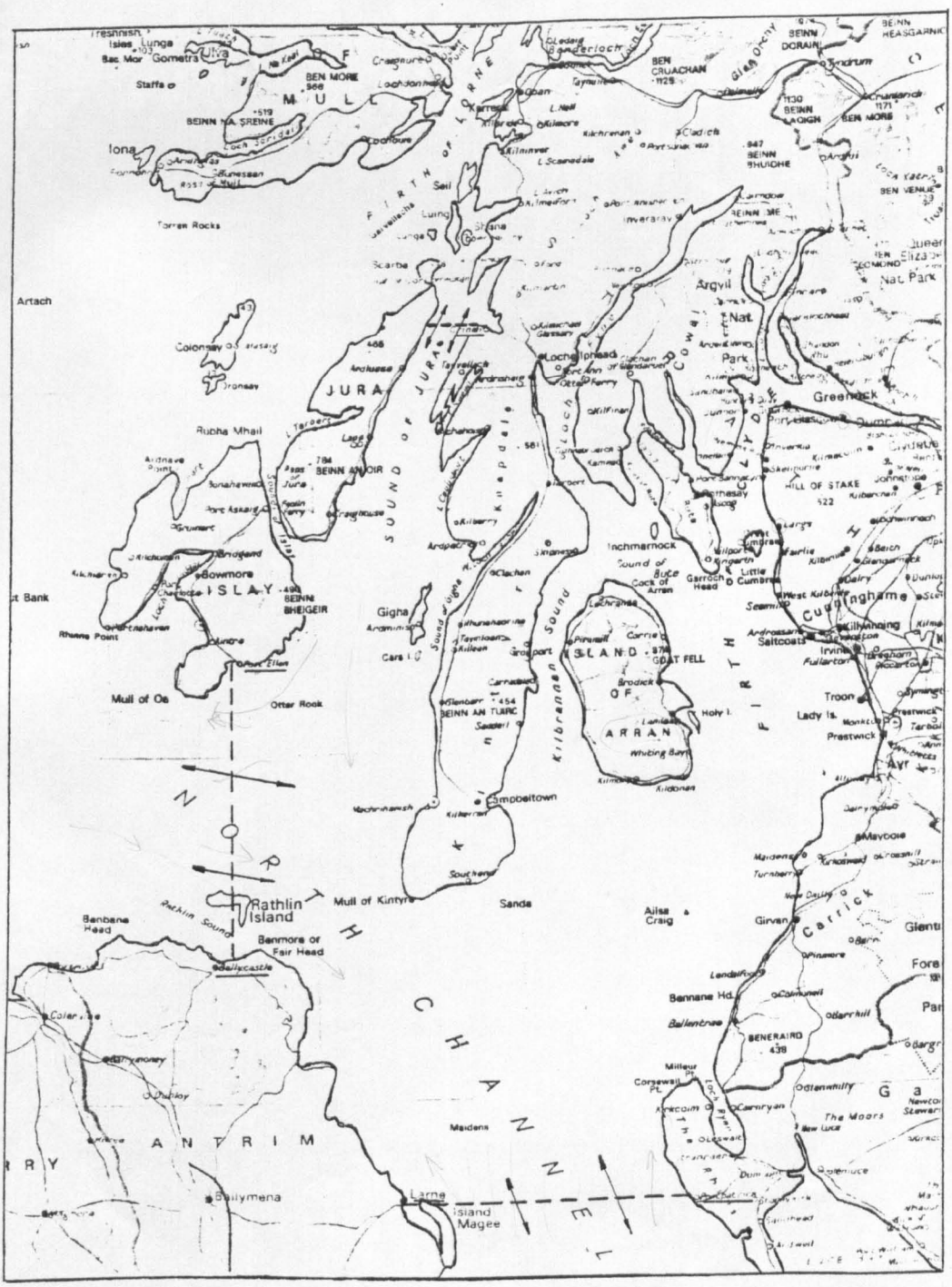

SCALE 1:1,000,000

Figure 6.1

At this point it is appropriate to note that in this research the term 'phase' is used to denote the time of high water of a particular tide. A more precise definition is that the phase of the tide is the mean time interval between the passage of the Moon over the Meridian of Greenwich and the time of the next high water at the place concerned. Hence the phase is sometimes termed the mean high water interval. In the tables that follow the phase is therefore expressed as a time relative to Greenwich (G.M.T.), although many other reference works seem to favour the use of a phase angle.

6.2 TIDE GAUGE INSTALLATION

The purpose of this survey was to install tide recording gauges at Ballycastle Bay, Port Ellen and Crinan, which would provide data for subsequent analysis of tides and surges. These gauges together with the permanent ones at Larne and Portpatrick would therefore reasonably define the boundary conditions at each sea boundary.

The field trips were accomplished in two stages, namely,

a) Portpatrick - Larne - Ballycastle Bay.

b) Crinan - Campbeltown - Port Ellen.

Both stages required the installation of tide gauges and tide poles for the establishment of the gauges' chart datums. This datum provides a means of relating a chart reading of water level to that of Ordinance Datum Newlyn (O.D.N.). The Ordinance Datum can be transferred from a Bench Mark to a tide pole using a level. From the pole and chart readings, the Ordinance Level can then be transferred from the pole to the chart and the chart datum marked thereon. The chart datums relative to O.D.N. are usually measured from the lowest astronomical tide and for most ports in the United Kingdom are obtained from the Tide Tables. It is important to establish these datums on the charts when comparing the recorded levels with those from the Tide Tables since the latter levels are relative to the chart datums.

The chart datum at Portpatrick was obtained by transferring the O.D.N. level from a bench mark to the chart. Unfortunately the chart datum at Larne could not be checked owing to harbour reconstruction at that time. The tide recorder and the tide pole situated in Portpatrick harbour are shown in Plate 1.

At Ballycastle Bay a tide pole was secured to the side of a small jetty and the tide gauge situated nearby. The instruments and their locations are shown in Plate 2. The tide gauge was a Negretti and Zambra recorder as were all the recorders used in this survey. The recorder was linked by a rubber tubing to a pressure-cell as shown in Plate 3 which responded to the hydrostatic head of water above it. The diaphragm in the head of the cell was maintained in an upright position on the sea bed by securing the cell to a concrete block. The pressure head arrangement was situated as far away as possible from the movement of boats and ships, since their disturbing action on the water would affect the gauge readings or even worse, their wake could invert the pressure head. The first stage of the survey was completed during the 5th - 7th February 1979.

During the 27th February to the 2nd March 1979 the second stage of operations was carried out. At Crinan the tide gauge was housed conveniently in a small lighthouse which is shown in Plate 4. The lighthouse is situated at the entrance of the harbour where fortunately a tide pole, which had been previously secured to the harbour wall, was still there.

The new pier at Campbeltown provided a suitable location for the tide pole and the lifeguard's house situated on the pier housed the tide gauge.

At Port Ellen, where the final tide gauge and pole were installed, the main problem was ensuring that the tide pole could be easily read on the jetty whilst shielding it from docking ships. Plate 5 shows the tide pole being secured to the jetty.

The tide gauge at Ballycastle Bay provided no records after the 12th March and it was found that in fact, the pressure head had been wrenched off its connecting rubber tubing possibly as a result of an approaching ship. Once all the gauges were installed it was expected that the recording period would be about six months without regular cleaning of the pressure head from seaweed and barnacles. The temporary gauges at Crinan, Port Ellen and Campbeltown provided records till the end of April at which time it was decided to remove them. A storm surge had been recorded between the 7th - 9th March 1979 and it was thought to be improbable that another significant surge would occur during the months following March.

Plate 1

Portpatrick harbour showing the tide gauge housing, part of the float chamber and the tide pole.

Plate 2

Securing the tide pole to the jetty at Ballycastle Bay; the tide gauge is shown in the foreground.

Plate 3

The jetty at Ballycastle Bay; the pressure cell and its concrete support are shown in the foreground.

Plate 4

Crinan lighthouse where the tide gauge was housed.

Plate 5

Securing the tide pole to the jetty at Port Ellen.

6.3 STORM SURGE FREQUENCY

Before conducting the tidal survey, a frequency analysis was performed to evaluate the probability of actually measuring a surge event during the months February to June. The analysis was based on recordings of surge heights exceeding 15.5 feet above chart datum at Broomielaw (Port Glasgow) during 1934 to 1970. These records were provided by the Clyde Port Authority and are presented in table 6.1 in such a way that the frequency of occurrence of a certain surge height can be obtained. For example a surge height greater than 3 feet occurs every 0.47 years according to the results in table 6.1. The approximate frequency of occurrence is therefore one surge every 1/0.47 years. In the table an indication of the monthly frequency of storm surges is also provided and shows that only 15% of all the surges occurred between March and June inclusively.

The data shown in table 6.1 shows a similar analysis performed for the months February to June which was the estimated duration of the survey. This analysis shows that a surge greater than 3 feet has a recurrence interval of 2.31 years. This figure indicated that there was a significant chance of measuring a surge of this size over those five months. Indeed a surge did occur between 7th - 9th March and was recorded at all the gauges situated at the sea boundaries. The surge elevations are presented in Chapter 8 together with the meteorological conditions for the period. At Broomielaw this surge attained a maximum height of 2.6 feet, which according to the figures in table 6.1 should occur on average every 1.75 years. This figure somewhat agrees with the fact that a surge occurred only once during the time the gauges were present.

6.4 THE TIDE RECORDS

It should be noted that a rigorous analysis of the tide records from each port, which involves the identification of those semi-diurnal, diurnal and shallow water constituents comprising the total tide, was not conducted for the following reasons:

ANALYSIS OF THE RECURRENCE INTERVAL BASED ON 37 YEARS OF SURGE MEASUREMENT AT THE BROOMIELAW DURING THE PERIOD 1934 TO 1970 INCLUSIVE

Month	Occurrences Within each Surge Interval								Total Monthly Surges	% Monthly Surges
	0-1'	1-2'	2-3'	3-4'	4-5'	5-6'	6-7'	7-8'		
Jan	8	15	11	4	3	1	2	0	44	17
Feb	7	10	9	5	1	0	0	0	32	13
Mar	4	6	4	2	0	0	0	0	16	7
Apr	0	3	5	4	0	0	0	0	12	5
May	0	1	1	0	0	0	0	0	2	1
Jun	0	0	1	3	1	0	0	0	5	2
Jul	0	0	0	0	0	0	0	0	0	0
Aug	0	0	0	0	0	0	0	0	0	0
Sept	1	5	8	6	0	1	0	0	21	8
Oct	1	9	9	4	5	1	1	2	32	13
Nov	1	7	7	9	2	2	0	0	28	11
Dec	4	13	21	12	5	3	0	0	58	23
Total	26	69	76	49	17	8	3	2	250	
% Surge	10	28	30	20	7	3	1	1		100

Recurrence Interval Based on Yearly Records								
Surge Greater Than	1'	2'	3'	4'	5'	6'	7'	8'
Σ Total	224	155	79	30	13	5	2	0
R.I	0.16	0.23	0.47	1.23	2.84	7.40	18.5	∞
Recurrence Interval for Period Feb-Jun Inclusive								
Total	11	20	20	14	2	0	0	0
Σ Total	56	36	16	2	0	0	0	0
R.I	0.66	1.02	2.31	18.5	∞	∞	∞	∞

Table 6.1

a) The main objective of this research was to simulate storm surge events in the Firth of Clyde. For this purpose the total tide and the surge can be specified as boundary conditions, without prior knowledge of the tidal constituents, by using the tidal records.

b) Tidal records from Greenock, Millport and Campbeltown showed that the tides were semi-diurnal and could be well represented by a single cosine constituent with a period of 44712 seconds. These records were assumed to be representative of tidal conditions in the Firth of Clyde and a similar conclusion was drawn from the records at Larne and Portpatrick.

c) It was concluded from b) that the tides in the area of interest could be represented by a single harmonic constituent. With this assumption, the verification of the convergence of the numerical scheme and its ability to reproduce the same periodic solution at all points in the model, could be shown. The verification of the periodicity would have been unnecessarily complicated had a number of constituents been used to obtain the transition for spring to neap tide and back.

d) It was only in the Sound of Jura that the tidal curves apparently could not be sufficiently defined by a single cosine curve. The tidal records from there, namely from Crinan and Port Ellen might have merited a complete tidal analysis had not the surge considerations suggested that it was not likely to be an important area.

In view of the considerations of d) it was important that the shape and phase of the spring and neap tide curves be obtained from the survey at Crinan and Port Ellen. Only after this step was completed could a reasonably accurate simulation of the tides in this area be achieved and the effect of the tides in this area, on other sea areas be assessed.

In his analysis of the tidal constituents in the Irish Sea, Defant (1961, Page 386) has shown that the diurnal tides are significant in the Sound of Jura. He used the term $\frac{K_1 + O_1}{M_2 + S_2}$ to indicate the

ratio of the diurnal to the semi-diurnal components. The relevant figures are reproduced in table 6.2 which shows a large ratio in the Sound of Jura in comparison to Greenock in the Firth of Clyde.

Port	Amplitude Of Tidal Components				$\frac{K_1+O_1}{M_2+S_2}$
	M_2 cm	S_2 cm	K_1 cm	O_1 cm	
Greenock	132.8	31.6	5.0	7.3	0.07
Belfast	122.5	29.0	7.9	12.8	0.14
Gigha Sound	18.9	16.2	9.4	8.2	0.50
Port Askaig	51.2	30.8	8.2	7.9	0.20
Carsaig Bay	46.0	25.0	8.5	8.2	0.24

Table 6.2

It was also noted that the complex nature of the tides in the Sound of Jura is suggested by the Admiralty Tide Tables (1979). The note at the foot of page 364 states that 'In the Sound of Jura, south of Loch Crinan, the rise of tide occurs mainly during the $3\frac{1}{2}$ hours following low water and the fall during the $3\frac{1}{2}$ hours following high water. At other times the changes in level are usually small and irregular and at neaps the tide is sometimes diurnal while the range is negligible'. These features are certainly apparent in the average spring and neap tides curves for Port Ellen, shown in figure 6.2. These curves were both calculated from three separate periods of tidal occurrences. The average spring tide curve has a semi- diurnal period and the high and low waters occur towards the ends of their respective positive and negative elevation taken from mean water level. There is also a similarity in tidal characteristics at high and low water judging from the shape of the curve. The average spring range was found to be 0.82 metres while the phase of the curve was 0540 G.M.T. For comparison a cosine curve of equivalent range and phase is also shown in figure 6.2 to illustrate the differences between the the two curves. The average recorded tide curve is higher on the rising tide and lower on the falling tide than the cosine curve. It is also shown in the figure that the average recorded curve can be well represented by a

summation of cosine curves defined as

$$\eta = 0.41\left(12\cos\theta_1 + 2\cos\theta_2 + \cos\theta_3\right)/10.92 \qquad (6.1)$$

where $\theta_1 = \theta - \phi$, $\theta_2 = 3(\theta-\phi) - 180^\circ$, $\theta_3 = \theta - \phi - 90^\circ$

In deriving the average neap tide curve it was noted that there was a fairly wide variation in the phase of each recorded neap tide. This feature was not evident in the neap tide curves of Crinan and Ballycastle Bay. The phase variation at Port Ellen may be a result of the diurnal constituent which was noticeable in each record. The average neap curve shown in figure 6.2 certainly indicates that the period is about 14 hours which is longer than the semi-diurnal period of 12 hours 25 minutes. In agreement with the tide tables note, the neap range is small measuring 0.25 metres, and the phase is given as 0800 G.M.T. The shape of the curve has the characteristic of the spring tide in that the high and low waters occur nearer the ends of the respective positive and negative elevations measured from mean water level.

Although Crinan is situated in the northern part of the Sound of Jura, whereas Port Ellen is in the south-west, both average spring tide curves have similar characteristics. The average spring tide curve shown in figure 6.3 was calculated from three separate periods of spring tide recordings. In comparison to the Port Ellen spring curve, the shape and phase of the Crinan curve which is 0545 G.M.T., is very similar. Only the range of the latter curve is different, being 1.9 metres, which is considerably larger than the Port Ellen spring range. For comparison, the cosine curve of equivalent range and phase is shown in figure 6.3 together with the more accurate composite cosine curve. This composite curve which was subsequently used as a boundary condition in the numerical model to represent the average spring tide variation at Crinan is defined by

$$\eta = 0.95\left(12\cos\theta_1 + 3\cos\theta_2 + 5\cos\theta_3\right)/14.144 \qquad (6.2)$$

where $\theta_1 = \theta - \phi$, $\theta_2 = 3(\theta-\phi) - 180^\circ$, $\theta_3 = \theta - \phi - 90^\circ$

The average neap tide curve at Crinan was calculated from three periods of its occurrence and is also shown in figure 6.3. It has a range of 0.40 metres and a phase of 1230 G.M.T. This phase is

about 6¼ hours different from the spring phase, which is as expected for a semi-diurnal tide. This difference is produced by the M_2 tide having a period 25 minutes longer than the S_2 period. The lag is therefore 50 minutes each day and there are 7.382 days between the spring and neap tides. In figure 6.3 the cosine representation is shown to be a good approximation to the average neap tide curve which was also found to be the case for the neap tide curve at Ballycastle Bay. With the exception of the average neap tide curve at Port Ellen, it appears that all the ports lying on the sea boundaries have their neap tides reasonably well represented by a single cosine constituent. The success or otherwise of a single cosine curve as a boundary condition in the model is investigated in Chapter 7.

Although Ballycastle Bay is not situated in the Sound of Jura and its spring phase was not in any doubt, the average spring curve is presented in figure 6.4 to illustrate its difference in shape from that of Port Ellen or Crinan. This average spring curve is characterised by the occurrence of high and low water nearer the beginning of positive and negative elevation measured from mean water level. The range of this curve is 0.8 metres and the spring phase is 0745 G.M.T. Again it is shown that the cosine curve with the range and phase of the recorded curve is a poor comparison. In figure 6.4 the composite curve compares more favourably with the recorded curve. The composite curve is given by the expression

$$\eta = 0.4\left(12\cos\theta_1 + 2\cos\theta_2 + \cos\theta_3\right)/10.92 \qquad (6.3)$$

where $\theta_1 = \theta - \phi$, $\theta_2 = 3(\theta - \phi) - 180^\circ$, $\theta_3 = \theta - \phi - 270^\circ$

In these expressions ϕ is the phase of the tide and θ is the angular time variation expressed as

$$\theta = \frac{360.t}{44712} \qquad (6.4)$$

with t as the time in seconds and the period of a semi-diurnal tide being 44712 seconds.

Since the tide recorder at Ballycastle Bay ceased to function from the 12th March, the only recorded occurrence of a neap tide was during the 6th and 7th March. Wind conditions over these two days were not strong enough to seriously affect the tidal measurement, although

they were effective in producing a positive surge on the 8th and 9th March. The average neap tide was calculated from the recordings in the 6th and 7th March and is presented in figure 6.4. This curve has a range of 0.56 metres and a phase of 0415 G.M.T. A cosine curve with these parameters is also shown and is in good agreement with the average neap curve.

As already mentioned in section 6.1 the tidal phases at spring and neap tides in the Sound of Jura, are of particular interest. For this reason the recorded spring and neap tide phases are presented for comparison with the predicted phases, in table 6.3, for Port Ellen. As well as the successive high water times, the corresponding low water times for each spring and neap tide are also shown. The predicted tidal phases were calculated by using the Admiralty Tide Tables (1979) and applying the phase correction to the Standard Port for Port Ellen. The phase corrections are listed in the Tide Tables and are also shown in tables 6.3. In tables 6.4 and 6.5 a similar analysis has been conducted for the ports, Crinan and Ballycastle Bay respectively.

For each port the comparison between the recorded and predicted times of high and low water is, in general, very good. Those few disagreements which occur at neap tides may be attributed to the difficulty in reading the exact time of high or low water, on a circular chart, when the range is small. These results certainly indicate that the Tide Tables provide a reasonably accurate means of obtaining the tidal phases at these ports.

It should be noted that the recorded phases were only tabulated for periods when the wind effect was judged not to be prominent. The tide record is sensitive to the small period surface waves, which result when a strong wind is present and under these circumstances the trace appears as a broad curve. Therefore a thin trace indicates that low wind speeds were present at the time of recording the tide level.

A comparison between the predicted and recorded phases for the data in tables 6.3, 6.4 and 6.5 may be more readily appreciated from figure 6.5. The curve shown was obtained by plotting the predicted and recorded phases against one another and represents the best fitting line. As the gradient of this line confirms the regression coefficient is very close to unity, the overall correlation is therefore good. It

Average recorded spring and neap tides at Port Ellen.

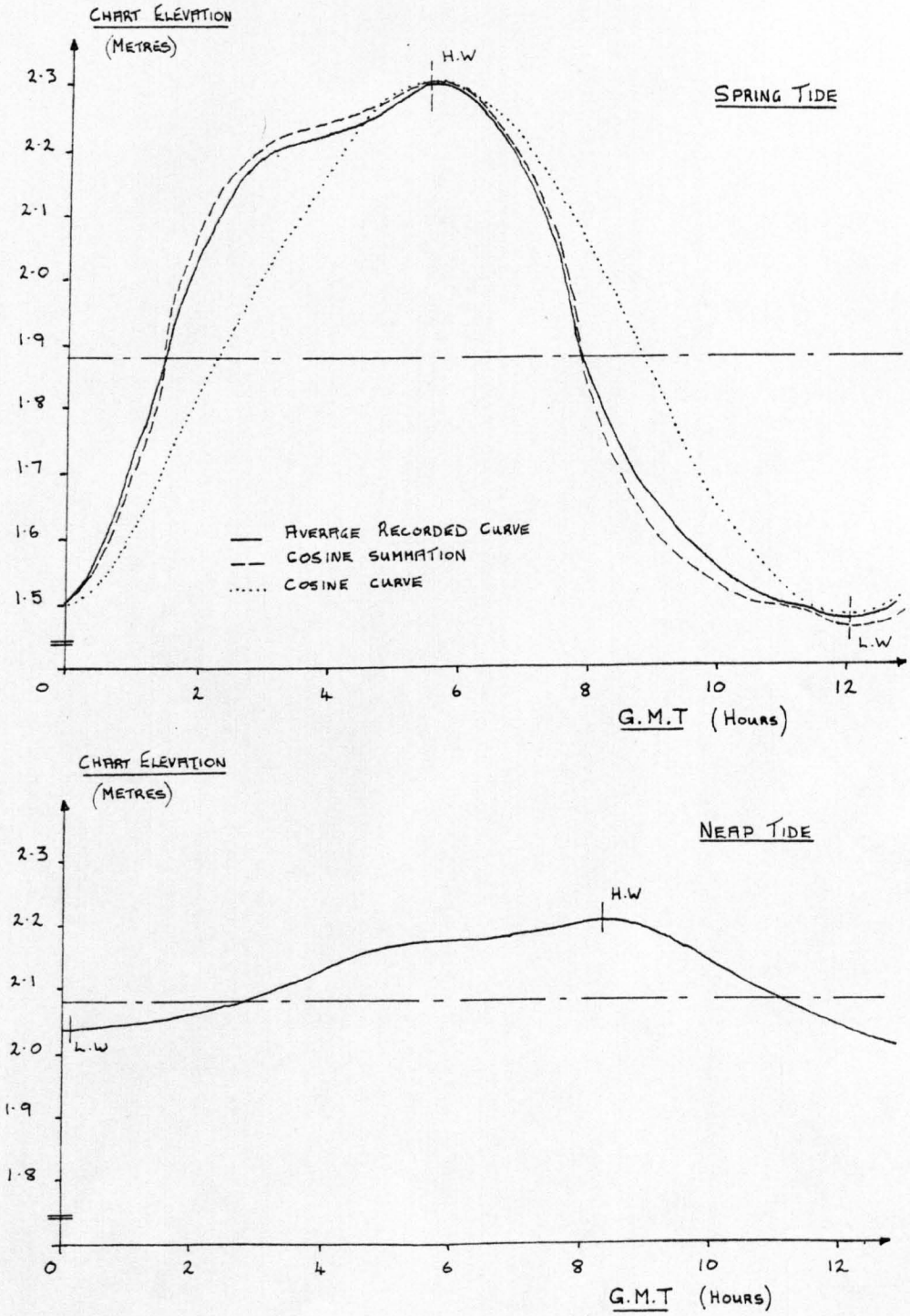

Figure 6.2

Average recorded spring and neap tides at Crinan.

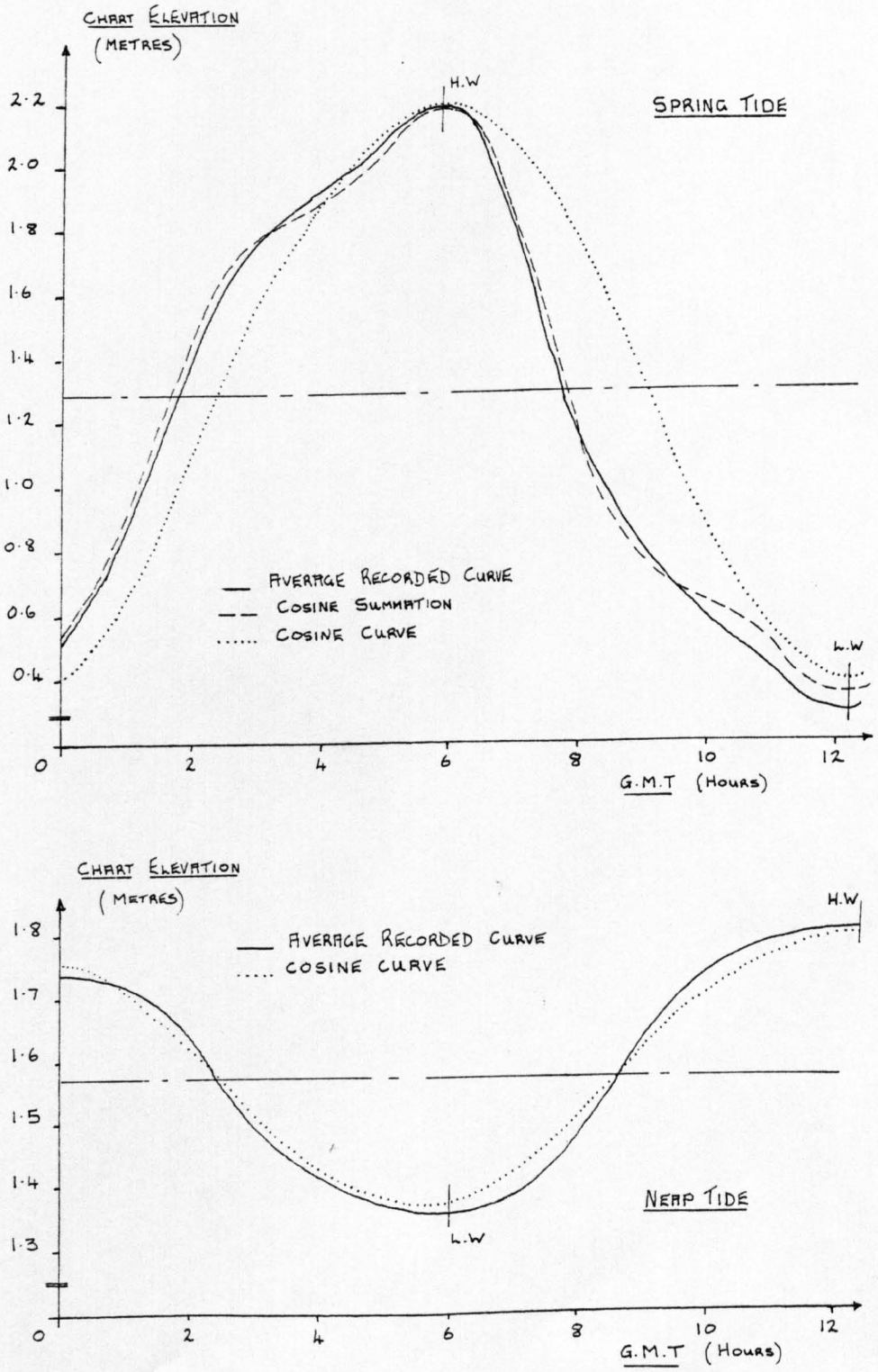

Figure 6.3

Average recorded spring and neap tides at Ballycastle Bay.

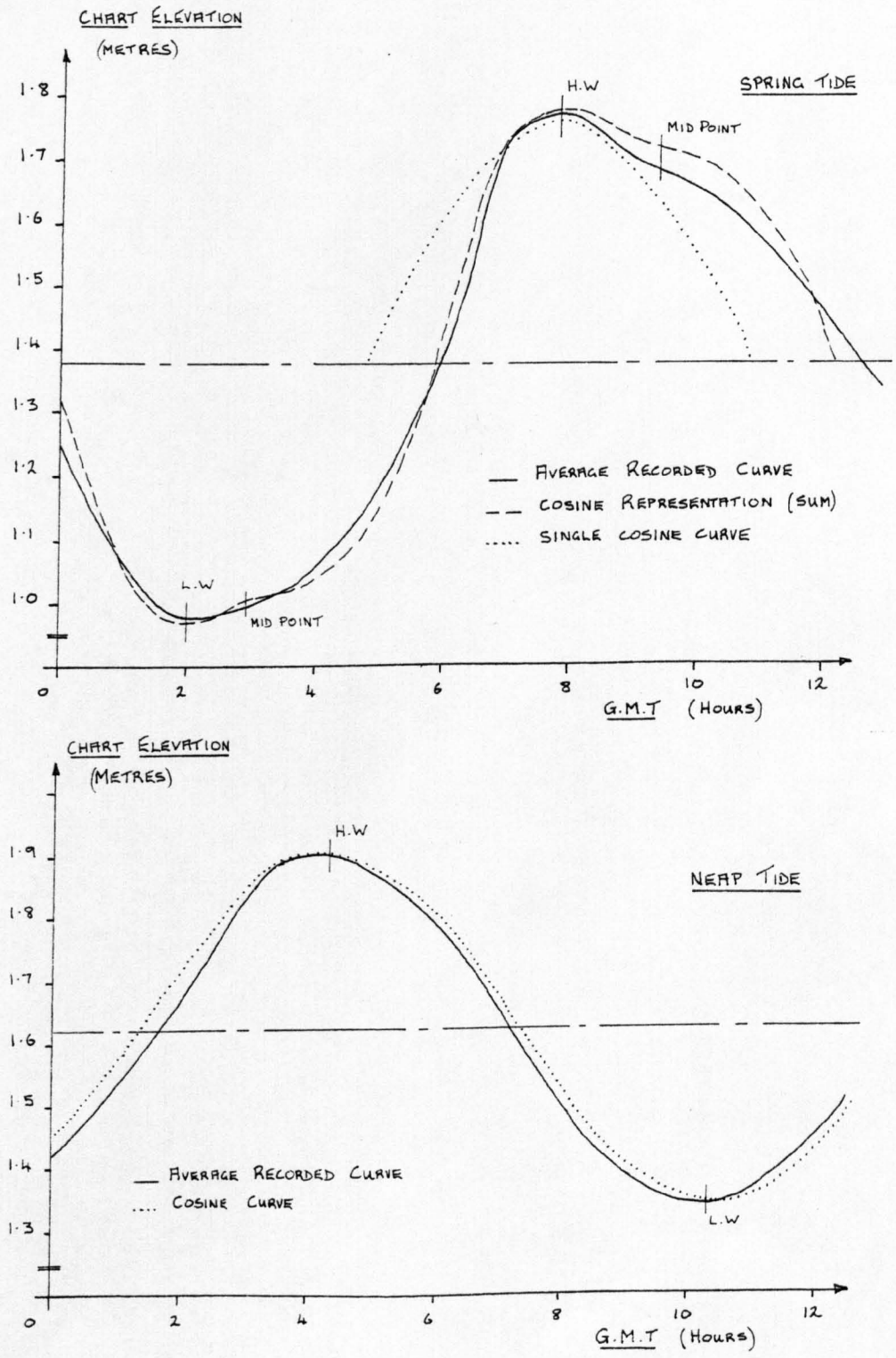

Figure 6.4

PREDICTED AND RECORDED TIDAL PHASE

AT PORT ELLEN DURING 1979

Date	Spring Tide			Date	Neap Tide		
	Oban	Port Ellen			Oban	Port Ellen	
	Predicted		Recorded		Predicted		Recorded
15/3	1302 L	1217	1208		1821 L	1251	1300
	1900 H	1810	1830	23/3	0119 H	1949	1940
	0104	0019	0000		0706	0136	0000
16/3	0658	0608	0630		1408	0838	0830
	1329	1244	1200		2000	1430	1420
	1926	1836	1900	24/3	0247	2117	2150
				6/4	0139 H	2009	2030
	1812 H	1722	1730		0801 L	0231	0100
29/3	0022 L	2337	2330		1417	0847	0630
	0631	0541	0600		1946	1416	1230
	1244	1159	1140	7/4	0251	2121	2230
	1844	1754	1800		0916	0346	0330
30/3	0103	0018	2350				
	0707	0617	0640	21/4	0106 H	1936	1830
					0654 L	0124	0130
					1355	0825	0900
14/4	0036 L	2351	2340		1936	1406	1500
	0633 H	0543	0545				
	1302	1217	1210				
	1902	1812	1830				
15/4	0110	0025	0015				
	0705	0615	0600				

$MHWS_{PE} = MHWS_{o} - 0050$

$MLWS_{PE} = MLWS_{o} - 0045$

$MHWN_{PE} = MHWN_{o} - 0530$

$MLWN_{PE} = MLWN_{o} - 0530$

All times in G.M.T.

Table 6.3

PREDICTED AND RECORDED TIDAL PHASE AT CRINAN, 1979

Date	Spring Tide			Date	Neap Tide		
	Oban	Crinan			Oban	Crinan	
	Predicted		Recorded		Predicted		Recorded
15/3	0630 H	0545	0545		1821 L	1736	1730
	1302 L	1227	1220	23/3	0119 H	0009	0000
	1900	1815	1800		0706	0621	0610
16/3	0104	0029	0015		1408	1258	1230
	0658	0613	0620		2000	1915	1900
	1329	1254	1250	24/3	0247	0137	0130
	1926	1841	1830				
				6/4	0139 H	0029	0030
	1812 H	1727	1710		0801 L	0716	0650
29/3	0022 L	2347	2340		1417	1307	1310
	0631	0546	0530		1946	1901	1915
	1244	1209	1200	7/4	0251	0141	0100
	1844	1759	1745		0916	0831	0830
30/3	0103	0028	0010				
	0707	0622	0610				
13/4	0004 L	2329	2320				
	0603 H	0518	0520				
	1232	1157	1120				
	1834	1749	1740				

All times in G.M.T.

$MHWS_c = MHWS_o - 0045$

$MLWS_c = MLWS_o - 0035$

$MHWN_c = MHWN_o - 0110$

$MLWN_c = MLWN_o - 0045$

Table 6.4

PREDICTED AND RECORDED TIDAL PHASE

AT BALLYCASTLE BAY DURING 1979

Date	Spring Tide			Date	Neap Tide		
	Londonderry	Ballycastle Bay			Londonderry	Ballycastle Bay	
	Predicted		Recorded		Predicted		Recorded
	1454 L	1329	1400				
	2039 H	1852	1930				
13/2	0244	0119	0200	6/2			—
	0851	0704	0750				
	1525	1400	1430		0357 H	0450	0530
	2110	1923	2000	7/3	1013 L	1110	1130
					1620	1713	1710
	0308 L	0143	0230		2207	2303	2330
28/2	0912 H	0725	0720				
	1535	1410	1600	6/3	1944 L	2040	2100
	2134	1947	1920		0134 H	0227	0300
1/3	0349	0224	0330		0825	0921	0915
	0955	0808	0815		1500	1553	1600

$MHWS_{BA} = MHWS_{LO} - 0147$

$MLWS_{BA} = MLWS_{LO} - 0125$

$MHWN_{BA} = MHWN_{LO} + 0053$

$MLWN_{BA} = MLWN_{LO} + 0056$

All times in G.M.T.

Table 6.5

Comparison of predicted and recorded spring and neap tide mean high water intervals at Crinan, Port Ellen and Ballycastle Bay.

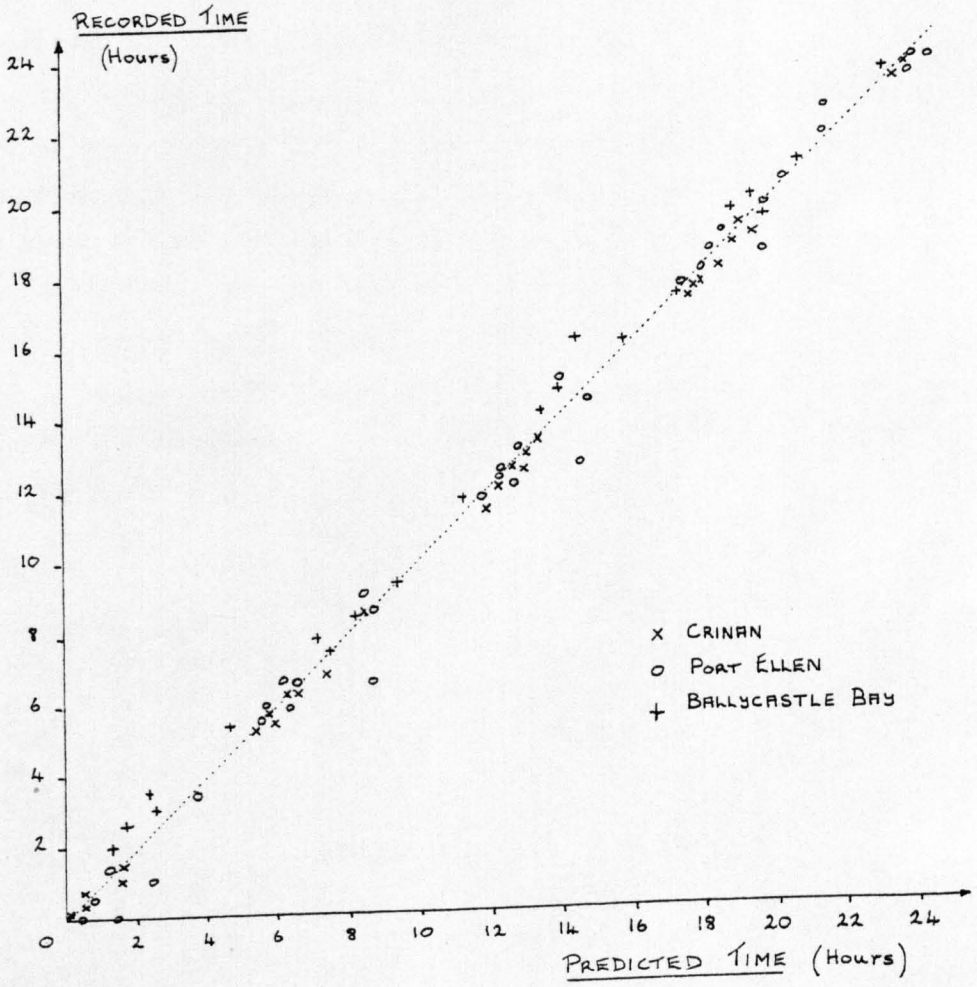

Figure 6.5

can be observed from figure 6.5 that the data exhibits four rather distinctive groups. These groups correspond to the times of the two high and low waters occurring over twenty-four hours. These groups occur irrespective of whether the tide is a spring or neap because the phase difference between these tides is 6.21 hours for a semi-diurnal tide. However the predicted and recorded times of high water at Port Ellen indicate that the phase difference between spring and neap tides is only about 2 hours. This figure again supports the argument that in the area between Port Ellen and Machrahanish the tides are not dominantly semi-diurnal in their occurrence.

To assess the accuracy of the spring and neap ranges and phases obtained from figures 6.1, 6.2 and 6.3 a comparison was made with data taken from the Tide Tables and the co-range co-tidal Chart No 5058. This chart covers the adjacent waters of the British Isles, and the part illustrating the co-range and co-tidal lines in the Sound of Jura, the North Channel, and the Firth of Clyde is shown in figure 6.6.

A comparison of the spring tide data is presented in table 6.6 for ports in the Sound of Jura, namely Crinan and Port Ellen and for Ballycastle Bay.

Mean Spring Tide Data						
Port	Chart 5058		Tide Tables (1979)		Tidal Survey	
	Range (m)	Phase (hrs)	Range (m)	Phase (hrs)	Range(m)	Phase (hrs)
Crinan	2.0	0200	2.0	0515	1.9	0545
Port Ellen	0.7	0800	0.6	0515	0.82	0540
Ballycastle	1.1	0745	1.1	0730	0.80	0745

Table 6.6

From these results some important conclusions can be made. Firstly, there is general agreement, between the three data sources, regarding the magnitude of the spring range at each port. Secondly, and of greater significance, is the fact that the spring phases from the Tide Tables and the survey are in close agreement with one another (as was

already shown in figure 6.5) but differ considerably from the spring phases at Crinan and Port Ellen, taken from the chart. In view of these figures some doubt must be cast on the accuracy of the co-tidal lines in the Sound of Jura as shown in figure 6.6. The tidal phases from this figure indicate that there is a 6 hour phase difference between the spring tides at the northern sea boundary (Crinan) and the western sea boundary extending from Port Ellen to Ballycastle Bay. This means that there is half a tidal period difference between the two sea boundaries. On the contrary, the Tide Table and survey phases suggest that these boundaries are almost in phase with one another (and the phase difference is therefore small). To support the idea of the northern and western sea boundaries being almost in phase with each other, the tidal streams from the Admiralty Stream Atlas (1974) are also in phase across these boundaries. These tidal streams, shown in figures 7.10 to 7.13 show that the inflow of water into the Sound of Jura across the two boundaries are in phase as are also the slack waters, at each boundary. In conclusion it can be said that had the tidal survey not been carried out, there would have been uncertainty as to the relative accuracies of the data from the Tide Tables and from the chart. It has now been established that the Tide Tables provide the more accurate data for the ports in the Sound of Jura.

A similar comparison of the neap tide ranges and phases in and around the Sound of Jura is shown in table 6.7.

Mean Neap Tide Data				
Port	Tide Tables		Survey	
	Range(m)	Phase(G.M.T.)	Range(m)	Phase(G.M.T.)
Crinan	0.61	1115	0.40	1230
Port Ellen	0.33	0655	0.25	0800
Ballycastle Bay	0.40	0331	0.56	0415

Table 6.7

The co-range chart data is not applicable for neap tides and so the recorded data is compared with that of the Tide Tables. It can thus be said that whilst the recorded neap ranges are satisfactory, the

PART OF ADMIRALTY CHART NO. 5058 SHOWING THE MEAN SPRING TIDE CO-RANGE AND CO-TIDAL LINES IN THE CLYDE SEA AREA, COMPILED BY THE DEUTCHES HYDROGRAPHISCHES INSTITUT FOR THE NORTH SEA COMMISSION.

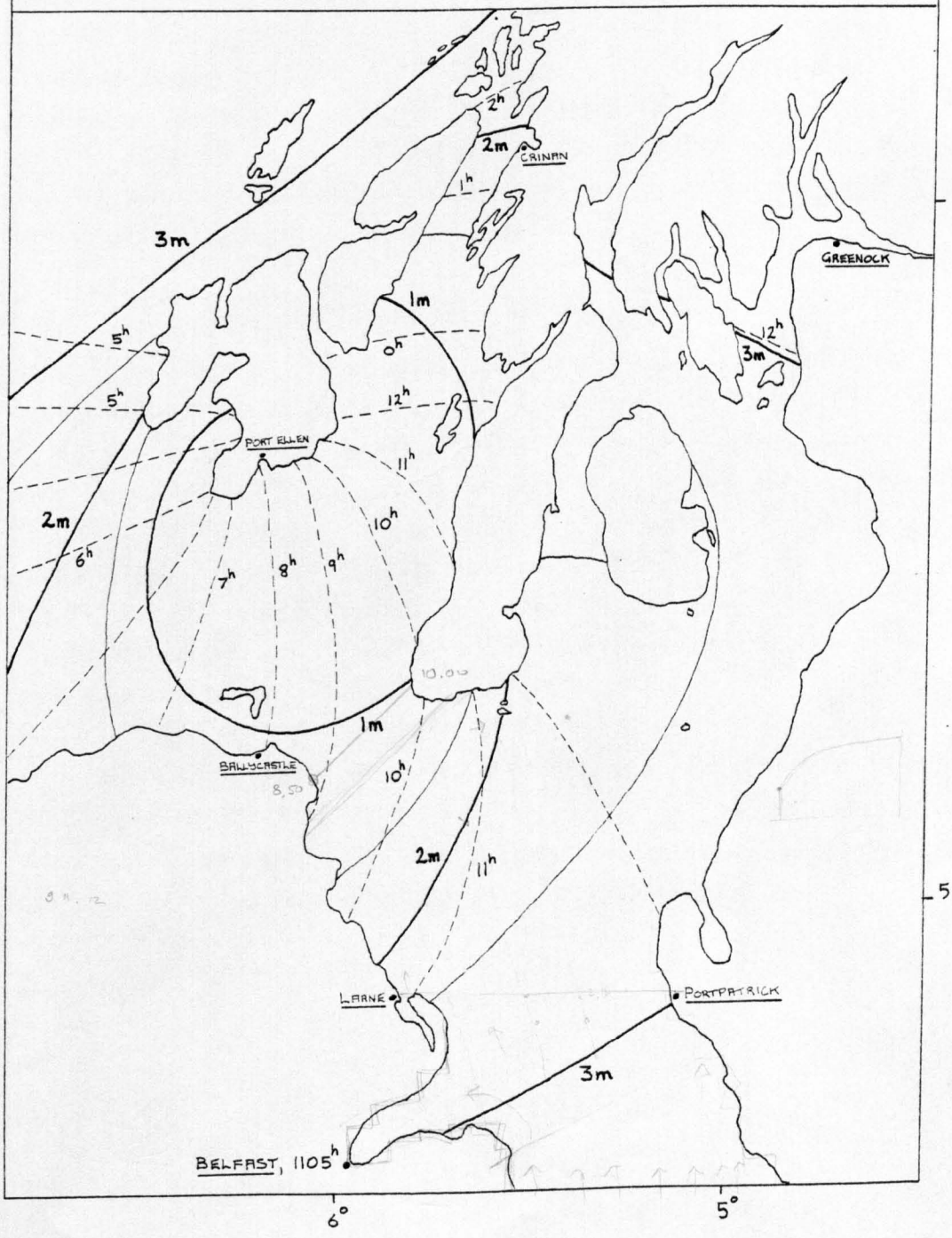

Figure 6.6

recorded phases require further explanation, being about 1 hour later than the Tide Table phases. It must be remembered that all the figures in table 6.7 represent average conditions, whilst during the survey period the tidal phase occurred later than average. For example the average yearly neap phase at the standard port, Oban, is 1225 G.M.T., whereas during the survey it was 0130 G.M.T., as noted in tables 6.3 and 6.4. This accounts for the 1 hour phase difference in table 6.7 between the predicted and recorded phases. A similar effect occurred in the spring tide results shown in table 6.6 for the same reason although the difference between predicted and recorded phase at each port was only about 0.5 hours.

6.5 PHASE CALCULATION FROM THE TIDE TABLES

The area comprising the Firth of Clyde and its approaches is not only topographically complex, but also problematic in the determination of the tidal phase at each coastal location, using Tide Tables. A major problem is that the area is represented by five Standard Ports and the Tide Tables do not provide the phase relationships between them, for average spring and neap tide conditions. One solution to this problem was to calculate the phase relationships between each Standard Port by analysing one year of spring and neap high water times which are listed in the Tide Tables. Thus by noting the differences between the times of high water at two Standard Ports over one year the average yearly phase difference was calculated for spring and neap tides during 1979.

The analysis of mean spring tide conditions is summarised in table 6.8 and the first column lists the Standard Ports.

Mean Spring Tide Phase Data					
Standard Port	Average Phase Diff (Hrs Mins)	Standard Deviation (Minutes)	Secondary Port	Phase Correction for Secondary Port (Hrs Mins)	Phase G.M.T. (Hrs Mins)
Belfast	0000	-			1105
			Larne	- 0005	1100
Greenock	+ 0130	10			1235
Oban	- 0500	14			0605
			Loch Beag	- 0050	0515
			Port Ellen	- 0050	0515
Londonderry	- 0250	8			0810
			Ballycastle Bay	- 0040	0730
Liverpool	+ 0015	6			1120
			Port-patrick	+ 0018	1138

Table 6.8

In columns two and three the average phase difference calculated between the Standard Ports, and the standard deviation of the calculation is respectively shown. The phase differences were calculated relative to Belfast since this port lies in an area of relatively constant spring phase (figure 6.6 shows this) and its phase of 1105 G.M.T., was thought to be accurate. In calculating the mean yearly spring phase differences it was convenient to have an indication of the variation in these differences at each port. For this purpose the standard deviation was calculated using the following expression

$$\bar{D} = \sqrt{\frac{\sum_{1}^{N} (\Delta\phi - \overline{\Delta\phi})^2}{N}} \qquad (6.5)$$

The standard deviations were sufficiently small enough at each port to indicate that the analysis produces mean values that are representative of the phase differences throughout the year. In the final column the phase for each Standard Port is obtained by applying the phase difference to the phase at Belfast. From the phase of the Standard Ports, the phase of the respective Secondary Ports can be obtained by applying

the phase correction shown in column five of figure 6.8. These phase corrections are listed in the Tide Tables for the substantial number of Secondary Ports located in the Firth of Clyde and its approaches. The Secondary Ports shown in table 6.8 correspond to the positions of the three sea boundaries represented in figure 6.1. Unfortunately Crinan is not listed in the Tide Tables and therefore its phase correction was taken as that from Loch Beag which is situated not far from Crinan.

An analysis similar to that for the spring tides was conducted for the neap tides to establish the average phase differences between the Standard Ports. The results are shown in table 6.9 and again the phase difference for each Standard Port is quoted relative to the neap tide phase at Belfast.

Mean Neap Tide Phase Data					
Standard Port	Average Phase Diff (Hrs Mins)	Standard Deviation (Minutes)	Secondary Port	Phase Correction for Sec Port (Hrs Mins)	Phase G.M.T. (Hrs Mins)
Belfast	0000	-			0514
			Larne	0000	0514
Greenock	+ 0046	12			0600
Oban	- 0514	18			1225
			Loch Beag	- 0110	1115
			Port Ellen	- 0530	0655
Londonderry	- 0236	14			0238
			Ballycastle Bay	+ 0053	0331
Liverpool	- 0001	9			0513
			Port-patrick	+ 0026	0539

Table 6.9

As an indication of the variation in the phase difference between the Standard Port and Belfast, for one year of phase differences, the standard deviation is shown in column three of this table. A comparison of phases at Greenock and Oban shows that there is a maximum variation in phase of nearly one half of a semi-diurnal period over the entire area.

By obtaining the average spring and neap tide phases as shown in tables 6.8 and 6.9 respectively, for the Standard Ports, the Tide Tables can thus be used to provide the average spring or neap phases at the Secondary Ports. Indeed, the Tide Table phases shown in tables 6.6 and 6.7 are taken from tables 6.8 and 6.9 respectively. In each of the latter tables the Secondary Ports, Larne and Portpatrick provide data for the numerical model's southern sea boundary. Ballycastle Bay and Port Ellen phases are appropriate at the western sea boundary and the Crinan (Loch Beag) phase is representative of the tidal phase at the small northern sea boundary. The accuracy of the simulation using a numerical model, with this data providing the boundary phase conditions was carried out and is assessed in Chapter 7. In addition the response of the model to the average tide data, obtained from the survey records and specified as boundary conditions was also found for comparison.

CHAPTER 7

TIDE SIMULATION IN THE FIRTH OF CLYDE AND ITS APPROACHES

7.1 INTRODUCTION

It has been shown in Chapter 4 that the analytical studies were important for establishing the accuracy of the interpolation and integration schemes in the model. To complete these tests it is required that the effect of the initial and boundary conditions be examined, using a configuration more complex than a geometrically simple channel. For this purpose the application of the numerical scheme to simulate the tidal motion in a shallow sea area is appropriate. By nature of the periodicity of the tides the effectiveness of the harmonic conditions at the sea boundaries in establishing a periodic solution throughout the model can be evaluated. It should be noted that only after the successful simulation of tidal motion in an irregular sea area, can the simulation of the tide and storm surge phenomenon be considered.

7.2 APPLICATION OF THE MODEL TO A REAL SITUATION

The difficulties in simulating tidal motion in a real configuration can be classified as follows:-

a) Limitations of the quantity and quality of data.

b) The effect of discretising an irregular coastline and sea bed.

The effect of a) is to hinder the verification of the accuracy of the simulation. The results from the model are ultimately compared to observed data to assess their accuracy and it is easy to wrongly attribute discrepancies in the comparison to limitations of the model, where in fact the difference may be the result of data errors. Resolving the differences becomes even more difficult when it is remembered that the model actually uses the incorrect data in its boundary conditions and so the accuracy of the simulation is effectively limited by the accuracy of the recorded data.

In terms of quantity, the physical data is usually in the form of a limited number of tidal records taken from recording gauges situated along the coastline with even fewer records available for offshore currents and displacements. Consequently the harmonic functions at the sea boundaries, which are based on either velocities or elevations with associated phases, are only known from the ports at the landward ends of these boundaries. Therefore the boundary data at grid points along the sea boundaries has to be obtained by linearly interpolating between the known points.

The sea area and the sea boundaries encompassing the numerical model have been shown already in figure 6.1. Since the tidal constituents at the sea boundary ports were unavailable, the average spring and neap tide conditions at these ports were obtained from the Admiralty Tide Tables (1979). This source of information, which is derived from harmonic analysis was used at the boundary ports in the model in preference to actual tidal records because the latter may not be free from meteorological effects. The Tide Table data was thought to be sufficiently accurate as an input to the model and was shown in section 6.4 to be in good agreement with the data obtained from the tidal survey. The comparison has been shown in tables 6.6 and 6.7, for mean spring and mean neap tide conditions respectively.

The Tide Tables also provided data at coastal locations, in sufficient quantity so that comparisons were made with the results from the model. For offshore locations the average spring tide ranges and phases were compared with those from Admiralty Chart 5058 although the chart's co-phase lines in the Sound of Jura have been shown in section 6.4 to be suspect.

Returning to point b), the limitations mentioned are directly related to the method by which the model represents the physical topography of the sea area, An irregular coastline is schematised in terms of a polygon with sides of equal length DS and positioned along the x and y axes. This length is termed the spacestep, and controls the degree of discretisation of the model. It is usually determined by the requirements of a reasonably representative grid, and yet cannot be so small that the numerical computations are beyond the capabilities of the computer. Having represented the area within the sea boundaries by a

suitable grid, the depths from mean water level at each grid point can be obtained by interpolating from the soundings on an Admiralty Chart or from a hydrographic survey. The whole process of schematisation using discrete points introduces an element of approximation into the construction of the model. For the model to provide reliable results this rounding error must be maintained as small as possible.

By constructing the grid to the scale of Admiralty Chart 2724, using a spacestep of 5 kilometres, the coastline schematisation and the soundings at each grid point were obtained for the sea area shown in figure 6.1. The schematisation and the soundings are shown in figure 7.4 from which it is apparent that the depths in the North Channel are much greater than for either the Sound of Jura or the Firth of Clyde. In fact quite a large depth range is covered in a relatively small sea area and together with the complex indentation of the coastline provided a thorough test for the model in simulating the movement of the tides.

In considering the physical processes taking place in a sea area as opposed to an idealised channel, the frictional stress at the sea bed must be accounted for. The friction parameter theoretically controlling this stress is a function of both depth and bed roughness. In general the values of the friction parameter at points on the sea bed are unknown unless an extensive survey has been conducted. Standard practice appears to be to assign a value to this parameter at each grid point in the model so that the correlation between the numerical and physical results is optimised. Indeed Leendertse (1967) chose a different value of the friction parameter at each grid point when simulating tides in the Rhine estuary. He obtained a high correlation between computed and recorded tide levels using a range of Chezy coefficients varying from $30\,m^{\frac{1}{2}}/s$ to $80\,m^{\frac{1}{2}}/s$. However a set of friction parameters chosen without full knowledge of the physical conditions at the sea bed and also the eddy currents above, whilst improving the simulation seems unjustified. A more rational approach is to use only one friction parameter for the entire sea area. The performance of the numerical scheme can therefore be evaluated more readily since the computations are not obscured by parametric adjustment of the friction parameter. A single friction parameter was considered by Heaps (1969) in his North Sea model which used a value of 0.0025 which is equivalent

to a Chezy coefficient of $63 m^{\frac{1}{2}}/s$.

In view of the points a) and b) the associated errors will combine to affect the output at each and every grid point. Therefore it is probable that the free friction parameter may be prescribed a value which is not entirely in agreement with the true physical friction coefficient.

7.3 TIDES IN THE FIRTH OF CLYDE AND ITS APPROACHES

7.3.1 Description of the Tide Motion.

It is perhaps easier to appreciate the tidal propagation in the Clyde sea area by placing this motion in contex with the tidal oscillations occurring southwards in the Irish Sea. This area is shown in figure 7.1, together with the co-range and co-phase lines for the M_2 tide as computed by Doodson and Corkan (1932).

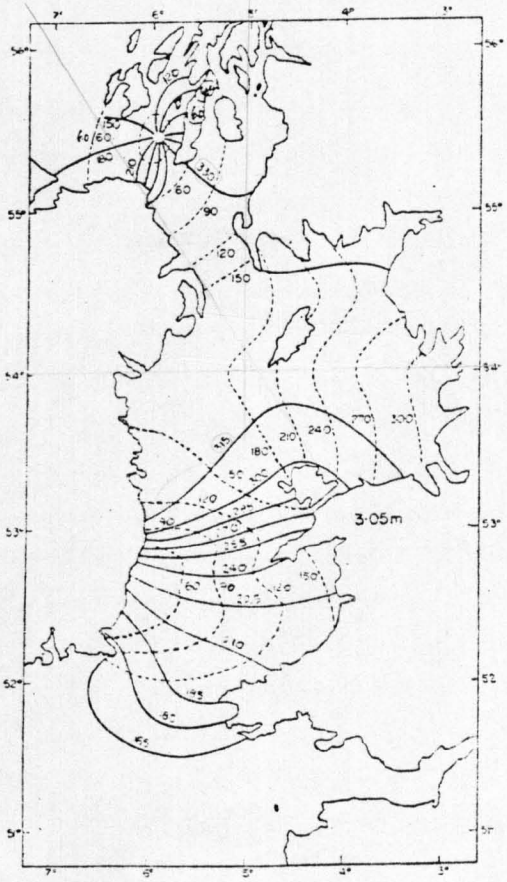

Co-tidal and co-range lines of the M_2 tide in the Irish Sea. —, phase in degrees referred to upper culmination of the moon in Greenwich; -----, amplitude in cm.

Figure 7.1

The figure shows that in both the North Channel and the St George's Channel there is a crowding of co-phase lines in comparison to the almost uniform time of high water in the Irish Sea. There is also an increase in range on entering the Irish Sea from either Channel and throughout the entire sea area the tidal streams are weakest where the ranges are largest. These features indicate standing wave characteristics in the Irish Sea.

The progression of the co-phase lines in the North Channel indicate that the Firth of Clyde tides are determined by tidal propagation across the coast of Northern Ireland from the Atlantic Ocean. Hence the Firth of Clyde tides are in co-oscillation with those in an area of the Atlantic, west of the Clyde. This is an interesting feature since the orientation of the Firth of Clyde is north - southwards and so is more exposed, yet apparently less influenced by the tidal oscillations in the Irish Sea. This feature is also evident in the tidal streams shown later in section 7.3.3.

A closer inspection of the area within the sea boundaries shown in figure 6.1, using the data obtained from the tidal survey and the Tide Tables has shown that the propagation of the tide from the western sea boundary to Greenock at the head of the Firth of Clyde, requires about six hours. The phase increases from about an average of 0630 G.M.T., at the western sea boundary to 1230 G.M.T., at Greenock, for mean spring tides whilst the corresponding ranges increase from an average of 0.8 metres to 3.1 metres. It has also been concluded from the Tide Table figures and the survey results that the western and northern sea boundaries are almost in phase with each other. Furthermore the Tide Table phases at the southern sea boundary extending from Larne to Portpatrick are in opposite phase with the northern and western sea boundaries. The average spring amplitude at the southern sea boundary is 1.3 metres and it occurs through the deceleration of flow and an increase in potential energy as the tide wave progresses from the western sea boundary and approaches the standing wave in the Irish Sea. A simplified representation of these conditions is depicted in figure 7.2 corresponding to the mean spring ranges along the axis of the North Channel. As shown, the ranges at each sea boundary are

in opposite phase with one another.

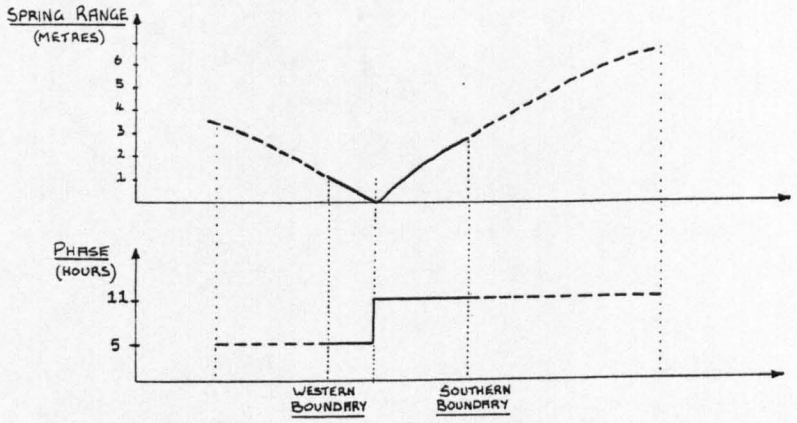

Figure 7.2

The situation is of course an idealised one but nevertheless highlights the fact that at a certain location there is a region of zero range. The position of the node will be located nearer to the western sea boundary as opposed to the southern sea boundary by virtue of the magnitude of the ranges at each boundary. The node which is termed an amphidromic point or an amphidrome is shown in figure 7.1 and is as postulated near the western sea boundary and is about ten miles west of Machrahanish on the Kintyre Peninsula.

In a study of the Irish Sea, Defant (1961) acknowledged the existence of the amphidromic point for average spring tide conditions in the North Channel. He produced profiles of the spring tide ranges and phases extending from the Scilly Isles to Tiree. The profiles extending from Tiree to Dublin, shown in figure 7.3, contain the western and southern sea boundaries and the curves are comparable

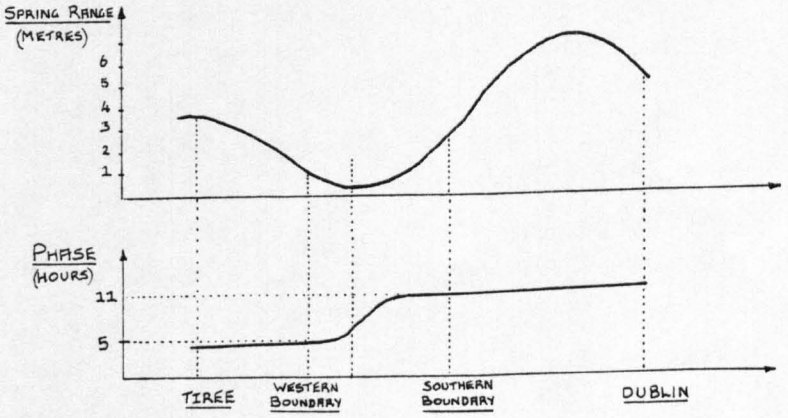

Figure 7.3

to figure 7.2. The difference between the two figures is that the former shows a nodal region while figure 7.2 shows a nodal point. Defant concluded that it is the effect of friction that causes the abrupt change of phase of half a tidal period to be replaced by a gradual change. The standing wave of the co-oscillating tide takes the character of a progressive wave which travels toward the closed end of the bay or any other type of restriction such as another wave in the opposite direction. If friction does not become too great the position of the nodal lines continues to be clearly perceptible by the crowding of the co-phase lines. The node where the amplitude of the tide is zero disappears and instead becomes a region with minimal range.

In large expanses of sea, where the Coriolis force is significant, such as in the North Sea, amphidromic points are produced. They have the inherent property that the co-phase lines travel anticlockwise round their centres when they occur in the Northern Hemisphere, as is the case with the amphidrome shown in figure 7.1. Considering for a moment a wave that limits itself in the case of wide canals to one side, namely the side that follows rotation, the wave is termed a Kelvin wave. Its salient feature is that transverse oscillations do not occur, as a result of the Coriolis force being in equilibrium with the gravitational component acting down the wave's transverse surface slope. Taylor (1920) has shown that perfect reflection of a Kelvin wave in a rectangular channel produces an amphidrome and similarly for two Kelvin waves travelling in opposite directions. It is unlikely that the amphidromic point shown in figure 7.1 is the result of the Coriolis effect since the sea area there is probably too small and confined. However Defant has concluded from the occurrence of amphidromic points in the Baltic and the Black Sea, which are also highly confined, that these amphidromes can be produced from a combination of longitudinal and transverse oscillations. Referring to the particular amphidromic point in the North Channel there is an oscillating motion between the northern and southern sea boundaries, the western and southern boundaries and possibly a reflection from the Kintyre Peninsula for waves progressing through the western sea boundary. It is therefore not unlikely that these oscillations are responsible for the formation of this amphidromic point.

The occurrence of the amphidromic point is one of the most interesting features of the sea areas close to the Firth of Clyde. In considering the formation of this amphidromic point an account of all the salient tidal features in the Sound of Jura and the North Channel have been mentioned. By comparison the tidal propagation in the Firth of Clyde is straightforward since it is a converging estuary which communicates with the North Channel through only one open sea boundary which can be taken from Campbeltown to Stranraer. The average spring range varies from 2.5 metres at the mouth to 3.1 metres at the head of the estuary while the phase difference along its length is only about thirty minutes.

Although the following model was developed to assess its ability to simulate storms surges in the Firth of Clyde, since this is the area of largest surge, the important areas for the complex nature of the tides are the Sound of Jura and the North Channel. It was these two areas that offered a stern challenge to the capabilities of the model.

7.3.2 General Description of the Models

A classification of the models which are considered in this and other chapters has been made, simply according to the gridsize, within which, a number of different tests have been performed. Some features of these tests are common to all models and are mentioned as follows to avoid later repetition;

a) Each numerical scheme contained friction and Coriolis terms and the non-linear depth and convective terms were also present.

b) In each test the initial conditions were an arbitrary linear free surface and zero velocities throughout. A periodic solution was established after the completion of two tidal cycles, checked to an accuracy of four decimal places.

c) The three sources of data, namely the Tide Tables (1979), the co-tidal chart 5058 and the survey records, which were compared in section 6.4, provided the ranges and phases for ports on the sea boundaries. Each source of data was in turn tested in the model and the response noted. At other grid points along the sea boundary, the ranges and phases were calculated by linearly interpolating from the known

A SUMMARY OF TESTS USING MODEL 1 TO SIMULATE THE SPRING TIDES IN THE FIRTH OF CLYDE AND ITS APPROACHES

Test	Nos of Sea Boundaries	Sea Boundary Data. Northern/Southern Western/	Numerical Scheme	Chezy Friction Factor	Assessment of the Final Solution
1	2	Chart 5058	⊕	Frictionless	Comparison to chart shows that computed ranges are too large
2	2	Chart 5058	⊕	100	Ranges and phases in Sound of Jura require improvement. Chart data is suspect
3	3	Chart 5058	⊕	90	
4	3	T. Tables/Chart	$\triangle_9$	90	Computed elevations are smaller than those from Tide Tables due to interpolation scheme
5	3	Tide Tables	⊗	140	
6	3	T. Tables/Chart	$\oplus_9$	90	Comparison of 45° and 90° characteristics. Results are satisfactory in both cases
7	3	T. Tables/Chart	⊕	90	
8	3	Survey/Chart	⊕	90	Improvement of phases in Jura Sound
9	3	Tide Tables	⊕	70	Results are satisfactory. Model used to simulate surges
10	3	Tide Tables	⊕ ⊗	140	Results are an improvement on Test 9, but friction factor unrealistic

Table 7.1

data. The boundary elevations were then specified as an harmonic cosine function of time representing the average total tide at a particular point. The sea boundary velocities were calculated by the numerical scheme.

It has been shown in Chapter 4 that boundary interpolation scheme 4 and I.S.1 derived from it were the most favourable schemes for simulating analytical motion. These schemes, when applied in turn to a real situation with an irregular coastline produced an excessive amount of damping of the elevations and velocities. In schematising such a coastline the 'corner points' represented by configuration numbers 5, 6, 7 and 8, each having boundary conditions U = 0, V = 0, were used quite extensively. The damping is thought to be produced as a result of using these boundary conditions, to a severe extent, in the velocity interpolations at the boundary points with configuration numbers 1, 2, 3 and 4.

In contrast, interpolation scheme 2 has been shown to be unstable when applied to a constant depth configuration with the condition $DT = DT_{max}$, However in the case of a forced oscillation in a real situation with irregular depths, this condition does not occur at the closed boundaries since the depths there are not as great as the maximum depth in the sea area. Therefore the numerical timestep is less than that obtained from the C.F.L. condition applied with the depth at a particular boundary point. The success of interpolation scheme 2 can only be attributed to the fact that the velocity interpolations at the boundary points, with configuration numbers 1, 2, 3 and 4, are not based on the adjacent boundary points and so exclude the 'corner points'. The tests conducted using Model 1 are presented in the next section and confirm the effect of using these boundary interpolations. Subsequent models were developed which also incorporate interpolation scheme 2 into the numerical scheme.

7.3.3 Simulation of the Mean Spring and Neap tides using Model 1

The schematisation of the Firth of Clyde and its approaches, based on a spacestep of 5 km and with the depths in metres is as shown in figure 7.4. As a stability requirement, the timestep was chosen as 69 seconds, which is less than the C.F.L. limiting timestep

of 78 seconds. The limiting timestep was based on the maximum depth of 205 metres occurring near the southern boundary in the North Channel. Together, the spacestep and timestep are sufficient to classify the arrangement as Model 1 which was applied to a number of tests. These tests for mean spring tides are listed in table 7.1 together with the features characterising each particular test. Essentially the objectives were to evaluate the effect of the available data as an input to the model and also to establish a favourable interpolation scheme. To facilitate the interpretation of the computations they were either compared according to the data source to the co-tidal chart shown in figure 6.6 or the range and phase data taken from the Tide Tables (1979). For mean spring tides the Tide Table data is shown in table 7.3 for all the coastal locations (including the ports situated at the input boundaries). The locations of all these ports are shown in figure 7.5.

The input of ranges and phases in Test 1 for a mean spring tide was extracted from the co-tidal chart, and specified along only the western and southern sea boundaries. As an initial simplification the northern sea boundary was treated as a land boundary and frictional stress was not applied throughout the grid. The simulated results are presented in table 7.4 for the coastal locations and the co-range and co-phase lines are depicted in figure 7.5. In the Firth of Clyde the ranges are about 15% larger than those of the chart, and in the Clyde estuary they are in excess of 3.5 metres. By comparison to the chart the simulated ranges and phases in the Sound of Jura are poor possibly as a result of closing the northern sea boundary.

By introducing a value of the Chezy friction factor equal to $100 m^{\frac{1}{2}}/s$ into the previous scheme, the stream flow especially in the shallower reaches was reduced. The results are listed as Test 2 in table 7.4. Comparing to test 1 the tidal range at Greenock has been reduced from 3.88 metres to 3.16 metres which is very close to that of the chart or Tide Table value. The frictional effect has caused the phases in the Firth of Clyde to be later than those of Test 1. This effect and the reduction of the ranges are in accordance with the findings of Proudman (1955) for a single progressive wave in a contracting estuary.

Mean water depths (in metres) at grid points which schematise the Clyde sea area.

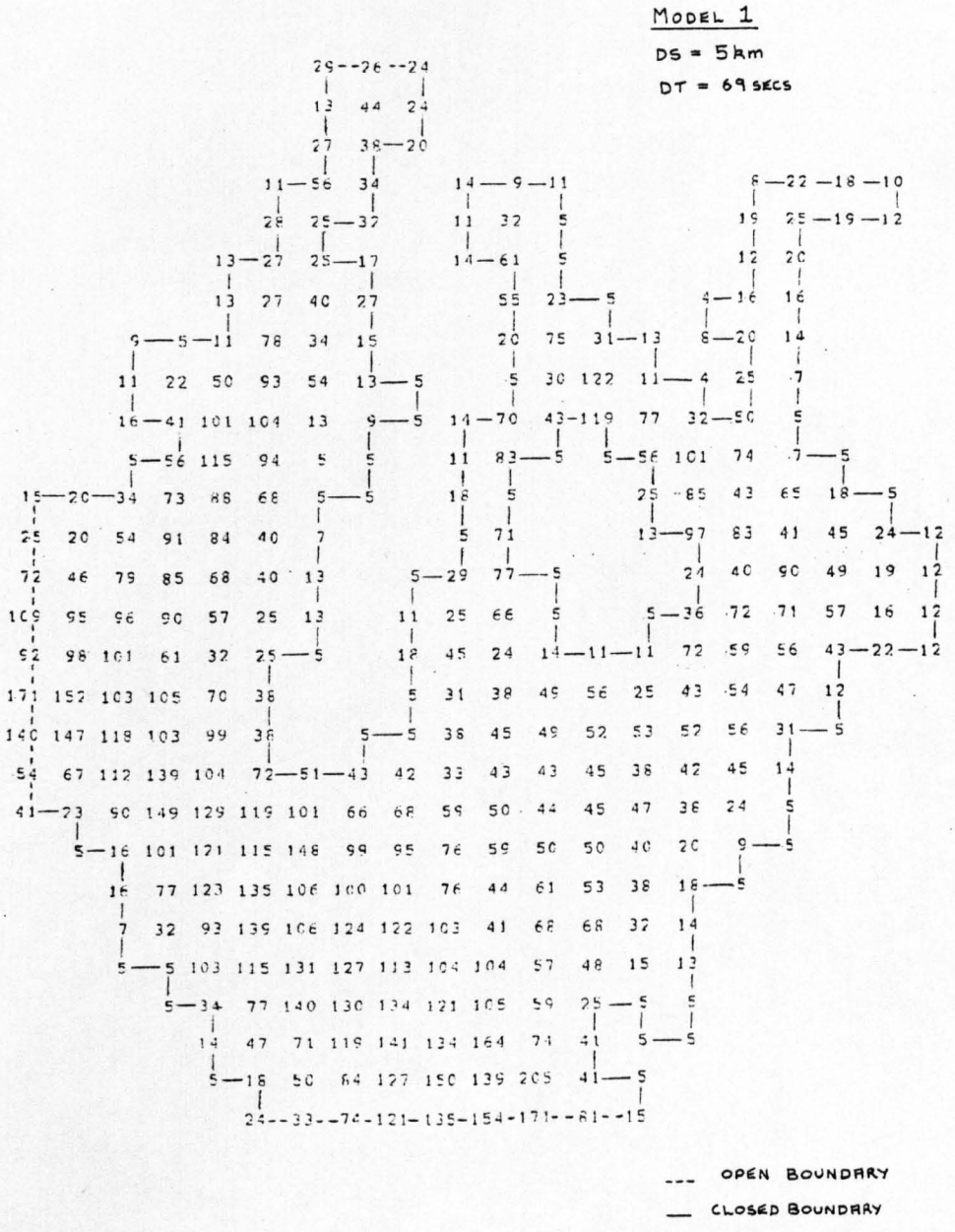

Figure 7.4

No significant change in elevation or phase in the North Channel has occurred on introducing the friction factor. This would be expected since the frictional stress is inversely proportional to depth and most depths in that region are in excess of 100 metres.

As a development from Test 2, the open sea boundary north of the Sound of Jura was represented in the scheme which constituted Test 3. The boundary conditions there were taken as the range and phase shown on Chart 5058 and the port of Crinan listed in Table 7.5 is indicative of these conditions. It has already been established in section 6.4 that the chart phases in the Sound of Jura are of doubtful accuracy however this test had been performed prior to the tidal survey. A comparison of co-range and co-phase lines from the chart with those from Test 3, shown in figure 7.6, indicate an improvement over the results from Test 2 although neither the chart data nor the simulation show the existence of an amphidromic point.

In the Firth of Clyde the computed ranges are in good agreement with the chart values although the computed phases are thirty minutes later than required at Greenock.

It was decided to specify the northern and western sea boundary conditions using data taken from the Tide Tables, to note its effect, if any, in producing the amphidromic point. At the same time, two boundary interpolation schemes, I.S.3 and I.S.1 were examined in Test 4 and Test 5 respectively. The previous three tests have used boundary interpolation scheme 2 and its effect has been discussed in section 7.3.2 together with the effect of I.S.1. Both Tests 4 and 5 produced a periodic solution in which the elevations and velocities were less than those from the Tide Tables. A comparison of the data in table 7.3 and the computations from table 7.6 verifies this feature. For example, in Test 4 the computed range and phase at Greenock are 1.51 metres and 0207 G.M.T., respectively while the corresponding Tide Table values are 3.08 metres and 0010 G.M.T. The computed values in Test 4 were obtained with a Chezy friction factor of $90 m^{\frac{1}{2}}/s$ and no significant improvement was noted in Test 5 on reducing the frictional stress by increasing the friction factor to $140 m^{\frac{1}{2}}/s$. It appears that interpolation schemes 3 and 1 are unsuitable when simulating tidal conditions in a complex configuration.

The next stage of development was to combine the boundary interpolation scheme of Test 3 with the sea boundary data of Test 4, to form Test 6. In this test the numerical scheme was based on 90° characteristics and for comparison Test 7 was performed using 45° characteristics. With a friction factor equal to $90m^{\frac{1}{2}}/s$ in both cases, the tests produced ranges and phases as shown in table 7.7. A comparison between both sets of results shows that the maximum difference in range is about 0.1 metres. In general both sets of results are very similar, probably because the numerical schemes are identical for an internal point with a configuration number equal to zero. The results from both these tests compare favourably with the Tide Table values shown in table 7.3, however the phases in Test 7, using the 45° characteristic scheme, are slightly superior to those from Test 6. For this reason and from similar deductions in section 4.4.2, the 45° characteristic scheme is the one used in further investigations.

In producing the results from Test 7 the optimisation of the interpolation and integration schemes and also the friction parameter has been achieved by performing Tests 1 to 7. It was not thought possible to further improve the results of Test 7 in the Firth of Clyde and the North Channel bearing in mind the gridsize and limitations of the boundary data. However it was felt that computations in the Sound of Jura could be improved by examining the remaining important determining factor, namely the northern and western sea boundary conditions. For this purpose Test 8 was performed.

In defining the boundary equations in Test 8 it is necessary to refer back to the results from the tidal survey which were presented in Chapter 6. The recorded spring ranges and phases were averaged and these results were in good agreement with the Tide Table values. From the records, the average spring tide elevations were plotted for Crinan, Port Ellen and Ballycastle Bay and from these curves it was concluded that the spring tides in the Sound of Jura are principally semi-diurnal It is possibly the shape of these curves which is the most interesting feature since each curve differs significantly from a cosine representation of equivalent range and phase. For each curve an harmonic composite cosine representation was derived and these functions were

used as sea boundary conditions in Test 8.

At the northern sea boundary, the Crinan curve defined by equation (6.2) was used to represent the variation in elevation. At Port Ellen and Ballycastle Bay the corresponding equations (6.1) and (6.3) for the tidal elevations represented conditions at the western sea boundary. The equations (6.1), (6.3) can be generalised in the form

$$\eta = \eta_{max}\left(A\cos\theta_1 + 2\cos\theta_2 + \cos\theta_3 \right)/\left(A+1\right) \qquad (7.1)$$

with $\theta_1 = \theta - \phi$

$\theta_2 = 3(\theta - \phi) - 180^\circ$

$\theta_3 = \theta - \phi - \Theta$

This equation was used to define the tidal elevation along the western sea boundary, using different values of A, the amplitude of the first component and Θ the phase of the third component, for each grid point. The values of these two parameters for the nine grid points are shown in table 7.2 and provided a transition from the tide curve at Ballycastle Bay to Port Ellen. At each grid point along this boundary the

	Ballycastle								Port Ellen
A	12	14	15	16	17	16	15	14	12
Θ	270	292	315	337	0	22	55	67	90

Table 7.2

range and phase was controlled to comply with the Tide Table data used in Test 5, whilst the important feature namely the shape of the tidal curve was retained. It was necessary in this respect to have the values of A as shown in the table. If A had taken the value of twelve throughout, the tidal curve would have had a double peak midway along the sea boundary. At the southern sea boundary the recorded tide showed that a single cosine representation of tidal elevation was adequate.

The average spring ranges and phases were computed in Test 8 using a Chezy friction coefficient of $90 m^{\frac{1}{2}}/s$ and these results are shown for coastal locations in table 7.8. These values are overall in good

agreement with the Tide Table figures shown in table 7.3. At Ayr and Troon the Tide Table ranges are 2.56 metres and 2.80 metres respectively, which is an appreciable difference considering their close proximity to one another. This distance is only two spacesteps and so localised influences on the tide may not be fully represented in the model. The computed ranges therefore at Ayr and Troon are 2.56 metres and 2.58 metres respectively.

From the results of Test 8, the co-range and co-phase lines are as shown in figure 7.7. These lines support the principles of tidal propagation in the Firth of Clyde and its approaches as discussed in section 7.3.1. The most important feature of these lines is the simulation of the amphidromic point situated west of the Kintyre Peninsula. In this region the computed ranges are less than 0.5 metres while the co-phase lines rotate anticlockwise from 6 hours to 12 hours. The model was unable to simulate the rotation of phases from 12 hours back to 6 hours and instead the phase progression appears as a 'phase jump' in which these phases occur as one phase line. This test was however the only one able to simulate the northward advance of the co-phase lines from 3.5 hours to 5 hours in the Sound of Jura. This effect is a consequence of specifying the composite cosine elevation curves at the northern and western sea boundaries.

As a comparison to the previous test, Test 9 was performed in which the sea boundary data was abstracted from the Tide Tables (1979). This test was very similar to Test 7 except the latter test used chart data at the southern sea boundary. For Test 9 the results are presented in table 7.9 for the coastal locations and were obtained with a Chezy friction factor of $70 m^{\frac{1}{2}}/s$. The co-range and co-phase lines are also presented as shown in figure 7.8 and the characteristics of an amphidromic point are in evidence. Indeed the simulation of this feature is comparable to that produced in Test 8 since the ranges are small and the variation of the co-phase lines is substantially in agreement with the theoretical variation.

Throughout the surface of the model the ranges, and to a lesser extent the phases, compare favourably with those from the Tide Tables. This indicates that the numerical scheme, the boundary equations (which use a single cosine constituent at each grid point) and the value of the

friction coefficient are satisfactory. It is therefore these equations and this approach that is used in simulating the tidal conditions during a surge event.

One of the features apparent in the simulations in previous tests was that the computed phases in the Firth of Clyde lagged the predicted phases by about thirty minutes. A method of reducing this lag was to simply increase the Chezy friction coefficient to $140 m^{\frac{1}{2}}/s$ which would also cause the ranges to increase. The ranges remained similar to those in Test 9 by replacing interpolation scheme 2 at the sea boundaries with interpolation scheme 1. Interpolation scheme 2 was retained at the closed boundaries. This arrangement, namely Test 10 succeeded in reducing the lag to about ten minutes and the results are shown in table 7.9. The results are close to those of the Tide Tables however the method of two different boundary interpolations was not pursued because the friction coefficient taken as $140 m^{\frac{1}{2}}/s$ was thought unrealistic. Concerning acceptable values, Dronkers (1964) has stated Chezy parameters ranging from 60 to 100 for typical estuaries. It is shown later, using Model 2 which has a finer grid, that the phase lag can be reduced.

In the Firth of Clyde, the phase difference between currents and elevations is almost that of a standing wave. By comparing the results of Tests 1 and 2 it was found that the effect of friction on the tidal oscillations was to delay the progression in the times of high water along the Clyde estuary, which is wedge shaped. It was also shown by comparing the results of Tests 1 and 2 that the frictional effect caused a reduction in range throughout the estuary, brought about by making high waters lower and low waters higher than they otherwise would be. To assess the effect of shallow water, which defines the waves to be of finite amplitude* in the Clyde estuary, the high and low waters from Test 8 were also included in table 7.8. These elevations show that the effect of decreasing depth (and hence celerity) along the estuary produce $|\text{high water}| > |\text{low water}|$ such that there is a rise in mean water level. On further analysis of the simulation, the ebb tide duration was found to be ten minutes longer than that of the flow tide. The effect is a result of the wave being finite, consequently the celerity of the flow tide is greater than that of the ebb tide, therefore high water occurs earlier and low water later than a wave

* SEE NOTE ON PAGE 130.

CLYDE SEA AREA AND ITS APPROACHES.

SPRING RANGES AND PHASES FROM ADMIRALTY TIDE TABLES 1979

Location	Grid Reference	MHWS	MLWS	Mean Spring Range	Mean Spring Phase
		m	m	m	Hrs Min (GMT)
Greenock	GR	3.44	0.36	3.08	0010
Wemyss Bay	WE	3.35	0.46	2.89	0005
Rothesay Bay	RO	3.44	0.36	3.08	0010
Millport	MI	3.41	0.49	2.92	0005
East Loch Tarbert	TA	3.41	0.33	3.08	0015
Loch Ranza	RA	3.01	0.36	2.65	1220
Brodick Bay	BR	3.23	0.40	2.83	0010
Ardrossan	AR	3.17	0.34	2.83	1215
Irvine	IR	3.14	0.37	2.77	1215
Troon	TR	3.20	0.40	2.80	1210
Ayr	AY	3.02	0.46	2.56	1210
Girvan	GI	3.11	0.43	2.68	1210
Campbeltown	CA	2.96	0.40	2.56	1215
Southend	SO	2.07	0.21	1.86	1215
Stranraer	ST	3.01	0.24	2.77	1215
Portpatrick	PO	3.78	0.34	3.44	1139
Larne	LA	2.80	0.43	2.37	1100
Red Bay	RE	1.55	0.18	1.37	1122
Ballycastle Bay	BA	1.25	0.25	1.00	0730
Port Ellen	PE	0.94	0.33	0.61	0515
Machrahanish	MA	-	-	0.48	0215
Gigha Sound	GS	1.52	0.61	0.91	0400
Craighouse	CR	1.16	0.31	0.85	0435
Crinan	C	2.13	0.30	1.83	0515

Table 7.3

CLYDE SEA AREA AND ITS APPROACHES.

SPRING RANGES AND PHASES FROM MODEL 1

Location	Grid Reference	Test 1		Test 2	
		Spring Range	Phase	Spring Range	Phase
		m	GMT	m	GMT
Greenock	GR	3.88	0006	3.16	0026
Wemyss Bay	WE	3.65	0000	3.00	0023
Rothesay Bay	RO	3.65	0008	2.99	0030
Millport	MI	3.54	0005	2.91	0015
East Loch Tarbert	TA	2.68	0102	2.34	0111
Loch Ranza	RA	2.83	0011	2.49	0021
Brodick Bay	BR	2.96	0012	2.52	0023
Ardrossan	AR	3.14	1218	2.67	0006
Irvine	IR	3.08	1220	2.64	0002
Troon	TR	3.11	1219	2.63	0002
Ayr	AY	3.08	1220	2.61	0004
Girvan	GI	2.72	1204	2.36	1136
Campbeltown	CA	2.85	1139	2.56	1154
Southend	SO	1.99	1123	1.96	1124
Stranraer	ST	2.57	1110	2.44	1108
Portpatrick	PO	3.20	1100	3.20	1100
Larne	LA	2.30	1100	2.30	1100
Red Bay	RE	1.51	1110	1.53	1123
Ballycastle Bay	BA	1.00	0730	1.00	0730
Port Ellen	PE	0.52	0800	0.52	0800
Machrahanish	MA	2.17	0845	1.23	0809
Gigha Sound	GS	2.18	0847	1.21	0818
Craighouse	CR	2.27	0835	1.26	0834
Crinan	C	2.08	1005	1.18	0936

Table 7.4

CLYDE SEA AREA AND ITS APPROACHES.

SPRING RANGES AND PHASES FROM MODEL 1

Location	Grid Reference	Test 3			
		MHWS	MLWS	Spring Range	MHWI
		m	m	m	GMT
Greenock	GR	1.69	-1.50	3.19	0028
Wemyss Bay	WE	1.59	-1.41	3.00	0025
Rothesay Bay	RO	1.59	-1.38	2.97	0031
Millport	MI	1.54	-1.35	2.89	0016
East Loch Tarbert	TA	1.22	-1.11	2.33	0111
Loch Ranza	RA	1.33	-1.18	2.51	0022
Brodick Bay	BR	1.36	-1.18	2.54	0022
Ardrossan	AR	1.42	-1.28	2.70	0006
Irvine	IR	1.40	-1.27	2.67	0002
Troon	TR	1.40	-1.26	2.66	0002
Ayr	AY	1.39	-1.25	2.64	0004
Girvan	GI	1.26	-1.11	2.37	1204
Campbeltown	CA	1.38	-1.20	2.58	1154
Southend	SO	1.08	-0.92	2.00	1123
Stranraer	ST	1.30	-1.18	2.48	1107
Portpatrick	PO	1.60	-1.60	3.20	1100
Larne	LA	1.15	-1.15	2.30	1100
Red Bay	RE	0.83	-0.73	1.56	1112
Ballycastle Bay	BA	0.50	-0.50	1.00	0730
Port Ellen	PE	0.26	-0.26	0.52	0800
Machrahanish	MA	0.42	-0.41	0.83	0800
Gigha Sound	GS	0.26	-0.24	0.50	0838
Craighouse	CR	0.41	-0.40	0.81	0907
Crinan	C	1.00	-1.00	2.00	0200

Table 7.5

CLYDE SEA AREA AND ITS APPROACHES.

SPRING RANGES AND PHASES FROM MODEL 1

Location	Grid Reference	Test 4		Test 5	
		Spring Range m	Phase GMT	Spring Range m	Phase GMT
Greenock	GR	1.51	0206	1.57	0220
Wemyss Bay	WE	1.53	0148	1.59	0200
Rothesay Bay	RO	1.56	0143	1.62	0155
Millport	MI	1.65	0108	1.73	0119
East Loch Tarbert	TA	1.57	0208	1.70	0216
Loch Ranza	RA	1.74	0101	1.86	0114
Brodick Bay	BR	1.77	0050	1.88	0100
Ardrossan	AR	1.86	0039	2.01	0046
Irvine	IR	1.91	0035	2.07	0039
Troon	TR	1.92	0037	2.10	0034
Ayr	AY	1.93	0034	2.07	0032
Girvan	GI	2.27	1204	2.28	1216
Campbeltown	CA	2.46	1204	2.42	0000
Southend	SO	1.97	1126	2.46	1139
Stranraer	ST	2.51	1141	1.99	1204
Portpatrick	PO	3.20	1126	3.44	1139
Larne	LA	2.30	1100	2.37	1100
Red Bay	RE	1.09	1146	1.45	1137
Ballycastle Bay	BA	1.00	0623	1.10	0730
Port Ellen	PE	0.52	0515	0.61	0530
Machrahanish	MA	0.87	0532	0.83	0642
Gigha Sound	GS	1.36	0438	0.69	0615
Craighouse	CR	1.10	0607	0.68	0620
Crinan	C	2.00	0515	2.00	0515

Table 7.6

CLYDE SEA AREA AND ITS APPROACHES.

SPRING RANGES AND PHASES FROM MODEL 1

Location	Grid Reference	Test 6		Test 7	
		Spring Range	Phase	Spring Range	Phase
		m	GMT	m	GMT
Greenock	GR	3.00	0058	3.05	0026
Wemyss Bay	WE	2.87	0058	2.99	0024
Rothesay Bay	RO	2.85	0103	2.91	0037
Millport	MI	2.79	0054	2.84	0025
East Loch Tarbert	TA	2.34	0148	2.45	0117
Loch Ranza	RA	2.38	0058	2.48	0039
Brodick Bay	BR	2.43	0059	2.55	0035
Ardrossan	AR	2.56	0041	2.66	0023
Irvine	IR	2.53	0038	2.63	0022
Troon	TR	2.53	0038	2.60	0017
Ayr	AY	2.51	0038	2.59	0017
Girvan	GI	2.26	0017	2.37	1220
Campbeltown	CA	2.47	0005	2.54	1222
Southend	SO	2.12	1146	2.02	1143
Stranraer	St	2.29	1152	2.26	1144
Portpatrick	PO	3.20	1126	3.20	1126
Larne	LA	2.30	1100	2.30	1100
Red Bay	RE	1.14	1140	1.09	1105
Ballycastle Bay	BA	1.00	0623	1.00	0623
Port Ellen	PE	0.52	0515	0.52	0515
Machrahanish	MA	1.13	0601	1.03	0634
Gigha Sound	GS	1.23	0515	1.19	0545
Craighouse	CR	0.89	0533	0.77	0556
Crinan	C	2.00	0515	2.00	0515

Table 7.7

CLYDE SEA AREA AND ITS APPROACHES.

SPRING RANGES AND PHASES FROM MODEL 1

Location	Grid Reference	Test 8			
		MHWS	MLWS	Spring Range	MHWI
		m	m	m	GMT
Greenock	GR	1.57	-1.46	3.03	0022
Wemyss Bay	WE	1.54	-1.44	2.98	0020
Rothesay Bay	RO	1.49	-1.40	2.89	0034
Millport	MI	1.46	-1.37	2.83	0022
East Loch Tarbert	TA	1.26	-1.17	2.43	0114
Loch Ranza	RA	1.27	-1.20	2.47	0037
Brodick Bay	BR	1.30	-1.23	2.53	0033
Ardrossan	AR	1.35	-1.29	2.64	0020
Irvine	IR	1.33	-1.27	2.60	0019
Troon	TR	1.32	-1.26	2.58	0014
Ayr	AY	1.31	-1.25	2.56	0015
Girvan	GI	1.21	-1.14	2.35	1219
Campbeltown	CA	1.29	-1.24	2.53	1220
Southend	SO	1.05	-1.00	2.05	1134
Stranraer	ST	1.14	-1.09	2.23	1135
Portpatrick	PO	1.60	-1.60	3.20	1126
Larne	LA	1.15	-1.15	2.30	1100
Red Bay	RE	0.46	-0.35	0.81	1026
Ballycastle Bay	BA	0.55	-0.55	1.10	0730
Port Ellen	PE	0.26	-0.26	0.52	0500
Machrahanish	MA	0.28	-0.18	0.46	0547
Gigha Sound	GS	0.79	-0.65	1.44	0428
Craighouse	CR	0.50	-0.34	0.84	0537
Crinan	C	1.00	-1.00	2.00	0530

Table 7.8

CLYDE SEA AREA AND ITS APPROACHES.

SPRING RANGES AND PHASES FROM MODEL 1

Location	Grid Reference	Test 9		Test 10	
		Spring Range	Phase	Spring Range	Phase
		m	GMT	m	GMT
Greenock	GR	3.10	0047	3.10	0013
Wemyss Bay	WE	3.04	0044	3.04	0011
Rothesay Bay	RO	2.96	0055	2.95	0024
Millport	MI	2.89	0041	2.88	0011
East Loch Tarbert	TA	2.64	0129	2.53	0104
Loch Ranza	RA	2.57	0053	2.45	0029
Brodick Bay	BR	2.61	0048	2.54	0025
Ardrossan	AR	2.73	0035	2.66	0012
Irvine	IR	2.69	0034	2.61	0011
Troon	TR	2.65	0029	2.59	0000
Ayr	AY	2.64	0029	2.57	0000
Girvan	GI	2.45	0006	2.46	1214
Campbeltown	CA	2.58	0006	2.44	1208
Southend	SO	1.83	1149	1.64	1136
Stranraer	ST	2.39	1155	2.36	1148
Portpatrick	PO	3.44	1139	3.44	1139
Larne	LA	2.37	1100	2.37	1100
Red Bay	RE	1.06	1114	1.07	1016
Ballycastle Bay	BA	1.10	0730	1.10	0730
Port Ellen	PE	0.61	0530	0.61	0530
Machrahanish	MA	1.02	0630	1.24	0655
Gigha Sound	GS	1.16	0559	1.44	0616
Craighouse	CR	0.63	0626	0.64	0640
Crinan	C	2.00	0515	2.00	0515

Table 7.9

The mean spring tide co-range and co-phase lines in the Clyde sea area computed by Model 1. (See also Table 7.1)

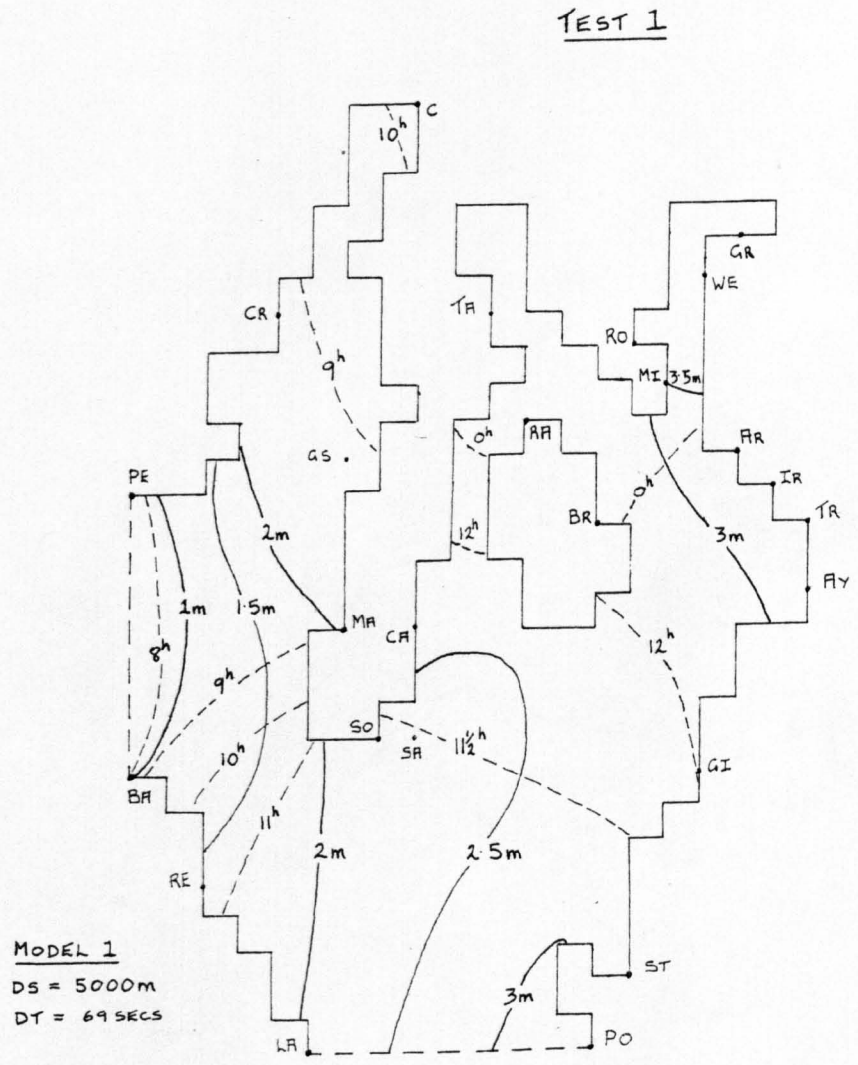

Figure 7.5

The mean spring tide co-range and co-phase lines in the Clyde sea area computed by Model 1. (See also Table 7.1)

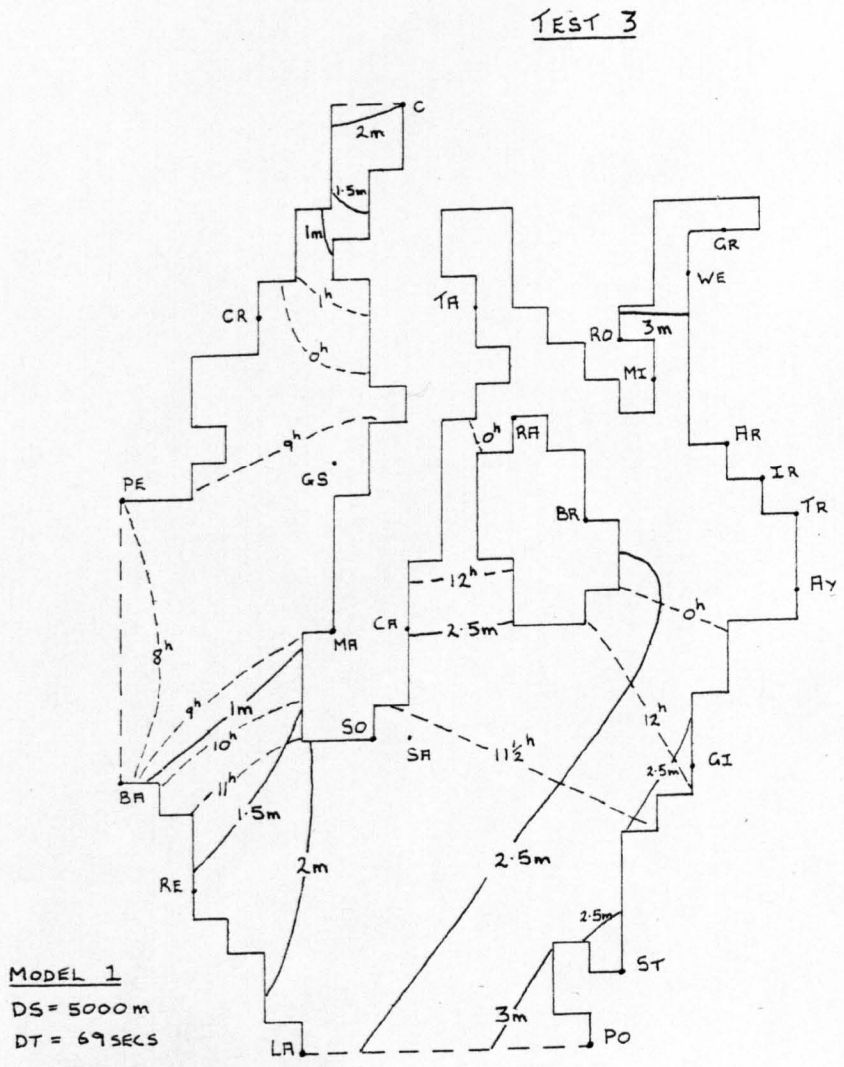

Figure 7.6

The mean spring tide co-range and co-phase lines in the Clyde sea area computed by Model 1 using the survey data as input.

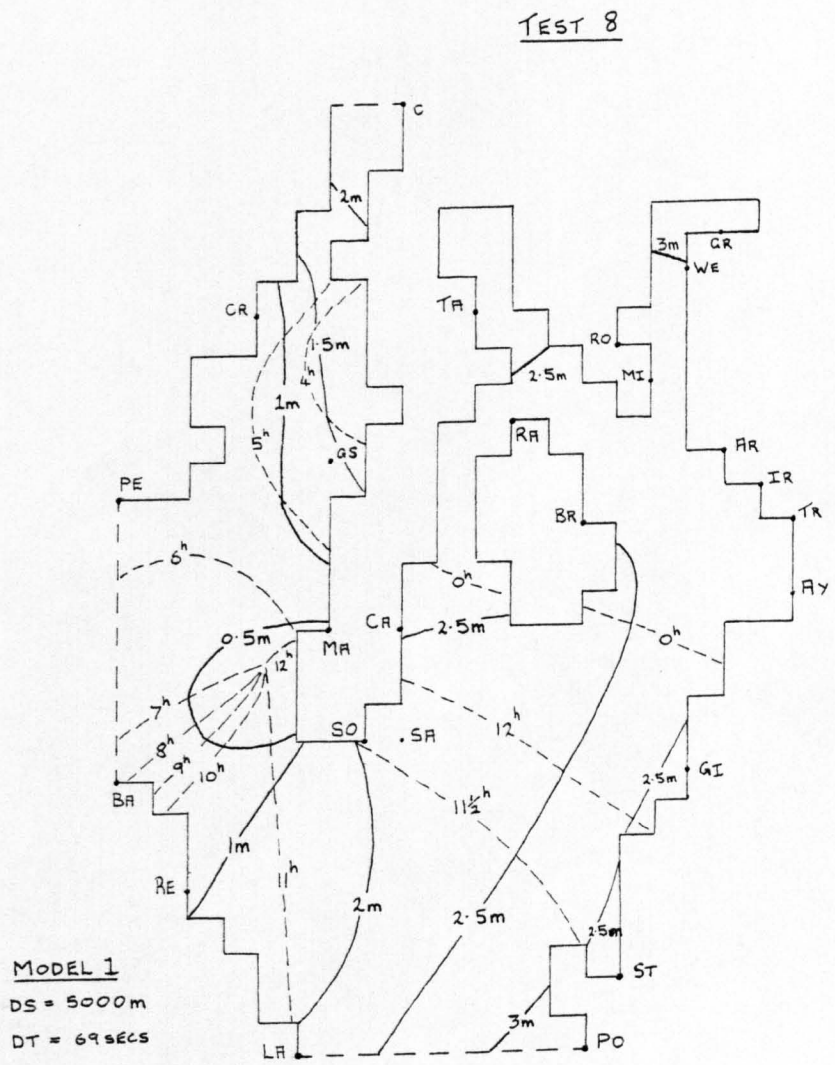

Figure 7.7

The mean spring tide co-range and co-phase lines in the Clyde sea area computed by Model 1 using the Tide Table (1979) data as input.

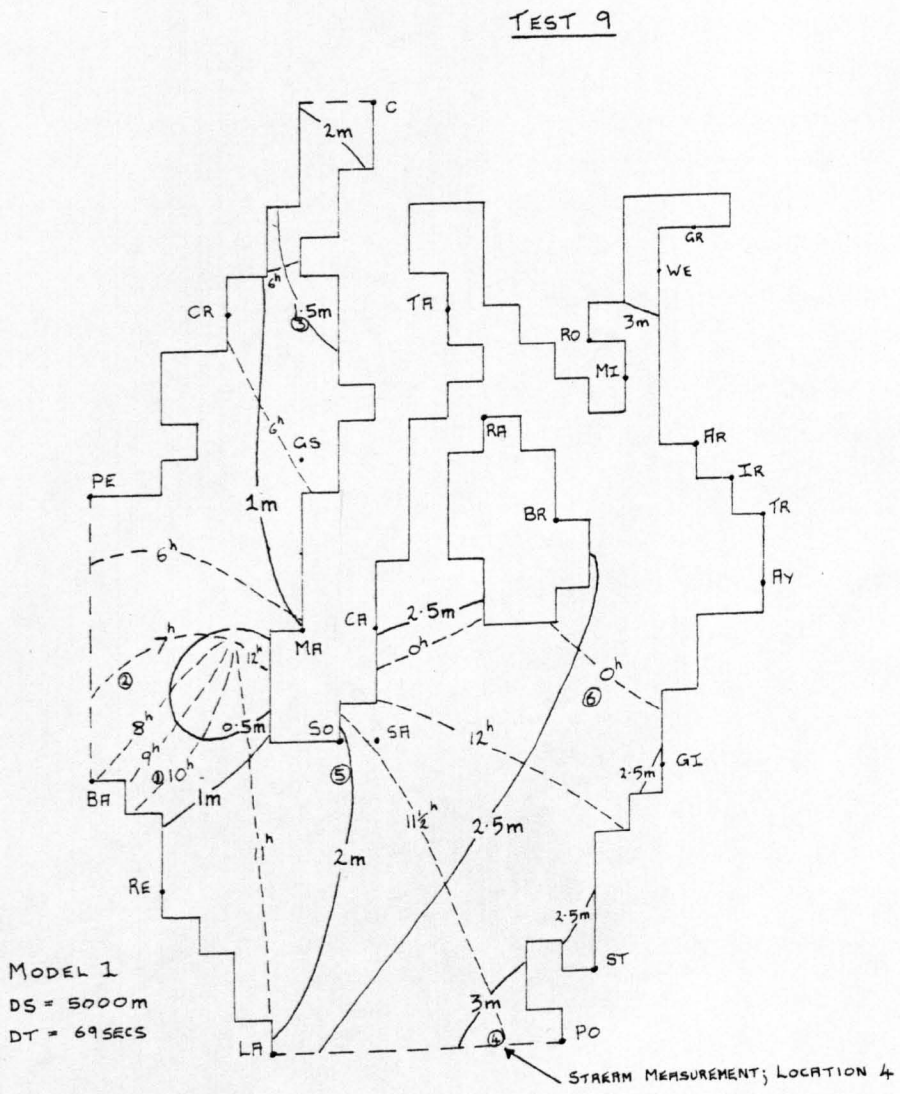

Figure 7.8

travelling at a constant rate. Note that this feature is characteristic of progressive wave motion where the flow is in phase with its elevation and so does not apply to a standing wave. The ten minute difference in ebb and flow tides in the Clyde estuary therefore indicates that the tidal oscillations are not totally in a standing mode.

To represent the stream flow in the Firth of Clyde and its approaches, six offshore locations were selected and are as indicated in figure 7.8. Points 1, 2, 4 and 5 are situated in the North Channel while point 3 is located in the Sound of Jura and point 6 is in the Firth of Clyde. At these points a comparison has been made between the computed depth averaged velocities obtained from Test 9 and the observed streams taken from the Admiralty Tidal Stream Atlas (1974). The comparison is presented in tables 7.10 and 7.11. In both tables the computed direction and the direction of the Atlas streams,measured as a whole circle bearing, are also provided for comparison. The Atlas streams are listed at hourly intervals preceding and following the time of high water at Dover which is 1100 G.M.T. These times were converted to times relative to Greenwich which accounts for the unusual time sequences used in the tables.

With reference to both tables it is evident that for the four locations situated in the North Channel, the Atlas streams are significantly larger than the computed ones. A similar feature is apparent for position 3 in the Sound of Jura. A possible explanation of the differences in magnitude is that the recorded streams in these deep waters were not measured at sufficient depth and so are not comparable in magnitude to the computed depth average velocities. It is interesting to note that at position 6 in the relatively shallower Firth of Clyde the computed and measured velocities in close agreement.

From the computed velocities shown in tables 7.10 and 7.11 the tidal ellipses at each point have been drawn and are shown in figure 7.9. Since the numerical solution is periodic, there is no net or residual drift and the velocities produce closed ellipses. It is also noted that the circulation is clockwise at points 3 and 6 and anticlockwise for the other four points. It has been shown by Defant (1961), that most current ellipses have a clockwise rotation however he has made it clear that when an amphidromic point is present with an

COMPARISON OF TIDAL ATLAS STREAMS WITH TEST 9 FOR SPRING TIDES

Time G.M.T.	Position 1				Position 2				Position 3			
	Atlas Stream		Computed Stream		Atlas Stream		Computed Stream		Atlas Stream		Computed Stream	
	Rate	Direction	Rate	Direction	Rate	Direction	Rate	Direction	Rate	Direction	Rate	Direction
	m/s	Deg	m/s	Deg	m/s	Deg	m/s	Deg	m/s	Deg	m/s	Deg
½	2.22	315	0.70	322	1.24	295	0.52	294	0.88	19	0.46	8
1½	2.38	312	0.59	322	1.45	293	0.44	288	0.93	19	0.32	9
2½	2.01	313	0.33	321	1.34	293	0.25	276	0.67	18	0.10	11
3½	1.14	316	0.01	210	0.98	295	0.09	197	0.67	18	0.11	175
4½	0.21	146	0.35	144	0.41	285	0.27	131	0.15	16	0.35	187
5	0.67	132	0.49	143	0.10	108	0.37	124	0.10	200	0.46	187
6	1.86	138	0.69	142	0.62	128	0.51	116	0.05	188	0.53	188
7	2.32	136	0.71	141	1.24	124	0.53	111	0.67	200	0.46	190
8	2.22	131	0.56	141	1.39	117	0.42	105	0.88	200	0.28	269
9	1.70	129	0.27	141	1.24	126	0.22	91	0.72	198	0.05	320
10	0.77	141	0.09	324	0.83	116	0.11	347	0.31	200	0.23	6
11	0.41	299	0.42	323	0.20	127	0.32	306	0.10	16	0.43	7
12	1.50	308	0.64	322	0.57	299	0.49	298	0.46	19	0.49	8

Table 7.10

COMPARISON OF TIDAL STREAM ATLAS WITH TEST 9 FOR SPRING TIDES

Time G.M.T.	Position 4				Position 5				Position 6			
	Atlas Stream		Computed Stream		Atlas Stream		Computed Stream		Atlas Stream		Computed Stream	
	Rate	Direction	Rate	Direction	Rate	Direction	Rate	Direction	Rate	Direction	Rate	Direction
	m/s	Deg	m/s	Deg	m/s	Deg	m/s	Deg	m/s	Deg	m/s	Deg
½	1.02	330	0.48	345	1.23	259	0.67	292	0.20	213	0.06	195
1½	1.18	338	0.32	342	1.70	246	0.59	285	0.31	229	0.20	215
2½	0.93	339	0.09	329	1.60	245	0.37	252	0.20	221	0.29	219
3½	0.67	335	0.17	175	1.13	247	0.15	213	0.26	228	0.32	221
4½	0.26	350	0.40	170	0.41	244	0.34	109	0.20	221	0.27	223
5	0.21	154	0.48	169	0.15	182	0.47	145	0.15	212	0.22	224
6	0.51	157	0.56	167	1.02	77	0.66	117	0.15	22	0.09	233
7	0.97	147	0.49	166	1.70	78	0.70	111	0.15	36	0.15	23
8	1.13	160	0.30	163	1.74	87	0.57	103	0.10	25	0.22	35
9	0.93	156	0.04	130	1.54	75	0.33	87	0.15	28	0.32	39
10	0.72	162	0.23	352	0.67	72	0.16	6	0.20	33	0.32	42
11	0.21	156	0.43	348	0.10	62	0.37	311	0.20	42	0.24	45
12	0.51	337	0.52	347	0.72	254	0.61	299	0.10	15	0.10	55

Table 7.11

Computed tidal stream ellipses (from test 9) for six locations in the Clyde sea area. (See figure 7.8 for locations)

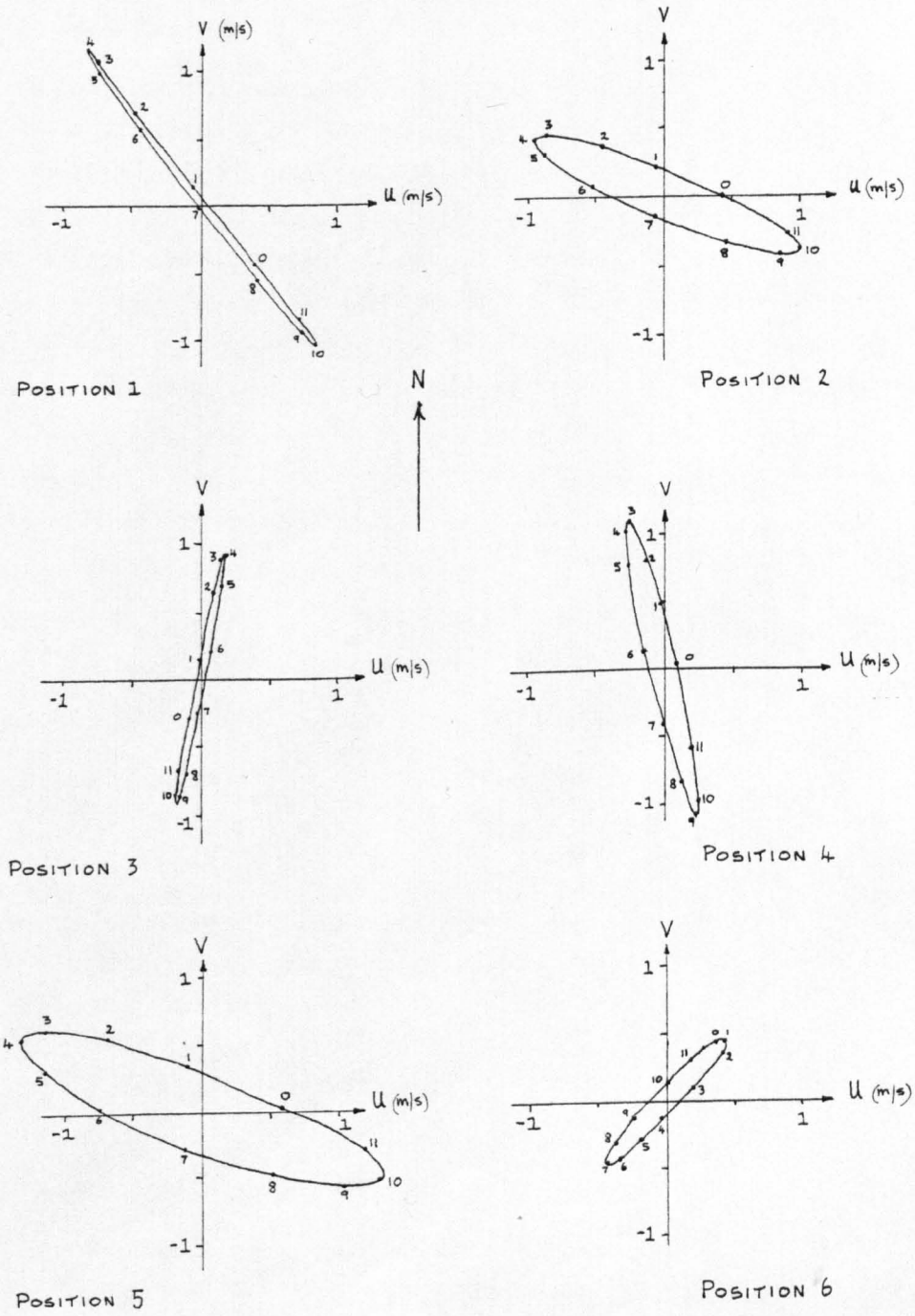

Figure 7.9

anticlockwise rotation of the co-phase lines then the current ellipses in that vicinity also rotate anticlockwise. A comparison of ellipses with those drawn from the Atlas streams cannot be made because the resolution of the streams in the Atlas was thought not to be good enough for this purpose.

A more complete but less numerical comparison of the computed and the Atlas streams is provided in figures 7.10 to 7.13. Each flow diagram indicates the stream flow and direction over the entire sea area covered by Model 1. The length of each arrow is proportional to the magnitude of the stream centred at the position of the arrow head. The comparison of computed and recorded flows can be made at corresponding times relative to G.M.T., and the set of diagrams represent the stream history over one tidal period. An assessment of the computed velocities through a comparison with the Atlas streams with flow direction as the main factor can be simplified by noting the computed and recorded times of flow tide as shown in table 7.12.

Location	Times of Flow Tide (G.M.T)	
	Computed	Recorded
	Hrs	Hrs
Northern Sea Boundary (Sound of Jura)	3.2 to 9.0	4.8 to 10.6
Western Sea Boundary	3.6 to 9.8	4.7 to 11
Southern Sea Boundary (North Channel)	3.0 to 9.1	4.5 to 10.8
Firth of Clyde	6.2 to 0.0	6.0 to 0.0

Table 7.12

At both the northern and western sea boundaries a substantial part of the duration of the flow tide is accompanied by a reduction in elevation from high to low water as flow enters the North Channel. At the same time namely 4.5 to 10.8 hours, the flow tide enters the Irish Sea from the North Channel by passing through the southern sea boundary

during which low water there is increasing to high water level. Therefore during the flow tide passing through the North Channel the average elevations along the western and southern sea boundaries are in opposite phase with one another. This situation is represented in figure 7.14 which shows the stream flow phase relationships and also the high and low water phases at each sea boundary. Not only are the flows in phase at each boundary and the elevations in opposite phase but also the times of high and low water at each sea boundary occur very close to the times of slack water. These points suggest that the state of motion is akin to a seiche action of half a wavelength occurring between the northern and western sea boundary at the one end and the southern sea boundary at the other. The motion is not precisely a standing wave since it is shown in figure 7.14 that the slack waters precede the times of high and low water by about half an hour at the southern sea boundary and by an average of one and a half hours at the western sea boundary. By comparison the computed slack waters at the western and southern sea boundaries precede the recorded slack waters by about one hour and one and a half hours respectively. These figures can be deduced from the flow times shown in table 7.12 and are representative of all locations in the Sound of Jura and the North Channel. This disagreement between the computed and recorded variables represented one rather unsatisfactory aspect of this model. Despite numerous tests with different boundary data and Chezy friction coefficient the disagreement remained. A test in which the velocities were specified at the sea boundaries and the elevations calculated throughout merely produced elevations unrepresentative of the area although the velocity phase was improved. Although the source of this discrepancy remained undiscovered computed velocities showed agreement in magnitude and phase with the Atlas streams in the Firth of Clyde.

The comments in the previous paragraph regarding the computed and recorded flow tide phase are equally applicable to the ebb tide, bearing in mind that the flow direction is reversed, which is apparent in figures 7.10 to 7.14. A point previously remarked upon is evident in the Atlas streams and to a lesser extent the computed velocities and is that the ebb and flow tides in the Firth of Clyde occur via the western and northern sea boundaries and not through the southern

Figure 7.10

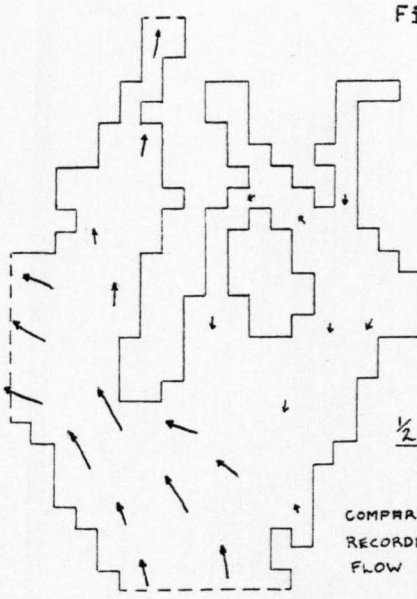

½ h G.M.T

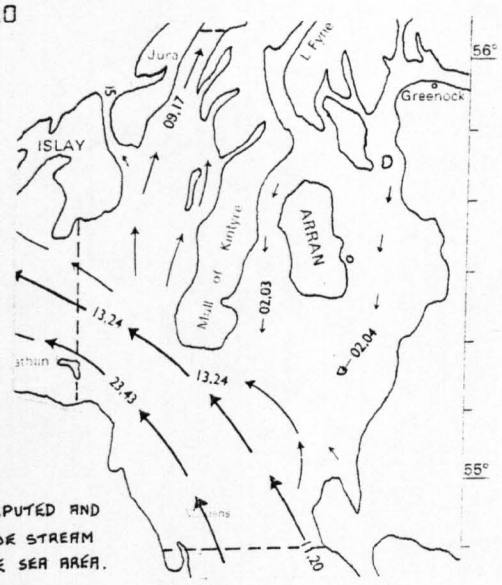

COMPARISON OF COMPUTED AND RECORDED SPRING TIDE STREAM FLOW IN THE CLYDE SEA AREA.

COMPUTED FLOW SCALE 10mm : 1m/s
ADMIRALTY FLOWS IN KNOTS

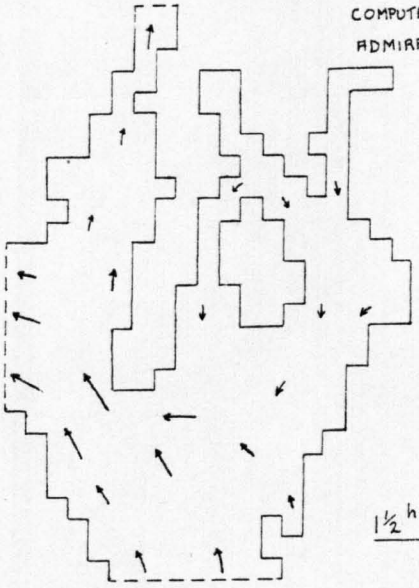

1½ h G.M.T

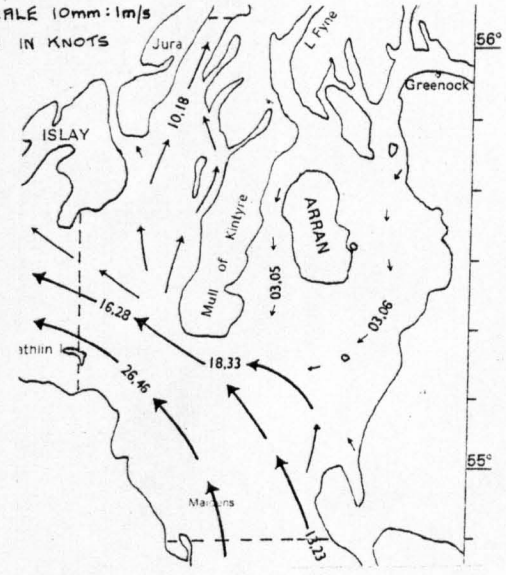

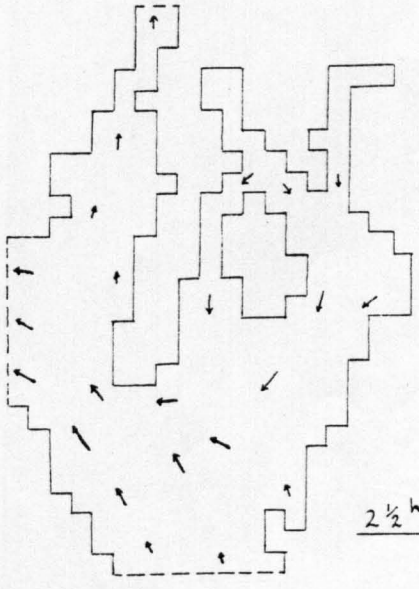

2½ h G.M.T

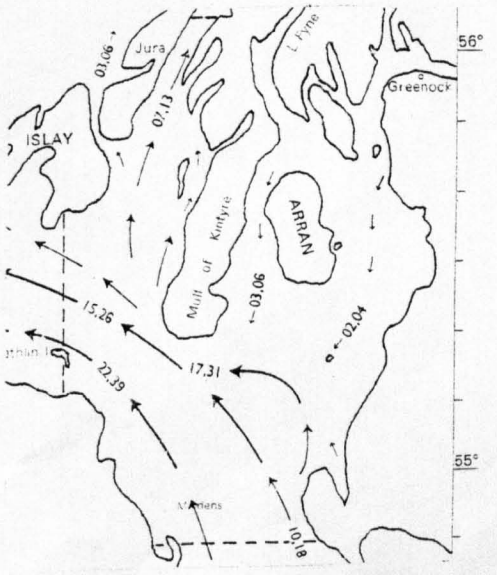

Figure 7.11

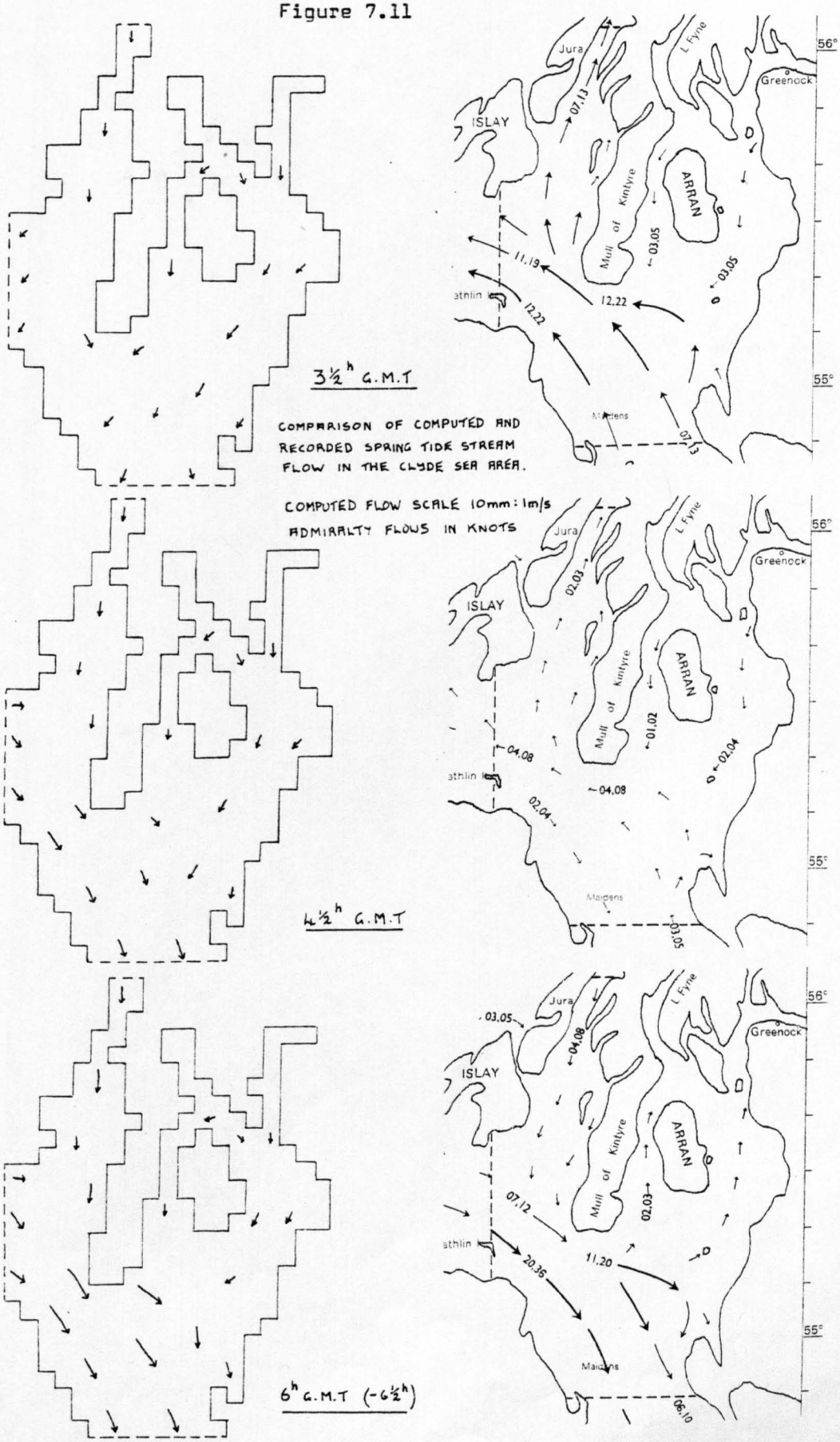

COMPARISON OF COMPUTED AND RECORDED SPRING TIDE STREAM FLOW IN THE CLYDE SEA AREA.

COMPUTED FLOW SCALE 10mm : 1m/s

ADMIRALTY FLOWS IN KNOTS

Figure 7.12

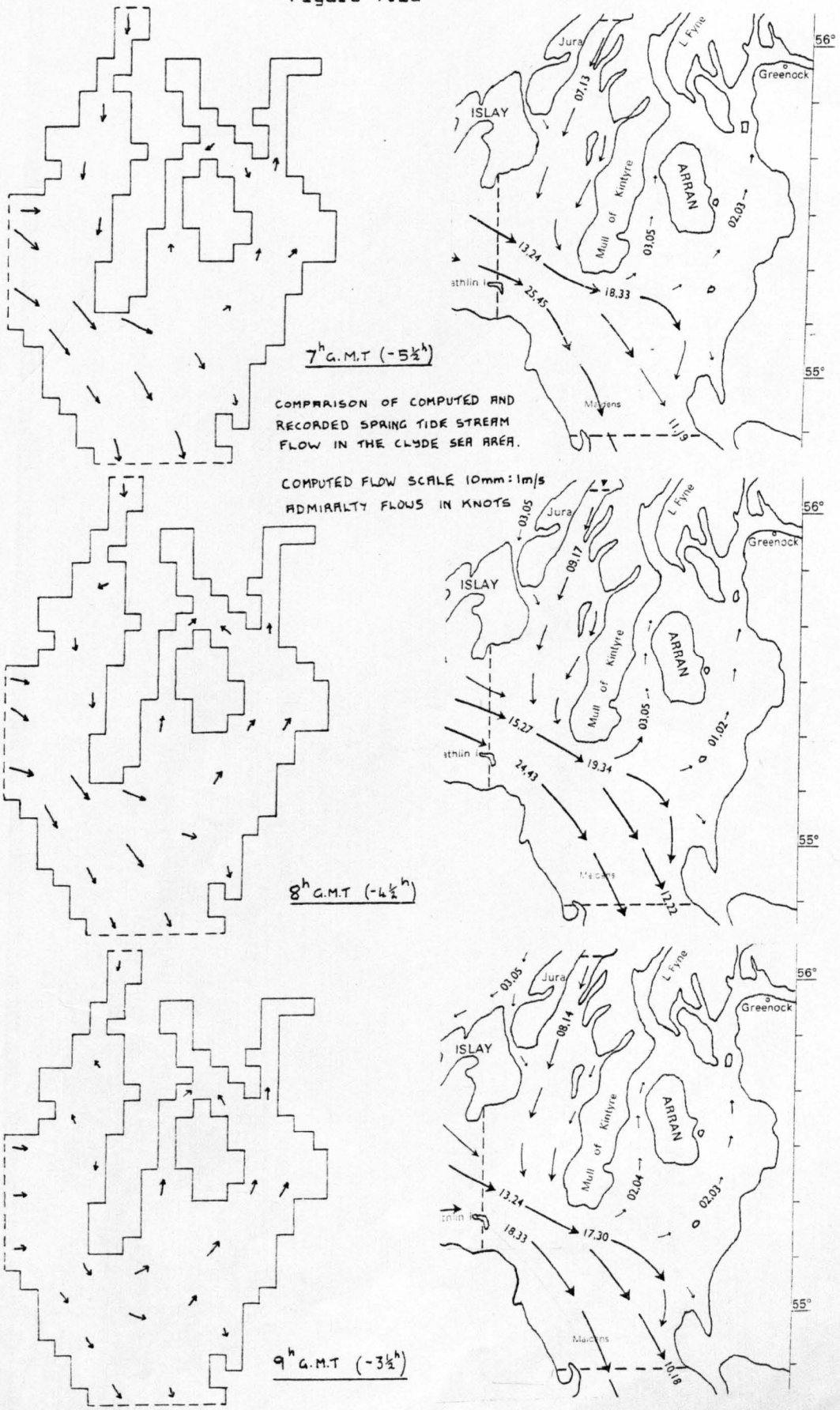
7h G.M.T (-5½h)
8h G.M.T (-4½h)
9h G.M.T (-3½h)
COMPARISON OF COMPUTED AND RECORDED SPRING TIDE STREAM FLOW IN THE CLYDE SEA AREA.
COMPUTED FLOW SCALE 10mm : 1m/s
ADMIRALTY FLOWS IN KNOTS
Jura
ISLAY
L Fyne
Greenock
ARRAN
Mull of Kintyre
56°
55°
07.13
13.24
25.45
18.33
01.05
02.03
11.19
03.05
08.17
15.27
19.34
24.43
01.02
12.22
03.05
08.14
13.24
18.33
17.30
02.04
02.03
10.18

Figure 7.13

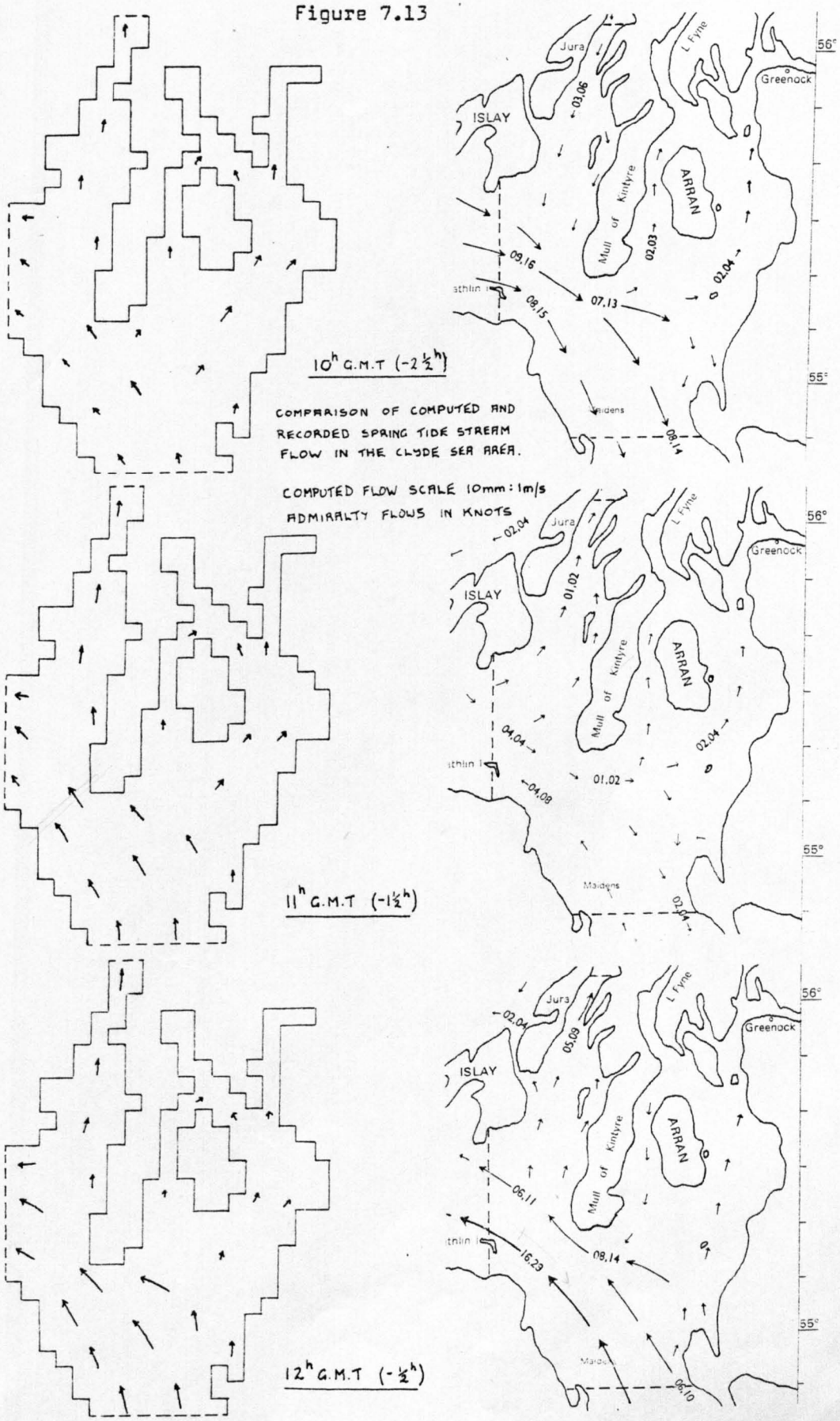
10h G.M.T (-2½h)
11h G.M.T (-1½h)
12h G.M.T (-½h)
COMPARISON OF COMPUTED AND RECORDED SPRING TIDE STREAM FLOW IN THE CLYDE SEA AREA.
COMPUTED FLOW SCALE 10mm : 1m/s
ADMIRALTY FLOWS IN KNOTS
Jura
L Fyne
Greenock
ISLAY
ARRAN
Mull of Kintyre
Maidens
56°
55°
03.06
09.16
08.15
07.13
02.03
02.04
08.14
02.04
01.02
04.04
04.08
01.02
02.04
02.04
05.09
06.11
08.14
16.23
04.10

The Tidal Atlas spring tide streams at two points on the western and southern sea boundaries during one tidal cycle.

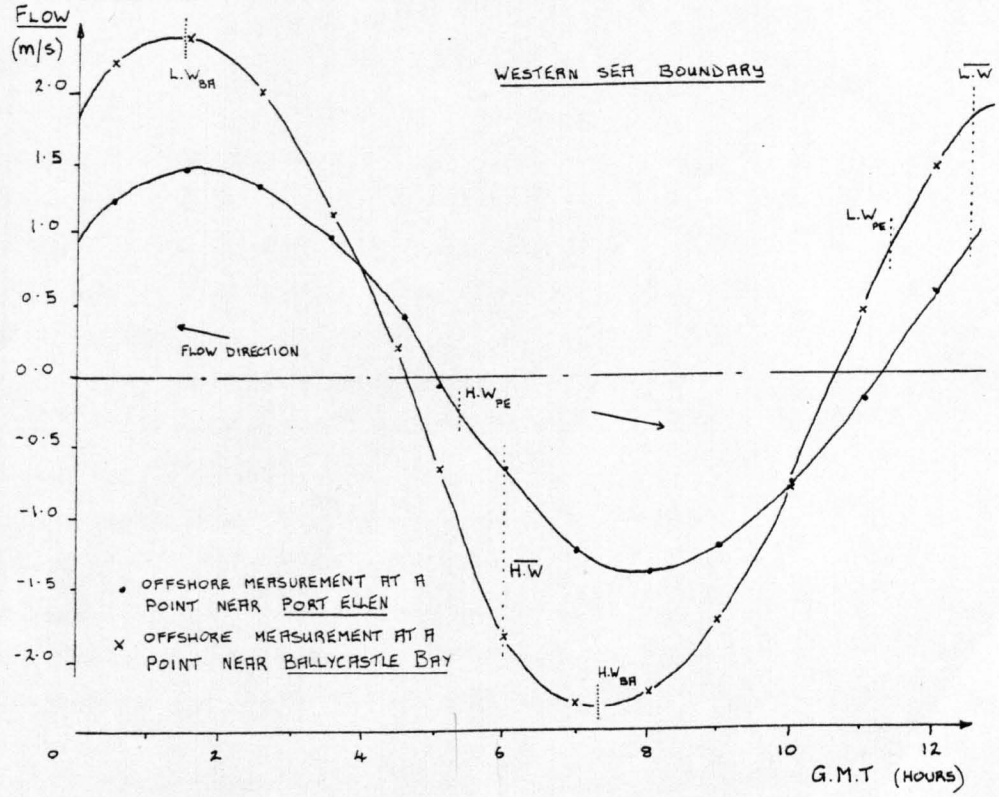

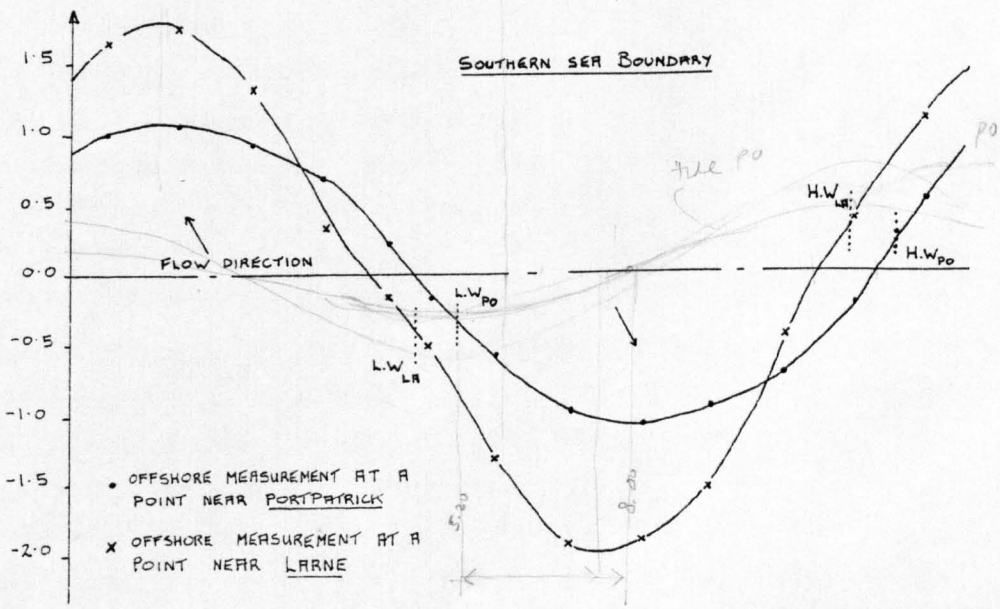

Figure 7.14

sea boundary. The former boundaries therefore provide a communication with the tides in the Atlantic Ocean.

The application of Model 1 to the mean neap tide situation proved interesting since the simulation of the amphidromic point was again in evidence. This test was performed in a similar manner as Test 9 since the sea boundary data was again based on Tide Table information and the boundary equations and the friction coefficient are unchanged. In fact the computations of elevation although smaller than those of Test 9 form a similar pattern of co-range lines as do the co-phase lines. A comparison of the computations with the Tide Table values at coastal locations is shown in table 7.13 and the co-tidal lines are presented in figure 7.15. The phase relationships between the elevations at the sea boundaries are also similar to those of Test 9 in that the phase at the northern sea boundary is the same as the average phase across the western sea boundary and both phases are in opposite phase with the southern sea boundary. This test namely Test 11 also produced a flow phase that was earlier than indicated in the stream Atlas, a problem that was noted in Test 9.

7.3.4 Simulation of the Mean Spring Tide using Model 2

In order to determine whether the computed flow phase in Test 9 was in some way related to the spacestep, or timestep, another model of the same area was constructed. This model namely Model 2 was developed with a spacestep of 3 km and a timestep of 46 seconds which represented a finer grid than that of Model 1. Its application required over four times as much computer time as that for Model 1, namely 650 seconds on the I.C.L. 2980 to complete one tidal cycle.

Although Model 1 was more suitable in terms of running time on the computer, it was thought that in some areas represented by this model the grid size was too large to represent the variation in the changing coastline with sufficient accuracy. In particular the schematisation representing the upper reaches of the Firth of Clyde namely Loch Fyne and the Clyde estuary required improvement. In this respect the grid used in Model 2 satisfied this requirement and its schematisation can be appreciated in figure 7.16.

The performance of Model 2 was evaluated using the sea boundary

data and the numerical scheme of Test 9 to simulate the mean spring tide. However to produce spring tide elevations comparable with those from the Tide Tables a Chezy friction factor $35 m^{\frac{1}{2}}/s$ was used. This factor is quite low and was necessary because in this model the time-step is closer to its maximum timestep than it was in Model 1. The fact that the friction factor is determined from the spacestep and timestep of the model supports the point already mentioned that this factor has a numerical implication and unfortunately is not solely a physical coefficient.

From the test, the ranges and phases at all the coastal locations are compared with the corresponding Tide Table values in table 7.14. On this basis the computed ranges are in good agreement while the phases in the Firth of Clyde are an improvement on those in Test 9. However the co-tidal lines shown in figure 7.16 do not show any improvement in the co-phase lines near the amphidromic point. More importantly though, the phase of the tidal streams was found to be identical to those produced in Model 1 therefore the effect of changing the schematisation has not influenced the calculation of the stream velocities. The cause of the computed flow phase being earlier than the Atlas flows is certainly not a result of poor schematisation of either model in the North Channel. Since the advantages of Model 2 such as the improvement of the times of high water in the Firth of Clyde, were outweighed by its requirements of computer time, the model was not used in this form for the simulation of storm surges.

7.4 TIDES IN THE FIRTH OF CLYDE

It is important to prove conclusively that the numerical scheme of Models 1 and 2 can accurately represent the physical process of tidal oscillation in a real situation. Models 1 and 2 have represented conditions in the Firth of Clyde quite accurately but their performance with the velocity phase in the North Channel was not so impressive. Not only must the tidal elevation and its associated phase be accurately simulated but also the stream flows and their related phases. For these reasons the tides in the Firth of Clyde were simulated but also from a practical viewpoint because the area is well represented in the Tide Tables.

CLYDE SEA AREA AND ITS APPROACHES.

NEAP RANGES AND PHASES FROM ADMIRALTY TIDE TABLES 1979 AND MODEL 1

Location	Grid Reference	Tide Tables		Test 11	
		MSR	MHWI	MSR	MHWI
		m	Hrs (GMT)	m	Hrs (GMT)
Greenock	GR	1.89	0600	2.15	0711
Wemyss Bay	WE	1.80	0555	2.11	0707
Rothesay Bay	RO	1.89	0539	2.05	0720
Millport	MI	1.83	0535	2.01	0708
East Loch Tarbert	TA	1.80	0605	1.73	0758
Loch Ranza	RA	1.67	0555	1.75	0720
Brodick Bay	BR	1.71	0600	1.80	0717
Ardrossan	AR	1.77	0540	1.89	0701
Irvine	IR	1.64	0540	1.86	0702
Troon	TR	1.71	0535	1.84	0657
Ayr	AY	1.49	0535	1.83	0657
Girvan	GI	1.71	0520	1.69	0635
Campbeltown	CA	1.61	0518	1.72	0636
Southend	SO	1.22	0520	1.50	0546
Stranraer	ST	1.92	0540	1.72	0601
Portpatrick	PO	2.10	0539	2.10	0539
Larne	LA	1.72	0514	1.72	0514
Red Bay	RE	1.22	0450	0.86	0559
Ballycastle Bay	BA	0.40	0329	0.40	0329
Port Ellen	PE	0.33	0655	0.33	0655
Machrahanish	MA	0.49	0705	0.45	0642
Gigha Sound	GS	0.58	0735	0.24	0740
Craighouse	CR	0.49	0755	0.37	0707
Crinan	C	0.61	1115	0.61	1115

Table 7.13

The mean neap tide co-range and co-phase lines in the Clyde sea area computed by Model 1.

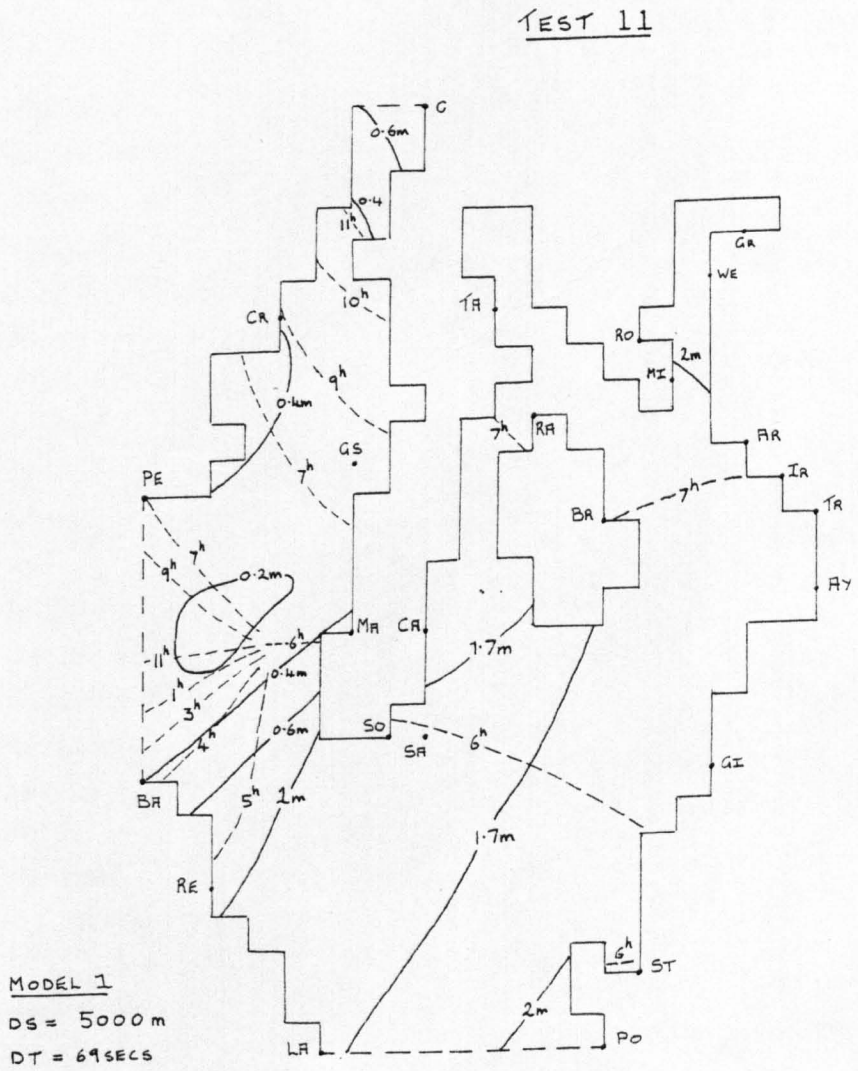

Figure 7.15

CLYDE SEA AREA AND ITS APPROACHES.

SPRING RANGES AND PHASES FROM MODEL 2

Location	Grid Reference	Tide Tables		Test 12	
		SR	MHWI	SR	MHWI
		m	Hrs	m	Hrs
Greenock	GR	3.08	0010	3.16	0027
Wemyss Bay	WE	2.98	0005	3.02	0019
Rothesay Bay	RO	3.08	0010	2.97	0016
Millport	MI	2.92	0005	2.92	0013
East Loch Tarbert	TA	3.08	0015	2.72	0052
Loch Ranza	RA	2.65	1220	2.76	0022
Brodick Bay	BR	2.83	0010	2.81	0013
Ardrossan	AR	2.83	1215	2.84	0007
Irvine	IR	2.77	1215	2.84	1225
Troon	TR	2.80	1210	2.83	1225
Ayr	AY	2.56	1210	2.82	0002
Girvan	GI	2.68	1210	2.69	1204
Campbeltown	CA	2.56	1215	2.67	1220
Southend	SO	1.86	1215	2.19	1152
Stranraer	ST	2.77	1215	2.69	1149
Portpatrick	PO	3.44	1139	3.44	1139
Larne	LA	2.37	1100	2.30	1100
Red Bay	RE	1.37	1122	1.52	1130
Ballycastle Bay	BA	1.00	0730	1.10	0730
Port Ellen	PE	0.61	0515	0.52	0515
Machrahanish	MA	0.48	0215	0.78	0625
Gigha Sound	GS	0.91	0400	0.78	0646
Craighouse	CR	0.85	0435	0.94	0550
Crinan	C	1.83	0515	2.00	0515

Table 7.14

Figure 7.16

MEAN SPRING TIDE

CO-RANGE AND CO-PHASE LINES FROM TEST 12.

MODEL 2 : SCHEMATISATION OF THE CLYDE SEA AREA AND APPROACHES

DS = 3000m , DT = 46 SECS

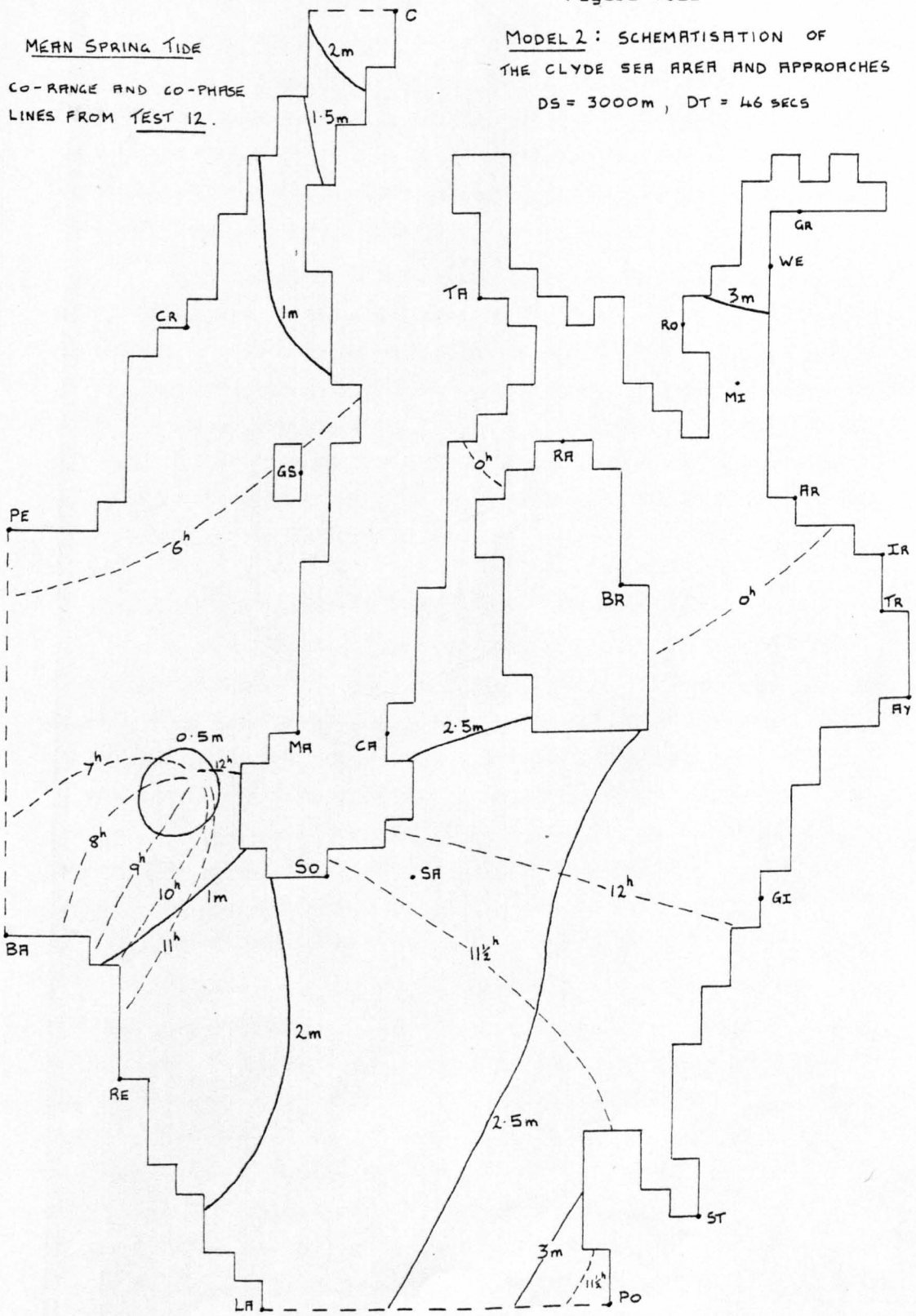

7.4.1 Description of Model 3

The Firth of Clyde includes all the waters north of a natural shelf which defines the Firth from the relatively deeper North Channel. The average depth on the shelf edge is about 72 metres which decreases going northwards to a depth of 25 metres at Greenock. There is also an associated contraction of breadth especially between the island of Bute and the mainland at Largs.

For the purposes of the model the sea boundary follows the shelf edge quite closely and extends from Sanda Sound, off the south east coast of the Kintyre Peninsula to Portpatrick. The schematisation of the land and sea boundaries together with the mean water depths at each grid point are shown in figure 7.17. This grid formed the basis of Model 3 and is in fact the Firth of Clyde section of Model 2. The spacestep of 3 km and timestep of 46 seconds are therefore the same grid parameters as defined in Model 2.

7.4.2 Simulation of the Mean Spring Tide using Model 3

With the Tide Tables providing the maximum elevations and the high water times at the extremities of the sea boundary namely Sanda Sound and Portpatrick, Model 3 was tested using the mean spring tide. The computations for the coastal locations are presented as Test 13 in table 7.15 together with the corresponding Tide Table ranges and phases. By comparison, the computed ranges are in good agreement while the computed times of high water are slightly later than the Tide Table phases. In this and other tests with Model 3 the Chezy coefficient was $35 m^{\frac{1}{2}}/s$ which was also the value used in Model 2.

Another source of data available at the time was the Admiralty co-tidal Chart 5058 which has been reproduced in part in figure 6.6. The appropriate sea boundary conditions were taken from this chart and used as input to Model 3 with the results at the coastal locations shown as Test 14 in table 7.15. A comparison of the sea boundary conditions at Sanda Sound and Portpatrick for both tests shows that the chart phases are earlier and the ranges are smaller than those of the Tide Tables. The phases computed in Test 14 are therefore earlier than the Tide Table phases but compare favourably with the chart phases shown in figure 6.6. To illustrate this point the computed ranges and phases from Test 14 are

Mean depths (in metres) at grid points in the Firth of Clyde model.

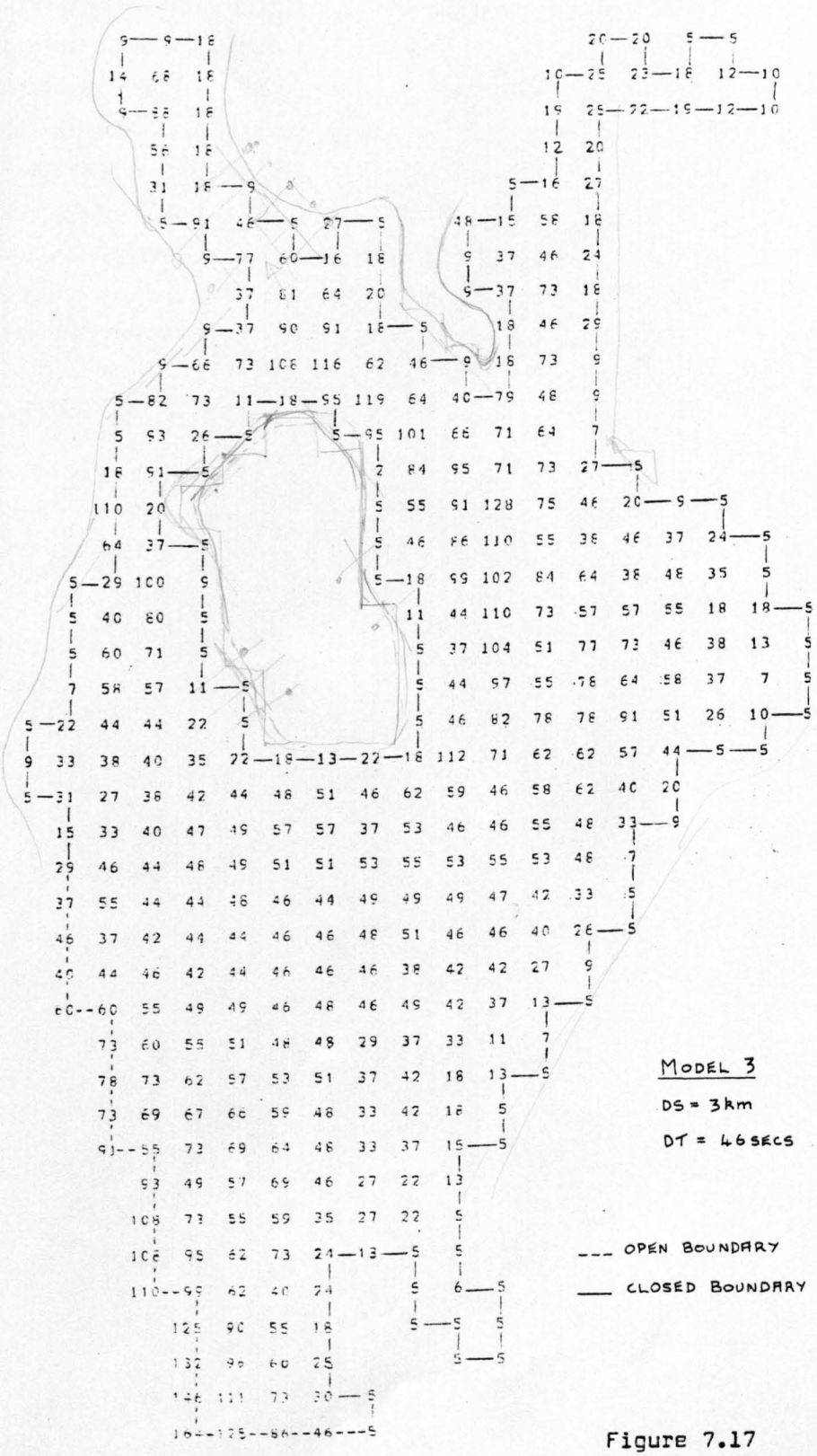

Figure 7.17

depicted as co-range and co-phase lines in figure 7.19 for comparison with figure 6.6. Also the co-range and co-phase lines from Test 13 are provided in figure 7.20 to illustrate the difference in the simulated results from those of figure 7.19 from using two different data sources. Both sources are in reasonable agreement concerning the spring ranges in the Firth of Clyde however the phases are slightly dissimilar. By considering the relative phases (in minutes) between the more significant ports as shown in figure 7.18 the differences between the two sources and also between the two simulations can be more easily understood. The Tide Table phase difference

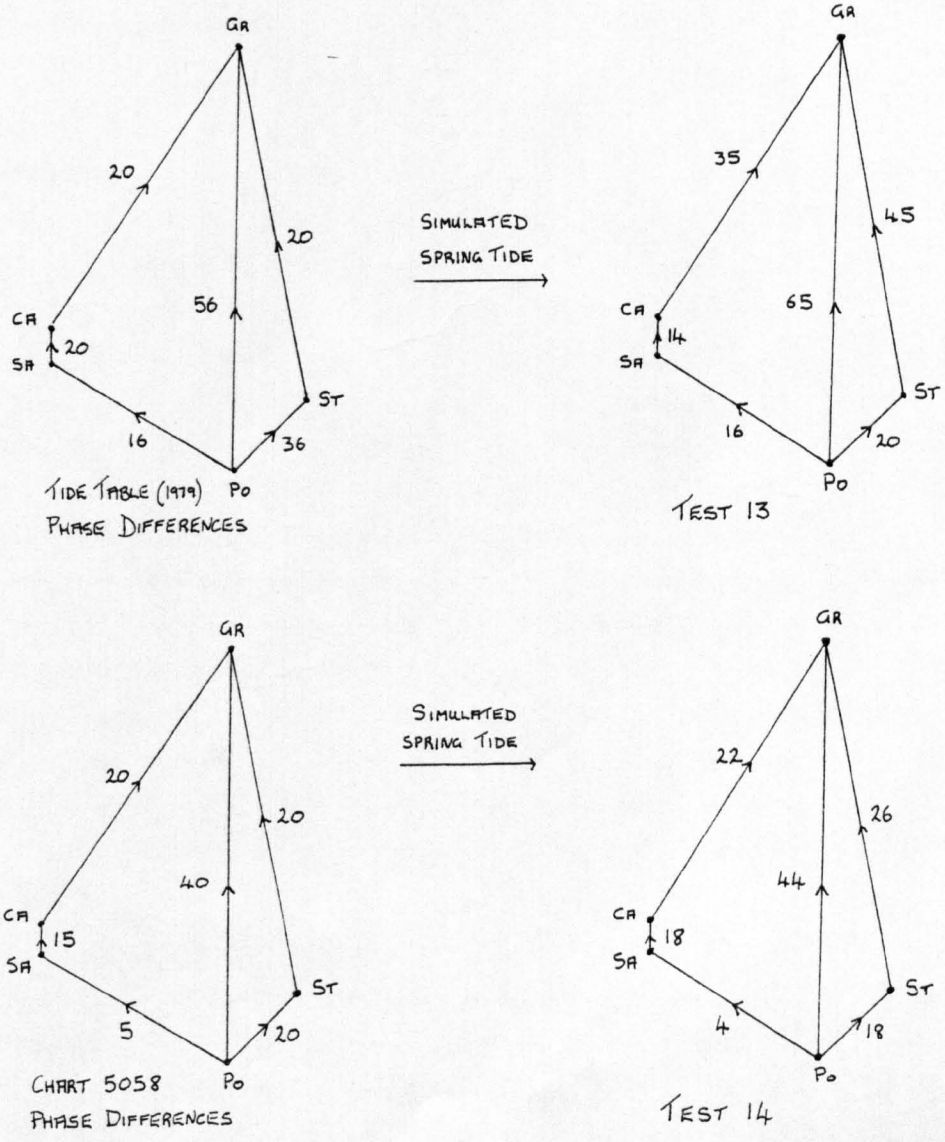

Figure 7.18

between Portpatrick and Sanda Sound is greater than that of Chart 5058 therefore the phase difference from Portpatrick to Greenock is likewise. Similarly the phase difference from Portpatrick to Greenock is greater in Test 13 than that of Test 14. Effectively the sea boundary phase from Portpatrick to Sanda Sound which is an input to the model determines the response at interior points in the model. The model has responded to this input, significantly enough in such a way that the computations are comparable with the data source at all corresponding grid points. In fairness to the two data sources namely the Tide Tables and the co-tidal chart there is in general good agreement between them in the Firth of Clyde and the phase differences shown in figure 7.18 are reasonably similar for both sources.

To assess the accuracy of the computed tidal streams in the Firth of Clyde, three points corresponding to positions of stream measurement in the stream Atlas were selected and the streams compared to those computed in Test 13. The locations of the three points are shown in figure 7.20 and the comparison of results is detailed in table 7.16. At each position the computed and recorded stream velocities and directions measured as a whole circle bearing are compared throughout hourly intervals of one tidal cycle. These intervals are specified in the stream Atlas in hours preceding and following high water at Dover which is 1100 G.M.T., however the computed streams correspond to Greenwich Mean Time. The times specified in table 7.16 are also relative to Greenwich so that two hours after high water at Dover becomes half an hour after high water at Greenwich and so on. At positions 2 and 3 the Atlas streams as published appear to suffer from being rounded off, nevertheless at each position the recorded and computed maximum stream flows on the ebb and flow tide are in quite good agreement. The times of maximum flow, slack waters and flow directions from Test 13 are also favourable with the Atlas values at each point.

From the computations of Test 13 a series of diagrams showing the mean spring tide stream magnitudes and directions at intervals of one-twelfth of the tidal period are presented in figure 7.21. At times 0 hours and 6.21 hours the respective high and low waters at Greenock are indicated corresponding to slack water at that location. Similarly

FIRTH OF CLYDE.

SPRING RANGES AND PHASES FROM MODEL 3

Location	Grid Ref	Tide Tables (1979)		Test 13		Test 14	
		SR	MHWI	SR	MHWI	SR	MHWI
		m	GMT	m	GMT	m	GMT
Greenock	GR	3.08	0010	3.16	0019	3.17	1210
Wemyss Bay	WE	2.89	0005	3.01	0011	3.02	1206
Rothesay Bay	Ro	3.08	0010	2.96	0008	2.96	1205
Millport	MI	2.92	0005	2.91	0005	2.92	1203
East Loch Tarbert	TA	3.08	0015	2.72	0044	2.71	0023
Loch Ranza	RA	2.65	1220	2.67	0012	2.73	1219
Brodick Bay	BR	2.83	0010	2.80	0005	2.78	1208
Ardrossan	AR	2.83	1215	2.84	1223	2.82	1201
Irvine	IR	2.77	1215	2.83	1217	2.83	1156
Troon	TR	2.80	1210	2.82	1217	2.82	1158
Ayr	Ay	2.56	1210	2.82	1219	2.82	1158
Girvan	GI	2.68	1210	2.71	1155	2.70	1138
Stranraer	ST	2.77	1215	2.87	1159	2.81	1144
Campbeltown	CA	2.56	1215	2.44	1209	2.49	1148
Sanda Sound	SA	-	1155	2.25	1155	2.15	1130
Portpatrick	PO	3.44	1139	3.44	1139	3.20	1126

Table 7.15

Mean spring tide co-range and co-phase lines in the Firth of Clyde computed with the input data taken from chart 5058.

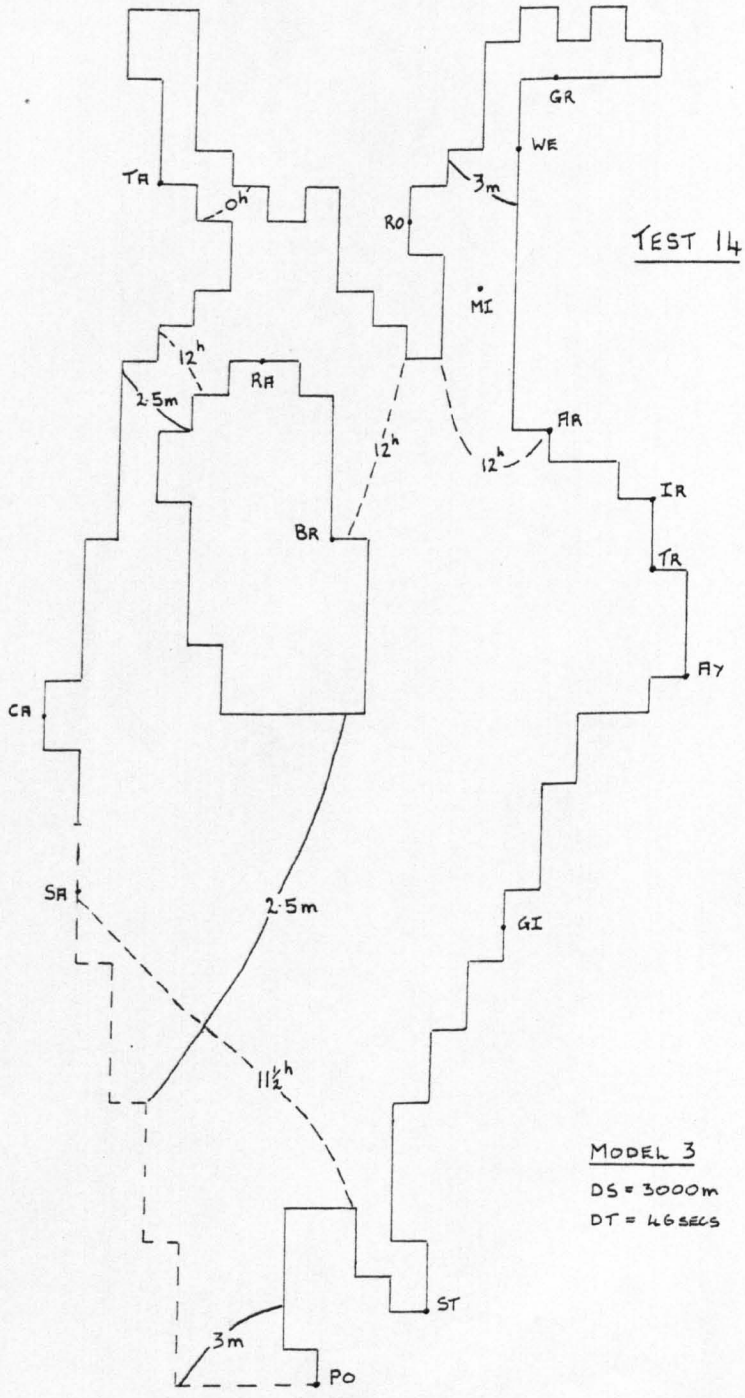

Figure 7.19

Mean spring tide co-range and co-phase lines in the Firth of Clyde computed with input data taken from the Admiralty Tide Tables (1979).

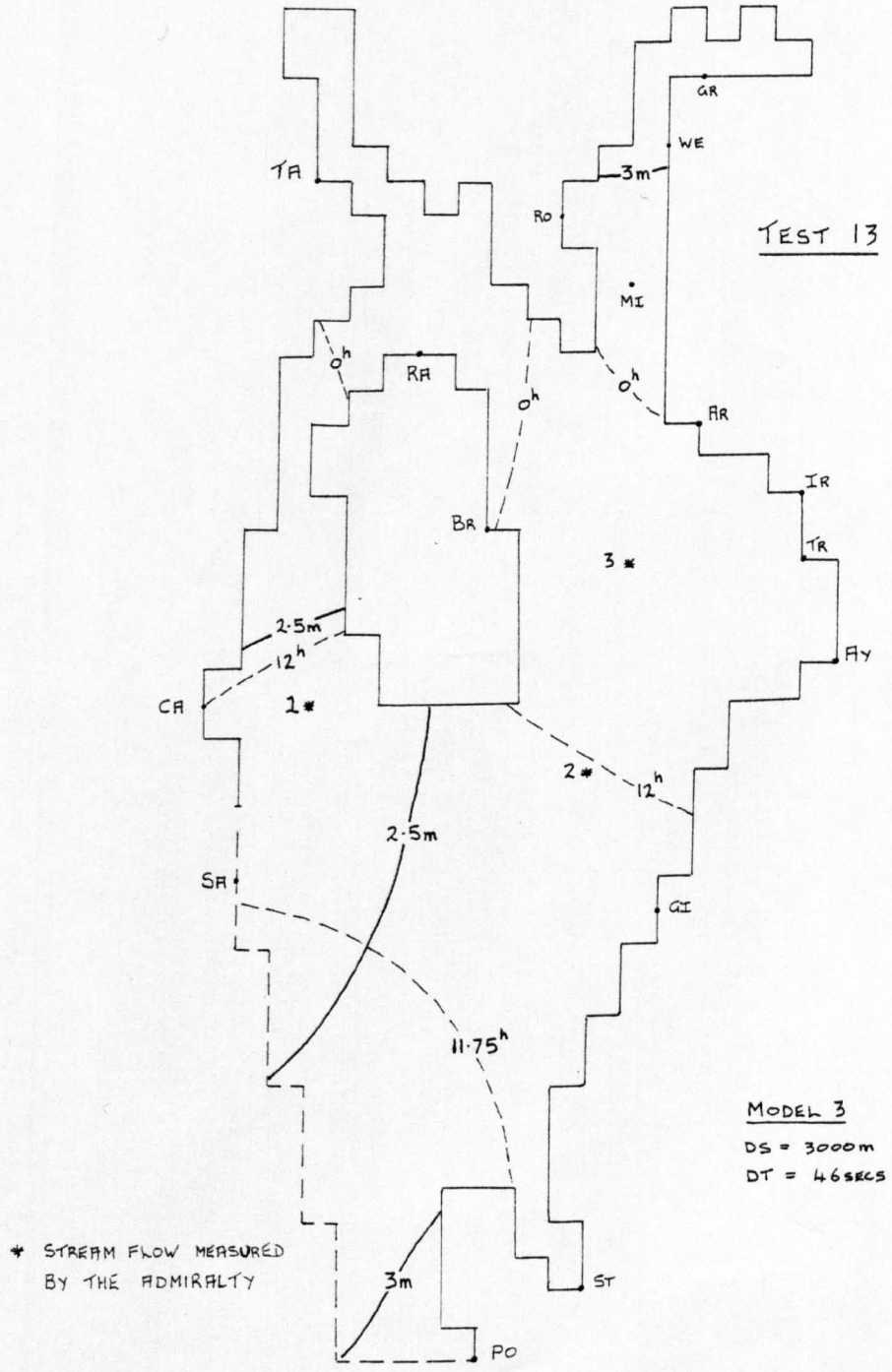

Figure 7.20

COMPARISON BETWEEN TIDAL ATLAS STREAMS AND THOSE FROM TEST 13 FOR SPRING TIDES

Time G.M.T.	Position 1				Position 2				Position 3			
	Atlas Stream		Computed Stream		Atlas Stream		Computed Stream		Atlas Stream		Computed Stream	
	Rate	Direction	Rate	Direction	Rate	Direction	Rate	Direction	Rate	Direction	Rate	Direction
	m/s	Deg	m/s	Deg	m/s	Deg	m/s	Deg	m/s	Deg	m/s	Deg
½	0.15	183	0.13	211	0.20	213	0.10	227	0.10	187	0.05	241
1½	0.26	193	0.21	226	0.31	229	0.21	226	0.15	180	0.14	180
2½	0.31	196	0.23	201	0.20	221	0.27	225	0.15	180	0.17	178
3½	0.26	191	0.22	197	0.26	228	0.27	225	0.15	184	0.17	177
4½	0.10	191	0.14	192	0.20	221	0.21	224	0.10	182	0.14	176
5	0.15	201	0.09	192	0.15	212	0.16	224	0.05	187	0.12	175
6	0.15	355	0.07	29	0.15	22	0.01	141	0.10	2	0.03	162
7	0.26	7	0.19	27	0.15	36	0.17	48	0.15	18	0.10	1
8	0.26	3	0.23	24	0.10	25	0.26	47	0.15	4	0.16	357
9	0.20	3	0.24	21	0.15	28	0.29	46	0.15	10	0.19	356
10	0.15	5	0.20	19	0.20	33	0.26	44	0.10	3	0.17	356
11	0.10	5	0.11	16	0.20	42	0.16	43	0.15	3	0.12	355
12	0.10	191	0.01	212	0.10	15	0.01	236	0.05	11	0.04	302

Table 7.16

Stream flows in the Firth of Clyde at intervals of one-twelfth of the mean spring tidal cycle. Ebb tide computed in Test 13 using Model 3.

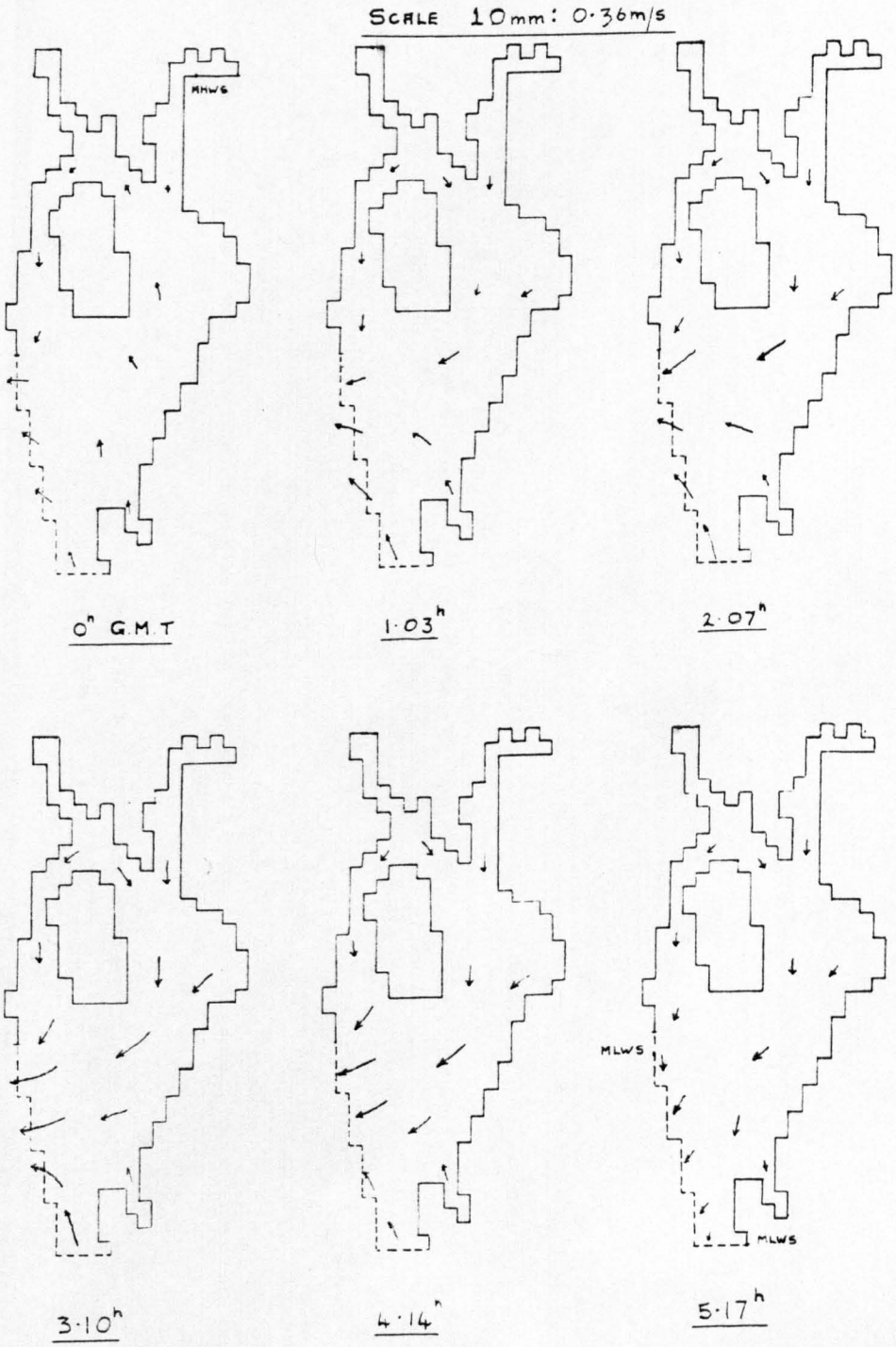

Figure 7.21

Stream flows in the Firth of Clyde at intervals of one-twelfth of the mean spring tidal cycle. Flow tide computed in Test 13 using Model 3.

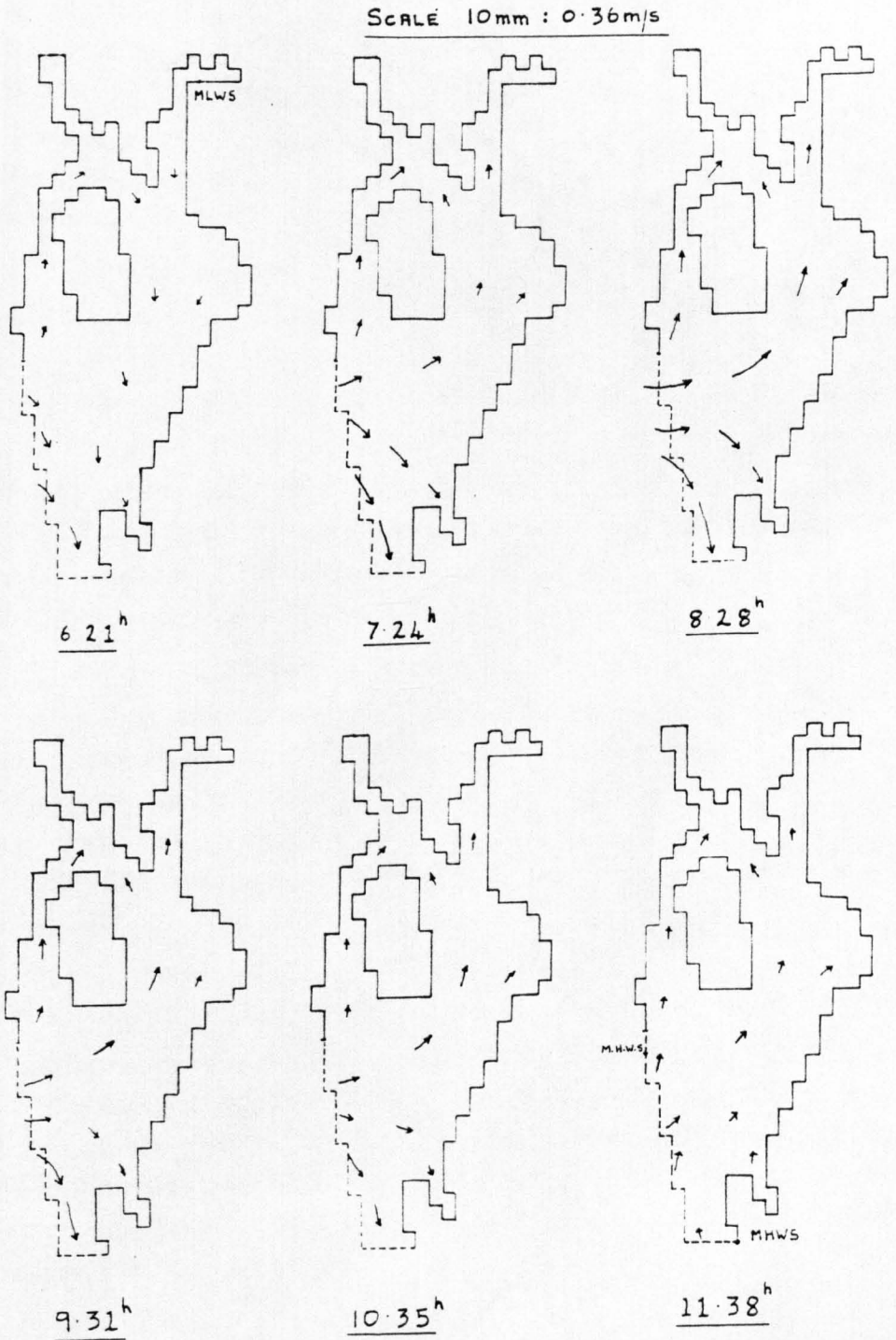

Figure 7.21(a)

at Portpatrick the high and low waters occurring at about 11.6 hours and 5.17 hours are also indicated and correspond to slack waters in that area. During the decrease in tidal elevation from high water to low water at both ports, ebb tide occurs and conversely an increase in elevation at both ports corresponds to the flow tide. It is apparent from these diagrams that the ebb and flow tides are strongly two-dimensional since tidal propagation occurs northeastwards towards Greenock while simultaneously propagating southeastwards towards Stranraer and Portpatrick before reversing direction.

Throughout the area the tidal behaviour has been simulated predominantly as a standing wave since the phase of the flows and elevations differ by about ninety degrees. The same tidal characteristics can be deduced from the Tide Table elevations together with the Atlas streams. The model therefore has not only simulated accurately the elevations and velocities in the Firth of Clyde but is also competent in producing the correct phase relationship between them. Since surge data was available from Campbeltown, near Sanda Sound and Portpatrick this model was also considered suitable for simulating storm surges.

In evaluating the accuracy of the tests presented in this chapter, the computations have been compared with the corresponding Tide Table values or the data from Chart 5058. On this basis, the comparison can be simplified by obtaining a single parameter $\bar{D}$ which represents the average variation in tidal range or phase between the computations and the known data. For this purpose the standard deviation expressed as

$$\bar{D} = \sqrt{\frac{\Sigma (x_c - x_d)^2}{N}} \qquad (7.2)$$

has been calculated with x_c and x_d being the computed and Tide Table values respectively. Equation (7.2) has been applied to ranges and phases at the coastal locations appropriate to the particular model. The standard deviation of the computed ranges and phases with respect to the Tide Table values have been calculated for Tests 1 to 14 and are presented in table 7.17.

Model	Test	$\bar{D}r$	$\bar{D}\phi$
		m	mins
1	1	0.62	-
1	2	0.27	-
1	3	0.25	-
1	4	0.82	73
1	5	0.75	88
1	6	0.30	47
1	7	0.25	38
1	8	0.27	37
		(0.26)	(30)
1	9	0.19	47
1	10	0.27	44
1	11	0.19	65
2	12	0.14	40
		(0.13)	(16)
3	13	0.13	10
3	14	0.13	-

(Values in brackets apply only to the Firth of Clyde).

Table 7.17

In Tests 1, 2, 3 and 14, the input data was taken from Chart 5058. The ranges of this data are in good agreement with the Tide Table values, however the agreement between the Chart and Tide Table phases is not so close, especially in the Sound of Jura. For this reason, the application of equation (7.2) to these tests was only performed for the computed ranges and not the phases. The Chart phases in addition to being of doubtful accuracy, are also difficult to estimate precisely from the co-phase lines and so were unavailable for use in equation (7.2).

In Test 1, the standard deviation obtained from the ranges is large as a result of frictionless conditions and is somewhat reduced in Test 2 when frictional forces are present. A comparison of standard deviations between Tests 4 and 6 for 90° characteristics and similarly for Tests 5 and 7 using 45° characteristics shows the improvement on

changing the boundary interpolation scheme.

Using 45° characteristics, boundary interpolation scheme 2 and the survey data, the optimum values of standard deviation in both ranges and phases were obtained in Test 8. The respective values of 0.27 metres and 37 minutes were the most satisfactory of all the tests using Model 1. Referring again to table 7.17, the standard deviations for Test 8, given in brackets, represent values calculated from results obtained only in the Firth of Clyde. Comparing the standard deviations between Tests 8 and 12 shows the improvement in changing from Model 1 to Model 2. In the Firth of Clyde the standard error in computed range has been reduced from 0.26 metres to 0.13 metres while the error in the computed phases has reduced from 30 minutes to 16 minutes. It is evident that the application of a finer grid improved the values of computed range and phase especially in the Firth of Clyde. The values of standard deviation in the Firth of Clyde obtained from Test 12 are almost as good as those derived from Test 13, using Model 3 which schematised solely the Firth of Clyde.

The important point, concerning the method of improving successive simulations, is that the variations in the computations from the accepted data may be accounted for and so the factors responsible may then be singled out for further improvement. It is this process that has been used to reduce the variations to the acceptable values shown in table 7.17 for Tests 8, 12 and 13. These variations are thought to be sufficiently small, when simulating average spring or neap tide conditions, to allow the application of the models for reproducing the storm surge phenomena.

CHAPTER 8

SIMULATION OF STORM SURGES IN THE FIRTH OF CLYDE AND ITS APPROACHES

8.1 INTRODUCTION

It is safe to say that the enlightenment on the understanding of storm surges began with the theory of tides as originally proposed by Airy (1845). Other important literary contributions prior to 1900 were relatively limited. However between 1900 and 1950 some important contributions appeared, the first of which was a paper by Chrystal (1906). He investigated the occurrence of seiches from a hydrodynamic viewpoint which included a field survey of Loch Earn.Of significance also were the works of Taylor (1916), Proudman and Doodson (1926) and a few others who investigated meteorological effects on the sea. For example Hellstrom's work (1941) on wind setup in lakes earned him recognition as the originator of a wind set-up theory. On meteorological oceanography there appeared an important text by Sverdrup (1942). In a study of non-linear waves Proudman (1955) succeeded in establishing solutions for non-harmonic waves and hence attempted to analyse the interaction of tide and surge in an estuary.

A considerable number of contributions have appeared since 1950 as a consequence of the development in computer technology. In this respect Hansen (1956) seems to have been the first author to record the successful application of a numerical model to surge simulation. His x-y-t finite difference model was applied to the North Sea. A later simulation of storm surges in this area was made by Heaps (1969) to predict surge characteristics on the continental shelf. Both authors used an explicit technique based on the use of a staggered grid described by Hansen (1957). The work of Leendertse (1967), (1970) and Abbott (1973) falls generally within this category. Where shallow water effects are important, Reid and Bodine (1968) have given a thorough account of their application of the straightforward Hansen method to analyse storm surges in Galveston Bay. A later development was the (x-y-z-t) model which operates at the very limit of machine storage, machine time and calibration possibilities. Heaps (1973) developed such a model in his investigation of wind driven currents in the Irish Sea while Leendertse and Liu (1975) have presented details of applying such models to estuarine flows. More recently Leendertse and Liu (1978) have reviewed

a considerable number of existing modelling techniques and their application to seas and estuaries.

To a lesser degree, another factor drawing attention to the investigation of storm surges was the disasterous flooding produced by a North Sea surge in 1953. This spectacular surge breached embankments and flooded coastal parts of Britain, The Netherlands and Germany and the magnitude of its propagation has been detailed by Rossiter (1954). Since 1953 considerable attention has been focussed on storm surges in the North Sea and especially the River Thames, principally by the Institute of Oceanographic Sciences. The notable works of Rossiter (1961), Banks (1974) and Prandle (1978) being some interesting examples of this endeavour. The focal point for these studies was the Thames area in which storm tides frequently reach 1.6 metres or more above predicted levels.

Possibly because the west coast of Scotland was relatively untouched by the surge of 1953, little attention has since been directed to the effect of surges in this area. The studies of Cartwright (1968) and Heaps (1969) have however considered the Scottish west coast but only in terms of providing data for storm surge analysis in the North Sea. However, with regard to the Scottish west coast some useful deductions can be made from Lennon's study (1963) of previous surges in the Irish Sea. As with the Thames area it required a flood situation to draw attention to the Scottish west coast. The devastation occurred during the 14th - 17th January 1968 when a severe gale of hurricane strength passed over the north of Scotland. For ports along the Scottish west coast, Milne (1971) has presented the surge history and shown that a maximum surge height of 2.25 metres above predicted tide level occurred in the Firth of Clyde at Rothesay Dock. One would expect the surge in this area to be high by considering the constricting nature of the topography of this region. Following the damage produced by this surge, the Department of Civil Engineering at Strathclyde University have monitored surge events on the Scottish west coast, principally in the Firth of Clyde. This study has led to the utilisation of the records as data for the proposed numerical model to facilitate a more complete understanding of the generation of storm surges in the Clyde sea area and its approaches.

8.2 THE STORM SURGE PHENOMENON

8.2.1 Definition of a storm surge

Most wind generated waves are of short wavelength. However meteorological conditions can produce long, shallow water gravity waves similar to tides. Although storm conditions are not essential to their development, such waves frequently accompany storm conditions, thus they are referred to as storm surges. Tides, storm surges and Tsunamis (generated by seismic displacement of the ocean floor) represent three common forms of long wave motion. Unlike tides however, storm surges are not periodic waves since neither their occurrence nor their magnitude can be anticipated with certainty. However deterministic models have recently been developed which attempt to forecast storm surge occurrences. Flather (1976) has taken this approach to a problem that has in the past been treated largely by statistical methods.

Storm surges are sometimes referred to as meteorological tides since they are caused by unusually high or low barometric pressures and associated strong or prolonged wind speeds. When these conditions differ from the norm there are corresponding differences between the actual and predicted tide which, if recorded, become a measure of the storm surge. In this way a positive surge is associated with a net transport of water towards the shore resulting in an increase in tidal level. Naturally enough, previous studies have been more concerned with low pressure distributions and in simulating positive surges because of their importance in flood prediction.

8.2.2 The effects of pressure and wind on the water's surface

The areas of low pressure, termed depressions, which affect the weather off the west coast of Europe develop over the Atlantic Ocean along the Atlantic Polar Front. Along this front the Polar Maritime and the Tropical Maritime air masses meet. Around the coasts of the British Isles the effect of a depression on the variation of mean sea level seldom exceeds 0.3 metres unless the depression is deep and moving quickly. However the depression can be important when coupled with the associated wind fields which are capable of producing dramatic changes in sea level. An account of the track of depressions and their effect on the surrounding waters of the British Isles has been comprehensively

assessed by Heaps (1965).

Considered statically, the equilibrium relationship between atmospheric pressure and the sea causes the latter to act as an inverted barometer. The static law governing this situation was first presented by Charnock and Crease (1957) and is

$$\Delta H = \frac{1}{\rho g}(p_a - p) \qquad (8.1)$$

This law implies that a change of approximately one millibar of pressure results in a change in sea level by one centimetre. This relationship, also quoted by Heaps (1967), has been established mainly through its extensive use in the derivation of empirical formulae for surge forecasting. The validity of equation (8.1) is only ensured when the pressure over the body of water is uniform and when the movement of the depression is sufficiently slow. Charnock and Crease (1957) have pointed out that this implies that the motion in the sea is small so that there is a free exchange of water between the areas inside and outisde the area covered by the depression. Cartwright (1968) has produced evidence to show that, at Aberdeen there is a departure from the static value for meteorological fluctuations with frequencies higher than 0.25 Hz.

For the case of a progressive pressure system, the dynamic effect, as a result of the speed of the depression, can be critical. A response, similar to that evoked by other tide generating forces can occur and its magnitude is dependent on the speed of travel of the depression. In shallow waters over the continental shelf, when the speed of the storm approaches the speed of the free wave given by $c = (gH)^{\frac{1}{2}}$, then resonance should be considered. Complete resonance will not occur because of frictional effects since without bottom friction at resonance, a dynamic theory would predict infinite elevation. Furthermore, Bretschneider (1967), suggested that the maximum height should not exceed the breaking limit presented by the solitary wave theory $\eta_{max} = 0.78H$.

Since the area represented in the Clyde sea area model is not large in relation to the size of a depression, the effect of pressure gradients in this area are small spatially and temporally. Hence the numerical terms representing these gradients in the model were not included when simulating the storm surges.

Changes in atmospheric pressure cause movements of air flows which constitute wind fields. As a result of the Coriolis effect, a wind field does not travel in the direction normal to the isobars but rather always anticlockwise round a low pressure point in the Northern Hemisphere.

The effect of wind on the sea level can be extremely variable and depends largely on the topography of the sea under consideration. Factors such as bottom stress, bottom configuration and the confines of the coastline are important. The direction of the surge is also influenced both by the direction of the wind and by the earth's rotation, this feature being noted by Ekman (1905). The wind stress may cause the movement of vast quantities of water with progressive changes in sea level as the coastline is approached. When this stress is released, the water returns to an equilibrium position but not without the despatch of a long wave to the surrounding zone. The storm waves have the specific connotation that they are still under the influence of the wind field and that their duration is only as long as the wind producing them. If they emerge from the wind field they have different characteristics and are termed 'swell waves'.

An account of the process of wind-wave interaction and the theory of wind stress has been given in section 5.2 in deriving analytical surge solutions. Accurate values of the wind stress coefficient become more important when considering a real surge event as opposed to an idealised one. For this reason their measurement over lakes and seas by other authors is discussed in this chapter. That the extent of the variation of the wind stress coefficient with wind speed is still rather uncertain, is evident from figure 8.1 which shows the relationships derived from some of the past research. However a linear relationship between the stress coefficient and wind speed seems to be favoured. Deacon and Webb (1962) proposed the following condition

$$k = (1.00 + 0.07\, W_{10}) \times 10^{-3} \quad : \quad W_{10} \leq 20 \qquad (8.2)$$

in which W_{10} is in m/sec. At 20m/sec this expression would give $k = 0.0024$ which agrees reasonably well with values from sea-slope data. Sheppard (1958) also proposed a linear relationship but with rather a greater slope. His proposal for the range 1 - 20m/sec was

$$k = (0.80 + 0.114\, W_{10}) \times 10^{-3} \qquad (8.3)$$

At 20m/sec Sheppard's formula gives $k = 0.0031$ which appears to be somewhat large. Prior to this Deacon, Sheppard and Webb (1956) had evolved the relationship

$$k = \left(0.9 + 0.123\, W_{10}\right) \times 10^{-3} \quad : \quad 5 \leq W_{10} \leq 13 \qquad (8.4)$$

which gives a stress coefficient of 0.0025 for wind speeds greater than 13m/sec. This value of the coefficient is in close agreement with the value proposed by Charnock and Crease (1957) namely

$$k = 0.002513 \quad : \quad W_{10} \geq 19.22 \text{ m/sec} \qquad (8.5)$$

This value in equation (8.5) has been accepted by Heaps (1965) to be sufficiently close to the actual drag on the sea surface at high wind speeds typical of storm surges. From a private communication with Sheppard, Heaps has also taken the wind stress relationship to be

$$k = 0.554 \times 10^{-3} \quad : \quad W_{10} < 5$$

$$k = \left(-0.12 + 0.137\, W_{10}\right) \times 10^{-3} \quad : \quad 5 \leq W_{10} \leq 19.22 \qquad (8.6)$$

which was inferred from wind measurements by application of the 'law of the wall'. The relationships (8.5), (8.6) are shown in graphical form in figure 8.1 and although smaller values of wind stress are obtained from these relationships than for the others, equations (8.5), (8.6) are apparently still used and widely accepted.

To summarise the storm surge effect at a location derived from recordings of sea level, it may be regarded as consisting of a part generated by wind stress acting tangentially over the sea surface and a part generated by changes in atmospheric pressure. The surge characteristics for a location on the open coast are different from those in an estuary. Bottom friction plays a greater role and the rotation of the earth a lesser role in estuaries than on the open coast. The dominant non-linearity of the surge on the open coast is the interaction between surface waves and the large scale flow. In estuaries it may be possible to neglect the surface waves in analysing the surge but non-linearities in the mean motion become more important. Open coast surges are sometimes given greater attention because they are more general, whereas each estuary presents some unique surge features.

The variation in wind stress coefficient in relation to wind speed as proposed by several authors.

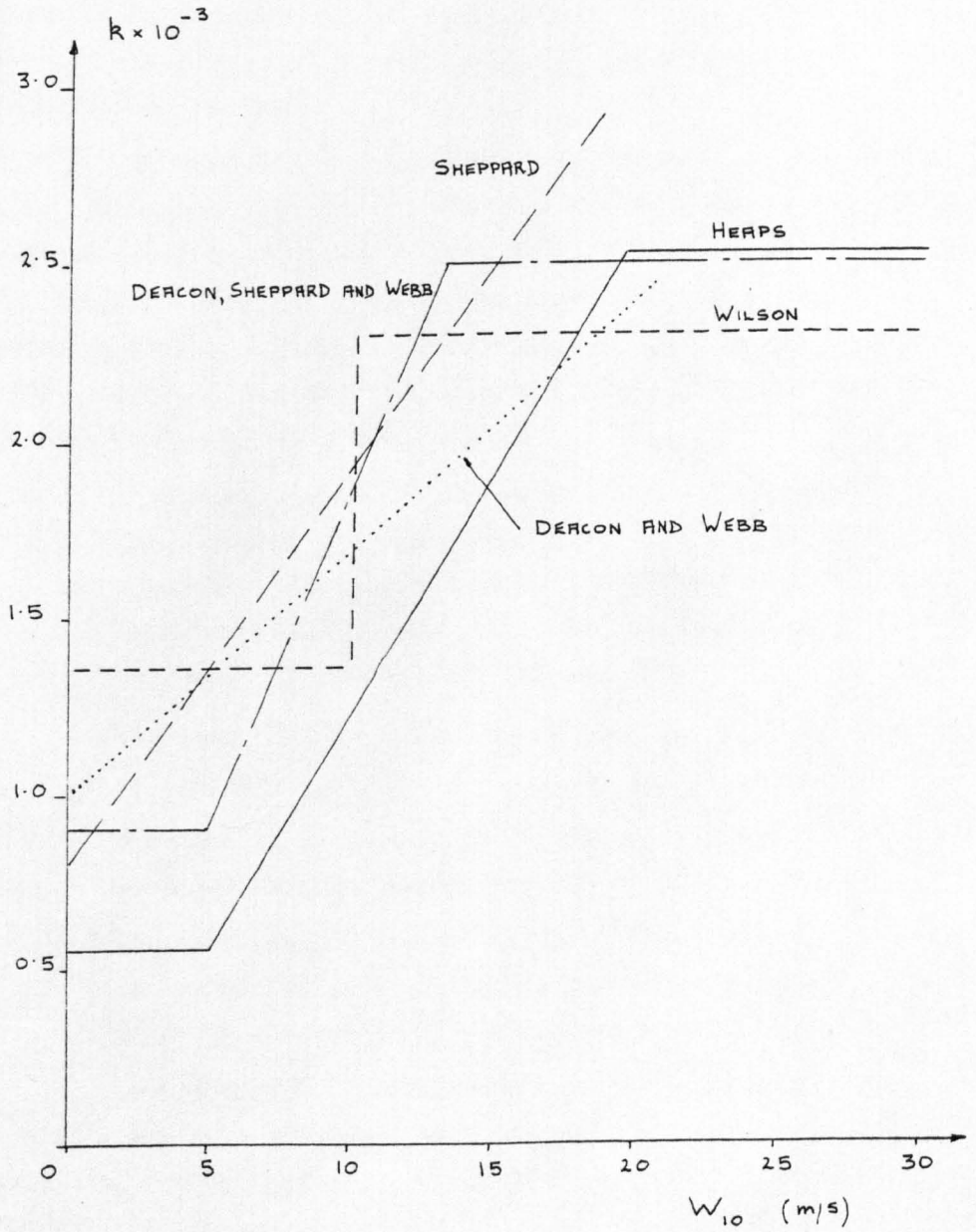

Figure 8.1

8.2.3 The weather conditions associated with major storm surges along the west coast of the British Isles

The intensity of the storm has been found by Harris (1966) to be the most important parameter for estimating the storm surge produced. The central pressure, the pressure gradient across the depression and the maximum wind speed are all valid indices of the storm intensity. The central pressure being the most stable of these parameters. The location of the peak surge is largely determined from the track of the storm and the area affected depends on both its track near the coast and its size.

An analysis similar to that of Harris was performed by Lennon (1963) for surge events along the west coast of the British Isles. He analysed seven depressions at both Liverpool and Avonmouth and noted the similarity of features in the depressions which were responsible for producing surges at either or both these ports. He concluded that a major surge could be expected along the west coast when four meteorological conditions occurred namely if:

a) A deepening and well developed secondary depression approaches the country from the Atlantic Ocean such that its right-rear quadrant acts upon the water surface en route to the ports. Hence the ports experiencing the greatest surge, lie to the right of the path of the depression.

b) The speed of approach of the depression is of the order of 40 knots.

c) A radius of depression up to 150 to 200 nautical miles is well defined by roughly concentric isobars.

d) The depression reaches a depth of 50 mb over the country and is associated with a pressure gradient of approximately 30 mb in 250 nautical miles in its right-rear quadrant.

Lennon further concluded that of these four conditions, the first pair are more important than the second. The occurrence of these features in the two recorded Scottish west coast surges are discussed later in this chapter.

8.3 THE NUMERICAL REQUIREMENTS OF A MODEL

The operation of a model for simulating storm surges properly also requires the reproduction of the tide conditions prevailing during the passage of the surge. The three requirements of the model of which the latter two are tide and surge data requirements may be specified as:-

a) Initial conditions.

b) Boundary conditions.

c) Wind and pressure data over the surface of the model.

These three categories are discussed in turn as follows:-

The surge problem differs from the purely tidal one in that an extra level of input is required, namely the meteorological conditions. However the problem is still of hyperbolic nature and so the initial conditions of null velocities and an arbitrary free surface are as previously mentioned for tidal simulation. The influence of the incorrect conditions disappear through the effect of the non-linear processes and the dominance of the impressed tidal elevations at the open sea boundaries.

The generation of a surge has been shown by Heaps (1969) to originate at the edge of the continental shelf. Its build up, through the tractive effect of the wind forces, results in it being well established on entry to the area covered by the model. This is assuming that the model is of the nearshore area and does not extend to the edge of the continental shelf. It is essential for simulating the storm surge that the external surge be represented in the model by its measurement at the open sea boundary or boundaries. The terminology of 'internal' and 'external' surges was first introduced by Corkan (1948) and external surges have been discussed by Corkan (1951) and Rossiter (1959), (1961). This type of surge is a free wave penetrating into a sea region from an open sea boundary, where it is induced by a changing sea-level disturbance of the adjacent open sea. The North Sea, English Channel and the Sea of Japan are examples of areas subject to external surges.

A periodic solution for tidal motion is established in the

model after less than two tidal cycles. Therefore at the beginning of the third tidal cycle the boundary conditions consist of the tidal elevations and also the contribution from the external surge at grid points along the open sea boundary or boundaries. These conditions can only be obtained from records from tide gauges placed at locations along the open sea boundary. The gauges record the tidal elevations (relative to mean sea level at Newlyn) which are modified by the meteorological conditions. With a tide gauge positioned at either end of the location of the sea boundary, the grid elevations along the sea boundary can be obtained by interpolating from the two sets of records. If only two gauges are present then the interpolation procedure has to be linear. This procedure obviously represents an oversimplification of the actual boundary conditions and is certainly a determining factor in the standard of the surge simulation.

Returning to point c) there is the problem of acquiring wind and pressure data over an area at least the size of the model. One method commonly used is to extract the geostrophic winds from the Meteorological Office daily weather charts. From the density, direction and curvature of the mean sea-level isobars on these charts, the geostrophic or gradient wind speeds and directions can be deduced. The wind conditions at the water surface are then calculated from the gradient winds using empirical relationships, see Findlater et al (1966). A relationship giving the surface winds as approximately two-thirds of the gradient winds has been suggested by Rossiter (1954).

An alternative approach to calculating surface winds from geostrophic winds is simply to use the wind measurements recorded at wind stations. A comparison of the effect of both methods on the computed surge has been presented by McIntyre (1979). His model used data from five wind stations based around a shelf model of the St George's Channel and the results were compared to those using the geostrophic winds. From his results he concluded that it seems to matter little whether the meteorological data comes from weather charts or directly from recorded wind values. This is an interesting finding because since the beginning of the present research the author has also found the use of weather station data for surge simulation to be perfectly acceptable. However care must be taken to ensure that the number of weather stations are not too few and that their locations are representative of the area covered by

the model. If these conditions are satisfied, the transformation of the recorded data at a discrete number of weather stations into a continuous function, covering all the grid points, can be accomplished. The method of transforming the wind data is to use surface fitting techniques. As a first trial for the Clyde area, an exact fitting surface through the data was used and is defined by the polynomial

$$Q = Ax^2 + By^2 + Cxy + Dx + Ey + F \qquad (8.7)$$

Q represents the dependent variable, wind speed or direction, or barometric pressure and x and y are the co-ordinates of the system of grid points defining the model. In this equation there are six unknown coefficients therefore wind data from six different weather stations is required for their solution. In practice the resulting surfaces for wind speed and direction were ill-conditioned in their solution. This was a result of errors associated with data measurement and the close proximity of some of the weather stations to each other. The next consideration was a least squares polynomial surface, its form being determined by the fact that the number of unknown coefficients must be less than the number of wind stations. Since the maximum number of wind stations providing data in the area was eight, a two-dimensional quadratic equation was chosen, which has the same form as equation (8.7). The surface obtained from the observed data at any given time level using the least squares analysis was found to be acceptable in that the wind speed and direction at any weather station was representative of the wind speeds and directions at the grid points. It was also found that for a uniform wind speed and direction at the six weather stations, at a given time level, the interpolating surface produced the required linear plane. In this way the interpolating quadratic surface was shown to be capable of reducing to a linear form expressed as

$$Q = Dx + Ey + F \qquad (8.8)$$

Using the least squares analysis the surfaces of wind speed and of wind direction were obtained at every grid point in the model. These values were maintained constant over successive time intervals until after an integral number of timesteps a new set of wind speeds and directions are calculated from the data which replaced the previous values

at each grid point.

In a similar manner the atmospheric pressure data at each weather station was used to provide surfaces of pressure over the model's grid. By applying the statical law (equation 8.1) at each grid point the change in mean water level as a result of a change in atmospheric pressure was obtained. It is of some importance to note that at the open sea boundaries only that part of the external surge, resulting from wind stress was added to the predicted tidal elevations above mean water level; that part of the external surge caused by the pressure effect, was added to mean water depth. The distinction between the two effects, namely that one is dynamic and the other treated as static, is the underlying reason for the aforementioned method of specifying these boundary conditions. The computations in the model therefore simulate the total storm surge since the pressure effect is included. These results are later compared to the recorded total surge. Some authors such as Heaps (1969), Prandle (1975) prefer to compare only the computed and recorded wind surge by extracting the pressure effect from the recorded tide. Either method seems acceptable; however in the first method the numerical scheme calculates the pressure effect whereas in the second method the reduction is performed manually.

8.4 THE STORM SURGE OF DECEMBER 1972

Originally it was intended that the storm surge produced by the 'Great Gale' of the 14th - 17th January 1968 be simulated. It was apparent that its long duration made it impractical for calculations on the ICL 1904S computer in which one tidal cycle required twenty-five minutes of machine time. Instead the storm surge of 5th December 1972 was selected from the available records primarily because the duration of the surge was reasonably short; less than two tidal cycles. Fortunately this surge was also of quite a large magnitude, reaching 1.5 metres in maximum height at Greenock. Of the available records, this surge is second only in magnitude to the surge of January 1968.

8.4.1 Wind, pressure and surge data

The daily weather charts published by the Meteorological Office provided information concerning the movement of the depression

during the 4th - 6th December 1972. On the 4th it was apparent that an area of low pressure, south of Iceland moved northeast towards the Faroes while another depression east of Newfoundland moved very rapidly across the Atlantic and started to deepen quickly during the early part of the 5th December. After this time this intense depression which was west of Ireland continued to deepen and moved northeastwards across the Orkneys and Shetlands into the Norwegian Sea. From the synoptic charts the following features were also deduced and are comparable to the weather conditions concluded by Lennon and mentioned in section 8.2.3.

a) At the time of maximum surge in the Firth of Clyde, which occurred at 1400 hours, the location of the centre of the depression was near the Orkneys. This depression was the primary cause of the surge.

b) The depression covered 960 nautical miles in twenty-four hours giving it an average speed of approach of 40 knots.

c) The radius of the concentric isobars was about 150 nautical miles.

d) The maximum depth of the depression reached 968 mb which is 45 mb below standard atmospheric pressure.

These indices are very much in agreement with the conditions prescribed by Lennon for a major surge on the west coast of Scotland. The track of the depression was however too far north to create a serious surge in the west coast of England.

The daily weather charts also provide wind speeds, wind directions and barometric pressures at six hour intervals. For simulation purposes these intervals are too long, therefore more detailed wind and pressure data was obtained from the Meteorological Office in Edinburgh. This data published on Metform sheets 3256B and 3257B provided hourly values of wind speed and direction and three hourly values of pressure for eight weather stations situated in and around the Firth of Clyde and its approaches. These stations were namely Abbotsinch, Prestwick, West Freugh (five miles east of Stranraer), Mull of Galloway, Aldergrove (Belfast Airport), Malin, Machrahanish and Tiree. A graphical representation of the wind speeds and directions for the eight stations during the 5th December 1972 is depicted in figures 8.2 and 8.3

respectively. This data formed the basis of the wind input to the model and the following remarks are applicable to this data.

a) Wind speeds and directions are mean values for the hour following the time stated in figures 8.2 and 8.3.

b) Wind data for Mull of Galloway and Malin were only available every three hours therefore hourly values were interpolated.

c) The wind directions are expressed as whole circle bearings and are therefore measured clockwise from true north.

d) In general the characteristics of wind speed and direction are evidently similar at each weather station. At all the stations the maximum wind speed occurs between 1100 hours and 1400 hours and is preceded by a marked change in direction from southerly to southwesterly.

e) The maximum wind speed varies from 29 knots at Aldergrove to 53 knots at Tiree and these are the most southerly and northerly locations respectively, of the eight stations selected. Also by contrast, Aldergrove is landlocked and the wind is subject to greater frictional forces than at Tiree which is the most exposed of all the stations.

The barometric pressures at the eight weather stations during the 5th December 1972 are listed in table 8.1 at three hourly intervals. Only the stations at Malin and Tiree are not in close proximity to the Firth of Clyde and its approaches whilst for the other six stations the spatial variation of pressure is only 8 mb. The production of flow in the sea during this surge as a result of pressure gradients will therefore be small and consequently the pressure gradient terms were not included in the numerical scheme governing the model. A small spatial variation in pressure across the area of the model also indicates that the area is not large in relation to the radius of the depression. The maximum temporal variation in pressure in the Firth of Clyde and its approaches resulting from the movement of the depression is about 12 mb. This occurs at Abbotsinch where the pressure drops from 990 mb to 978 mb. According to the statical law this represents a rise in mean water level of about 0.12 metres which, again, is not large by comparison to the effect of the wind stress.

Surface wind speeds recorded on the 5th December 1972.

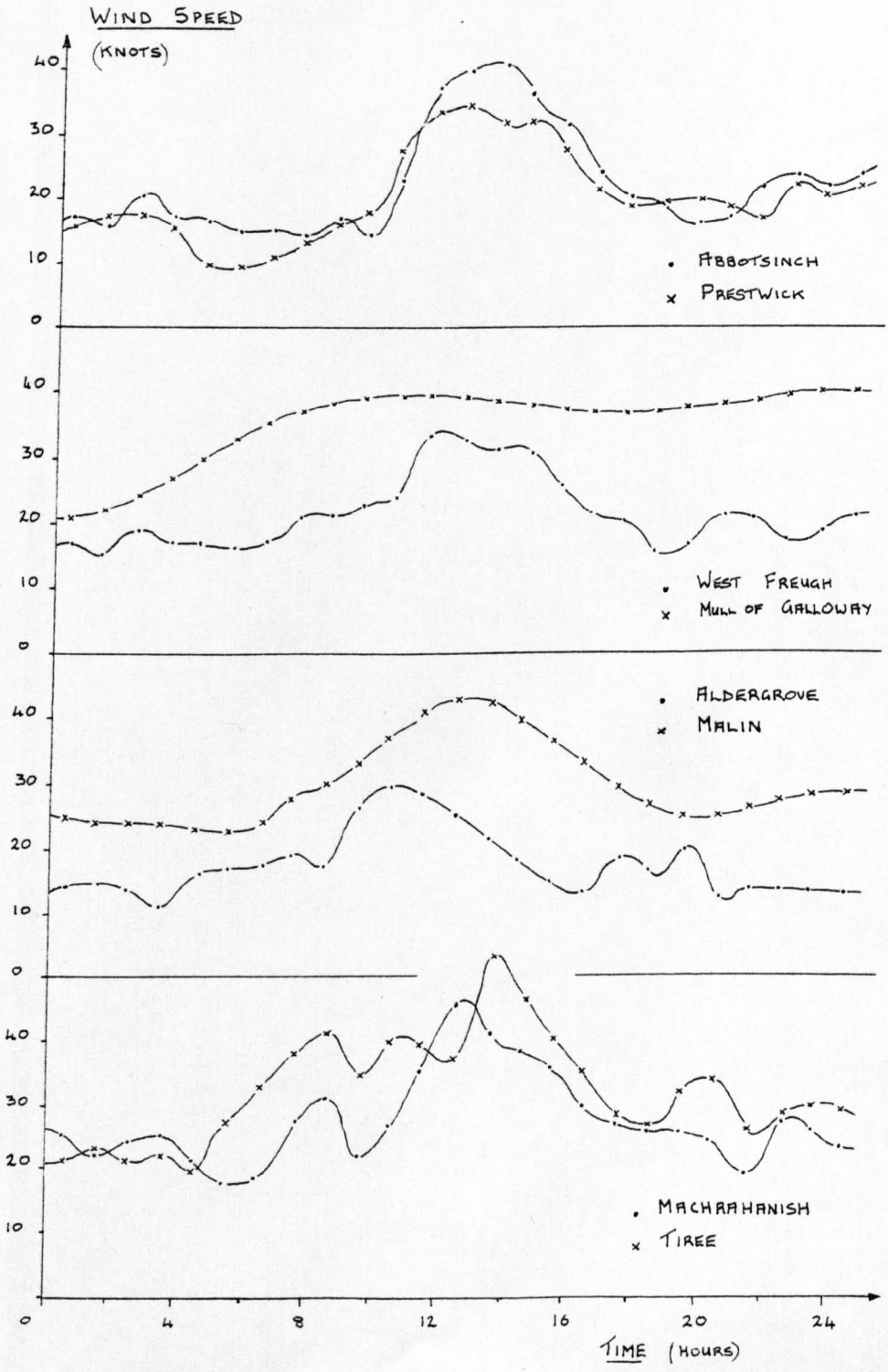

Figure 8.2

Surface wind directions recorded on the 5th December 1972.

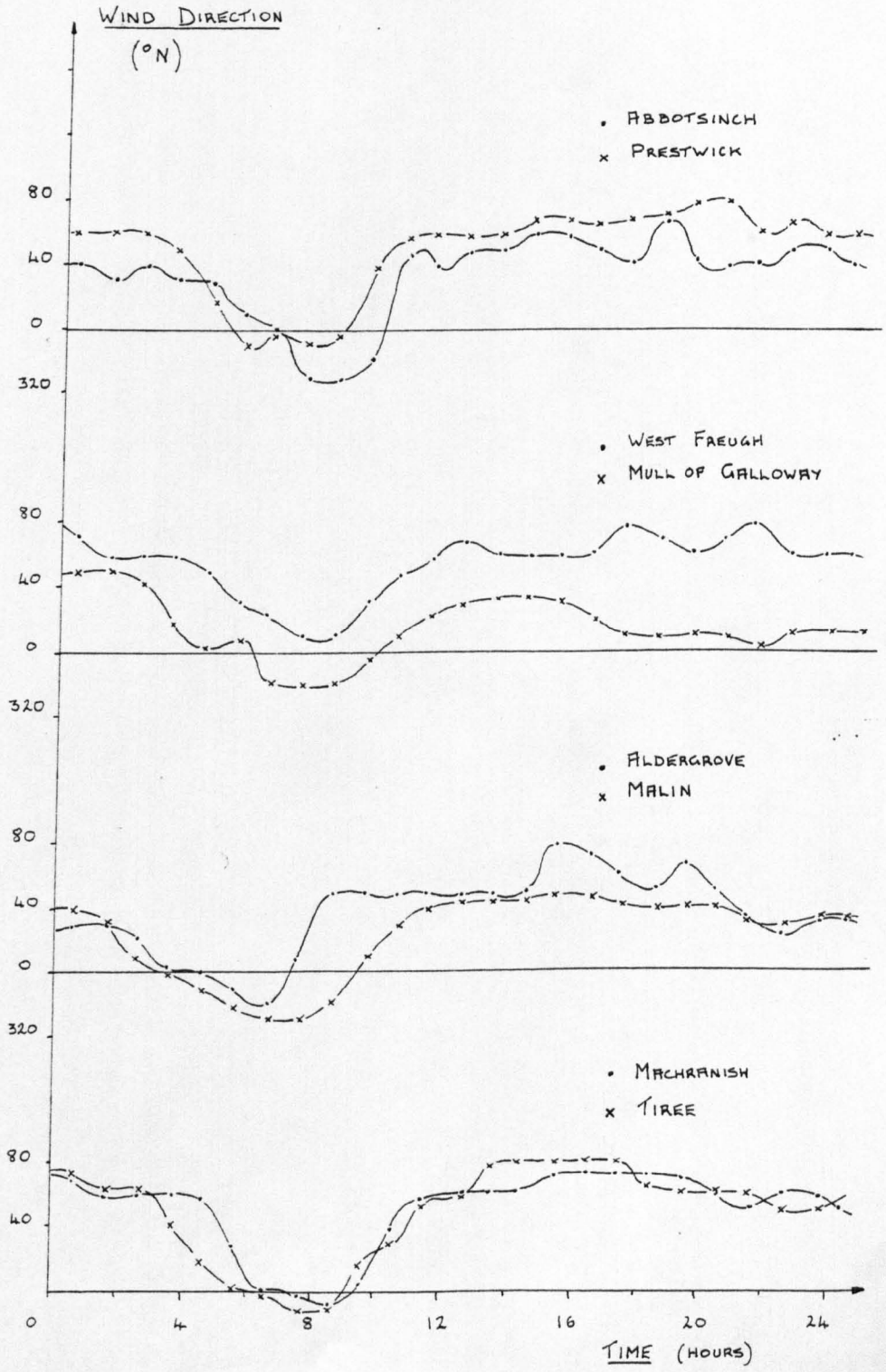

Figure 8.3

THE VARIATION OF BAROMETRIC PRESSURE WITH TIME AT WEATHER STATIONS DURING 5TH DECEMBER 1972 (Pressure in Millibars)

Time	Abbotsinch	Prestwick	West Freugh	Mull of Galloway	Aldergrove	Malin	Machrahanish	Tiree
0000	990.6	991.8	992.8	994.0	995.0	990.8	990.0	986.8
0300	991.8	993.5	994.1	994.8	995.2	991.8	992.1	992.1
0600	990.0	990.7	990.6	990.6	989.2	982.8	988.7	982.7
0900	982.8	982.5	982.4	982.4	982.4	980.6	980.1	972.8
1200	977.7	980.8	982.4	984.4	985.1	978.5	979.0	968.4
1500	981.0	982.8	984.0	985.3	986.8	981.9	982.7	976.6
1800	984.0	985.6	986.0	986.3	988.0	985.4	985.2	981.1
2100	986.0	987.7	988.1	988.5	991.0	986.5	987.1	982.5
2400	988.4	989.3	990.0	990.8	991.3	987.6	989.0	982.5

Table 8.1

For the purpose of simulating storm surges using Model 1 (which has been described in Chapter 7) the meteorological effect on the tides must be recorded at the open sea boundaries of the model. Model 1 has three such open sea boundaries which are shown in figure 6.1. For the particular surge of the 5th December 1972, no tide recorders were present at the northern and western sea boundaries, however the surge record was available at Malin which is west of the western sea boundary. The only means of providing surge data at the northern and western sea boundaries was to take the surge recorded at Malin as representative of surge conditions at these sea boundaries. In figure 8.4 the recorded tide+surge elevations at Malin are shown together with the predicted tide. The difference between those curves is the recorded surge at Malin which is shown in figure 8.5. The recorded surge at Malin together with the predicted tides at Ballycastle Bay and Port Ellen provided the surge and tide input conditions at the western sea boundary ports. Similarly the surge at Malin together with the predicted tides at Crinan formed the input conditions for the smaller northern sea boundary. The tide and surge elevations at these three ports, found in this way are represented in figure 8.6.

At the southern sea boundary the available surge data was more satisfactory. Recording gauges were present at the landward ends of the boundary, namely Larne and Portpatrick. For many years, Portpatrick has been a class A port for tide measurement. For both ports the tide+surge elevations, together with their respective predicted tides are shown in figure 8.4. From this data the storm surge was calculated at each port and is shown in figure 8.5. A comparison of the surges in this figure at Larne and Portpatrick shows strong similarity of features, with the Portpatrick surge being slightly the larger. It is also evident from the ranges of the predicted tides at these ports that the surge of the 5th December 1972 occurred midway through a spring-neap tide transition.

8.4.2 Comparison of simulated results with recorded data

Tide gauge records of the December 1972 surge were used as a basis for comparison with the surge elevations computed at certain closed boundary points corresponding to the locations of the gauges. In the area represented by the model, only two gauges, one at Greenock, the

other at Millport, were able to provide surge records for this purpose. Both of these ports are situated in the upper Firth of Clyde, an area of complex topography and consequently an area which could not be accurately schematised using Model 1.

The recorded tide+surge elevations at both Millport and Greenock are reproduced in figure 8.7. The predicted tides are also shown so as to indicate the effects of the surge on the tide. It is apparent from both records that the maximum elevation occurs shortly after the predicted tidal high water at 1200 G.M.T. Also of importance is the fact that the duration of the peak elevations from 1200 G.M.T., to 1500 G.M.T., closely corresponds to the time interval when the maximum wind speeds occurred in the Firth of Clyde. These features were also produced in the surge simulation and are evident from the computed tide+surge elevations at Millport and Greenock shown in figure 8.8.

The maximum difference between the recorded and computed tide+surge elevations is 0.4 metres at 1200 G.M.T., at Greenock and in general the recorded elevations are slightly higher than the computed elevations. A comparison of the recorded and computed times of maximum elevation at both ports shows a phase difference of about forty minutes, the recorded phases being the earlier of the two. This phase lag also occurred in the results when simulating tide motion using this model (Model 1) and is evident from the results of Test 9 shown in table 7.9. It is therefore a limitation of the model which causes the computed phase to lag the predicted phase. Nevertheless the overall agreement between the recorded and computed tide+surge elevations at both Millport and Greenock is quite good.

In figure 8.9 the recorded and computed storm surges are depicted for comparison at both Millport and Greenock. The recorded surge has been obtained from figure 8.7 by subtracting the predicted tide from the recorded tide plus surge. Similarly the computed surge has been calculated from figure 8.8 by subtracting the computed tide from the computed tide plus surge. At both ports the phase difference between the recorded and computed surges is apparent and, as already mentioned, is considered to be a schematisation effect. A comparison at both ports also shows that the simulated and recorded surges at Millport have a higher correlation than at Greenock. This is possibly

because the model's schematisation is more representative at Millport than at Greenock, since the latter port is situated in the relatively narrow Clyde estuary. The overall agreement between the recorded and computed surge is quite good at both ports considering the accuracy of the sea boundary data.

An appreciation of the total magnitude of the surge in the Firth of Clyde is obtained from the curves in figure 8.9 which represent the total surge; that is the contribution from the external surge, wind stress and atmospheric pressure. The individual effects of these three components was subsequently analysed using the model. At this stage it can be concluded from the records at Malin, Larne, Portpatrick, Millport and Greenock that in this order, there is a corresponding increase in maximum surge from one port to the other. The highest maximum surge elevation of 1.55 metres occurring at Greenock. The increase in magnitude of the surge as it develops in its passage from Malin to Greenock can be attributed to a funnelling of the surge in that direction as a result of ever decreasing mean water depths and increasing confinement of the coastline.

At this point it is appropriate to consider the interaction existing between tides and surges, which has been identified by Proudman (1955) to be of hydrodynamic origin. More precisely, the interaction is caused by the action of friction and variations in the speed of propagation which modify a surge in the presence of a tide. These effects can be incorporated into the numerical scheme through the non-linear terms in the governing hydrodynamic equations.

As a means of studying the effects of the tide+surge interaction, the surge of the 5th December 1972 was simulated without the presence of the tides and the computed elevations compared to the computed surge obtained from the tide+surge simulation. This comparison between the surges, computed using the two different approaches is also presented in figure 8.9 for the ports Millport and Greenock. The simulation of the surge without the tidal presence required the external surge to be specified at the sea boundaries and so the input is effectively the data shown in figure 8.5. Referring to figure 8.9 it is apparent that the values of the surge computed without the tides are, in most instances, larger than for the surge computed with the tides. The differing results can be partly attributed to the way in which friction at the sea bed is calculated in the model. In this respect,

Taylor (1919) has shown that the frictional force is defined as

$$F = k_b \rho u^2 \tag{8.9}$$

where u is the mean velocity. Furthermore he showed that the work done by the frictional force E, can be expressed as

$$E = \tfrac{4}{3} k_b \rho \frac{u^3}{\pi} \tag{8.10}$$

It can be concluded from equation (8.10) that when the tide and surge waves are modelled simultaneously, the frictional dissipation will be proportional to the cube of the sum of their associated velocities. When modelled separately the net dissipation will be proportional to the sum of each velocity cubed. This conclusion has also been drawn by Prandle (1975) when simulating surges in the southern part of the North Sea.

The action of bottom friction in the manner described may also be one reason why a large maximum surge apparently seldom occurs on a high water spring tide in an estuary.

One of the distinct advantages of numerical modelling, as opposed to hydraulic modelling is the ease of isolating specific parameters so as to evaluate the importance of various components of a system. Such a technique has been applied to the storm surge of 5th December 1972 in order to assess the relative importance of the various terms which contribute to the generation of the surge.

The effect of each component of the surge at Millport and Greenock as computed by the model is as shown in figure 8.10. At both ports, the external surge, as a result of wind stress only, is the largest component of the peak surge, measuring 0.86 metres at Greenock. This effect is the largest since the generation of this component occurs over an area extending from the edge of the continental shelf to the locations of the model's open sea boundaries.

The contribution to the peak surge at both ports from the wind stress over the surface of the model is the second largest component. It has a maximum amplitude of 0.6 metres at Greenock and is a result of the effect of the shallow inlets of the Firth of Clyde on the wind stress terms.

At any point on the model's surface, pressure variations

introduce a slowly varying change in mean water level. The amplitude of this component is about 0.36 metres at its maximum and was evaluated in the model by the interpolating surface obtained from the atmospheric pressures measured at the weather stations. This component is therefore the smallest of all three in the Firth of Clyde during the occurrence of this storm surge. It can therefore be stated that in general the surge comprises the external wind surge at the open boundaries, the surge produced by the wind stress over the surface of the model, and the effect of low atmospheric pressures.

The simulation of each surge component was conducted in the presence of the tide and hence in figure 8.10 the components are compared to the recorded total surge which is also influenced by the tide. An interesting feature of the computed surges at Millport and Greenock obtained either from the external surge or from the wind stress effect, is that the peak surge in both cases is later than the recorded surge. It is concluded that the recorded peak surge produces the greatest depth of water and as a result the celerity is greater for this case than for the surge components. It is also found from a summation of the surge components at Greenock that the peak surge is about 1.72 metres. This value is greater than both the recorded maximum surge of 1.55 metres and the maximum surge of 1.44 metres computed with all components present at the same time. A possible explanation for this behaviour may yet again be related to interaction effects, notably the operation of the friction term in the model. It appears that with frictional dissipation proportional to the cube of velocity that a summation of frictional dissipation during each component surge is obviously less than the frictional dissipation produced when the components are present together, when producing the surge.

In many cases, an important consideration is the effect of the tide+surge interaction upon the extraction of surge from the recorded tide+surge elevations. This problem is fundamentally difficult to accomplish accurately because the phenomena are dynamically non-linear such that

$$\eta_s \neq \eta_{T+S} - \eta_T \qquad (8.11)$$

where η_T is the predicted tide free from surge interaction. Therefore a simple subtraction of the predicted tide from the recorded

elevations fails because of coupling effects. For example, as a result of the water depth being increased by the action of the storm the ordinary predicted tide will arrive ahead of schedule and will be lower in amplitude, but the total tide will be higher. As a result, the time of arrival of the tide is affected by the surge and a simple subtraction will make the difference, obtained in this way, show a more or less pronounced secondary oscillation having a tidal period. This effect has been pointed out by Groen and Groves (1962). One method of separating the two phenomenum is to account for the effect of the surge on the time of the tide by first shifting the time scale by a proper amount and then subtracting the predicted tide. This method has been proposed by Bretschneider (1967) but does not account for the reduction in tide elevation when coupled with the surge.

For the storm surge of the 5th December 1972, the calculation of the predicted tide at hourly intervals and its subsequent subtraction from the recorded tide+surge elevations is quite a lengthy and laborious procedure. Its execution could be more easily accomplished by developing a procedure for use on the computer. Referring to figures 8.4 and 8.7 it is apparent from the predicted times of high water at Malin and Greenock that they differ by about six hours. This time lag represents the required time for a tidal wave to propagate between these two ports. In contrast, figures 8.5 and 8.9 show that the time difference in the occurrence of maximum surge at Malin and Greenock is only about two hours. These values indicate the difference in propagation rate between the tide and surge processes. Another feature, which is related to the rapid occurrence of the surge, is its effect on the timing of the high waters near the time of peak surge. With reference to figures 8.4 and 8.7 it is evident that the recorded time of high water of the tide+surge elevations are as expected, not earlier than those of the predicted tide at all five ports. The subsequent extraction of the surge from these records, therefore, did not require a shift of time scale for the predicted tide in the manner already proposed. Instead a simple subtraction process seemed justified. It appears that the sea area has responded as a whole to the wind and pressure effect. The differences between surge heights at each location are a result of the local topography, especially the effect of shallow water, affecting surge generation in the Firth of Clyde.

Tide and surge elevations recorded on the 5th December 1972.

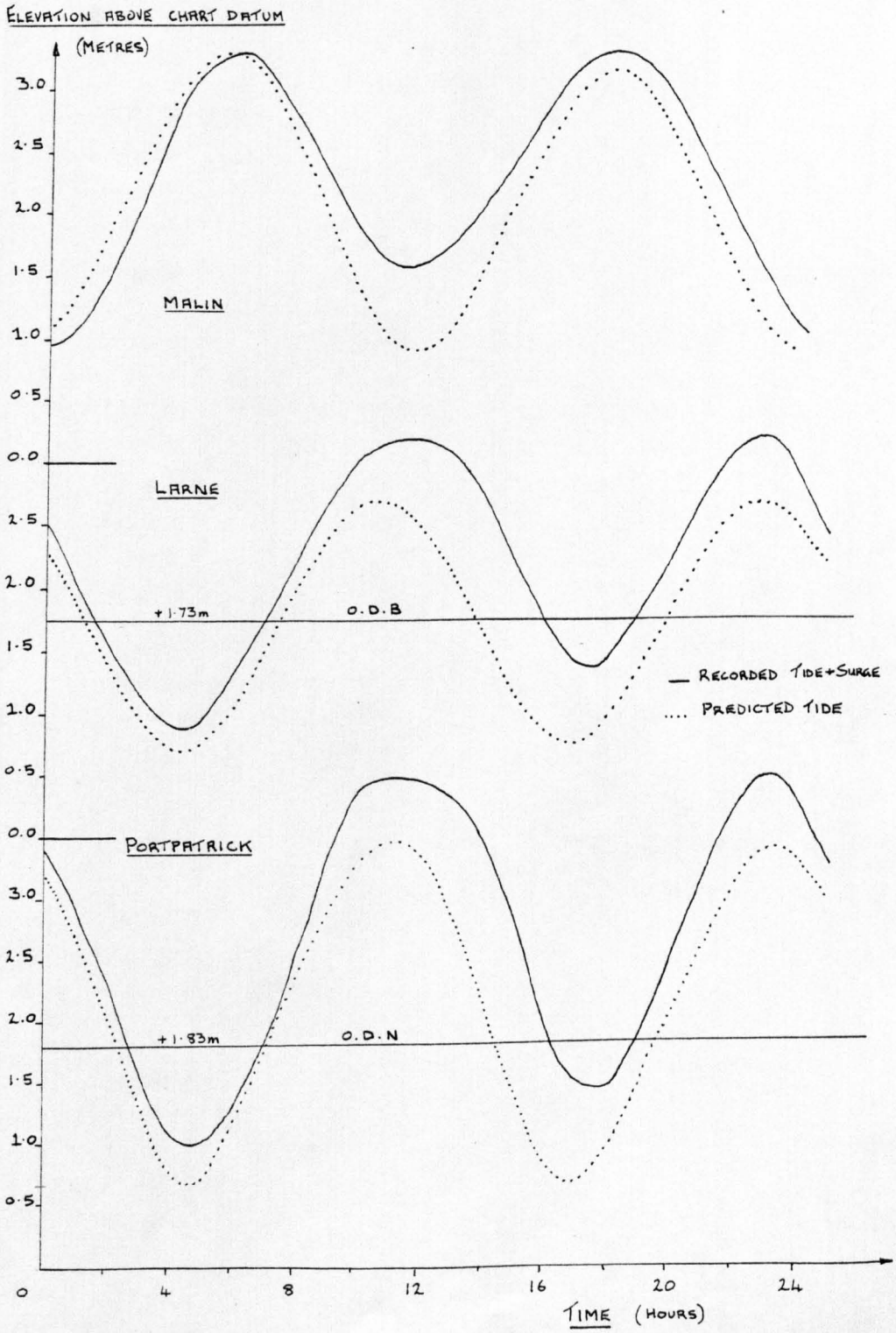

Figure 8.4

Recorded surge elevations for the 5th December 1972.

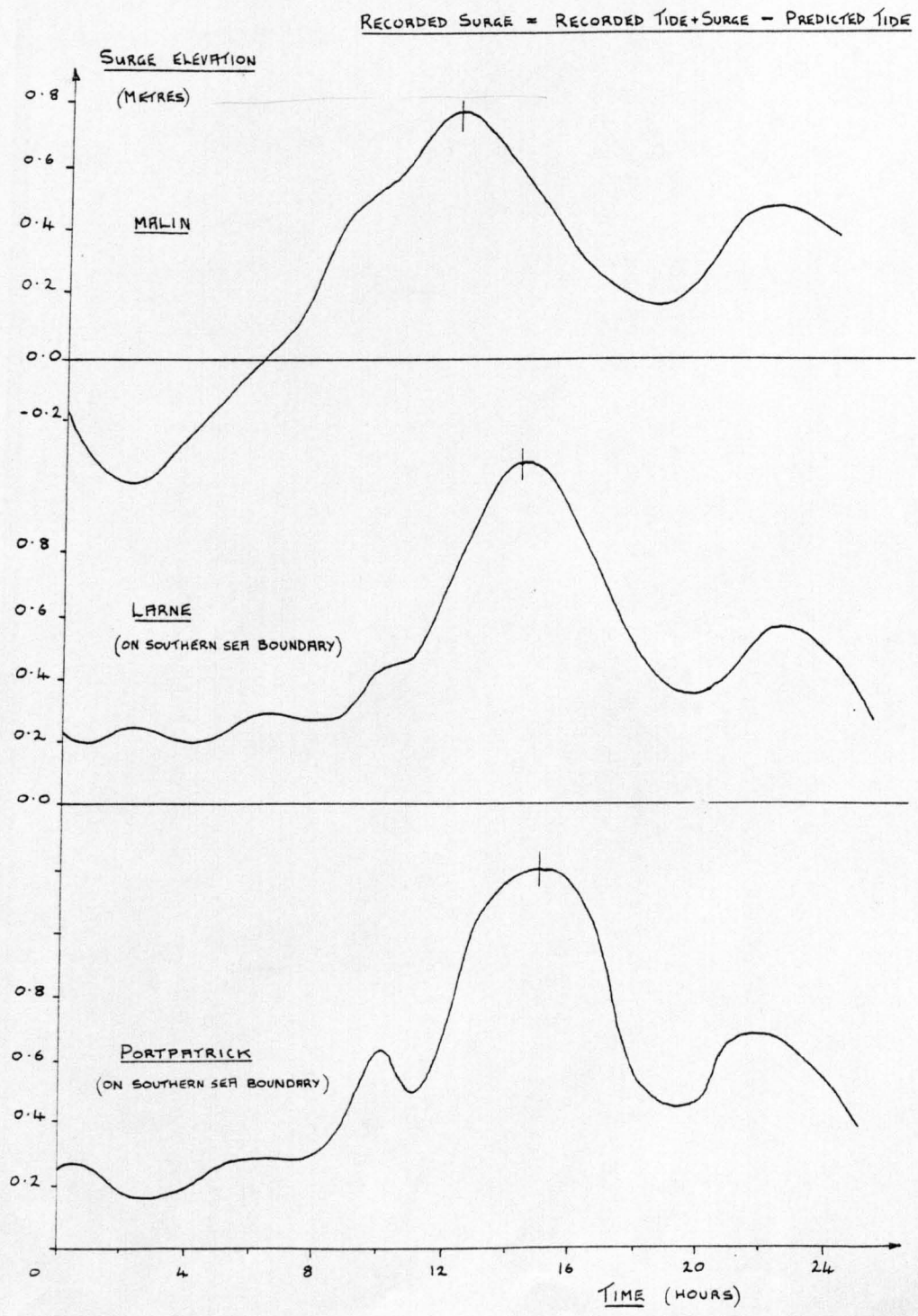

Figure 8.5

'Recorded' tide and surge elevations for the 5th December 1972 obtained from measurements at Malin.

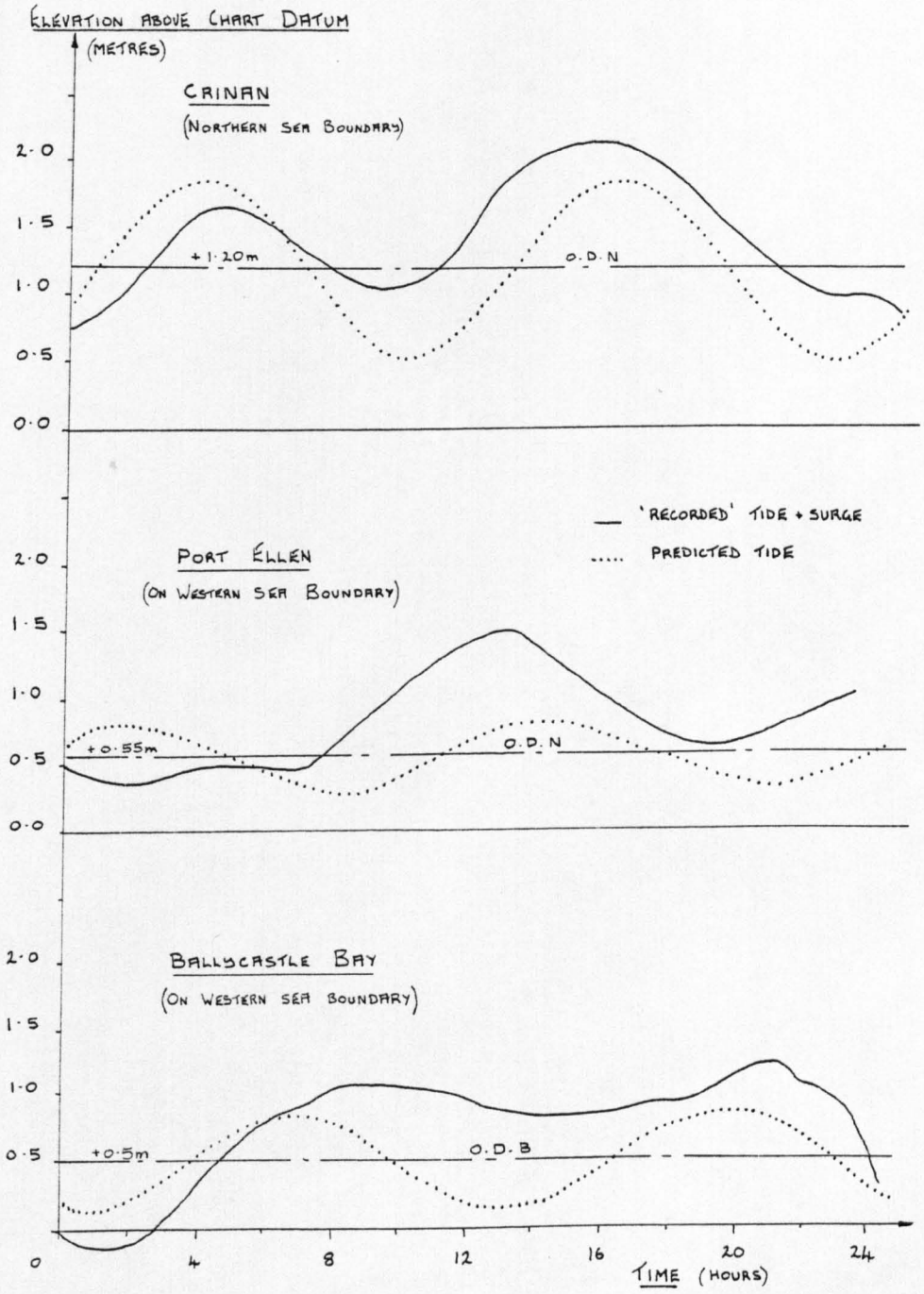

Figure 8.6

Tide and surge elevations recorded on the 5th December 1972 at interior locations in the model.

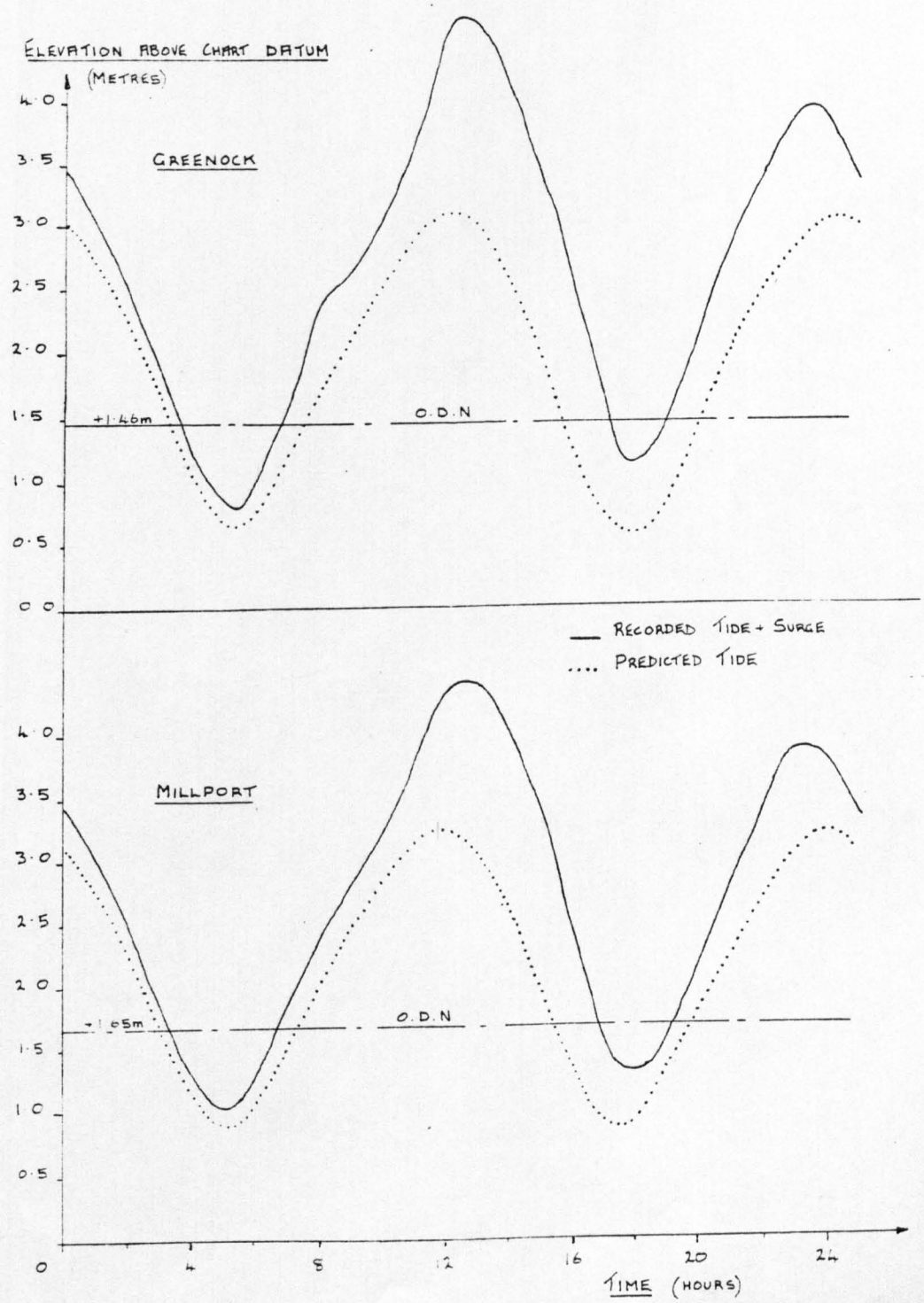

Figure 8.7

Computed tide and surge elevations for the 5th December 1972 at interior locations in the model.

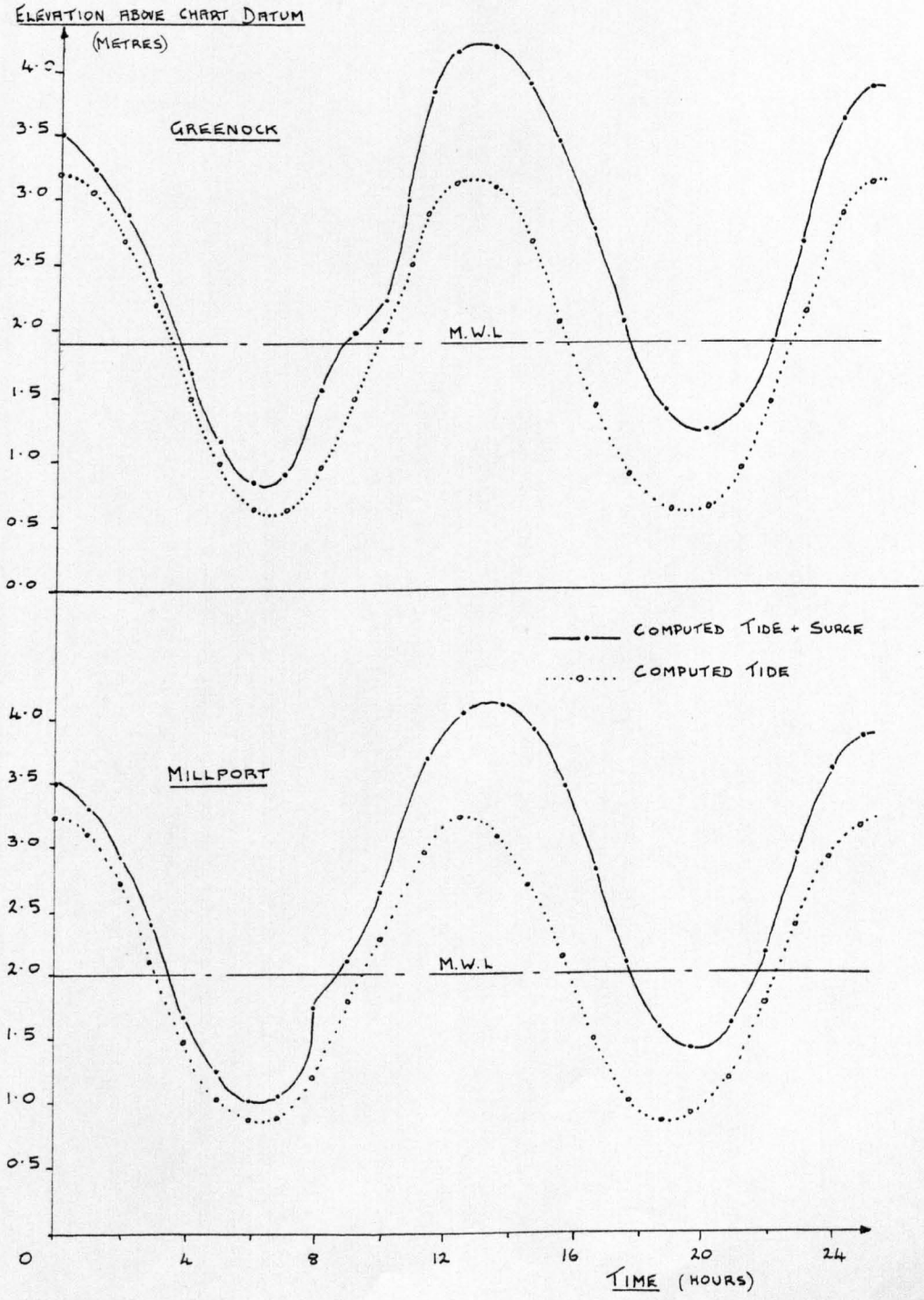

Figure 8.8

Comparison of computed and recorded surges at ports in the Firth of Clyde for the 5th December 1972.

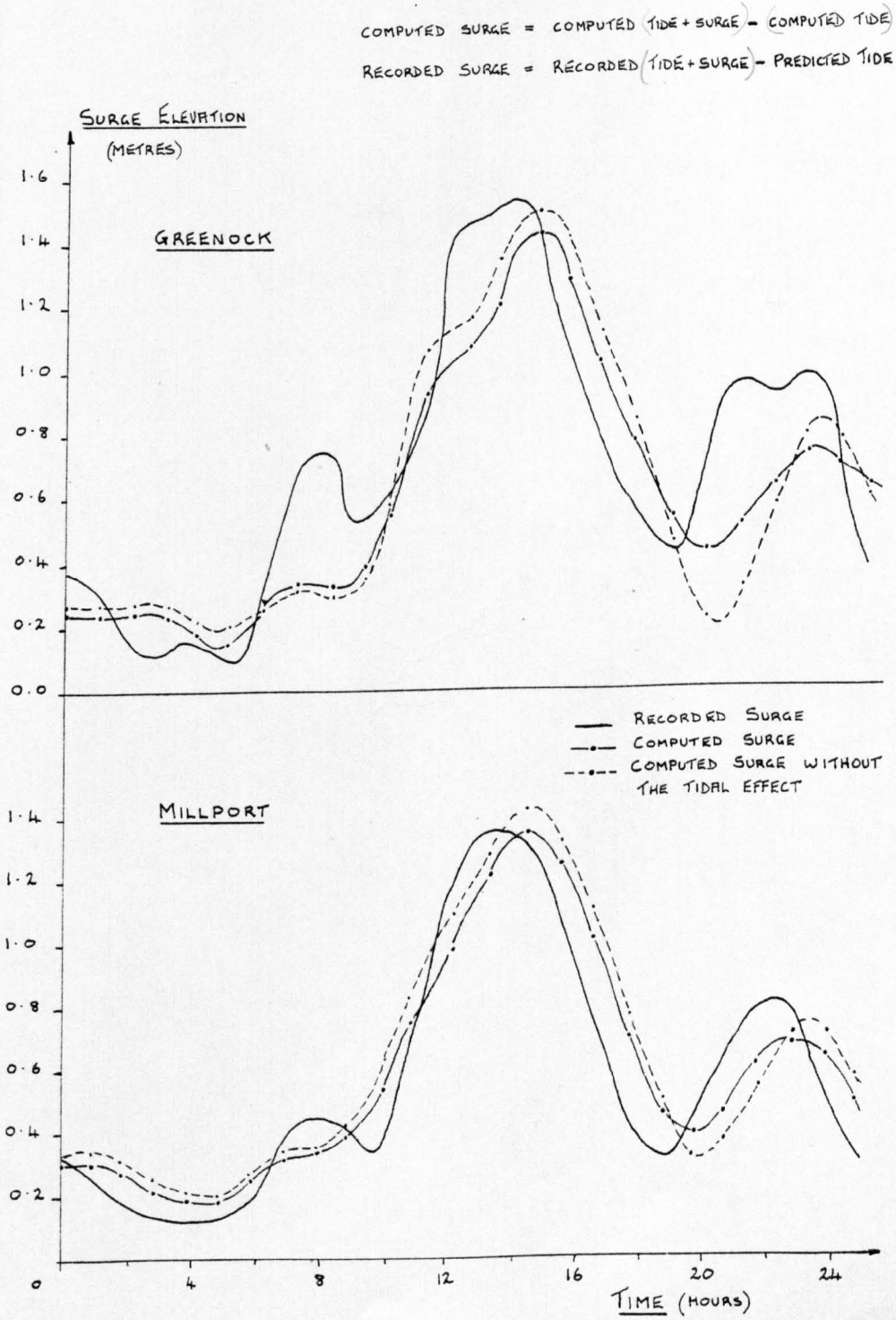

Figure 8.9

Computed surge components for the 5th December 1972 and a comparison with the recorded total surges at ports in the Firth of Clyde.

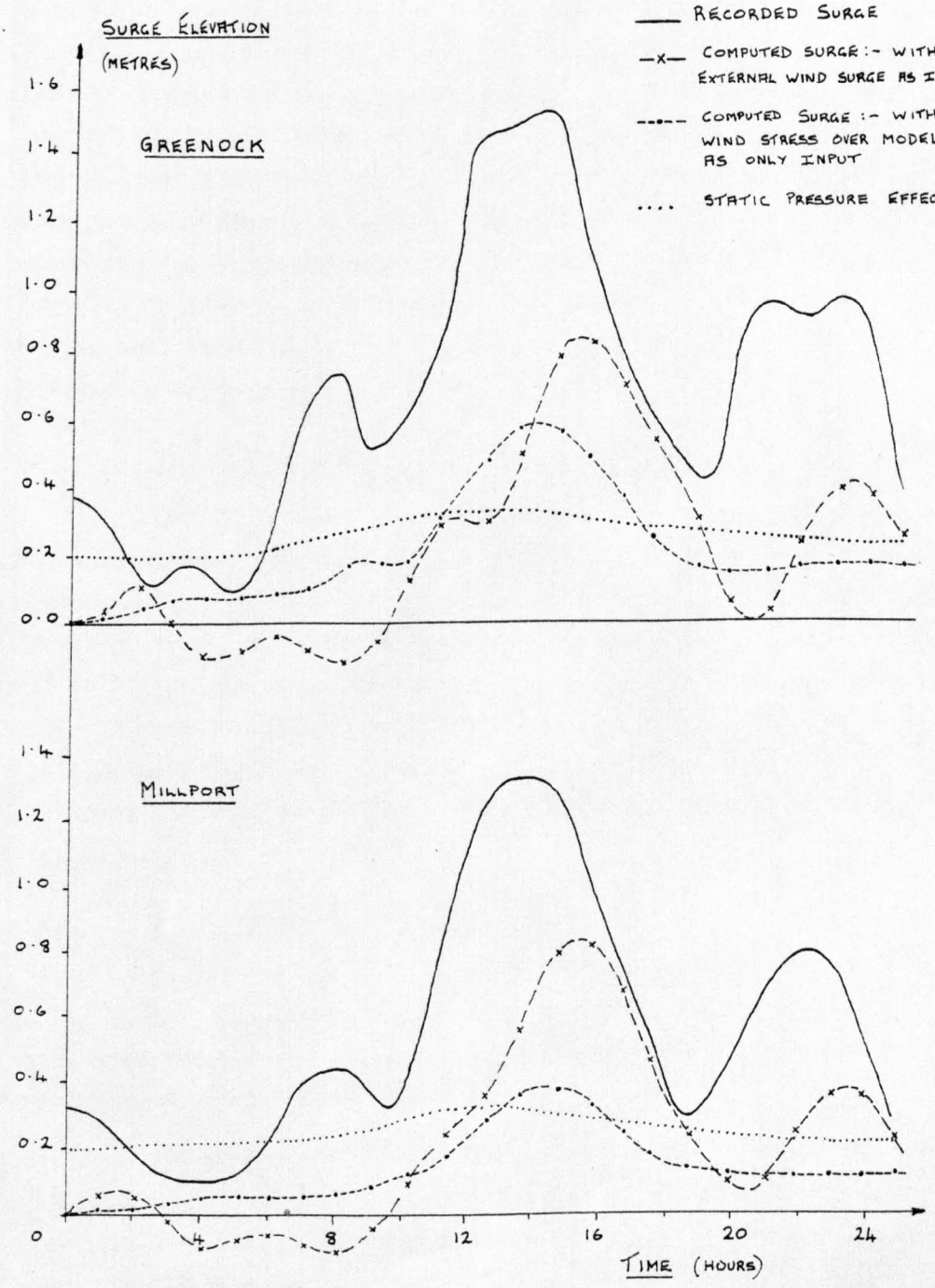

Figure 8.10

It can therefore be concluded that for the surge of December 1972 its duration or period is longer than either the tidal period or the natural period of the partly enclosed sea area considered. As a result, the surge and tide frequencies do not overlap to any great extent and the non-linear difficulties discussed previously are not serious. In more general terms this surge can be classified as being of low frequency, and this type of surge has in the past been extensively studied because of its damaging effect in small partly enclosed sea areas. In contrast there exists the high frequency transient surges of duration two to five hours that travel over a sea area which is large in comparison with the atmospheric disturbance involved. These surges of the running wave type can strongly determine the arrival of the tide since their frequencies overlap with those of the tide. The progression of these surges and the response of the sea surface at the open coast has been studied in Chapter 5.

8.5 THE STORM SURGE OF 7TH - 9TH MARCH 1979

Having successfully simulated a storm surge event using Model 1, another storm surge was considered for this purpose for two reasons. Firstly this surge, which occurred during 7th - 9th March 1979, was recorded on the tide gauges installed during the tidal survey and so surge data was available at all three open sea boundaries in the model. The same amount of information was not available for the 1972 storm surge. Secondly, by using the 2980 I.C.L. computer at Edinburgh it became feasible to simulate a storm surge with a duration of two and a half days.

8.5.1 Wind, pressure and surge data

Firstly the meteorological conditions during the 7th to the 9th of March are considered. These conditions were obtained from the daily synoptic weather charts, published by the Meteorological Office, and are summarised as follows.

During the 7th March a depression (Low C) to the northwest of Scotland moved away northeastwards and a new shallow depression (Low S) formed on the frontal trough between Scotland and Norway. On the 8th March a small but deep depression (Low R) close to southwest Norway moved

steadily northeast while another deep depression (Low L) to the west of Iceland moved slowly east. Accompanying frontal troughs moved close to northern Britain later in the day. During the next twenty-four hours the Icelandic depression intensified, moving slowly northeast between Scotland and Iceland. During the 9th to the 10th March this depression (Low L) moved north away from east of Iceland while its associated fronts over Britain moved away eastwards. During this period pressure remained low north of Scotland.

As a result of the presence of Low L, a positive surge occurred during the 8th and 9th of March 1979 on the west coast of Scotland. The magnitude of this surge was smaller than that of the 5th December 1972 because, the tract of the March 1979 storm was further away from Scotland and the depression moved more slowly. The depression was however deeper than that of the December 1972 storm. The parameters defining the storm are as follows and are comparable with those presented by Lennon, discussed previously.

a) The maximum surge occurred during 1800 G.M.T. on the 8th till 0800 G.M.T. on the 9th March. During this time the centre of the depression was about three hundred nautical miles north of the Orkneys.

b) During a thirty-hour time interval the depression travelled 820 nautical miles therefore its average speed was 27 knots.

c) The radius of depression was measured as 100 nautical miles.

d) The maximum depth of the depression below standard atmospheric pressure was 57 millibars.

The daily weather charts also provided pressure data at six-hourly intervals at six weather stations; this data is presented in table 8.2. No pressure data was available for the weather stations, Islay and Machrahanish and so was obtained by interpolating from the existing data. From the data it is apparent that the spatial variation of pressure over the Firth of Clyde and its approaches was small during the presence of the surge. The temporal variation however was more significant in this area, dropping by 25 millibars, during the 8th of March.

Wind speeds and directions at three hourly intervals were

THE VARIATION OF BAROMETRIC PRESSURE WITH TIME AT WEATHER STATIONS

DURING 7TH - 9TH MARCH 1979 (Pressure in millibars)

Time	Abbotsinch	Prestwick	Machrahanish	Mull of Galloway	Aldergrove	Malin	Islay	Tiree
7th								
1200	1003.0	1003.0	1000.0	1001.7	982.0	980.0	991.5	984.0
1800	1006.0	1007.4	1007.7	1007.9	1009.6	1008.4	1007.9	1006.5
8th								
0000	1009.0	1010.3	1009.7	1011.8	1011.7	1008.7	1009.5	1005.8
0600	1005.0	1006.7	1005.1	1007.4	1007.1	1003.0	1004.8	1000.1
1200	999.2	1006.0	1002.4	1001.7	1001.7	996.9	1001.4	993.9
1800	989.0	990.9	990.1	992.5	992.6	988.4	989.6	984.7
9th								
0000	982.0	983.5	983.6	986.7	987.6	983.7	983.6	979.5
0600	980.9	983.1	983.3	985.9	986.4	983.6	983.3	978.8
1200	983.1	984.4	985.0	987.7	989.9	987.2	985.8	982.5
1800	991.8	993.9	995.2	996.1	998.7	998.0	995.9	993.8
0000	1004.5	1001.6	1001.8	1003.2	1004.6	1002.0	1001.8	999.4

Table 8.2

Figure 8.11

Surface wind speeds recorded during the 7th - 9th March 1979.

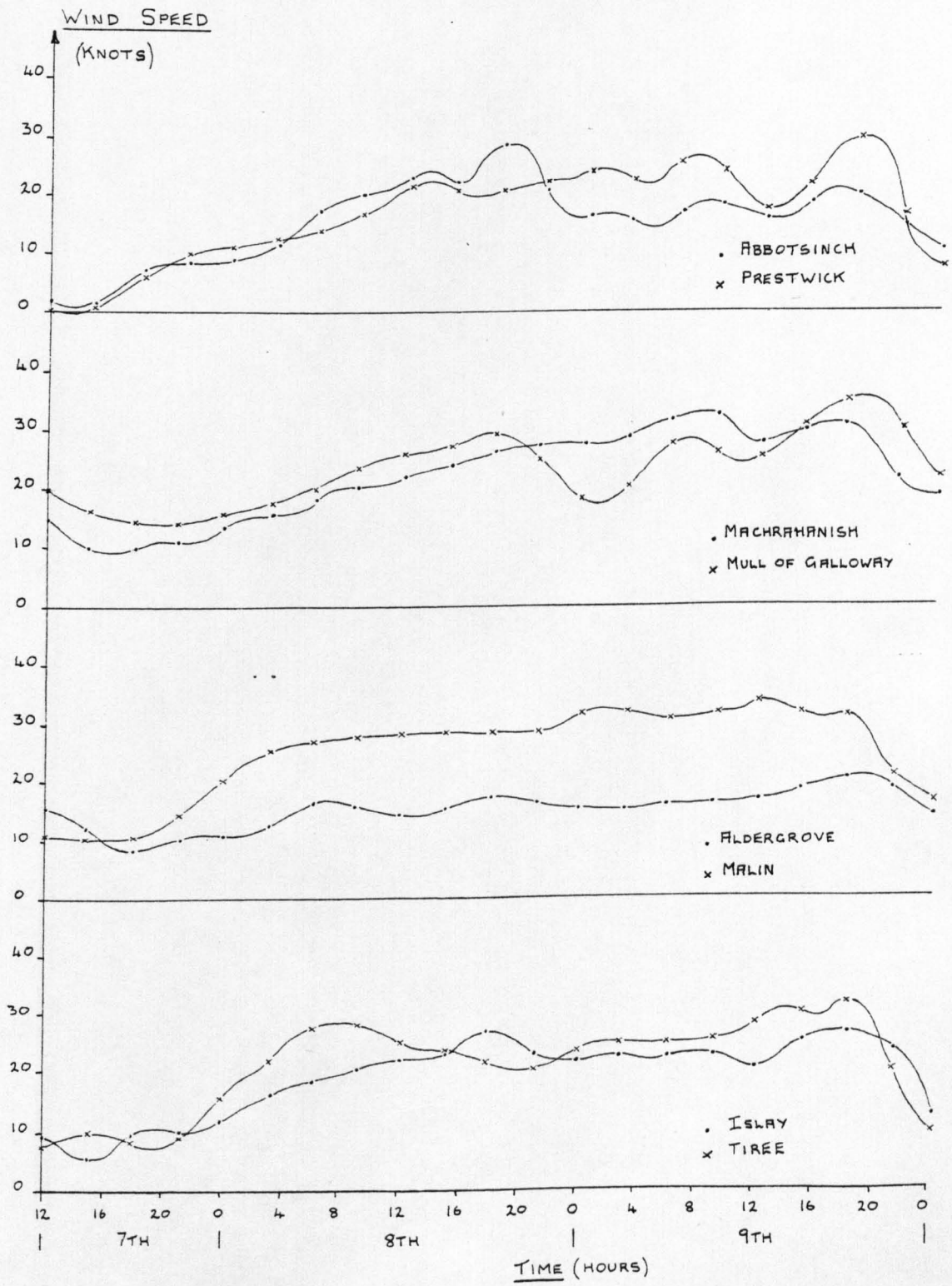

Figure 8.12

Surface wind directions recorded during the 7th - 9th March 1979.

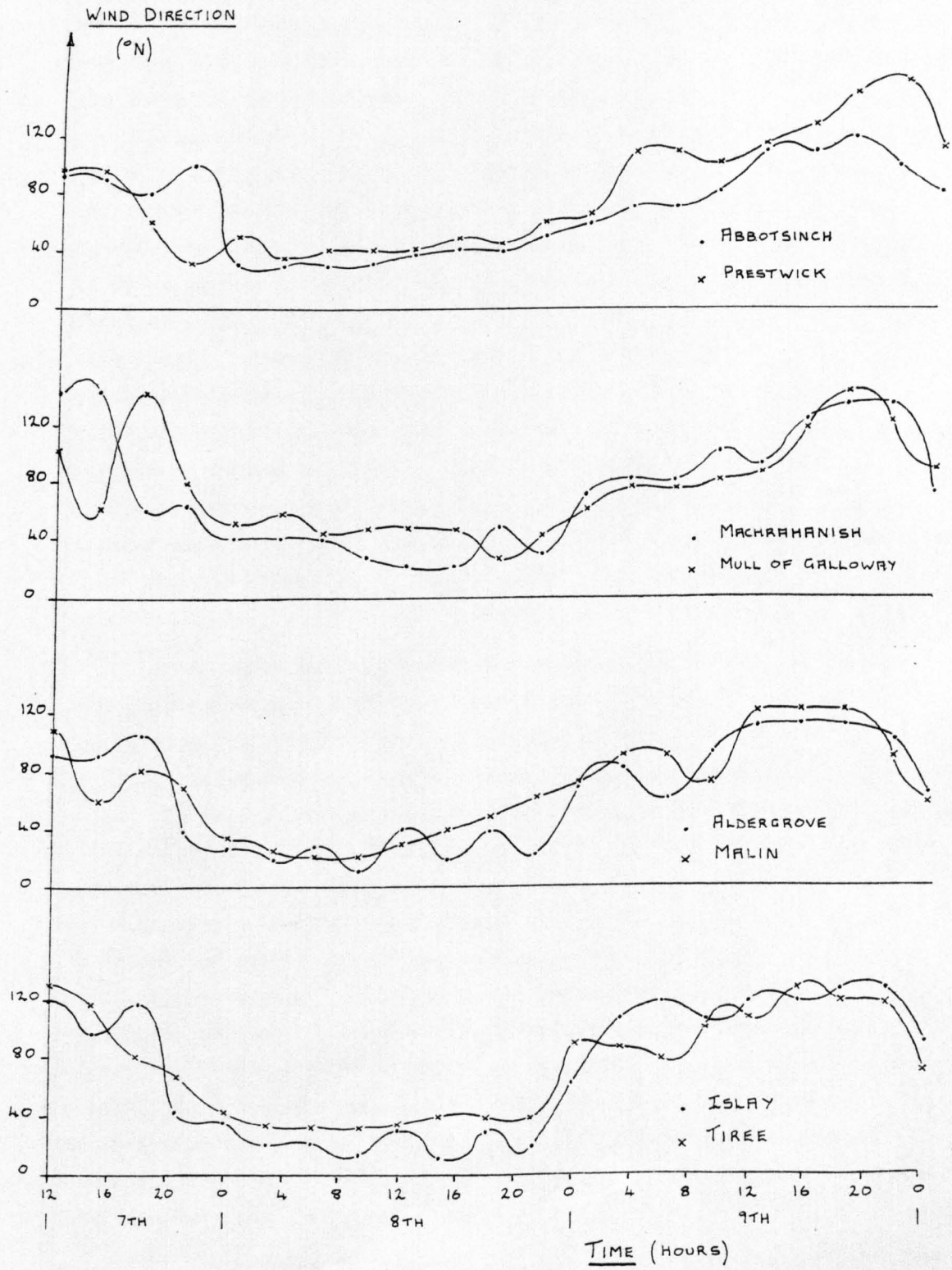

obtained from the Glasgow Meteorological Office for the eight weather stations; Abbotsinch, Prestwick, Machrahanish, Mull of Galloway, Aldergrove, Malin, Islay and Tiree. These wind speeds and directions are shown in figures 8.11 and 8.12 for the duration of the storm surge, and were obtained from measurements in the ten minute interval preceding the hour. With reference to the wind speeds in figure 8.11 there is general agreement for each station with an exception at Aldergrove where the wind speeds are slower. As already mentioned in section 8.4.1, Aldergrove is severely land-locked which accounts for the low wind speeds. At this station the maximum wind speed was 17 knots whereas at Malin it was 32 knots during the period of a positive surge in the Firth of Clyde. At many of the stations there was no distinct maximum wind speed; instead a gradual increase in wind speed occurred which remained relatively constant during the 8th and 9th of March. This state can be attributed to the relatively slow movement of the depression during this time. Also in good agreement are the wind directions at each weather station as shown in figure 8.12. During a greater part of the 8th, the wind direction is shown to be south-westerly which changes on the 9th to westerly and later still to a north-westerly wind direction.

A requirement of the model is that the external surge be specified as an input; this condition was satisfied as a result of having tide recorders at each sea boundary. Thus a tide recorder at Crinan provided the tide+surge elevations at the northern sea boundary whilst the Ballycastle Bay and Port Ellen gauges represented the western sea boundary and similarly the Larne and Portpatrick records provided data for the southern sea boundary. The records together with the corresponding predicted tides at the five ports are shown in figure 8.13. The predicted ranges and phases during this period namely the 7th - 9th March represent neap tide conditions occurring at that time. The important feature of all the curves is that the recorded tide+surge elevations do not arrive ahead of the predicted tide. This effect is possibly more apparent in the curves in which the tidal ranges are greater than the surge. Since no perceptible phase shift occurred and since the duration of the surge is relatively long, it can be concluded that the surge is of low frequency.

The duration of the surge can be more readily appreciated in

figure 8.14 in which the recorded surge at each of the five ports is presented. Certain major features of the surge should be highlighted since these characteristics are evident in the records at each port to a greater or lesser extent. Firstly, wind conditions were not of storm intensity during the 7th March yet negative surges were recorded at all ports. At some ports these negative surges were sustained till 1200 G.M.T. on the 8th March. These negative surges, which may be attributed to the stormy conditions on the 5th and 6th March, could have been produced by dynamic oscillations following a release of the positive surge or surges occurring during the 6th March. Secondly, from 1200 G.M.T. on the 8th March till 2000 G.M.T. on the 9th wind speed remained fairly constant while its direction progressively changed from south-westerly to northwesterly. During this time interval a flat shaped surge was recorded at each of the five ports. The recorded maximum height of the surge at these ports was about 0.6 metres and occurred during 0000 G.M.T. and 0400 G.M.T. on the 9th March. The final gross characteristic of the recorded surge occurs from 1800 G.M.T. on the 9th March and is a small negative surge. At this time the wind speeds are diminishing and the negative surge possibly corresponds to a release of the earlier positive surge.

These aforementioned observations describe the surge features such that they occur almost simultaneously at each port. This follows from the fact that the spatial extent of the storm surge is large in comparison to the area represented in the model. A similar reasoning applied to the storm surge of 5th December 1972.

8.5.2 Comparison of simulated results with recorded data

An evaluation of the accuracy by which Model 1 reproduced the storm surge conditions of the 7th - 9th March 1979 was made at certain locations corresponding to the availability of tide records. For this purpose, records from tide gauges situated at Campbeltown, Millport and Greenock were obtained. Campbeltown is situated at the southwest entrance to the Firth of Clyde whilst Millport and Greenock are located at the head of the Firth with Greenock the most northerly port.

The recorded tide+surge elevations at the three ports are

reproduced, together with their respective predicted tides, in figure 8.15. Most apparent in all three sets of curves is that the surge effect has not radically modified the tidal oscillations, since the latter effect dominates the total displacements. Another distinction of the recorded tide+surge elevations at the three ports is that their times of high water did not occur before those of the predicted tides. In fact during the period of positive surge the phases of recorded and predicted tides are very similar. For comparison with figure 8.15, the computed tide+surge elevations and the computed tide at each of the three ports are shown in figure 8.16. The computed tide+surge elevations also exhibit the general features of the recorded tide+surge elevations. An interesting feature occurring in both figures is that during the time interval of the positive surge there is no apparent growth in the surge from Campbeltown to Greenock at the times of recorded or predicted high water. This is evident from a comparison of the differences between the recorded and predicted elevations at each port. In contrast, the same comparison of differences at the three ports at times of low water shows that there is an increase in surge magnitude proceeding from Campbeltown to Greenock. At each occurrence of low water the increase in surge elevation between Campbeltown and Millport was found to be 0.13 metres. Similarly the increase in surge height between Campbeltown and Greenock at low waters was measured at 0.25 metres. The growth of the surge between these ports at low water is more apparent in the recorded elevations and is a very interesting feature. It may possibly be produced as a result of frictional effects being smaller at low water than at high water but this would not explain why there was no surge growth at high water.

The accuracy of the computed surge can be properly assessed by comparing it with the recorded surge as shown in figure 8.17. Both the computed and recorded surges at each port were derived from respective curves in figures 8.16 and 8.15. On comparison, the largest discrepancy between the computed and recorded surges occurs at Campbeltown and Millport during the negative surges on the 7th and early 8th of March. Possibly the recorded negative surges are produced by storm conditions on the 5th and 6th of March. If this is the case, then the model cannot reproduce the negative surges because conditions on the 5th and 6th are not included in the input. Supporting this idea is the fact

that the model reproduced the negative surge at the end of the 9th March without any difficulty. Considering the computed and recorded positive surge at the three ports in figure 8.17 it is apparent that in general the computed surge is the higher, by about 0.2 metres at some points.

The smoothness of the computed surges and the greater similarity of shape at the three ports, in comparison to the recorded surges, suggests that the resolution of the model insufficiently represents variations in the local topographic features of the upper Firth of Clyde. For example, at 1600 G.M.T. on the 9th March a small positive surge occurring at tidal low water increased in magnitude on proceeding from Campbeltown to Millport, and then to Greenock. The same growth of this small surge was not reproduced by the model. It is also evident from the recorded surge, that the peak surge of 0.86 metres at Greenock occurring at 1800 G.M.T. emerged from a smaller positive surge further south, since at Campbeltown the corresponding surge is only 0.4 metres. At this time the wind direction being southwesterly, was favourable to the orientation of the Firth of Clyde. The wind direction later changed to northwesterly and as a result, another peak surge at Greenock of the order of 0.8 metres was not produced. It appears that a wind direction with a northerly component is not so effective as a southerly wind in generating surges in the upper Firth of Clyde, which may be intuitively obvious.

The simulation of the storm surge of the 7th - 9th March 1979 was also performed using Model 3 which represents the Firth of Clyde and has a finer gridsize than Model 1. As mentioned previously in section 7.4 the sea boundary of Model 3 extends from Sanda-Sound, near Campbeltown to Portpatrick. The external surge can therefore be specified in the model using the Campbeltown and Portpatrick records as shown in figures 8.15 and 8.13 respectively.

A comparison of the computed and recorded surges at Millport and Greenock is presented in figure 8.18, and the agreement at both ports is very good. It would be misleading to assume that the agreement, although superior to that shown in figure 8.17 using Model 1, was totally achieved through using a finer grid. The gridsize was no doubt a significant factor but of possibly greater importance were the open sea boundary conditions. In comparison to Model 1, the sea boundary

conditions for Model 3 are more similar to the conditions recorded at locations in the interior of the model. The dominance of the boundary conditions, namely the external surge, can be appreciated in figure 8.18 by comparing the computed total surge with the smaller surge computed using only the wind stress terms over the model's surface. For example at Greenock the total recorded maximum surge elevation was about 0.8 metres while the wind surge contribution over the Firth of Clyde was only 0.2 metres in maximum height. The maximum positive wind surge as shown in figure 8.18 was computed with slowly increasing wind speeds until 0800 G.M.T. on the 8th March and thereafter constant wind speed conditions. The significant feature was that the maximum positive wind surge resulted from a southwesterly wind direction. After 0000 G.M.T. on the 9th, the wind direction was westerly resulting in a reduction in size of the positive wind surge. Later on the 9th March the wind direction changed from westerly to northwesterly producing a negative wind surge at Greenock and Millport from 1400 G.M.T. to 2200 G.M.T. on the 9th March. Thus the three wind directions mentioned evidently have markedly differing effects on the computed wind surge, with southerly wind directions producing positive wind surges in the upper Firth of Clyde and northerly wind directions producing negative surges.

An accurate assessment of the model's ability to reproduce the surge conditions, is restricted by the limitations of the data providing the input to the model and used for comparison with the output. Nevertheless the simulation of both surge events appears to be comparable with the recorded data and from this analysis some useful observations were made regarding the effects of wind direction on surges in the Firth of Clyde.

While the model has demonstrated an ability to simulate storm surges in a nearshore environment the method of simulation is strongly dependent on prior knowledge of the external surge elevations. Only by extending the model to the edge of the continental shelf, where the storm surge originates, can the wind stress terms in the model be more accurately assessed. This possibility is examined in Chapter 9.

Figure 8.13

Tide and surge elevations recorded during the 7th - 9th March 1979 at ports on the open sea boundaries of Model 1.

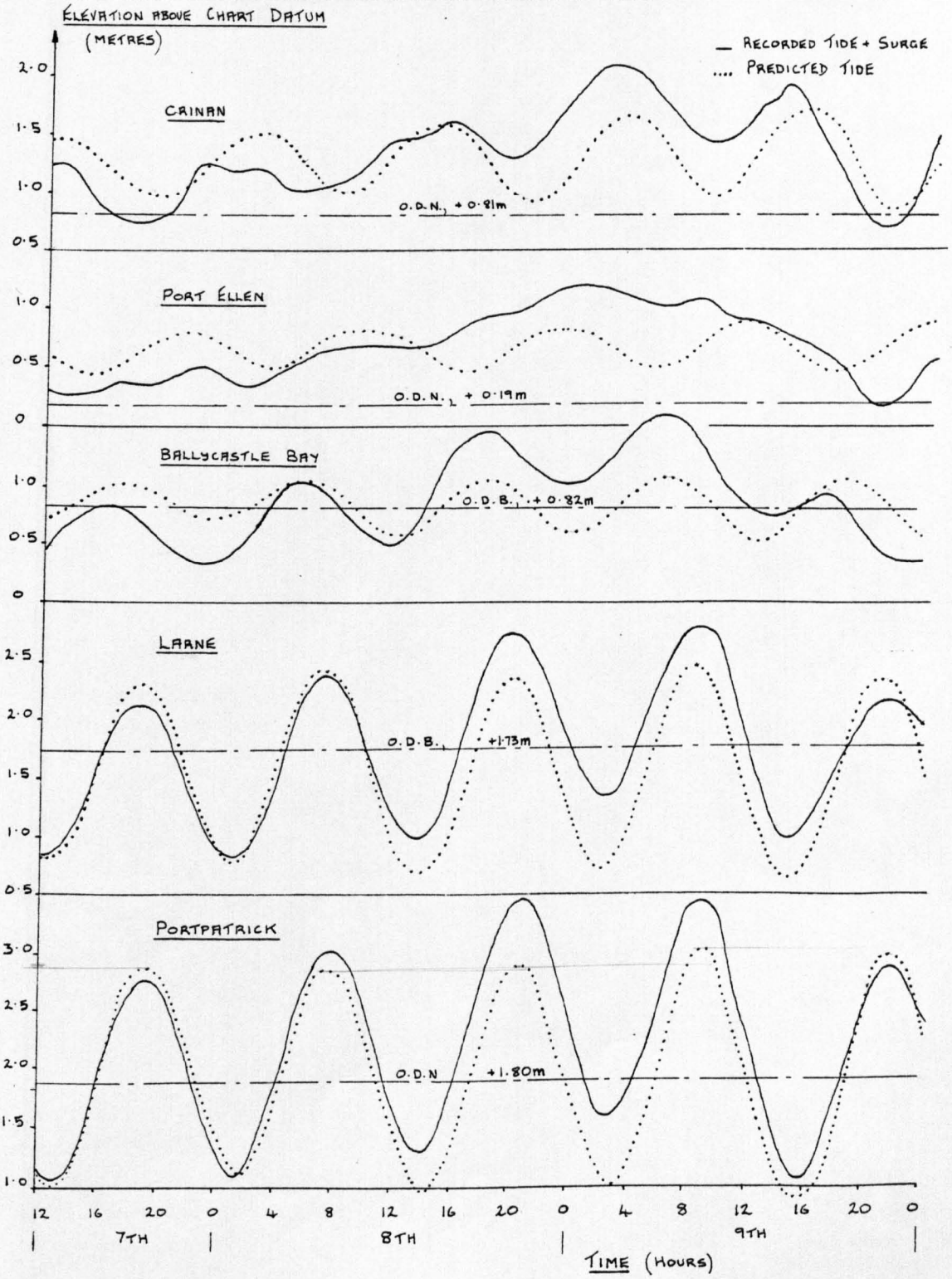

Figure 8.14
Recorded surge elevations for the 7th - 9th March 1979 at ports on the open sea boundaries of Model 1.

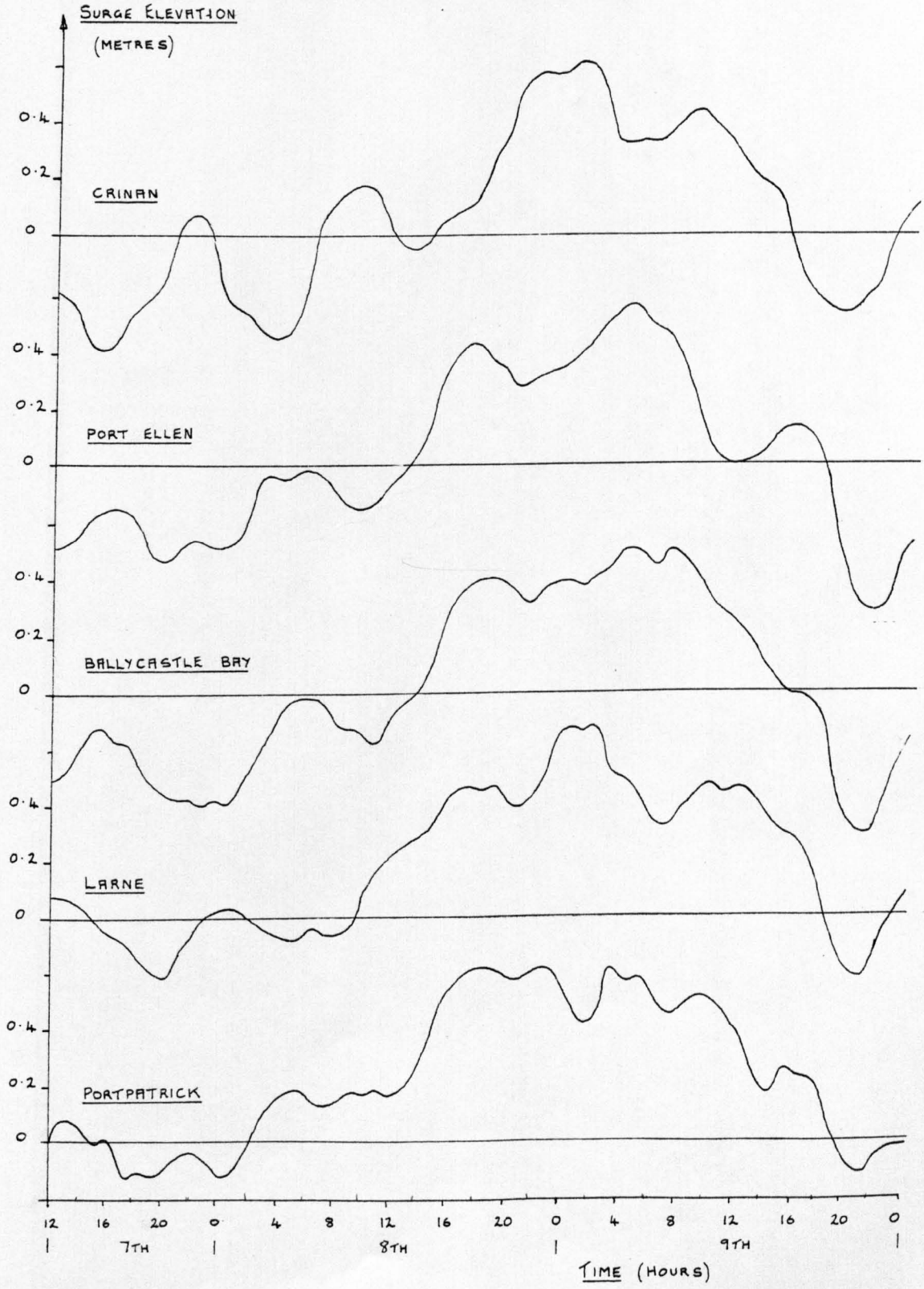

Figure 8.15

Tide and surge elevations recorded during the 7th - 9th March 1979 at ports in the Firth of Clyde.

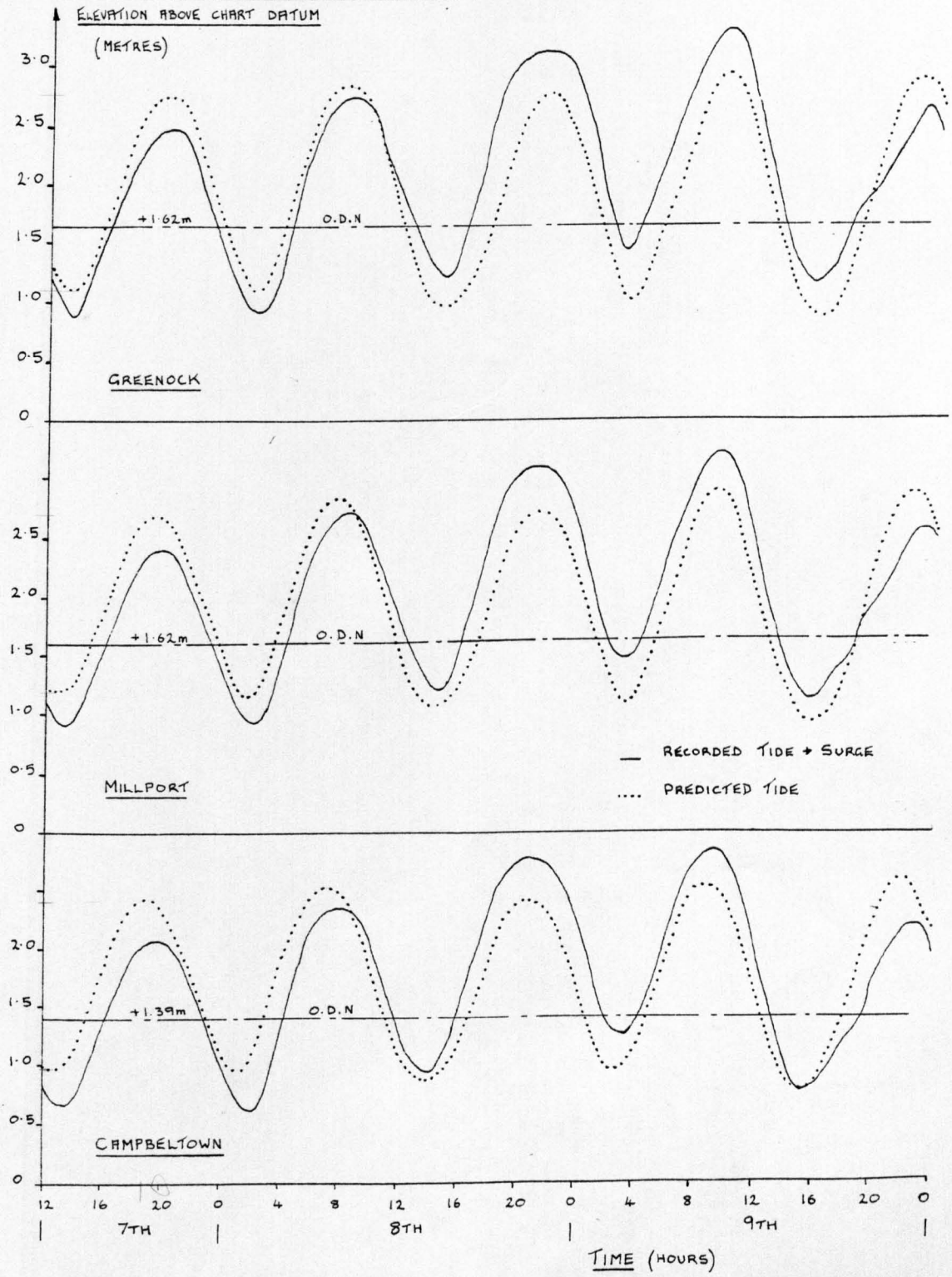

Figure 8.16

Computed tide and surge elevations for the 7th - 9th March 1979.

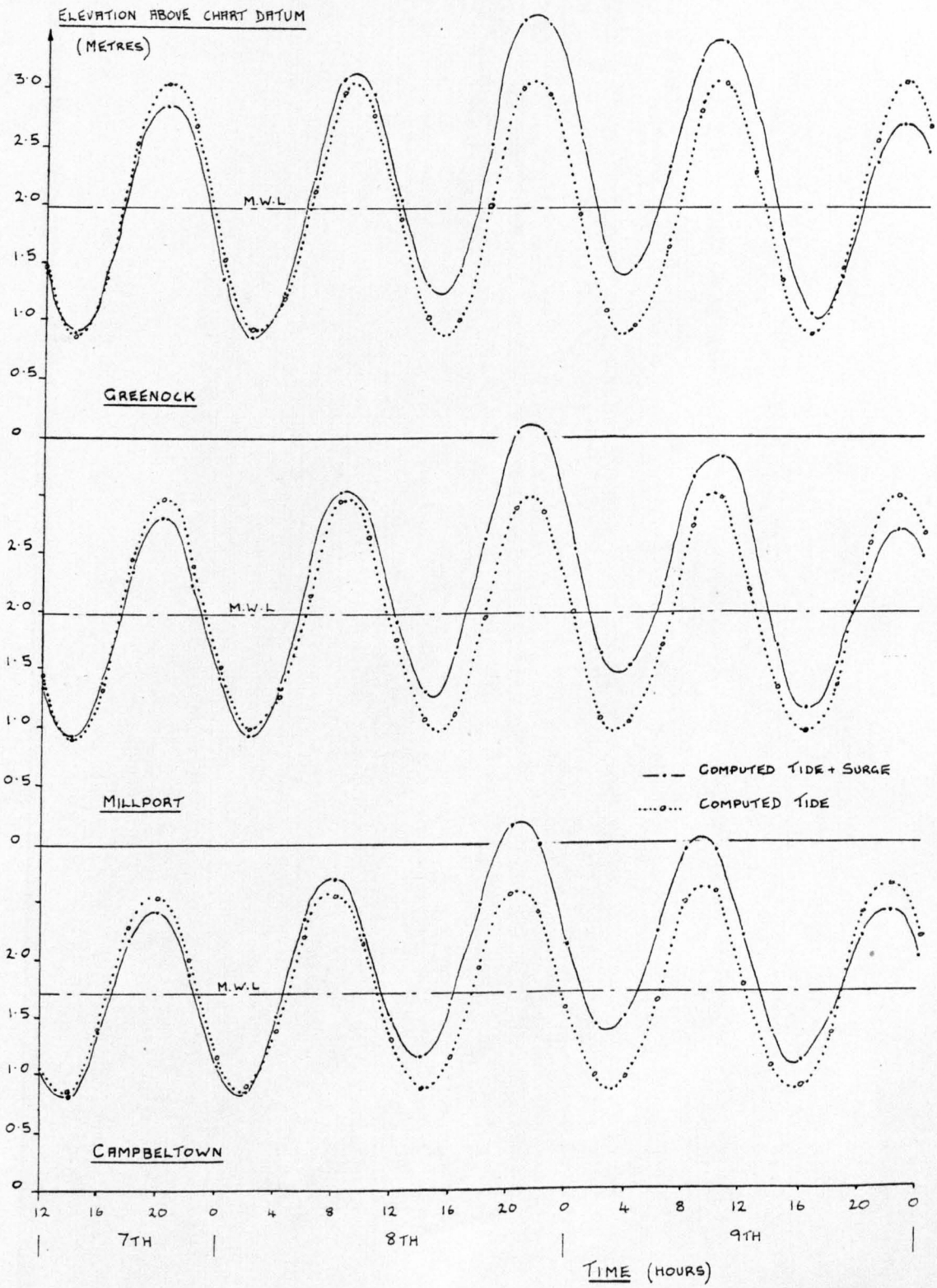

Figure 8.17

Comparison of computed and recorded surges at ports in the Firth of Clyde for the 7th - 9th March 1979.

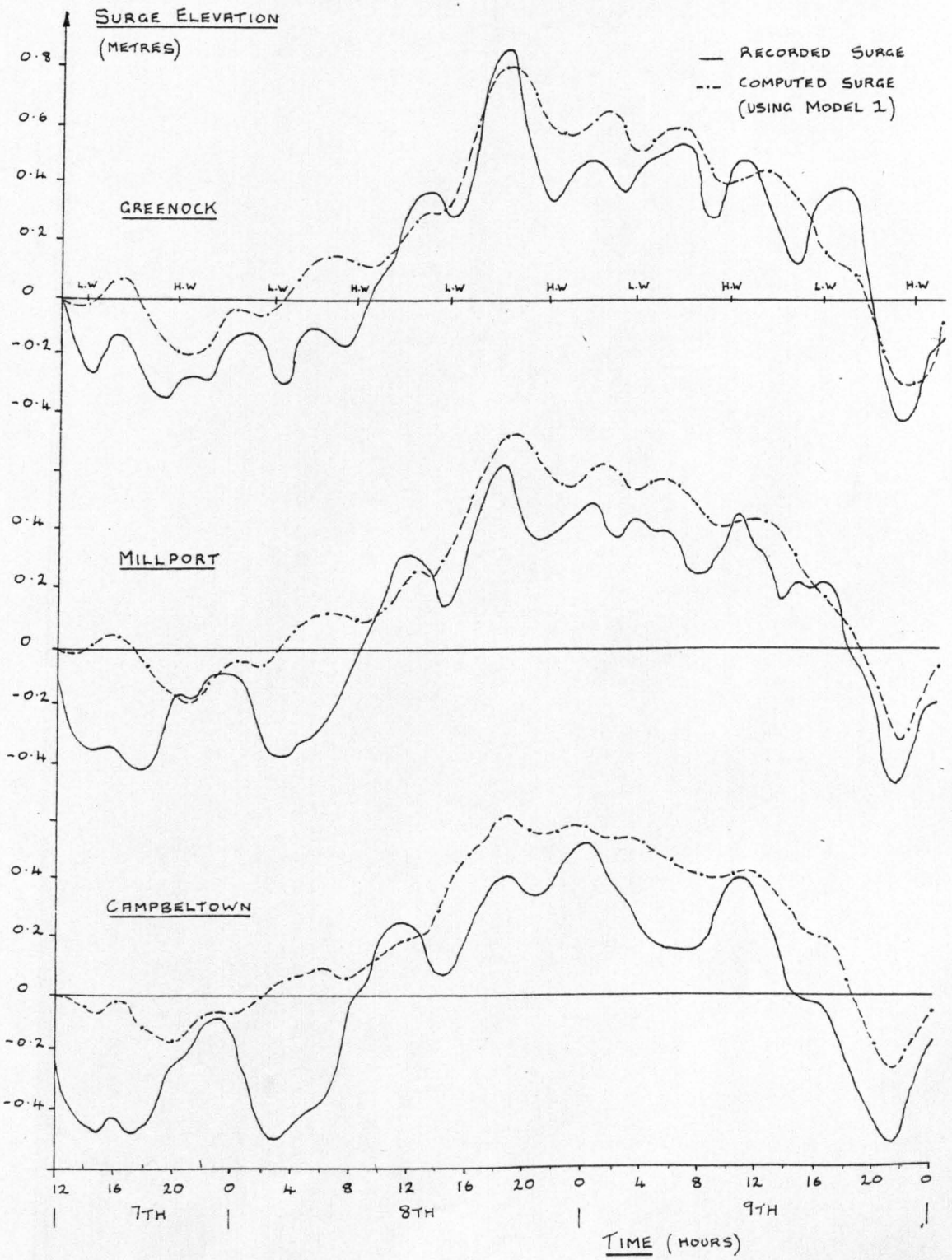

Figure 8.18

Comparison of computed and recorded surges at ports in the Firth of Clyde for the 7th - 9th March 1979.

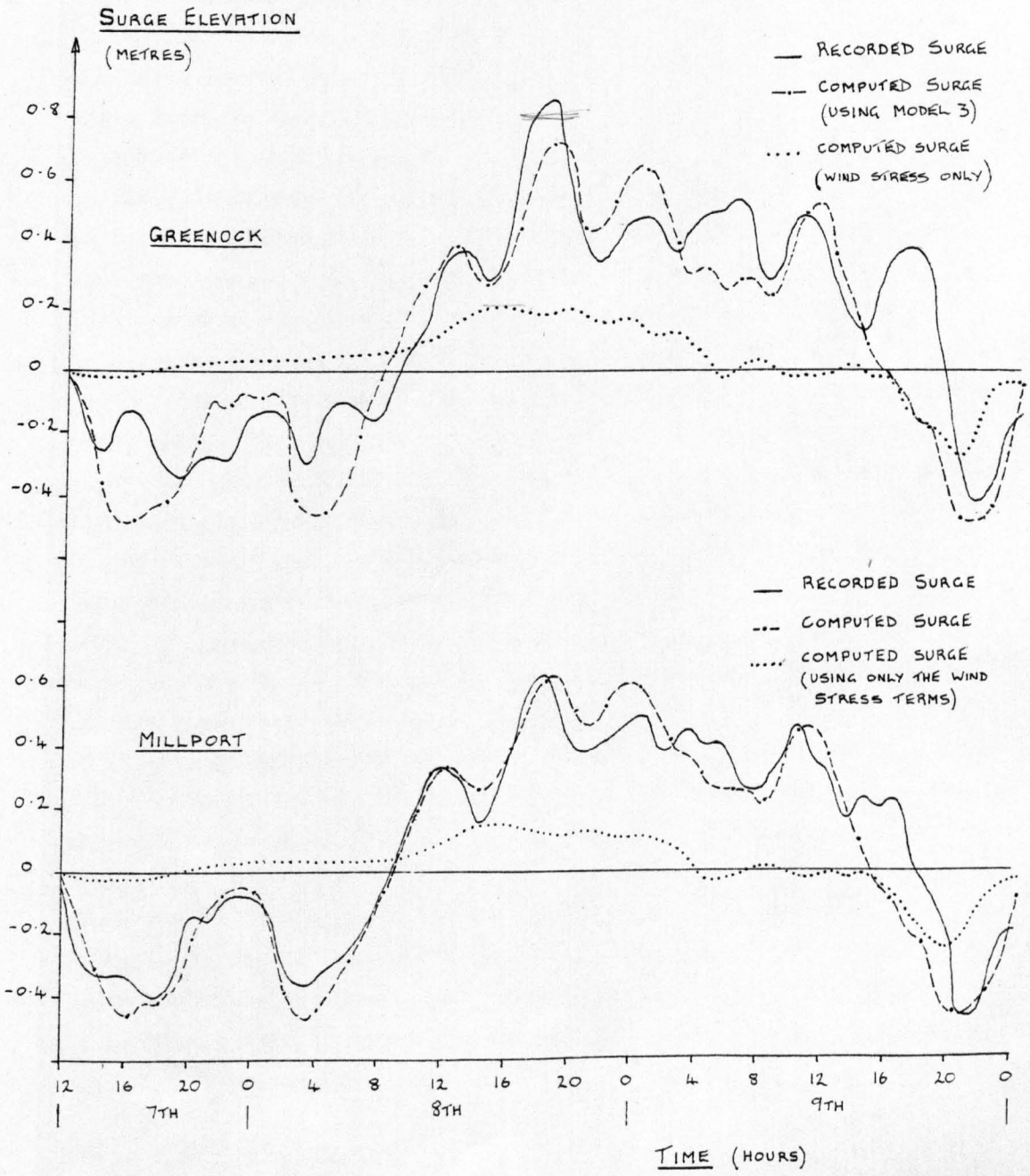

CHAPTER 9

A CONTINENTAL SHELF MODEL FOR THE WEST COAST OF CENTRAL SCOTLAND

9.1 INTRODUCTION

Previous surge simulations have shown that the 'external surge' was required as an input to the model in order to specify the surge conditions completely. Referring to the two surges analysed in Chapter 8, it is apparent that in each case, the largest component of the surge in the Firth of Clyde was produced by the external surge. Apart from the difficulties caused by incomplete data for representing the external surge at the open sea boundaries of the model, it also complicates the problem of evaluating the response of the model to the wind stress effect. A more effective method of assessing the wind stress effect is to develop a model which considers the topographical features of the area, and uses a variable wind stress coefficient in a manner similar to the Clyde sea area models, but which also extends to the edge of the continental shelf. With these features the model represents a more refined version of the shelf model used in section 5.6 which was limited to linear mean depths, a constant wind stress coefficient and a wind direction normal to the shore. In both the model tested in section 5.6 and the shelf model outlined in the next section, the external surge was assumed to be negligible. Thus at the open sea boundary corresponding to the edge of the continental shelf, the condition $S = 0$ was applied in the models. This condition has been studied theoretically by Veltkamp (1954) and Weenink (1954) for the case of a rectangular shallow sea bordering on an infinite ocean and being in equilibrium with a wind blowing over it. It appears from these studies that the above boundary condition is indeed a good approximation to actual conditions, especially if the ocean is very deep. In a practical contex, Heaps (1969) investigated the contribution of the oceanic surge to the disturbance in the North Sea. From a comparison of surge response in the North Sea using two models, of which only one included the oceanic areas, he concluded that a surge is generated on the shelf with little contribution from the ocean.

9.2 THE SHELF MODEL

The extent of the continental shelf off the west coast of Scotland

The Scottish west coast continental shelf and the sea area enclosed by the shelf model. (Model 4).

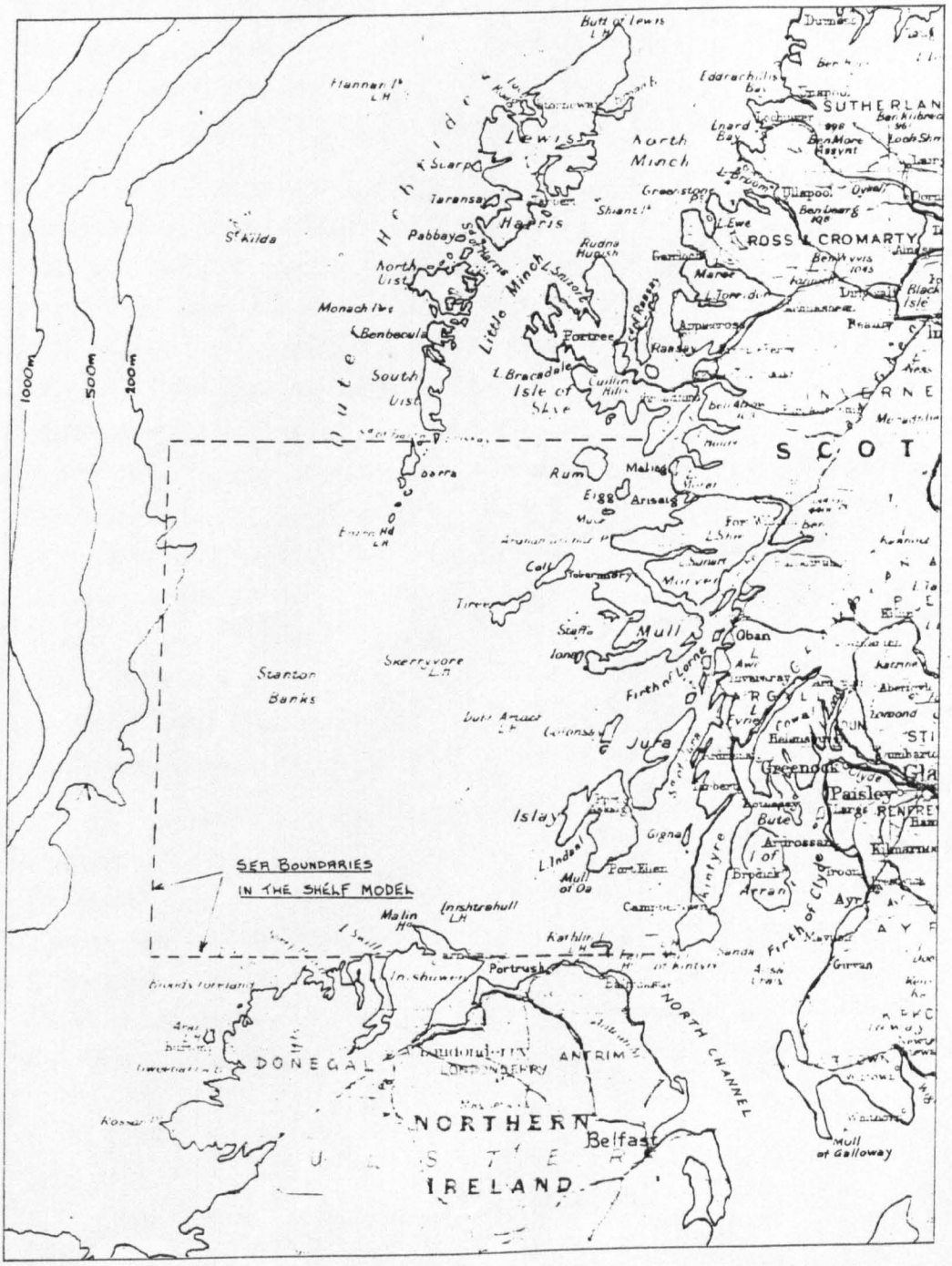

SCALE 1: 2,500,000

Figure 9.1

and the shelf area represented by the model are shown in figure 9.1. This shelf area situated off the west coast of central Scotland effectively comprises of the shallower waters of the Atlantic Ocean. In comparison to the Clyde Sea area, the shelf area has a simpler bathymetry and is less influenced by the coastal topography. Consequently the model was contructed with a larger spacestep than the Clyde models without undue loss in accuracy. Indeed a shelf model covering this area with a fine grid is impractical owing to its demand on machine time.

With a spacestep of 12 km and a timestep of 207 seconds, the shelf model namely Model 4 extends across a shelf width of 216 km (116 nm) until a depth of 160 metres is reached. The mean water depths were found from Admiralty Chart 2635 and are shown in figure 9.3 for all grid points. The coastline schematisation is also apparent from this figure. From the mean depths shown in this figure, the average longitudinal mean depths on the shelf were calculated and are plotted in figure 9.4. Shown also are the linear mean depths chosen to represent the bathymetry of the shelf for the semi-analytical study in Chapter 5. It is apparent from the non-linear depth profile that depths greater than 165 metres occur over a relatively short distance and so mark the change to the oceanic depths. By comparison, the shelf model tested by Heaps (1969) took the depth at the shelf edge in the west coast sea area, to be 100 fathoms (183 metres), while Cartwright (1968) took the 200 metre contour to define the edge of the continental shelf.

In general the nature and width of the offshore shelf area varies greatly, it being influenced as much by tectonic movements as by sedimentation. In this respect, average characteristics of continental shelves are of little significance to the engineer but the values provided by Shepard (1963) do however give a sense of proportion. These values are shown in figure 9.2 and although smaller than those of the Scottish west coast, the general shape of both bed profiles is similar.

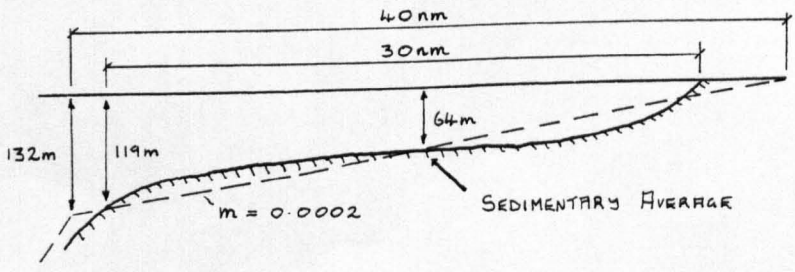

Average Profile of Continental Shelves

Figure 9.2

Mean water depths (in metres) at grid points in Model 4 (DS = 12km, DT = 207 secs). This model schematises the continental shelf off the west coast of Central Scotland.

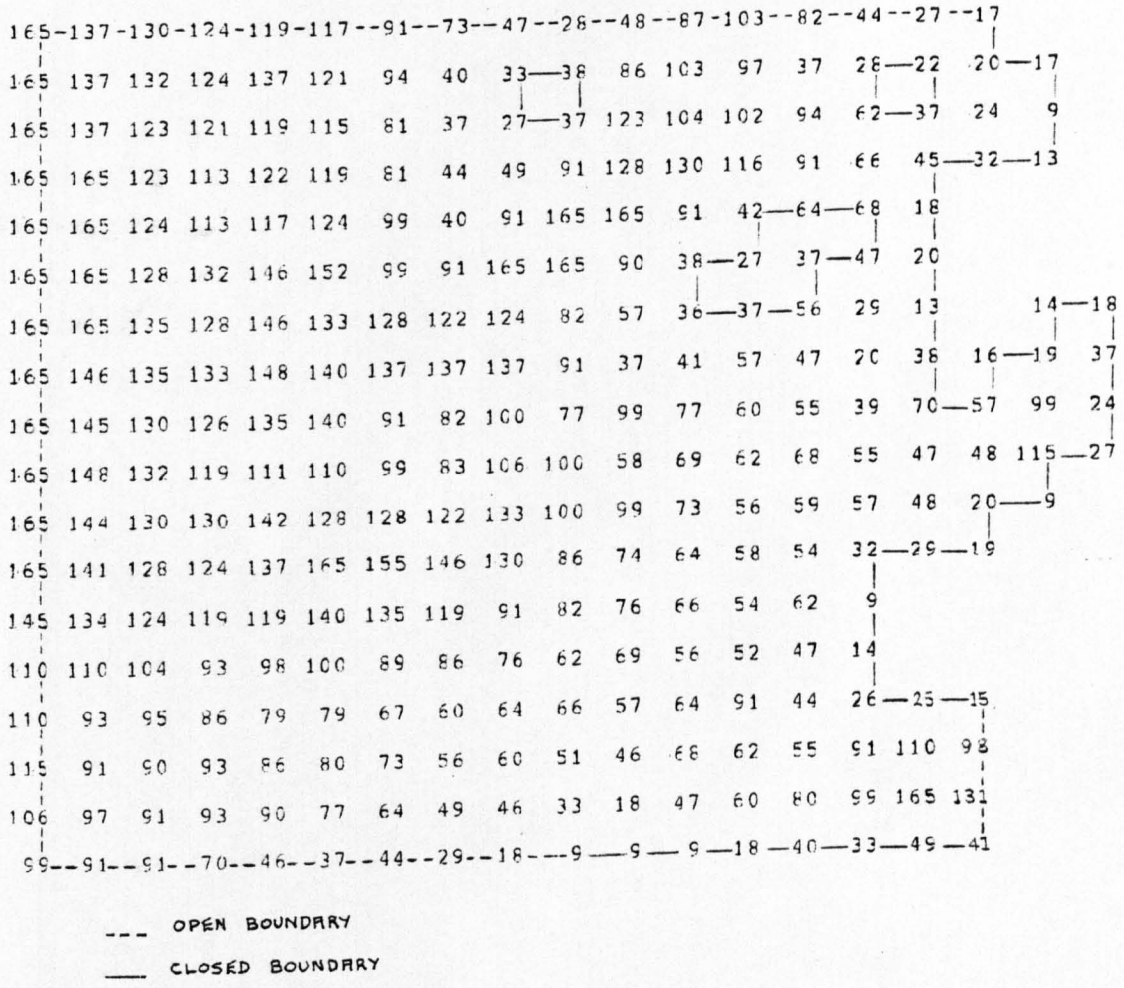

Figure 9.3

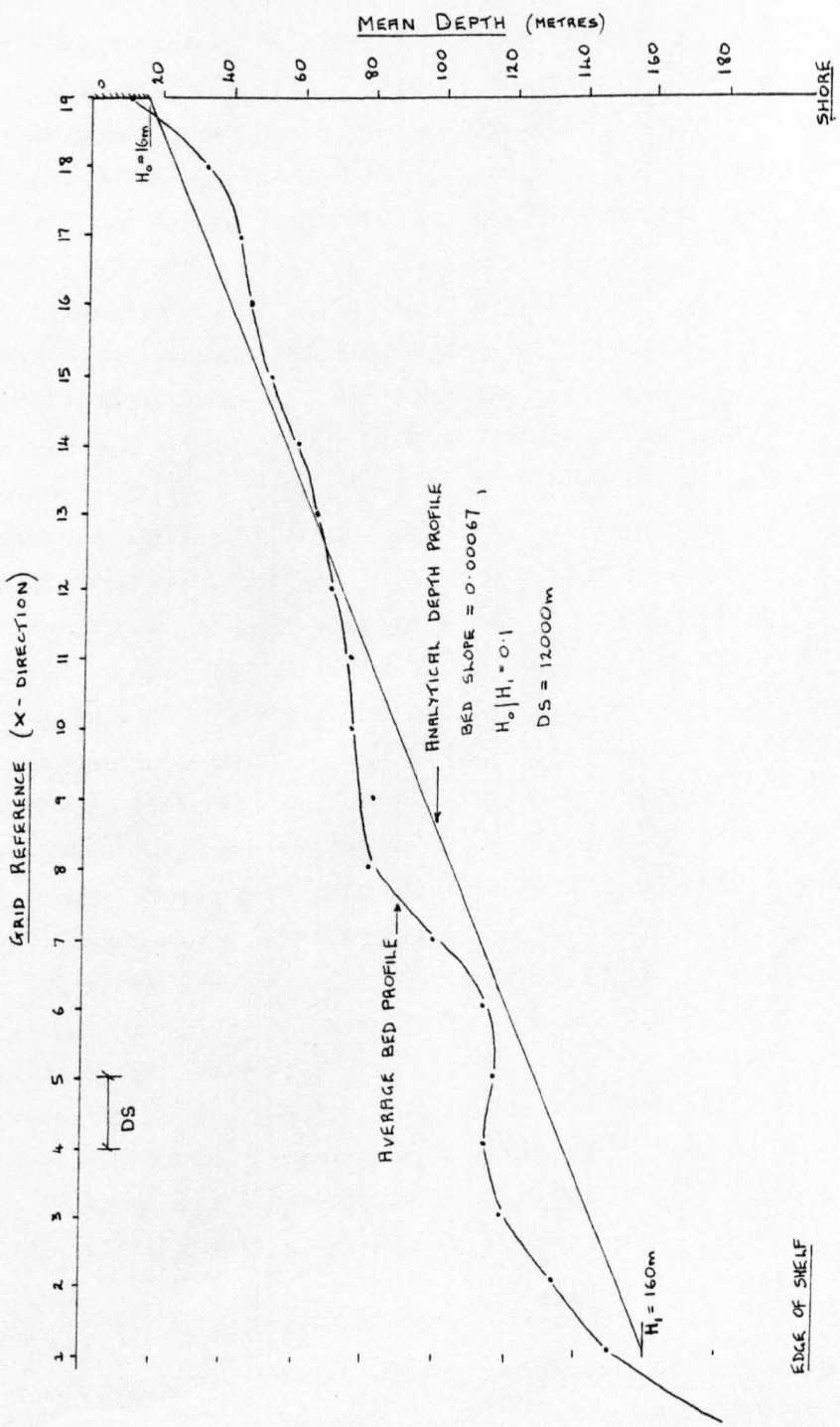

Figure 9.4

Average shelf profile of the west coast of Central Scotland.

The shelf model extends far enough offshore and sufficiently away from the coast so that wind surges generated on the model boundaries can be neglected. On the other hand a very fine computational grid is necessary to resolve the bathymetric irregularities in the complex nearshore area. Ideally then, two models are required; a large shelf model and a smaller, more detailed local model. Surges generated on the ocean model can then be transferred as boundary conditions to the local model. In this way the shelf model, Model 4 with a spacestep of 12 km could have been connected to the Clyde sea area model, Model 2 which has a spacestep of 3 km. The connection between the models could have occurred at the common boundaries namely the western and northern sea boundaries. Linking of the two models was not attempted because the Clyde sea area is susceptible not only to wind surges travelling across the shelf and round the coast of Northern Ireland, but also to wind surges travelling northwards from the Irish Sea. Therefore to fully represent the surge conditions from their origins to the Firth of Clyde, another model extending through the Irish Sea and out to the shelf edge southwest of Ireland is required, in addition to the two existing models. Constructing a model of the Irish Sea out to the shelf edge, in itself poses difficulties because the proximity of coastlines there would require a relatively fine grid, yet the area is too large to model accurately bearing in mind limitations in computer capacity. For this reason the Irish Sea and the part of the Atlantic Ocean extending to the shelf edge off southwest Ireland was not schematised. Instead the shelf model, Model 4 representing the west coast of Central Scotland was developed to verify that a wind surge can be simulated that originates on the shelf. This is shown by comparing the computed surge elevations to the recorded surge measured at coastal locations (outwith the Firth of Clyde) which are susceptible mainly to surges produced by winds with a strong westerly component.

9.3 SIMULATION OF THE MEAN SPRING TIDE

As with previous models, tidal simulation was required primarily because of its inclusion when simulating a surge event but also because it provides a convenient means of calibrating the shelf model. Once again mean spring tide conditions were simulated and then compared to

those provided by co-range, co-phase Chart 5058. The co-range and co-phase lines from the chart covering the area represented by the shelf model are shown in figure 9.5. In the northeast of this area, the co-range lines indicate an increase in range associated with the onshore progression of the tide into an area of decreasing depth. Across the coast of Northern Ireland the opposite occurs; a progressive reduction in range takes place as flow enters the North Channel. The influence of this channel is apparent from the co-range lines and extends out, at least to the area southeast from Malin and Oban. Also the tidal streams through the sea boundary between Port Ellen and Ballycastle Bay are larger than anywhere else in the shelf. As the tide wave moves onshore, it appears to turn anticlockwise in latitudes north of Oban and to move clockwise south of Oban. The anticlockwise advance of the co-range lines is possibly caused by refraction of the tide wave as a result of the shallower depths in the surrounding waters of Barra. Similarly the clockwise movement of the co-range lines possibly results from the influence of shallow depths along the Irish coast although the influence of the North Channel is a much stronger factor.

Good agreement exists between the chart data and the Tide-Table data, for a comparison made at coastal locations. Only in the North Channel, where the change in phase is rapid, notably around Port Ellen and Ballycastle Bay, do the two sources of data disagree. Hence the tidal ranges and phases at the open sea boundary representing the edge of the continental shelf in the model were taken from Chart 5058 and were assumed to be sufficiently accurate to be used as an input to the model. In all the tests the tidal elevations were specified as cosine functions along this sea boundary and the Chezy friction co-efficient was taken as 35 $m^{\frac{1}{2}}/s$ throughout. The Coriolis force was also represented in each tidal simulation.

As an initial attempt to simulate tidal motion across the shelf the schematisation of the model was taken as that shown in figure 9.6. With regards to the schematisation, the most important physical feature was that the open sea boundary in the North Channel was treated as a closed boundary. In the figure, the computed co-range lines lie in a direction almost parallel to the shelf and increase in magnitude on moving shorewards. These characteristics indicate that the shelf system responds similarly to a rectangular channel with one open boundary and

a progressive wave travelling across it. In general the computed ranges are too large and the co-range and co-phase lines display features that are far removed from the chart co-range and co-phase lines shown in figure 9.5. The comparison is poor because the model did not represent the North Channel as an open passage.

The simplest means of transforming the schematisation so as to include an open sea boundary in the North Channel was to position it between Ballycastle Bay and Machrahanish. Tidal elevations and phases were specified as cosine functions in the usual manner at grid points along this boundary. The boundary modifications together with the co-range and co-phase lines drawn from the computations using this schematisation are shown in figure 9.7. These results are a marked improvement in comparison with the co-tidal lines shown in figure 9.6 and show greater similarity with the co-tidal chart data shown in figure 9.5. However the computations of the ranges in the North Channel and in the Sound of Jura are too large in comparison with the chart although the relative magnitudes are similar in both cases. As for the computed phases, they did not reproduce the rapid change of phase in the Sound of Jura associated with the presence of the amphidromic point. It was concluded therefore that it was unrealistic to represent the Sound of Jura in the schematisation since its complex topography and bathymetry could not be accurately represented using the present grid size.

The exclusion of the Sound of Jura in the model was accomplished by positioning the open sea boundary in the North Channel between Port Ellen and Ballycastle Bay. Also the small northern passage to the Sound of Jura has been treated as a closed boundary. With these changes, the co-range and co-phase lines were drawn from the computations and are shown in figure 9.8. These results compare most favourably with those from the chart shown in figure 9.5. The only discrepancy between both sets of results is a minor one and is that the computed phases in the Firth of Lorne near Oban are about thirty minutes later than the chart phases. The difference may be a result of closing the northern passage of the Sound of Jura in the model. Another feature shown on the Admiralty chart is the direction of the five hour co-phase lines which run almost parallel to each other in the sea area west of Islay. The model is incapable of reproducing this phenomenum (if it exists

at all) possibly as a result of the limitations associated with the resolution of the grid. In figure 9.8, the symbols at certain grid points give the positions of coastal locations which are listed in table 9.1. This table gives a comparison at the coastal locations between the computed ranges and phases and those obtained from the Admiralty Tide Tables (1979). The comparison is very good considering the simplicity of the schematisation and the fact that tidal conditions were only specified at the edge of the shelf and not at the northern and southern sea boundaries.

Previous simulations have all included the effect of the Coriolis force since the shelf area is sufficiently large for this effect to be significant. A measure of this effect can be obtained by comparing the results in figures 9.8 and 9.9 since the latter figure was produced without the Coriolis effect. Its effect has been to increase the ranges particularly in the sea area north of Oban. The phases in this area computed with the Coriolis force are also earlier than those without this force. For example the range at Tobermory increased from 3.62 metres to 3.98 metres while the phase changed from 0609 G.M.T. to 0545 G.M.T. on retaining the Coriolis terms. These changes are in accordance with the effect of the Coriolis force which is to shift water eastwards in the Northern Hemisphere.

9.4 SIMULATION OF THE 7TH - 9TH MARCH 1979 STORM SURGE

The resolution of the shelf model has been shown to be sufficiently accurate for simulating the tidal elevations and phases at the coastal locations. Hence the model can be applied with a fair degree of confidence to simulating a surge event. Since the tide-surge elevations have been recorded at Crinan, Port Ellen and Ballycastle Bay during the storm surge of the 7th - 9th March 1979 it appeared logical to consider again this surge event. These surge records have been fully described and reproduced in section 8.5 and so are not recounted in this chapter. However wind and pressure data obtained from the daily weather charts for two additional weather stations, namely Benlecula in the Outer Hebrides and Offshore Weather Station 'L' which is approximately 650 km westwards from the edge of the shelf, were also included as meteorological input to the model. This data augments the existing data from the eight weather stations considered in section 8.5. The wind speeds and directions at both

stations are shown in figure 9.10 for the duration of the storm surge. It is noticeable that at weather station 'L' the wind speeds are much larger than the other relatively more sheltered coastal weather station. However the wind directions at both stations always have a strong westerly component.

It is worth restating that the objective of developing the shelf model was to simulate a surge event without the need to specify the external surge at any of the open sea boundaries. Simulating the mean spring tide using this model has shown that tidal conditions are required as an input at the open sea boundary from Port Ellen to Ballycastle Bay. Therefore when simulating a surge event, both the tide and surge elevations are theoretically required as an input at this boundary. Such a specification of the surge heights is contrary to the objectives of developing this model. However as a first step, the storm surge of the 7th - 9th March 1979 was simulated with the inclusion of the tide-surge elevations specified at the sea boundary in the North Channel. The computed surge levels obtained by removing the computed tide from the total elevations are shown in figure 9.11 at five coastal locations. At Crinan, the computed surge elevations on comparison with the recorded surge shown in figure 8.14 show the same general trend. The computed peak surge is 0.51m occurring at 0300 G.M.T. on the 9th March while the recorded peak surge height is 0.62m at 0100 G.M.T. on the same day. In both cases the positive surge is of long duration without any real distinct maximum and so the term 'peak' is somewhat misleading and is used only to convey the magnitude of the surge. At other coastal locations the general shape and magnitude of the computed surge is similar to that at Crinan. This feature is probably a result of the surge being mainly produced by a widespread change in atmospheric pressure. Thus on the open coastline, as opposed to a confined estuary, the effect of pressure is more significant in comparison to the wind stress effect. In figure 9.11 the maximum computed wind stress effect on elevation is shown at the five ports and occurs between 0000 G.M.T. and 0400 G.M.T. on the 9th March. The total surge was computed from the combined wind and pressure effects, the latter being the more significant.

To some extent, the computed surge elevations throughout the model are dependent on the input of surge elevations at the open sea

boundary in the North Channel. As a means of assessing this dependence the surge simulation was repeated but with only the tidal elevations specified at the North Channel boundary. From this test, the computed surge elevations at Tiree, Crinan and Malin have been plotted in figure 9.11 for comparison with the previous test. At all three ports, the surge heights from both tests are very similar especially during the occurrence of the positive surges, with the elevations from the second test being slightly the smaller. It can therefore be concluded that the absence of surge elevations at the sea boundary between Ballycastle Bay and Port Ellen does not greatly affect the surge computations at other locations. The influence of this boundary on surges is small and a result of the surge generation increasing eastwards and the fact that this boundary lies on the eastern side of the model. This surge generation at Malin for example would not be strongly dependent on the surge height at Ballycastle Bay because the surge currents flowed in an easterly direction.

At the sea boundary in the model representing the connection between the Atlantic Ocean and the North Channel, the ideal condition would be one in which both the unknown velocities and the elevations were calculated in a similar manner as for an internal grid point. In fact such conditions already exist at the northern and southern edges of the shelf model and were present when simulating the mean spring tide and the surge event. The incorporation of this type of boundary at these locations did not present any problems judging from the results of the simulation. However when this type of sea boundary was used for computing the tidal elevations and velocities at the North Channel sea boundary the results were not as required. The test (which has not been presented) showed that the simulation of purely tidal flow out of the model was in accordance with the stream Atlas (1974). The corresponding tidal elevations were also satisfactory. The limitations of this type of boundary appear on the ebb tide, where the flow direction from the North Channel is into the region of the Atlantic Ocean represented by the model. At the grid points along the adjoining sea boundary the computed ebb tide streams are virtually zero while the tidal elevations did not reach their required maximum negative values. It is thought the failure of these sea boundary conditions is related to the fact that flows across this boundary are calculated from a one-sided finite

difference expression. A boundary condition based on central differences in the spatial domain might be preferable but is not possible by virtue of considering boundary points. The effect of one-sided difference terms can be examined on considering the positions of the characteristic and particle paths shown in figure 9.12. The diagrams represent the ebb and flow tide conditions at a grid point on the sea boundary in the North Channel.

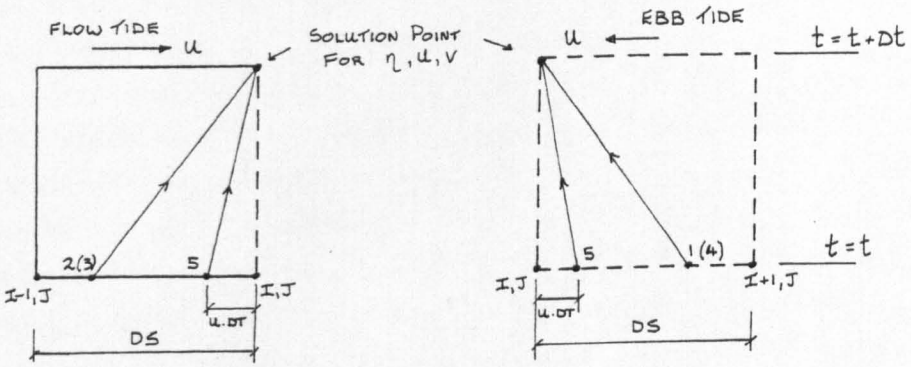

Figure 9.12

During the flow tide the bottom of the characteristic path points 2 and 3 and the particle path point 5 lie within the confines of the model. Therefore the position of the path points can be obtained by interpolating between the known grid point values. Hence by forming the appropriate backward finite difference expressions the elevation and velocities can be calculated at a given time level. With regards to the ebb tide at the same grid point the computations are less straightforward. At a given time level, the particle and characteristic paths lie outside the spatial domain of the model. The necessary forward difference equations therefore cannot be formed and their replacement with the available backward difference expressions appears to give less than satisfactory results.

The inconvenience of not having central differences at this type of sea boundary is also present when computing velocities in other sea boundaries such as along the edge of the shelf model where the tidal elevations are specified. However the effect of calculating both the elevations and velocities at the North Channel sea boundary using one-sided difference schemes appears to compound the errors when simulating inflow into the model. At the northern and southern sea boundaries of

the shelf model, the computation of all three unknown was probably only possible because the tidal flow across these boundaries was very weak and so the errors remained small. In other words, it was reasonable to replace forward differences with backward differences and vice-versa.

It is interesting to note that using a sea boundary with no specifications in the North Channel, tidal outflow from the model was well simulated, therefore this boundary would have been suitable for surge simulation in which the currents are always eastwards. However the surge would require to be simulated without the presence of the tides since the tidal inflow at this boundary cannot be satisfactorily reproduced. As a result of this restriction, this test was not conducted. Instead the more conventional sea boundary with specified elevations was used in the tide-surge computations. However further research should be conducted into improving the open sea boundary conditions especially at boundaries where all three unknown variables are calculated in the model.

PART OF ADMIRALTY CHART NO.5058 SHOWING THE MEAN SPRING TIDE CO-RANGE AND CO-TIDAL LINES IN THE CONTINENTAL SHELF SEA AREA OFF THE WEST COAST OF CENTRAL SCOTLAND.

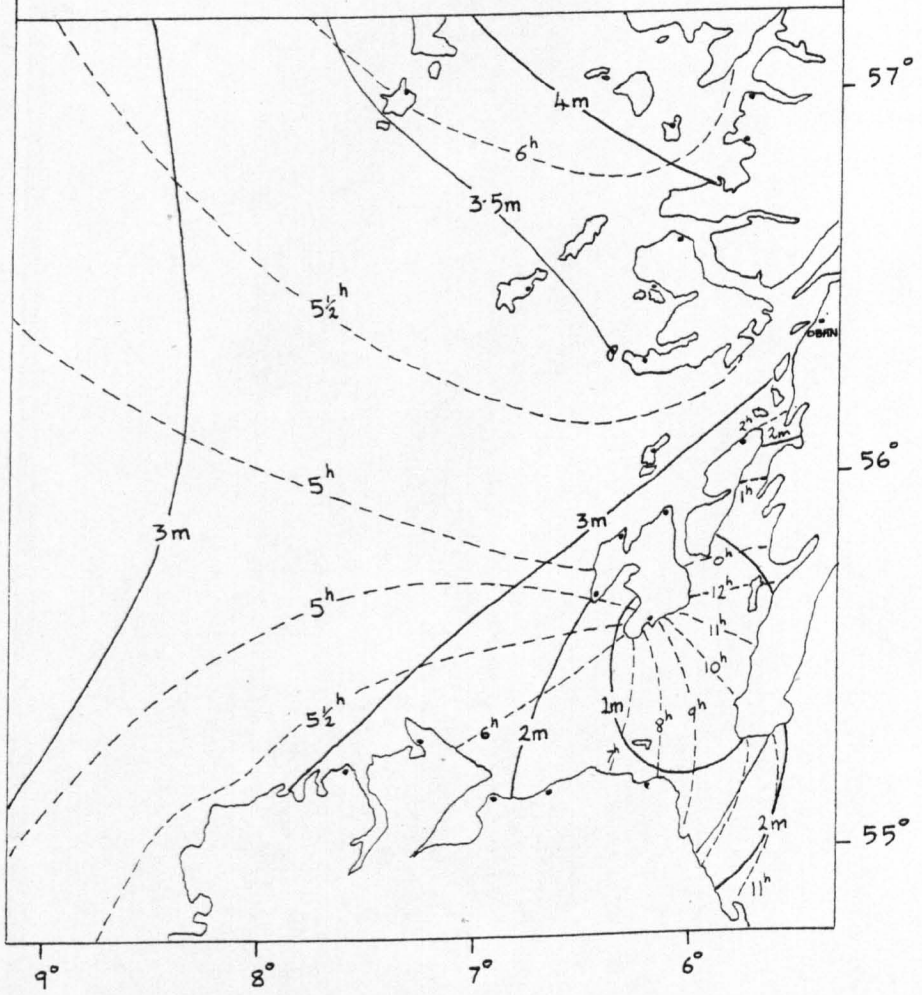

Figure 9.5

Mean spring tide co-range and co-phase lines computed by the shelf model.

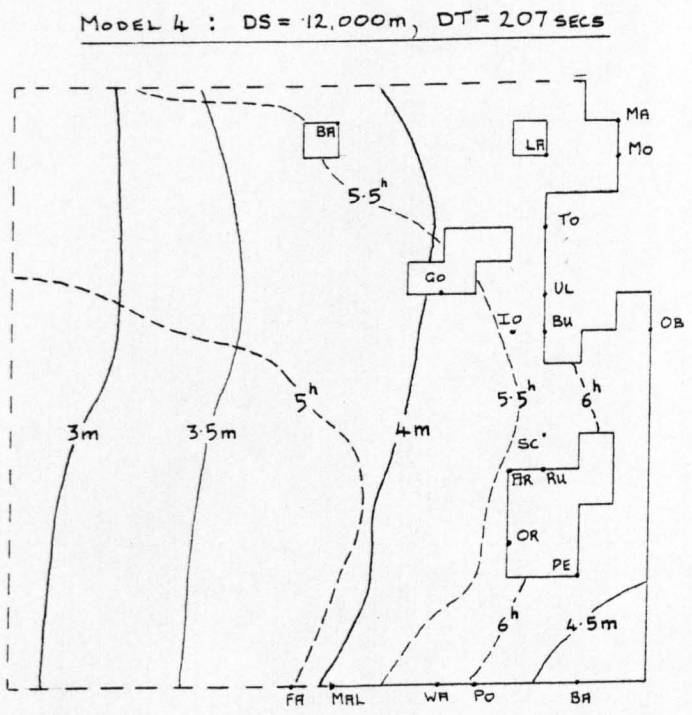

Figure 9.6

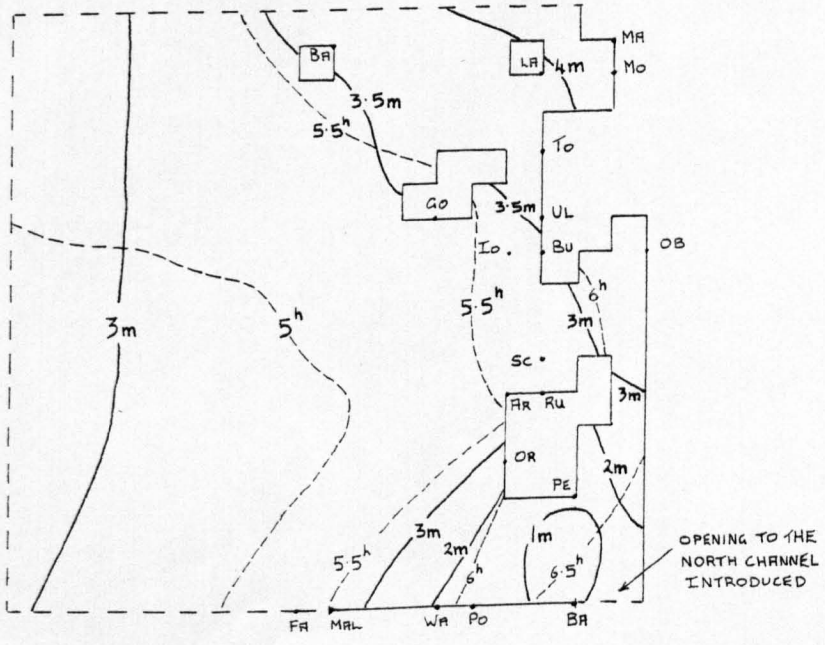

Figure 9.7

Mean spring tide co-range and co-phase lines computed by the shelf model.

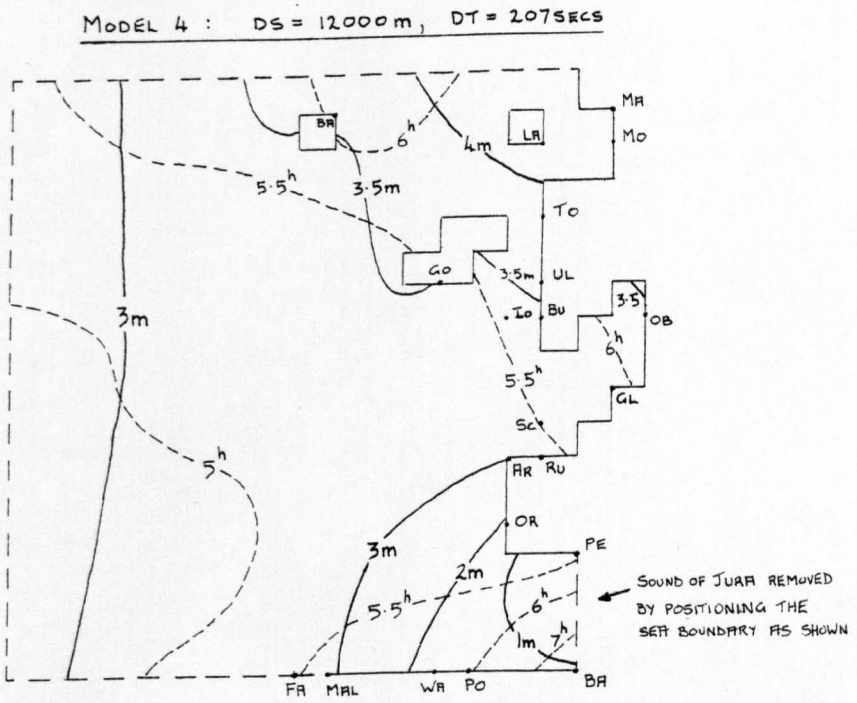

Figure 9.8 (SEE ALSO TABLE 9·1)

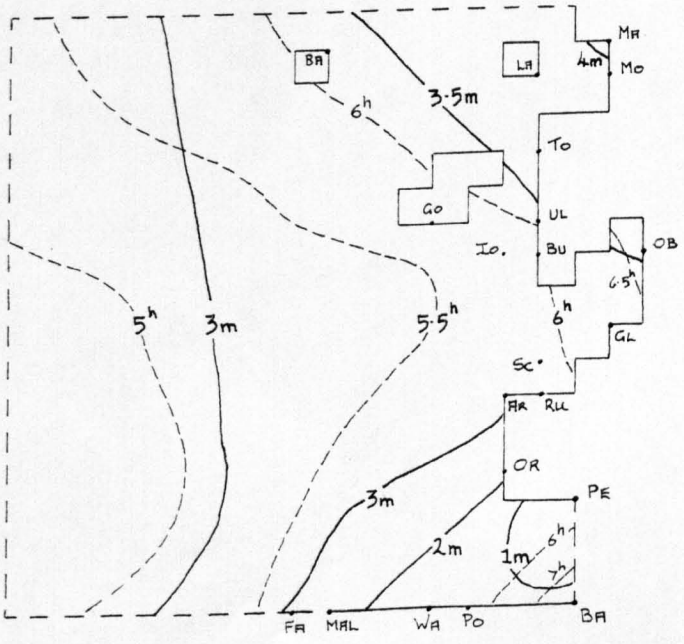

Figure 9.9 (CORIOLIS EFFECT NOT PRESENT)

CONTINENTAL SHELF OF WEST COAST OF CENTRAL SCOTLAND AND NORTHERN IRELAND.

RECORDED AND COMPUTED SPRING TIDE RANGES AND PHASES

Location	Grid Reference	Tide Tables 1979		Computed	
		Range	MHWI	Range	MHWI
		m	Hrs	m	Hrs
Barra North	BA	3.6	0612	3.60	0624
Malaig	MA	4.2	0608	4.40	0549
Bay of Laig, Eigg	LA	4.1	0618	4.15	0541
Loch Moidart	MO	4.3	0602	4.35	0549
Gott Bay, Tiree	GO	3.5	0548	3.52	0517
Tobermory	TO	3.7	0543	3.98	0545
Ulva Sound, Mull	UL	3.8	0533	3.58	0541
Iona, Mull	IO	3.4	0543	3.45	0531
Bunessen, Mull	BU	3.6	0533	3.42	0538
Oban	OB	3.3	0533	3.46	0609
Scalasaig, Colonsay	SC	3.4	0543	3.45	0535
Glengarrisdale Bay	GL	3.1	0548	3.46	0555
Rubna A'Mhail	RU	3.2	0533	3.51	0527
Ardnave Pt, Islay	AR	3.0	0543	3.33	0535
Orsay Is, Islay	OR	2.1	0543	1.95	0514
Port Ellen, Islay	PE	0.6	0500	0.60	0514
Ballycastle Bay	BA	1.0	0700	1.0	0730
Portrush	PO	1.7	0620	1.37	0555
Warren Pt	WA	1.9	0620	1.61	0545
Malin	MAL	3.3	0556	3.32	0556
Fanad Head	FA	3.5	0536	3.51	0521

Table 9.1

Figure 9.10

Surface wind speeds and directions recorded at two weather stations during the 7th - 9th March 1979.

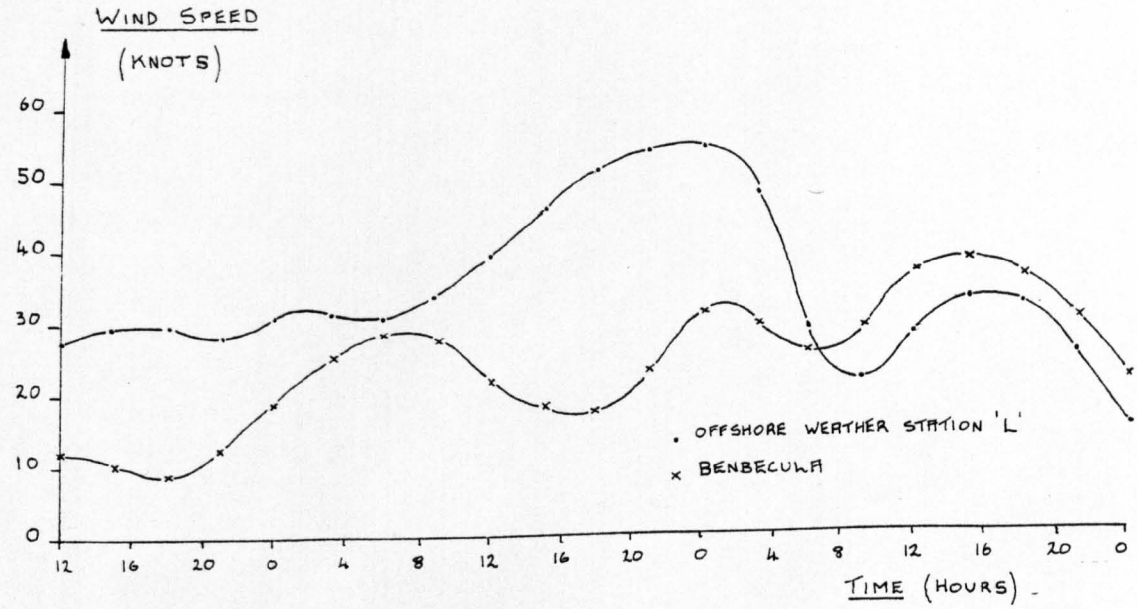

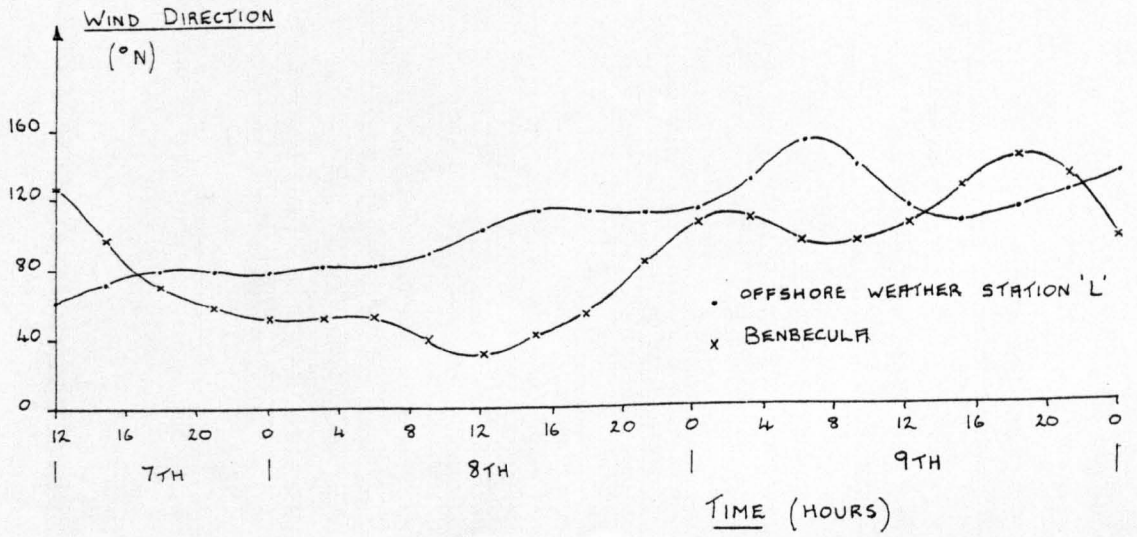

Figure 9.11

Surge elevations for the 7th - 9th March 1979 computed at coastal locations in the shelf model.

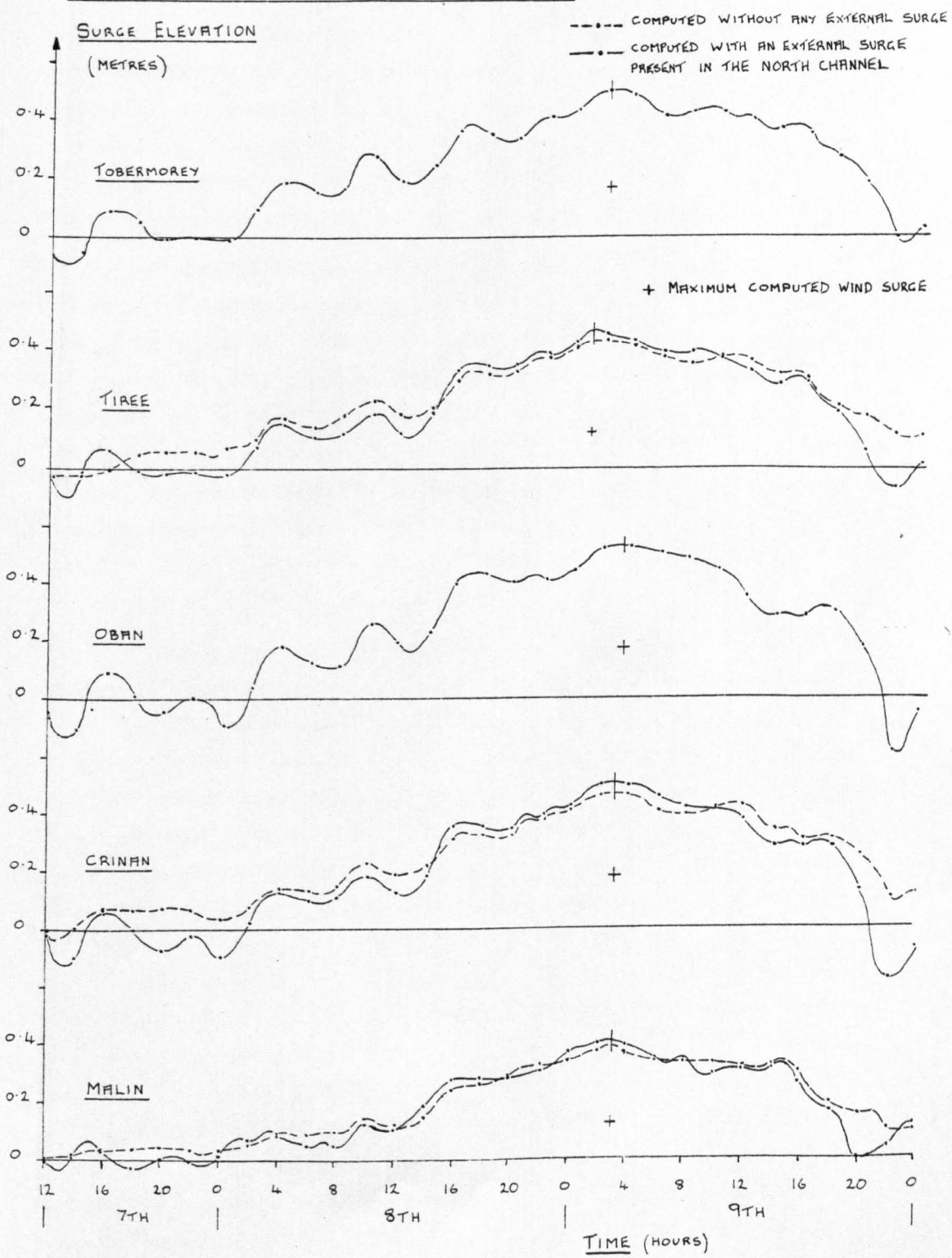

CHAPTER 10
RESULTS AND CONCLUSIONS

The present research has been concerned with the possibility of numerically simulating storm surges in x-y-t space using the method of characteristics. In pursuing this objective it was essential to establish the degree of confidence to be placed in the results of such simulations. It therefore became necessary to place this problem in the wider context of establishing the general reliability of results by using the method of characteristics under a wider variety of circumstances.

The method of characteristics closely follows the wave fronts along which information propagates and so is potentially capable of providing a highly accurate solution. Indeed the theoretical derivation of the characteristic conditions at an internal point has been shown to provide, not in an arbitrary manner, but in a unique way the means of integrating the system of hyperbolic long wave equations. Furthermore it has been shown here and also by Matsoukis (1980) that by introducing a linear interpolation scheme of the form $Q = Ax + By + C$ there results a finite difference scheme which is consistent with the original first-order partial differential equations.

Once the theoretical basis for a numerical scheme was shown to be sound, thereafter any difficulties encountered were necessarily the result of the manner in which the model was applied. It is for this reason that a verification of the model was required. In practice, the CFL criterion is evidently extremely useful in providing both a necessary and sufficient stability condition. In addition, the CFL criterion, at its limiting condition (the equality) provides a very important practical relationship between numerical and physical celerity. In other words it determines the correct size of the domain of dependence of the difference scheme and ensures physical consistency in the model. This requirement has been investigated for free wave oscillations in geometrically simple channels. The tests applied here follow the general philosophy of Liggett and Woolhiser (1967) who stressed the importance of seiches in verifying the accuracy of the integration procedure. Of particular importance was the unimodel seiche in a channel of trapezoidal profile which showed attenuation of the free wave. Since this attenuation did not occur in constant depth cases,

the attenuation was taken to indicate that the domain of dependence of the difference scheme did not accurately represent the differential one. It was also shown that the method of subdivisions could significantly reduce the amount of free wave attenuation in a trapezoidal channel. From a theoretical viewpoint the method's main attractive feature is that it attempts to maintain physical consistency more rigorously than did a system based on no subdivisions of the spacestep. It is concluded from the tests with free waves that the key to successful simulation lies in observing physical consistency and hence the CFL criterion at all times and at all points along the channel. It is from this consideration that the methods of subdivisions offers an interesting line of development for future research. Finally it is concluded that the notion of physical consistency must also be a valid requirement in other explicit numerical techniques.

It was also from free wave considerations that the opportunity arose of testing the accuracy of the integration scheme under conditions of truly two-dimensional flow. The case referred to is the two-dimensional unimodel seiche in a channel of constant depth for which an analytical expression is available for comparison with the model's results. It was in reproducing this analytical solution that it was shown that the boundary equations must be formulated from characteristics with a 45° orientation rather than 90° directions. This result verifies the findings of Matsoukis (1980). It is also evident from any of the analytical tests that the correct orientation of the characteristics is extremely important at the boundary points in achieving an accurate simulation.

The simulation of forced waves, for which analytical solutions were available, showed that highly accurate results were obtained throughout, even in a channel of linearly varying mean depth (trapezoidal profile). It appears that physical consistency at all grid points is not so essential for forced waves as it is for free wave simulation. A possible explanation in the case of forced waves is that physical inconsistency is not readily apparent since temporal attenuation cannot occur in the presence of a forced boundary condition. By virtue of being harmonic, this boundary condition ensures that the disturbances at all other points also have a harmonic variation and in no test was attenuation ever apparent.

A perfect example typifying the relative behaviour of simulated free and forced waves occurred in the simulation of a steady state wind surge in a channel of linearly varying mean depth. The free wave oscillations set up by the initial application of the wind field subsequently attenuated in magnitude whilst the forced component of the surge retained a steady value throughout. In terms of accuracy the simulation of forced waves does not present any major problems to the method of characteristics. This is supported by the simulation of transient surges on a shelf of linearly varying mean depth where, in each case, the maximum surge elevation at the shore was shown to agree favourably with the results obtained from a semi-analytical method presented by Reid (1956). The accuracy of these tests also confirms that the wind stress terms may be incorporated into the characteristic equations in the form of external forces based upon the usual stress coefficients. More generally, the analytical studies of tides and surges in simplified situations have shown most satisfactorily that the method of characteristics is capable of performing the necessary integration of the governing long wave equations.

With the integration procedure verified, attention was then focussed on the tides and surges in the Clyde sea area. Records of large storm surges in the Firth of Clyde had suggested that an examination of the causal factors be undertaken. The establishment of the tidal motion although interesting in itself and possessing some intriguing features was regarded primarily as a means of calibrating the model and evaluating its results before simulating particular storm surges.

Tidal ranges and phases taken from the Admiralty Tide Tables (1979) augmented by similar data from Admiralty Chart 5058 for offshore areas were used as sources of data for tidal simulation in the Clyde sea area. These two data sources disagree substantially in their values of the mean high water interval in the Sound of Jura. A tidal survey, undertaken to resolve this problem, installed tide recorders at Ballycastle Bay, Port Ellen, Crinan and Campbeltown. The tidal records obtained from these ports were shown to be in good agreement with the Tide Table values and so cast considerable doubt on the accuracy of the high water times in the Sound of Jura given by the chart. The tidal survey also provided measurements of the external surge elevations at two sea

boundaries for the period 7th - 9th March 1979. These results were later used as input data for a simulation of the surge during that period.

The schematisation of the Clyde sea area required three open sea boundaries and the optimum spring tide simulation (test 8) was conducted using the tidal records obtained from the survey. These records represented sea boundary elevations in the Sound of Jura and the western approach to the North Channel. The elevations were shown to consist of several harmonic constituents which could not be represented by a single cosine curve. A grid size of 5km and a Chezy friction factor $90m^{\frac{1}{2}}/s$ were also used in test 8. The results, on comparison with the Tide Table data at coastal locations, were found to have a standard deviation of 0.27 metres in range. This value is small in relation to the magnitude of the ranges in the Clyde sea area which have a variation in range from 0.5 metres to 3.1 metres. Similarly the standard deviation of the mean high water intervals was shown to be 37 minutes which is relatively small compared to the six hour variation which occurs in the area.

Evidence has been presented which confirms that an amphidromic point exists in the southern part of the Sound of Jura during total spring tide. This is thought to originate rather from a combination of longitudinal and transverse wave motions and their reflections, than from the more usual causal factor namely the Coriolis force. The model was able to reproduce the very small ranges associated with the amphidromic point, although the anticlockwise phase rotation was not entirely reproduced. This may be one result of having insufficient data along the open sea boundaries. The simulations certainly suggested a heavy dependence on such data.

In general, computed depth averaged velocities were of smaller magnitude than the recorded velocities given in the Admiralty Stream Atlas for certain offshore locations. Only in the relatively shallow waters of the Firth of Clyde where the stream flows do not exceed 0.35 m/s was there an exception to this rule. In this area the maximum velocity (0.31 m/s) was found to be representative of the maximum depth averaged velocity (0.32 m/s) and throughout the tidal cycle both sets of values were of comparable magnitude.

A model of the Firth of Clyde based on a 3km grid spacing was shown to reproduce tidal elevations and velocities accurately. However in this model, the Chezy friction factor of 35 $m^{\frac{1}{2}}/s$ contrasts with the value of 90 $m^{\frac{1}{2}}/s$ used in the Clyde sea area model. The results from the two models confirm the findings of Davies (1979) concerning the friction factor and its dependence on the ratio DT/DTmax. If this ratio is close to unity throughout the model there will be little tidal dissipation which if required is controlled by an appropriate value of the friction factor. This means that the friction factor is not solely physical coefficient and that unfortunately models of this type cannot be used as a means of evaluating the true bottom stress coefficient. A more rigorous assessment of numerical and physical energy loss can only be accomplished by further research into the behaviour of bottom frictional stress and the complete process of tidal dissipation.

Non-linear effects associated with shallow water conditions only affected to a small extent mean water levels and the duration of the ebb and flow tide. The scale of these effects is more the result of shallow depths not being encountered in the Clyde rather than a limitation of the model. A more complete investigation of shallow water effects using the method of characteristics therefore remains as an avenue for future research.

The meteorological requirements associated with a major storm surge on the west coast of the British Isles have been given by Lennon and stated in Chapter 8. These requirements identify the extent and depth of the depression and the region under greatest influence along its track. The meteorological reports from the two storm surges considered in this research substantiated these requirements. From a hydrodynamic viewpoint the records for both surges show that surge characteristics occur almost simultaneously at each port in the Clyde sea area. This suggests that the motion is similar to that of a standing wave. Only the magnitude of the surge varies significantly from port to port and is affected by the local bathymetry and coastline confinement. Surge propagation in the Clyde sea area occurs in this way since the area is relatively small in relation to the size of the depression. A related feature of major storm surges is their long duration, longer than the tidal period and so tide-surge interaction does not unduly complicate identification of the gross surge characteristics.

The meteorological data required for surge simulation was in the form of surface measurements taken at eight weather stations in and around the Clyde sea area. A second-order, least-squares, polynomial interpolation scheme transformed this data into surfaces of pressure, wind speed, and direction for use at each grid point. Such a scheme is thought to be at least as accurate as the original weather station data and so acceptable for the purpose of simulation.

The components of a storm surge in the Firth of Clyde or any other sea area are the atmospheric pressure contribution, the external wind surge and the wind surge over the study area. An assessment of the relative proportions of the surge components for the Firth of Clyde is shown in table 10.1 and is based on the records of the maximum elevations from two storm surges presented in Chapter 8. See p 287

		Atmos Pressure	External Wind Surge at Southern Boundary	Wind Surge Growth in the Firth of Clyde	Greenock Surge
Dec 1972	Surge Elevation. % Greenock Surge	0.34m 22	0.80m 52	0.41m 26	1.55m 100
Mar 1979	Surge Elevation. % Greenock Surge	0.22m 25	0.42m 50	0.22m 25	0.86m 100

Table 10.1

The results in this table for each storm surge are in very good agreement with one another regarding the relative proportions of their components. It is evident that the external wind surge is the largest component constituting approximately 50% of the total surge. The remaining two components have approximately the same proportion namely 25%. A similar analysis of the March 1979 surge in the Clyde sea area taking the external wind surge to occur at the western sea boundary reveals the following proportions; the pressure component was 25% (0.22m), the external wind surge was found to be 36% (0.31m) and the surge growth in the Clyde sea area is therefore 39% (0.33m). All these figures suggest that 25% of the surge growth occurs in the Firth of Clyde and 39% of the surge growth

occurs in the Clyde sea area. Further analysis of storm surge records should be undertaken to assess more accurately the proportions of surge components in the Firth of Clyde and in the Clyde sea area.

It was also shown that the sum of each component's surge effect, simulated individually, was greater than their combined surge effect when simulated together and also greater than the recorded surge. This feature is an interaction effect shown to be related to bottom friction. The same interaction process causes the peak surge simulated in the presence of tides to be smaller than the peak surge simulated in the absence of tides. Any conclusions regarding the magnitude of a positive surge in connection with wind direction were found to agree with intuitive deductions based on the orientation of the Firth of Clyde,

The Clyde sea area model has shown that the external surge is a necessary input and hence that its measurement is required at the open sea boundaries. It is more convenient to simulate the storm surge from its origins by extending the model at least as far as the edge of the continental shelf. A shelf model was developed using a 12km grid size and which complemented the Clyde sea area model. Establishing the accuracy of the surge simulation in the period 7th - 9th March 1979 would have been more straightforward had not an open sea boundary been required to represent the entrance to the North Channel. With regard to this boundary, it was shown as far as possible, that the model satisfactorily reproduced this surge at the few ports where surge records were available for comparison. The limitations of data were not so serious in the tidal simulation which was shown to be accurate at quite a number of coastal locations.

Although it is acknowledged that the results from tide and surge simulations have not provided radically new physical information about the Clyde sea area, it is emphasised that the main objective was verification of the model's accuracy which may only be accomplished using accepted existing information. This verification process was not solely restricted to the simulation of real tides and surges since it also covered the simulation of transient semi-analytical surges and revealed some important conclusions regarding free waves. In the latter case the method of characteristics was able to show, through the idea of physical consistency, the limitations in its application and offered a means of

improving the situation. The verification has finally established beyond doubt that the method of characteristics is an accurate numerical technique for nearly all those forms of long wave motion which were investigated.

APPENDIX A

RESULTS FROM ANALYTICAL TESTS OF CHAPTER 4

1-D FORCED OSCILLATION.
THE ANALYTICAL ELEVATIONS AND VELOCITIES IN A
FRICTIONLESS RECTANGULAR CHANNEL OF CONSTANT DEPTH

$$\eta = \bar{\eta} \cdot \frac{\cos(kx)}{\cos(ka)} \cdot \cos(\sigma t)$$

$$u = \bar{\eta} \frac{c}{H} \frac{\sin(kx)}{\cos(ka)} \cdot \sin(\sigma t)$$

Coords		Elevation		Velocity		M.H.W.I	Coords		Elevation		Velocity	
		t=0,PE,..	t=0.5PE, 1.5PE,..	t=0.25PE, 1.25PE,..	t=0.75PE, 1.75PE,..				Time 0,PE,2PE,.	Time 0.5PE, 1.5PE,.	Time 0.25PE, 1.25PE,.	Time 0.75PE, 1.75PE,.
I	J	m	m	m/s	m/s	Hrs	I	J	m	m	m/s	m/s
1	7	0.200	-0.200	-0.12	0.12	0.0	1	7	0.200	-0.200	0.12	-0.12
3	7	0.217	-0.217	-0.11	0.11	0.0	3	7	0.216	-0.216	0.11	-0.11
5	7	0.232	-0.232	-0.10	0.10	0.0	5	7	0.230	-0.230	0.10	-0.10
7	7	0.245	-0.245	-0.09	0.09	0.0	7	7	0.243	-0.243	0.08	-0.08
9	7	0.256	-0.256	-0.07	0.07	0.0	9	7	0.254	-0.254	0.07	-0.07
11	7	0.266	-0.266	-0.06	0.06	0.0	11	7	0.264	-0.264	0.06	-0.06
13	7	0.273	-0.273	-0.04	0.04	0.0	13	7	0.271	-0.271	0.05	-0.05
15	7	0.279	-0.279	-0.03	0.03	0.0	15	7	0.277	-0.277	0.03	-0.03
17	7	0.282	-0.282	-0.02	0.02	0.0	17	7	0.281	-0.281	0.02	-0.02
19	7	0.283	-0.283	0.00	0.0	0.0	19	7	0.283	-0.283	0.01	-0.01
19	13	0.283	-0.283	0.00	0.0	0.0	20	7	0.283	-0.283	0.0	0.0
19	1	0.283	-0.283	0.00	0.0	0.0	20	13	0.283	-0.283	0.0	0.0
							20	1	0.283	-0.283	0.0	0.0

Table A.1

1-D FORCED OSCILLATION.
THE COMPUTED ELEVATIONS AND VELOCITIES FROM TESTS 1, 2, 3 AND 4 IN A FRICTIONLESS RECTANGULAR CHANNEL OF CONSTANT DEPTH

Coords		Tests 1 and 2 (5th Period)					Test 3 t≤ 0, PE, 2PE...				Test 4 t≤ 0, PE, 2PE...		
I	J	η max	η min	u max	u min	M.H.W.I.	η max	η min	u max	M.H.W.I.	η max	u max	M.H.W.I.
		m	m	m/s	m/s	Hrs	m	m	m/s	Hrs	m	m/s	Hrs
1	7	0.200	-0.200	0.14	-0.10	0.00	0.200	-0.200	0.12	0.0	0.200	0.12	0.0
3	7	0.218	-0.216	0.13	-0.09	12.30	0.217	-0.217	0.11	0.0	0.217	0.11	0.0
5	7	0.234	-0.230	0.12	-0.08	12.25	0.232	-0.232	0.10	0.0	0.232	0.10	0.0
7	7	0.248	-0.243	0.10	-0.07	12.19	0.245	-0.245	0.09	0.0	0.245	0.09	0.0
9	7	0.260	-0.254	0.09	-0.06	12.13	0.257	-0.257	0.07	0.0	0.257	0.07	0.0
11	7	0.270	-0.263	0.07	-0.05	12.07	0.266	-0.266	0.06	0.0	0.266	0.06	0.0
13	7	0.278	-0.270	0.05	-0.04	12.07	0.274	-0.274	0.04	0.0	0.274	0.04	0.0
15	7	0.284	-0.275	0.04	-0.02	12.02	0.279	-0.279	0.03	0.0	0.279	0.03	0.0
17	7	0.287	-0.278	0.02	-0.01	12.02	0.282	-0.283	0.02	0.0	0.282	0.02	0.0
19	7	0.288	-0.279	0.0	0.00	12.02	0.283	-0.284	0.0	0.0	0.283	0.0	0.0
19	1	0.288	-0.279	0.0	0.00	12.02	0.283	-0.284	0.0	0.0	0.283	0.0	0.0
19	13	0.288	-0.279	0.0	0.00	12.02	0.283	-0.284	0.0	0.0	0.283	0.0	0.0

Table A.2

TEST 4 $\left\{ \begin{array}{l} \eta_{MAX} = -\eta_{MIN} \\ u_{MAX} = -u_{MIN} \end{array} \right\}$

1-D FORCED OSCILLATION.
THE COMPUTED ELEVATIONS AND VELOCITIES FROM TESTS 5, 6 AND 7 IN A FRICTIONLESS RECTANGULAR CHANNEL OF CONSTANT DEPTH

Coords		Test 5			Test 6				Test 7		
		t≤ 0, PE, 2PE...			t≤ 0, PE, 2PE...				t≤ 0, PE, 2PE.....		
I	J	η max	u max	M.H.W.I.	η max	η min	u max	M.H.W.I.	η max	u max	M.H.W.I.
		m	m/s	Hrs	m	m	m/s	Hrs	m	m/s	Hrs
1	7	0.200	0.12	0.0	0.200	-0.200	0.12	0.0	0.200	0.12	0.0
3	7	0.216	0.11	0.0	0.216	-0.216	0.11	0.0	0.216	0.11	0.0
5	7	0.230	0.10	0.0	0.230	-0.230	0.09	0.0	0.230	0.09	0.0
7	7	0.243	0.08	0.0	0.243	-0.242	0.08	0.0	0.243	0.08	0.0
9	7	0.254	0.07	0.0	0.254	-0.253	0.07	0.0	0.254	0.07	0.0
11	7	0.264	0.06	0.0	0.263	-0.262	0.06	0.0	0.263	0.06	0.0
13	7	0.271	0.05	0.0	0.271	-0.270	0.05	0.0	0.271	0.05	0.0
15	7	0.277	0.03	0.0	0.276	-0.275	0.03	0.0	0.276	0.03	0.0
17	7	0.281	0.02	0.0	0.280	-0.279	0.02	0.0	0.280	0.02	0.0
19	7	0.283	0.01	0.0	0.282	-0.281	0.01	0.0	0.282	0.01	0.0
20	7	0.283	0.0	0.0	0.283	-0.281	0.0	0.0	0.282	0.0	0.0
20	1	0.283	0.0	0.0	0.283	-0.281	0.0	0.0	0.282	0.0	0.0
20	13	0.283	0.0	0.0	0.283	-0.281	0.0	0.0	0.282	0.0	0.0

TEST 5 $\left\{ \begin{array}{l} \eta_{MAX} = -\eta_{MIN} \\ u_{MAX} = -u_{MIN} \end{array} \right\}$

TEST 7 $\left\{ \begin{array}{l} \eta_{MAX} = -\eta_{MIN} \\ u_{MAX} = -u_{MIN} \end{array} \right\}$

Table A.3

1-D FORCED OSCILLATION.
THE COMPUTED ELEVATIONS AND VELOCITIES FROM TESTS 8, 9 AND 10 IN A FRICTIONLESS RECTANGULAR CHANNEL OF CONSTANT DEPTH

Coords		Test 8				Test 9					Test 10				
		5th Tidal Cycle				5th Tidal Cycle					t≤ 0, PE, 2PE....				
		η max	η min	U max	U min	η max	η min	U max	U min	M.H.W.I.	η max	η min	U max	U min	M.H.W.I.
I	J	m	m	m/s	m/s	m	m	m/s	m/s	Hrs	m	m	m/s	m/s	Hrs
1	7	0.200	-0.200	0.19	-0.14	0.200	-0.200	0.13	-0.10	0.00	0.200	-0.200	0.12	-0.11	0.00
3	7	0.225	-0.261	0.16	-0.12	0.216	-0.216	0.12	-0.09	12.36	0.216	-0.213	0.11	-0.10	0.00
5	7	0.425	-0.298	0.11	-0.10	0.231	-0.230	0.11	-0.08	12.30	0.230	-0.230	0.10	-0.09	12.36
7	7	0.345	-0.283	0.12	-0.10	0.244	-0.242	0.10	-0.07	12.25	0.243	-0.243	0.09	-0.08	12.36
9	7	0.277	-0.276	0.13	-0.09	0.256	-0.254	0.08	-0.06	12.19	0.254	-0.254	0.08	-0.07	12.36
11	7	0.272	-0.269	0.14	-0.10	0.265	-0.264	0.07	-0.05	12.19	0.264	-0.263	0.06	-0.06	12.36
13	7	0.321	-0.316	0.11	-0.07	0.275	-0.273	0.05	-0.04	12.13	0.271	-0.271	0.05	-0.04	12.30
15	7	0.344	-0.270	0.05	-0.04	0.282	-0.278	0.04	-0.03	12.13	0.277	-0.277	0.04	-0.03	12.30
17	7	0.474	-0.389	0.09	-0.09	0.286	-0.282	0.02	-0.02	12.13	0.281	-0.280	0.02	-0.02	12.30
19	7	0.468	-0.430	0.17	-0.18	0.288	-0.284	0.01	-0.01	12.13	0.283	-0.282	0.01	-0.01	12.30
20	7	0.692	-0.491	0.0	0.0	0.289	-0.284	0.0	0.0	12.13	0.283	-0.283	0.0	-0.00	12.30
20	1	7.762	-1.101	0.0	0.0	0.289	-0.284	0.0	0.0	12.13	0.283	-0.283	0.0	-0.00	12.30
20	13	3.975	-7.277	0.0	0.0	0.289	-0.284	0.0	0.0	12.13	0.283	-0.283	0.0	-0.00	12.30

Table A.4

1-D FORCED OSCILLATION.
THE COMPUTED ELEVATIONS FROM TESTS 11 AND 12
IN A RECTANGULAR CHANNEL OF CONSTANT DEPTH

Coords		Test 11					M.H.W.I.	Test 12				
		t=0	PE	2PE	3PE	4PE	4PE	η max	η min	M.H.W.I.	U max	U min
I	J	m	m	m	m	m	Hrs	m	m	Hrs	m/s	m/s
1	7	0.200	0.200	0.200	0.200	0.200	0.00	2.000	-2.00	0.0	1.16	-1.16
3	7	0.210	0.212	0.212	0.213	0.214	12.19	2.158	-2.158	0.0	1.06	-1.06
5	7	0.221	0.222	0.225	0.228	0.230	12.05	2.302	-2.302	0.0	0.95	-0.95
7	7	0.231	0.234	0.238	0.241	0.244	11.96	2.430	-2.430	0.0	0.84	-0.84
9	7	0.242	0.247	0.250	0.253	0.255	11.96	2.541	-2.541	0.0	0.72	-0.72
11	7	0.252	0.258	0.261	0.263	0.265	12.02	2.635	-2.635	0.0	0.59	-0.59
13	7	0.263	0.267	0.269	0.271	0.272	12.07	2.711	-2.711	0.0	0.47	-0.47
15	7	0.274	0.277	0.277	0.277	0.278	12.13	2.768	-2.768	0.0	0.33	-0.33
17	7	0.284	0.285	0.284	0.283	0.283	12.19	2.807	-2.807	0.0	0.20	-0.20
19	7	0.295	0.290	0.288	0.286	0.285	12.25	2.826	-2.826	0.0	0.07	-0.07
20	7	0.300	0.290	0.288	0.287	0.286	12.25	2.828	-2.828	0.0	0.00	0.00
20	1	0.300	0.290	0.288	0.287	0.286	12.25	2.828	-2.828	0.0	0.00	0.00
20	13	0.300	0.290	0.288	0.287	0.286	12.25	2.828	-2.828	0.0	0.00	0.00

Table A.5

1-D FORCED OSCILLATION OF SMALL AMPLITUDE.
A COMPARISON OF ANALYTICAL AND COMPUTED
ELEVATIONS IN A FRICTIONLESS CHANNEL OF
CONVERGING BRIDTH AND CONSTANT DEPTH

Coords		Analytical		Test 13		Test 14 (Elevation)					M.H.W.I.
		η max	M.H.W.I.	η max	M.H.W.I.	t=0	0.25PE	1.25PE	2.25PE	3.25PE	3rd Period
I	J	m	Hrs	m	Hrs	m	m	m	m	m	Hrs
1	6	0.200	0.0	0.200	0.00	0.0	0.200	0.200	0.200	0.200	3.00
3	6	0.207	0.0	0.208	0.06	0.0	0.213	0.208	0.208	0.208	3.11
5	6	0.213	0.0	0.216	0.17	0.0	0.226	0.215	0.215	0.215	3.11
7	6	0.218	0.0	0.222	0.22	0.0	0.235	0.222	0.222	0.222	3.17
9	6	0.222	0.0	0.229	0.28	0.0	0.246	0.229	0.229	0.229	3.39
11	6	0.226	0.0	0.234	0.33	0.0	0.254	0.233	0.233	0.233	3.44
13	6	0.229	0.0	0.238	0.39	0.0	0.261	0.238	0.238	0.238	3.44
15	6	0.232	0.0	0.241	0.44	0.0	0.266	0.241	0.241	0.241	3.50
17	6	0.233	0.0	0.243	0.56	0.0	0.270	0.243	0.243	0.243	3.67
19	6	0.234	0.0	0.244	0.56	0.0	0.273	0.244	0.244	0.244	3.72
20	6	0.235	0.0	0.245	0.56	0.0	0.273	0.245	0.245	0.245	3.78

$\eta = \bar{\eta} \frac{J_o(kx)}{J_o(ka)} \cdot \cos(\sigma t)$.

TEST 13 $\begin{cases} \eta_{MAX} = -\eta_{MIN} \\ u_{MAX} = -u_{MIN} \end{cases}$

TEST 14 $\begin{cases} \eta_{MAX} = -\eta_{MIN} \\ u_{MAX} = -u_{MIN} \end{cases}$ AFTER $t = 2PE$

Table A.6

1-D FORCED OSCILLATION OF SMALL AMPLITUDE.
THE COMPUTED ELEVATIONS FROM TESTS 15 AND 16 IN
A FRICTIONLESS CHANNEL OF CONVERGING BRIDTH
AND CONSTANT DEPTH

Coords		Elevation					M.H.W.I.	Elevation					M.H.W.I.
		t=0	0.25PE	1.25PE	2.25PE	3.25PE	3rd Period	t=0	0.25PE	1.25PE	2.25PE	3.25PE	3rd Period
I	J	m	m	m	m	m	Hrs	m	m	m	m	m	Hrs
1	6	0.0	0.200	0.200	0.200	0.200	3.00	0.0	0.200	0.200	0.200	0.200	3.00
3	6	0.0	0.222	0.210	0.210	0.200	3.06	0.0	0.212	0.208	0.208	0.208	3.06
5	6	0.0	0.241	0.218	0.218	0.218	3.06	0.0	0.226	0.215	0.216	0.216	3.11
7	6	0.0	0.256	0.226	0.226	0.226	3.11	0.0	0.245	0.222	0.222	0.222	3.11
9	6	0.0	0.270	0.232	0.232	0.232	3.17	0.0	0.262	0.229	0.229	0.229	3.17
11	6	0.0	0.283	0.236	0.238	0.238	3.22	0.0	0.271	0.233	0.233	0.233	3.22
13	6	0.0	0.294	0.242	0.241	0.241	3.28	0.0	0.282	0.236	0.239	0.239	3.33
15	6	0.0	0.303	0.246	0.248	0.248	3.28	0.0	0.288	0.240	0.242	0.242	3.44
17	6	0.0	0.308	0.248	0.250	0.250	3.33	0.0	0.296	0.244	0.244	0.244	3.44
19	6	0.0	0.311	0.250	0.252	0.252	3.33	0.0	0.298	0.245	0.245	0.245	3.44
20	6	0.0	0.311	0.250	0.252	0.252	3.33	0.0	0.299	0.242	0.246	0.246	3.44

TEST 15 : $\eta_{MAX} = -\eta_{MIN}$ AFTER $t = 2PE$.

TEST 16 : $\eta_{MAX} = -\eta_{MIN}$ AFTER $t = 2PE$.

Table A.7

1-D FORCED OSCILLATION, FINITE AMPLITUDE.

A COMPARISON OF ANALYTICAL AND COMPUTED ELEVATIONS IN A FRICTIONLESS CHANNEL OF CONVERGENT BRIDTH AND CONSTANT DEPTH

Coords		Analytical			Test 17		
		η max	η min	M.H.W.I.	η max	η min	M.H.W.I.
I	J	m	m	Hrs	m	m	Hrs
1	6	1.00	-1.00	0.0	1.00	-1.00	0.0
3	6	1.04	-1.04	0.0	1.05	-1.05	0.0
5	6	1.08	-1.08	0.0	1.09	-1.09	0.0
7	6	1.11	-1.11	0.0	1.12	-1.12	0.0
9	6	1.13	-1.13	0.0	1.15	-1.15	0.06
11	6	1.15	-1.15	0.0	1.17	-1.17	0.06
13	6	1.17	-1.17	0.0	1.19	-1.19	0.11
15	6	1.19	-1.19	0.0	1.21	-1.21	0.11
17	6	1.20	-1.20	0.0	1.22	-1.22	0.17
19	6	1.20	-1.20	0.0	1.23	-1.22	0.17
20	6	1.20	-1.20	0.0	1.23	-1.22	0.17

Table A.8

1-D FORCED OSCILLATION, FINITE AMPLITUDE.
A COMPARISON OF ANALYTICAL AND COMPUTED
ELEVATIONS IN A FRICTIONLESS CHANNEL OF CONVERGENT
BRIDTH AND CONSTANT DEPTH

Coords		Analytical		Test 18		Test 19	
		η max	M.H.W.I.	η max	M.H.W.I.	η max	M.H.W.I.
I	J	m	Hrs	m	Hrs	m	Hrs
1	4	1.000	0.0	1.000	0.00	1.000	0.00
2	4	1.006	0.0	1.007	0.045	1.007	0.045
3	4	1.012	0.0	1.011	0.09	1.012	0.090
4	4	1.017	0.0	1.016	0.135	1.017	0.135
5	4	1.021	0.0	1.019	0.18	1.022	0.18
6	4	1.025	0.0	1.021	0.225	1.026	0.225
7	4	1.029	0.0	1.021	0.270	1.029	0.270
8	4	1.032	0.0	1.022	0.315	1.033	0.315
9	4	1.034	0.0	1.025	0.315	1.037	0.315
10	4	1.036	0.0	1.028	0.36	1.040	0.36
11	4	1.037	0.0	1.030	0.36	1.041	0.36
12	4	1.038	0.0	1.030	0.36	1.042	0.36
13	4	1.038	0.0	1.031	0.36	1.043	0.36

IN EACH CASE $\eta_{MAX} = -\eta_{MIN}$.

Table A.9

1D FORCED OSCILLATION.
THE ANALYTICAL FREE SURFACES FOR FRICTIONLESS CHANNELS WITH LINEARLY VARYING MEAN DEPTH AND DIFFERING PROFILES

Coords		Triangular Profile		Trapezoidal Profile	
		Elevation	Phase	Elevation	Phase
		t= 0, PE, 2PE...		t = 0, PE, 2PE...	
I	J	m	Hrs	m	Hrs
1	6	1.30	0.0	1.30	0.0
3	6	1.41	0.0	1.41	0.0
5	6	1.53	0.0	1.52	0.0
7	6	1.65	0.0	1.64	0.0
9	6	1.77	0.0	1.75	0.0
11	6	1.90	0.0	1.86	0.0
13	6	2.04	0.0	1.97	0.0
15	6	2.18	0.0	2.07	0.0
17	6	2.32	0.0	2.16	0.0
19	6	2.47	0.0	2.21	0.0

Triangular Profile:- Lamb's Solution $\eta = \bar{\eta} \cdot \dfrac{J_o\left(2k^{\frac{1}{2}}x^{\frac{1}{2}}\right)}{J_o\left(2k^{\frac{1}{2}}a^{\frac{1}{2}}\right)} \cos(\sigma t)$

Trapezoidal Profile:- Chrystal's Solution $\eta = A \cdot \left(Y_1(\sigma\beta) \cdot J_o(\omega) - J_1(\sigma\beta) \cdot Y_o(\omega) \right) \cdot \cos(\sigma t)$

Table A.10

FORCED OSCILLATION IN A FRICTIONLESS CHANNEL WITH LINEARLY VARYING DEPTH.

SUCCESSIVE HIGH AND LOW WATERS FROM TEST 20

Coords		High Water					M.H.W.I.	Low Water			
		t=0	PE	2PE	3PE	4PE	4PE	0.5PE	1.5PE	2.5PE	3.5PE
I	J	m	m	m	m	m	Hrs	m	m	m	m
1	6	1.30	1.30	1.30	1.30	1.30	0.0	-1.30	-1.30	-1.30	-1.30
3	6	1.41	1.43	1.42	1.43	1.43	0.0	-1.41	-1.41	-1.41	-1.41
5	6	1.53	1.56	1.55	1.55	1.56	0.06	-1.51	-1.52	-1.53	-1.52
7	6	1.65	1.69	1.67	1.68	1.69	0.06	-1.62	-1.64	-1.65	-1.63
9	6	1.77	1.83	1.79	1.81	1.82	0.06	-1.73	-1.75	-1.76	-1.74
11	6	1.90	1.96	1.92	1.94	1.95	0.06	-1.84	-1.87	-1.88	-1.85
13	6	2.04	2.08	2.03	2.06	2.07	0.06	-1.95	-1.98	-2.00	-1.96
15	6	2.18	2.20	2.14	2.17	2.19	0.06	-2.05	-2.09	-2.10	-2.06
17	6	2.32	2.28	2.22	2.26	2.28	0.11	-2.12	-2.17	-2.18	-2.13
19	6	2.47	2.31	2.24	2.28	2.29	0.23	-2.14	-2.18	-2.20	-2.15
19	1	2.47	2.32	2.26	2.92	2.30	0.29	-2.15	-2.20	-2.22	-2.17
19	11	2.47	2.30	2.26	2.29	2.30	0.29	-2.15	-2.20	-2.22	-2.17

Table A.11

FORCED OSCILLATION IN A FRICTIONLESS CHANNEL WITH LINEARLY VARYING MEAN DEPTH.

SUCCESSIVE HIGH AND LOW WATERS COMPUTED IN TEST 21

Coords		High Water					M.H.W.I.	Low Water				
		t =0	PE	2PE	3PE	4PE	4PE	0.5PE	1.5PE	2.5PE	3.5PE	4.5PE
I	J	m	m	m	m	m	Hrs	m	m	m	m	m
1	6	1.30	1.30	1.30	1.30	1.30	0.0	-1.30	-1.30	-1.30	-1.30	-1.30
3	6	1.41	1.43	1.42	1.42	1.42	0.0	-1.40	-1.41	-1.41	-1.41	-1.41
5	6	1.53	1.56	1.55	1.55	1.55	0.06	-1.50	-1.52	-1.52	-1.51	-1.51
7	6	1.65	1.70	1.66	1.67	1.68	0.06	-1.60	-1.63	-1.64	-1.62	-1.63
9	6	1.77	1.83	1.78	1.80	1.81	0.06	-1.69	-1.74	-1.75	-1.73	-1.73
11	6	1.90	1.97	1.90	1.92	1.94	0.06	-1.79	-1.84	-1.86	-1.84	-1.84
13	6	2.04	2.10	2.02	2.05	2.06	0.11	-1.89	-1.96	-1.98	-1.94	-1.95
15	6	2.18	2.22	2.12	2.16	2.18	0.11	-1.98	-2.06	-2.08	-2.04	-2.05
17	6	2.32	2.30	2.20	2.24	2.26	0.17	-2.05	-2.12	-2.16	-2.11	-2.13
19	6	2.47	2.34	2.23	2.27	2.29	0.34	-2.06	-2.16	-2.18	-2.13	-2.15
19	1	2.47	2.33	2.22	2.26	2.28	0.40	-2.05	-2.14	-2.17	-2.12	-2.13
19	11	2.47	2.33	2.22	2.26	2.28	0.40	-2.05	-2.14	-2.17	-2.12	-2.13

Table A.12

FORCED OSCILLATION IN A FRICTIONLESS CHANNEL OF LINEARLY VARYING MEAN DEPTH.

SUCCESSIVE HIGH AND LOW WATERS COMPUTED IN TEST 22

Coords		High Water					M.H.W.I.	Low Water				
		t =0	PE	2PE	3PE	4PE	4PE	0.5PE	1.5PE	2.5PE	3.5PE	4.5PE
I	J	m	m	m	m	m	Hrs	m	m	m	m	m
1	6	1.30	1.30	1.30	1.30	1.30	0.0	-1.30	-1.30	-1.30	-1.30	-1.30
3	6	1.41	1.42	1.41	1.42	1.42	0.0	-1.40	-1.42	-1.42	-1.41	-1.41
5	6	1.53	1.54	1.52	1.53	1.53	0.0	-1.50	-1.54	-1.54	-1.53	-1.53
7	6	1.65	1.67	1.63	1.65	1.65	0.0	-1.60	-1.66	-1.66	-1.64	-1.65
9	6	1.77	1.79	1.74	1.77	1.77	0.0	-1.71	-1.78	-1.78	-1.75	-1.77
11	6	1.90	1.91	1.85	1.89	1.89	0.0	-1.81	-1.91	-1.90	-1.87	-1.88
13	6	2.04	2.03	1.95	2.01	2.01	0.0	-1.91	-2.00	-2.00	-1.98	-2.00
15	6	2.18	2.15	2.05	2.12	2.12	0.06	-2.00	-2.15	-2.13	-2.08	-2.11
17	6	2.32	2.25	2.13	2.20	2.20	0.11	-2.06	-2.23	-2.22	-2.16	-2.19
19	6	2.47	2.26	2.15	2.23	2.23	0.11	-2.09	-2.25	-2.24	-2.18	-2.22
19	1	2.47	2.24	2.13	2.21	2.21	0.17	-2.07	-2.24	-2.27	-2.17	-2.20
19	11	2.47	2.24	2.13	2.21	2.21	0.17	-2.07	-2.24	-2.27	-2.17	-2.20

Table A.13

FORCED OSCILLATION IN A FRICTIONLESS CHANNEL WITH LINEARLY VARYING MEAN DEPTH.

SUCCESSIVE HIGH AND LOW WATER COMPUTED IN TEST 23

Coords		High Water					M.H.W.I.	Low Water			
		t=0	1.25PE	2.25PE	3.25PE	4.25PE	4.25PE	0.75PE	1.75PE	2.75PE	3.75PE
I	J	m	m	m	m	m	Hrs	m	m	m	m
1	6	0.0	1.30	1.30	1.30	1.30	3.10	-1.30	-1.30	-1.30	-1.30
3	6	0.0	1.36	1.47	1.41	1.39	3.10	-1.53	-1.35	-1.38	-1.44
5	6	0.0	1.43	1.64	1.52	1.49	3.10	-1.77	-1.51	-1.46	-1.58
7	6	0.0	1.51	1.82	1.64	1.59	3.10	-2.03	-1.62	-1.54	-1.73
9	6	0.0	1.61	2.01	1.76	1.69	3.10	-2.29	-1.75	-1.64	-1.88
11	6	0.0	1.73	2.20	1.89	1.78	3.10	-2.56	-1.88	-1.72	-2.03
13	6	0.0	1.87	2.39	2.00	1.87	3.10	-2.83	-2.01	-1.81	-2.18
15	6	0.0	2.00	2.58	2.11	1.96	3.10	-3.08	-2.15	-1.89	-2.33
17	6	0.0	2.11	2.72	2.21	2.03	3.10	-3.27	-2.25	-1.96	-2.44
19	6	0.0	2.15	2.75	2.22	2.04	3.28	-3.32	-2.27	-1.98	-2.47
19	1	0.0	2.13	2.73	2.21	2.03	3.33	-3.30	-2.25	-1.96	-2.45
19	11	0.0	2.13	2.73	2.21	2.03	3.33	-3.30	-2.25	-1.96	-2.45

Table A.14

FORCED OSCILLATION IN A FRICTIONLESS CHANNEL WITH LINEARLY VARYING MEAN DEPTH .

SUCCESSIVE HIGH AND LOW WATER COMPUTED IN TEST 24

Coords		High Water						M.H.W.I.	Low Water				
		t=0	PE	2PE	3PE	4PE	5PE	4PE	0.5PE	1.5PE	2.5PE	3.5PE	4.5PE
I	J	m	m	m	m	m	m	Hrs	m	m	m	m	m
1	6	1.30	1.30	1.30	1.30	1.30	1.30	0.0	-1.30	-1.30	-1.30	-1.30	-1.30
3	6	1.41	1.42	1.41	1.41	1.41	1.41	0.0	-1.41	-1.41	-1.42	-1.41	-1.41
5	6	1.52	1.55	1.53	1.53	1.53	1.53	0.06	-1.52	-1.52	-1.54	-1.53	-1.53
7	6	1.64	1.67	1.64	1.64	1.65	1.65	0.06	-1.63	-1.64	-1.66	-1.65	-1.65
9	6	1.75	1.80	1.76	1.76	1.77	1.77	0.06	-1.74	-1.75	-1.78	-1.76	-1.76
11	6	1.86	1.93	1.87	1.87	1.89	1.89	0.06	-1.85	-1.87	-1.90	-1.88	-1.88
13	6	1.97	2.06	1.98	1.99	2.01	2.01	0.06	-1.95	-1.98	-2.01	-1.99	-1.99
15	6	2.07	2.17	2.08	2.09	2.12	2.12	0.11	-2.06	-2.08	-2.11	-2.10	-2.10
17	6	2.16	2.26	2.17	2.17	2.20	2.20	0.17	-2.14	-2.16	-2.20	-2.18	-2.18
19	6	2.21	2.28	2.19	2.20	2.23	2.23	0.34	-2.16	-2.19	-2.25	-2.21	-2.20
19	1	2.21	2.27	2.18	2.19	2.22	2.22	0.40	-2.15	-2.18	-2.24	-2.20	-2.19
19	11	2.21	2.27	2.18	2.19	2.22	2.22	0.40	-2.15	-2.18	-2.24	-2.20	-2.19

Table A.15

FORCED OSCILLATION IN A FRICTIONLESS CHANNEL WITH LINEARLY VARYING MEAN DEPTH.

SUCCESSIVE HIGH AND LOW WATERS COMPUTED IN TEST 25

Coords		High Water					M.H.W.I.	Low Water				
		t=0	PE	2PE	3PE	4PE	4PE	0.5PE	1.5PE	2.5PE	3.5PE	4.5PE
I	J	m	m	m	m	m	Hrs	m	m	m	m	m
1	6	1.30	1.30	1.30	1.30	1.30	0.0	-1.30	-1.30	-1.30	-1.30	-1.30
3	6	1.41	1.42	1.41	1.41	1.41	0.0	-1.40	-1.41	-1.41	-1.41	-1.41
5	6	1.52	1.53	1.52	1.52	1.53	0.06	-1.51	-1.52	-1.53	-1.52	-1.52
7	6	1.64	1.66	1.63	1.63	1.64	0.06	-1.62	-1.63	-1.65	-1.64	-1.63
9	6	1.75	1.78	1.75	1.74	1.76	0.06	-1.72	-1.74	-1.77	-1.75	-1.74
11	6	1.86	1.90	1.86	1.85	1.88	0.06	-1.83	-1.85	-1.89	-1.88	-1.85
13	6	1.97	2.02	1.97	1.96	1.99	0.06	-1.94	-1.96	-2.00	-1.98	-1.96
15	6	2.07	2.13	2.07	2.06	2.10	0.06	-2.04	-2.06	-2.11	-2.08	-2.06
17	6	2.16	2.21	2.14	2.13	2.17	0.11	-2.11	-2.14	-2.19	-2.16	-2.14
19	6	2.21	2.24	2.17	2.15	2.20	0.17	-2.14	-2.16	-2.21	-2.19	-2.16
19	1	2.21	2.24	2.17	2.15	2.20	0.23	-2.14	-2.16	-2.21	-2.19	-2.16
19	11	2.21	2.24	2.17	2.15	2.20	0.23	-2.14	-2.16	-2.21	-2.19	-2.16

Table A.16

FORCED OSCILLATION IN A FRICTIONLESS CHANNEL WITH LINEARLY VARYING MEAN DEPTH.

SUCCESSIVE HIGH AND LOW WATERS IN TEST 26

Coords		High Water					M.H.W.I.	Low Water			
		t=0	PE	2.PE	3PE	4PE	4PE	0.5PE	1.5PE	2.5PE	3.5PE
I	J	m	m	m	m	m	Hrs	m	m	m	m
1	6	1.30	1.30	1.30	1.30	1.30	0.0	-1.30	-1.30	-1.30	-1.30
3	6	1.41	1.42	1.41	1.41	1.42	0.0	-1.41	-1.41	-1.42	-1.41
5	6	1.52	1.55	1.53	1.53	1.54	0.0	-1.52	-1.52	-1.53	-1.53
7	6	1.64	1.68	1.65	1.65	1.66	0.0	-1.63	-1.63	-1.66	-1.65
9	6	1.75	1.81	1.77	1.76	1.79	0.0	-1.75	-1.74	-1.78	-1.76
11	6	1.86	1.95	1.89	1.88	1.91	0.0	-1.86	-1.85	-1.91	-1.88
13	6	1.97	2.08	2.01	2.00	2.03	0.0	-1.97	-1.96	-2.03	-2.00
15	6	2.07	2.20	2.12	2.10	2.13	0.0	-2.08	-2.07	-2.15	-2.11
17	6	2.16	2.30	2.20	2.19	2.23	0.0	-2.15	-2.15	-2.24	-2.19
19	6	2.21	2.31	2.20	2.20	2.23	0.0	-2.15	-2.17	-2.25	-2.19
19	1	2.21	2.31	2.20	2.20	2.23	0.0	-2.15	-2.17	-2.25	-2.19
19	11	2.21	2.31	2.20	2.20	2.23	0.0	-2.15	-2.17	-2.25	-2.19

Table A.17

FORCED OSCILLATION IN A FRICTIONLESS CHANNEL OF LINEARLY VARYING MEAN DEPTH.

SUCCESSIVE HIGH AND LOW WATERS COMPUTED IN TEST 27

Coords		High Water					M.H.W.I.	Low Water			
		t=0	PE	2PE	3PE	4PE	4PE	0.5PE	1.5PE	2.5PE	3.5PE
I	J	m	m	m	m	m	Hrs	m	m	m	m
1	6	0.100	0.100	0.100	0.100	0.100	0.0	-0.100	-0.100	-0.100	-0.100
3	6	0.109	0.109	0.109	0.109	0.109	0.0	-0.108	-0.109	-0.109	-0.109
5	6	0.117	0.119	0.117	0.117	0.117	0.0	-0.117	-0.118	-0.118	-0.118
7	6	0.126	0.129	0.126	0.126	0.126	0.0	-0.126	-0.128	-0.127	-0.127
9	6	0.135	0.139	0.135	0.135	0.135	0.0	-0.135	-0.137	-0.136	-0.136
11	6	0.143	0.149	0.144	0.144	0.144	0.0	-0.144	-0.147	-0.145	-0.145
13	6	0.152	0.158	0.152	0.153	0.154	0.0	-0.152	-0.156	-0.153	-0.153
15	6	0.160	0.167	0.160	0.161	0.162	0.11	-0.160	-0.165	-0.161	-0.161
17	6	0.166	0.174	0.167	0.170	0.170	0.17	-0.165	-0.171	-0.167	-0.167
19	6	0.170	0.176	0.168	0.169	0.172	0.34	-0.168	-0.173	-0.170	-0.170
19	1	0.170	0.175	0.167	0.168	0.171	0.40	-0.167	-0.172	-1.168	-0.168
19	11	0.170	0.175	0.167	0.168	0.171	0.40	-0.167	-0.172	-0.168	-0.168

Table A.18

1-D FREE OSCILLATIONS.

THE ANALYTICAL AND COMPUTED ELEVATIONS AND VELOCITIES IN A FRICTIONLESS RECTANGULAR BASIN OF CONSTANT DEPTH

Coords		Analytical Elevations		Analytical Velocities		Coords		Test 28 Computed Elevations				
x	y	t=0,PE,.. m	t=0.5PE,.. m	t=0.25PE 1.25PE,. m/s	t=0.75PE, 1.75PE,. m/s	I	J	t=0 m	PE m	2PE m	3PE m	4PE m
1	7	-0.200	0.200	0.00	0.00	1	7	-0.20	-0.19	-0.18	-0.17	-0.16
3	7	-0.188	0.188	-0.04	0.04	3	7	-0.19	-0.18	-0.17	-0.16	-0.15
5	7	-0.153	0.153	-0.08	0.08	5	7	-0.15	-0.14	-0.14	-0.13	-0.12
7	7	-0.100	0.100	-0.11	0.11	7	7	-0.10	-0.10	-0.09	-0.09	-0.08
9	7	-0.035	0.035	-0.12	0.12	9	7	-0.03	-0.03	-0.03	-0.03	-0.03
11	7	0.035	-0.035	-0.12	0.12	11	7	0.03	0.03	0.03	0.03	0.02
13	7	0.100	-0.100	-0.11	0.11	13	7	0.10	0.09	0.09	0.08	0.08
15	7	0.153	-0.153	-0.08	0.08	15	7	0.15	0.15	0.14	0.13	0.12
17	7	0.188	-0.188	-0.04	0.04	17	7	0.19	0.18	0.17	0.16	0.15
19	7	0.200	-0.200	0.00	0.00	19	7	0.20	0.19	0.18	0.17	0.16

$$\eta = \sum_{m=1} H.\cos\left(\frac{m.\pi.x}{l}\right).\cos(\sigma t), \quad u = H.\frac{c_o}{H}.\sin\left(\frac{m.\pi.x}{l}\right).\sin(\sigma t)$$

Table A.19

1-D FREE OSCILLATIONS.
THE COMPUTED ELEVATIONS FROM TESTS 29, 30, 31 IN A FRICTIONLESS RECTANGULAR BASIN OF CONSTANT DEPTH

Coords		Test 29					Test 30				Test 31			
		Computed Elevations					Computed Elevations				Computed Elevations			
		t=0	PE	2PE	3PE	4PE	PE	2PE	3PE	4PE	PE	2PE	3PE	4PE
I	J	m	m	m	m	m	m	m	m	m	m	m	m	m
1	7	-0.20	-0.20	-0.19	-0.19	-0.18	-0.198	-0.195	-0.191	-0.187	-0.191	-0.182	-0.174	-0.166
3	7	-0.19	-0.18	-0.18	-0.18	-0.17	-0.186	-0.183	-0.180	-0.176	-0.179	-0.171	-0.163	-0.156
5	7	-0.15	-0.15	-0.15	-0.15	-0.14	-0.152	-0.149	-0.146	-0.143	-0.146	-0.139	-0.133	-0.127
7	7	-0.10	-0.10	-0.10	-0.10	-0.10	-0.099	-0.097	0.096	-0.093	-0.095	-0.091	-0.087	-0.083
9	7	-0.03	-0.03	-0.03	-0.03	-0.03	-0.034	-0.034	-0.033	-0.032	-0.033	-0.032	-0.030	-0.029
11	7	0.03	0.03	0.03	0.03	0.03	0.034	0.034	0.033	0.032	0.033	0.032	0.030	0.029
13	7	0.10	0.10	0.10	0.10	0.09	0.099	0.097	0.096	0.093	0.095	0.091	0.087	0.083
15	7	0.15	0.15	0.15	0.15	0.14	0.152	0.149	0.146	0.143	0.146	0.139	0.133	0.127
17	7	0.19	0.19	0.19	0.18	0.18	0.186	0.183	0.180	0.176	0.179	0.171	0.163	0.156
19	7	0.20	0.20	0.20	0.20	0.19	0.198	0.195	0.191	0.187	0.191	0.182	0.174	0.166

Table A.20

1-D FREE OSCILLATIONS.
THE COMPUTED ELEVATIONS FROM TESTS 32, 33 AND 34
IN A FRICTIONLESS RECTANGULAR BASIN OF CONSTANT DEPTH

Coords		Test 32					Test 33				Test 34				
		Computed Elevations					Computed Elevations				Computed Elevations				
		t=0	PE	2PE	3PE	4PE	PE	2PE	3PE	4PE	t=0	PE	2PE	3PE	4PE
I	J	m	m	m	m	m	m	m	m	m	m	m	m	m	m
1	7	-0.200	-0.205	-0.210	-0.215	-0.219	-0.199	-0.198	-0.197	-0.196	-0.200	-0.171	-0.160	-0.152	-0.145
3	7	-0.189	-0.194	-0.199	-0.203	-0.207	-0.188	-0.187	-0.186	-0.185	-0.158	-0.156	-0.148	-0.141	-0.135
5	7	-0.158	-0.162	-0.166	-0.170	-0.173	-0.157	-0.156	-0.155	-0.155	-0.116	-0.116	-0.115	-0.112	-0.108
7	7	-0.109	-0.113	-0.115	-0.118	-0.120	-0.109	-0.108	-0.108	-0.107	-0.074	-0.072	-0.072	-0.072	-0.071
9	7	-0.049	-0.051	-0.052	-0.053	-0.054	-0.049	-0.049	-0.048	-0.048	-0.032	-0.030	-0.030	-0.030	-0.030
11	7	0.017	0.017	0.017	0.018	0.018	0.016	0.016	0.016	0.016	0.010	0.010	0.010	0.011	0.012
13	7	0.080	0.083	0.085	0.086	0.088	0.080	0.080	0.079	0.079	0.052	0.051	0.052	0.054	0.053
15	7	0.135	0.139	0.143	0.146	0.148	0.135	0.134	0.133	0.133	0.095	0.095	0.096	0.094	0.092
17	7	0.176	0.181	0.185	0.189	0.192	0.175	0.174	0.173	0.172	0.138	0.138	0.133	0.127	0.122
19	7	0.197	0.203	0.208	0.212	0.216	0.196	0.195	0.194	0.193	0.179	0.165	0.154	0.145	0.138
20	7	0.200	0.205	0.210	0.215	0.219	0.199	0.198	0.197	0.196	0.200	0.169	0.157	0.148	0.141

Table A.21

1-D FREE OSCILLATIONS.
THE COMPUTED ELEVATIONS AND VELOCITIES FROM TESTS 35, 36 AND 37
IN A FRICTIONLESS RECTANGULAR BASIN OF CONSTANT DEPTH

Coords		Test 35			Test 36				Test 37			
		Elevations		Velocities	Elevations				Elevations			
		t=0,PE,. 2PE,.	t=0.5PE,. 1.5PE,.	t=0.75PE, 1.75PE,.	t=0	PE	2PE	3PE	t=0	PE	2PE	3PE
I	J	m	m	m/s	m	m	m	m	m	m	m	m
1	7	-0.200	0.200	0.00	-0.200	-0.191	-0.183	-0.175	-0.200	-0.112	-0.063	-0.035
3	7	-0.188	0.188	0.042	-0.188	-0.179	-0.172	-0.164	-0.188	-0.105	-0.059	-0.033
5	7	-0.153	0.153	0.078	-0.153	-0.146	-0.140	-0.134	-0.153	-0.086	-0.048	-0.027
7	7	-0.100	0.100	0.105	-0.100	-0.095	-0.091	-0.087	-0.100	-0.056	-0.031	-0.018
9	7	-0.035	0.035	0.120	-0.035	-0.033	-0.032	-0.030	-0.035	-0.019	-0.011	-0.006
11	7	0.035	-0.035	0.120	0.035	0.033	0.032	0.073	0.035	0.019	0.011	0.006
13	7	0.100	-0.100	0.105	0.100	0.095	0.090	0.087	0.100	0.056	0.031	0.018
15	7	0.153	-0.153	0.078	0.153	0.146	0.140	0.134	0.153	0.086	0.048	0.027
17	7	0.188	-0.188	0.042	0.188	0.179	0.172	0.164	0.188	0.105	0.059	0.033
19	7	0.200	-0.200	0.00	0.200	0.191	0.183	0.175	0.200	0.112	0.063	0.035

Table A.22

2-D SEICHE MOTION.

THE ANALYTICAL ELEVATIONS AND VELOCITIES IN A FRICTIONLESS SQUARE BASIN OF CONSTANT DEPTH (ALSO TESTS 38 AND 39)

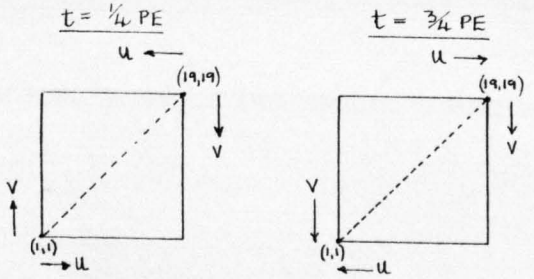

Coords		Elevation	Velocities U,V	Velocities U,V	
		t=0, PE, 2PE,..	$t=\frac{1}{4}PE,\ 1\frac{1}{4}PE,..$	$t=\frac{3}{4}PE,\ 1\frac{3}{4}PE,..$	M.H.W.I.
I	J	m	m/s	m/s	Hrs
1	1	0.200	0.00	-0.00	0.0
2	2	0.194	0.02	-0.02	0.0
3	3	0.177	0.04	-0.04	0.0
5	5	0.117	0.06	-0.06	0.0
7	7	0.050	0.05	-0.05	0.0
9	9	0.006	0.02	-0.02	0.0
10	10	0.000	0.00	0.00	0.0
11	11	0.006	-0.02	0.02	0.0
13	13	0.050	-0.05	0.05	0.0
15	15	0.117	-0.06	0.06	0.0
17	17	0.177	-0.04	0.04	0.0
18	18	0.194	-0.02	0.02	0.0
19	19	0.200	0.00	0.00	0.0

$$\eta = A \cdot \cos\left(\pi \cdot (I-1)/(M-1)\right) \cdot \cos\left(\pi \cdot (J-1)/(N-1)\right) \cdot \cos(\sigma t)$$

Table A.23

2-D SEICHE MOTION.

THE ELEVATIONS COMPUTED IN TESTS 40 AND 41 IN A FRICTIONLESS SQUARE BASIN OF CONSTANT DEPTH

Coords		Elevations from Test 40					M.H.W.I.	Elevations from Test 41				M.H.W.I.
		t=0	0.5PE	PE	1.5PE	2PE	4th Period	t=0	PE	2PE	3PE	4th Period
I	J	m	m	m	m	m	Hrs	m	m	m	m	Hrs
1	1	0.200	-0.199	0.201	-0.198	0.202	0.0	0.200	0.201	0.201	0.201	0.00
2	2	0.194	-0.193	0.195	-0.193	0.195	0.0	0.194	0.194	0.194	0.195	0.00
3	3	0.177	-0.176	0.177	-0.176	0.178	0.0	0.177	0.177	0.177	0.177	0.00
5	5	0.117	-0.117	0.117	-0.117	0.117	0.0	0.117	0.118	0.118	0.118	0.00
7	7	0.050	-0.050	0.050	-0.050	0.050	12.07	0.050	0.050	0.050	0.050	0.00
9	9	0.006	-0.005	0.008	-0.004	0.010	11.38	0.006	0.006	0.006	0.006	0.00
10	10	0.000	-0.001	0.002	-0.002	0.003	11.04	0.000	0.000	0.000	0.000	0.00
11	11	0.006	-0.005	0.008	-0.004	0.010	11.38	0.006	0.006	0.006	0.006	0.00
13	13	0.050	-0.050	0.050	-0.050	0.050	12.07	0.050	0.050	0.050	0.050	0.00
15	15	0.117	-0.117	0.117	-0.117	0.117	0.0	0.117	0.118	0.118	0.118	0.00
17	17	0.177	-0.176	0.177	-0.176	0.178	0.0	0.177	0.177	0.177	0.177	0.00
18	18	0.194	-0.193	0.195	-0.193	0.195	0.0	0.194	0.194	0.195	0.195	0.00
19	19	0.200	-0.199	0.201	-0.198	0.202	0.0	0.200	0.201	0.201	0.201	0.00

$|\text{High Water}| > |\text{Low Water}|$ $|\text{HW}| = |\text{LW}|$

Table A.24

1-D FREE OSCILLATION.

THE ANALYTICAL ELEVATIONS FOR A FRICTIONLESS BASIN OF TRAPEZOIDAL PROFILE

Coords		η max	η min	M.H.W.I.
		t=0, T,...	t = 0.5T, 1.5T,..	
I	J	m	m	Hrs
1	6	-0.10	0.10	2.13
3	6	-0.10	0.10	2.13
5	6	-0.09	0.09	2.13
7	6	-0.07	0.07	2.13
9	6	-0.04	0.04	2.13
11	6	-0.01	0.01	2.13
13	6	0.04	-0.04	0.0
15	6	0.09	-0.09	0.0
17	6	0.14	-0.14	0.0
19	6	0.17	-0.17	0.0

Chrystal's Solution:- $\eta = A \cdot \left(Y_1(\sigma\alpha) \cdot J_0(\omega) - J_1(\sigma\alpha) \cdot Y_0(\omega) \right) \cos(\sigma t)$

Table A.25

1-D FREE OSCILLATION.

THE COMPUTED ELEVATIONS FROM TESTS 42 AND 43

FOR A FRICTIONLESS BASIN OF TRAPEZOIDAL PROFILE

Coords	Elevations from Test 42					M.H.W.I.	Elevations from Test 43					M.H.W.I.
	t=0	0.5T	T	1.5T	2T	3rd Period	t=0	0.5T	T	1.5T	2T	3rd Period
	m	m	m	m	m	Hrs	m	m	m	m	m	Hrs
1 6	-0.10	0.087	-0.035	0.049	-0.029	2.13	-0.10	0.088	-0.067	0.058	-0.046	1.95
3 6	-0.10	0.084	-0.053	0.048	-0.028	2.18	-0.10	0.085	-0.065	0.056	-0.044	1.95
5 6	-0.09	0.075	-0.047	0.043	-0.025	2.18	-0.09	0.075	-0.058	0.050	-0.039	2.01
7 6	-0.07	0.060	-0.037	0.035	-0.019	2.24	-0.07	0.059	-0.046	0.039	-0.031	2.07
9 6	-0.04	0.041	-0.022	0.023	-0.010	2.36	-0.04	0.037	-0.028	0.024	-0.019	2.18
11 6	-0.01	0.006	-0.001	0.010	0.001	2.93	-0.01	0.015	-0.006	0.008	-0.005	2.82
13 6	0.04	-0.031	0.027	-0.016	0.018	0.06	0.04	-0.042	0.027	-0.026	0.020	0.06
15 6	0.09	-0.070	0.057	-0.036	0.034	0.06	0.09	-0.080	0.062	-0.053	0.042	0.06
17 6	0.14	-0.099	0.082	-0.054	0.048	0.06	0.14	-0.113	0.095	-0.076	0.064	0.06
19 6	0.17	-0.107	0.088	-0.059	0.051	0.29	0.17	-0.123	0.104	-0.083	0.070	0.06

Table A.26

1-D FREE OSCILLATION.

THE COMPUTED ELEVATIONS FROM TESTS 44 AND 45

FOR A FRICTIONLESS BASIN OF TRAPEZOIDAL PROFILE

Coords		Elevations from Test 44						M.H.W.I.	Elevations from Test 45				M.H.W.I.
		t=0	0.5 T	T	1.5 T	2 T	2.5 T	3rd Period	t=0	0.5 T	T	1.5 T	3rd Period
I	J	m	m	m	m	m	m	Hrs	m	m	m	m	Hrs
1	6	-0.10	0.09	-0.08	0.08	-0.06	0.06	2.13	-0.10	0.09	-0.08	0.08	2.07
7	6	-0.10	0.09	-0.08	0.07	-0.06	0.06	2.13	-0.10	0.09	-0.08	0.07	2.07
13	6	-0.09	0.08	-0.07	0.07	-0.05	0.05	2.13	-0.09	0.08	-0.07	0.07	2.09
19	6	-0.07	0.07	-0.06	0.05	-0.04	0.04	2.18	-0.07	0.06	-0.06	0.05	2.13
25	6	-0.04	0.04	-0.04	0.04	-0.03	0.03	2.24	-0.04	0.04	-0.03	0.04	2.20
31	6	-0.01	0.02	-0.01	0.01	-0.01	0.01	2.76	-0.01	0.01	-0.01	0.00	2.70
37	6	0.04	-0.03	0.03	-0.02	0.02	-0.02	0.06	0.04	-0.04	0.03	-0.03	0.02
43	6	0.09	-0.07	0.07	-0.06	0.05	-0.04	0.06	0.09	-0.08	0.07	-0.07	0.02
49	6	0.14	-0.12	0.11	-0.10	0.08	-0.07	0.06	0.14	-0.12	0.11	-0.11	0.02
55	6	0.17	-0.14	0.13	-0.11	0.10	-0.08	0.23	0.17	-0.14	0.13	-0.12	0.02

Table A.27

REFERENCES

Abbot, M.B., 1973.
"(Jupiter) A design system for 2-D nearly horizontal flows",
J. Hydraul. Res., Vol.11, No. 1.

Abbot, M.B., 1976.
"Mathematical models in Hydraulics and Coastal Engineering",
Terra et Aqua., No.11, pp.8-17.

Admiralty Tide Tables, 1972. 1979.
"European waters", Vol.1.

Admiralty Tidal Stream Atlas, 1974.
"West coast of Scotland, North coast of Ireland".

Airy, G.B., 1845.
"Tides and waves",
Encyclopedia Metropolitana, London, p.309.

Alembert, J.Le.R.d'., 1747.
"Researches sur differens points importans du systeme du monde".

Baltzer, R.A., and Shen, J., 1961.
"Flows of homogeneous density in tidal reaches",
U.S. Dept. of Interior, Geol. Surv.

Banks, J.E., 1974.
"A mathematical model of a river - shallow sea system
used to investigate tide, surge and their interaction
in the Thames - Southern North Sea region",
Phil. Trans. Roy. Soc., A.275, pp.567-608.

Bretschneider, C.L., 1967.
"Storm Surges",
Advances in Hydroscience, Vol.4, pp.341-418.

Butler, D.S., 1960.
"The numerical solution of hyperbolic systems of partial differential equations in three independent variables",
Proc. Roy. Soc., A.255, p.232.

Cartwright, D.E., 1968.
"Tides and surges round north and east Britain",
Phil. Trans. Roy. Soc., A.263, pp.1-55.

Charnock, H., and Crease, J., 1957.
"North Sea Surges",
Science Prog. Lond., Vol.45, pp.494-511.

Chrystal, G., 1904.
"On the hydrodynamic theory of Seiches",
Trans. Roy. Soc. Edin., 41,(3), pp.579-649.

Chrystal, G., 1906.
"Investigation of Seiches of Loch Earn by the Scottish Loch Survey",
Trans. Roy. Soc. Edinb., 45,(2), pp.382-387.

Coburn, N., and Dolph, C.L., 1949.
"The method of characteristics in the three-dimensional stationary supersonic flow of a compressible gas",
Proc. First. Symp. Appl. Math., Am. Math. Soc., p.55.

Corkan, R.H., 1948.
"Storm Surges in the North Sea",
Vols. 1 and 2, U.S. Hydrographic Office., Misc., 15702, Washington D.C.

Corkan, R.H., 1951.
"Further investigations of North Sea Surges - Storm effects in the Irish Sea",
Rept. Abstr. Commun. Intern. Union Geodesy Geophys., Assoc. Phys. Oceanog. Brussels, pp.71-74.

Courant, R., Friedrichs, K.O., and Lewy, H., 1928.
"Uber die partiellen Differenzialgleichung der mathematischen Physick",
Math. Ann.,Vol.100, p.32.

Courant, R., and Hilbert, D., 1962.
"Methods of mathematical Physics",
Vol.1, Interscience Publications, New York.

Daubert, A., and Graffe, O., 1967.
"Quelques aspects des ecoulements presque horizontaux a deux dimensions en plan et non permanents application aux estuaires",
La Houille Blanche, No.8, p.847.

Davies, M., 1979.
"1-D Characteristics applied to the Severn Estuary and other phenomena",
Unpublished M.Sc. thesis, Strathclyde University.

Deacon, E.L., Sheppard, P.A., and Webb, E.K., 1956.
"Wind profiles over the sea and the drag at the sea surface",
Austral. J. Phys. Vol.9, pp.511-541.

Deacon, E.L., and Webb, E.K., 1962.
"Small scale interaction",
The Sea, Vol.1, pp.43-87, Interscience Publications, New York.

Defant, A., 1961.
"Physical Oceanography",
Vol.II, Pergammon Press, Oxford.

Doodson, A.T., 1956.
"Tides and storm surges in a long uniform gulf",
Proc. Roy. Soc., A.237, p.325.

Doodson, A.T., and Corkan, R., 1932.
"The principle constituent of the tides in the English
and Irish Channels",
Phil. Trans. Roy. Soc., A.234.

Dronkers, J.J., 1964.
"Tidal Computations in Rivers and Coastal Waters",
North Holland. Amsterdam.

Dronkers, J.J., and Schonfeld, J.C., 1955.
"Tidal computations in Shallow Water",
Proc. A.S.C.E., Vol.91, No.714.

Ekman, V.W., 1905.
"On the influence of the earth's rotation on ocean currents",
Ark. F. Mat., Astron. och. Fysik, Vol.2, pp.1-52.

Findlater, J., Harrower, T.N.S., Howkins, G.A., and Wright, H.L., 1966.
"Surface and 900mb wind relationships",
Scient. Pap. Met. Off. London, No.23.

Flather, R.A., 1976.
"Practical aspects of the use of numerical models for surge prediction",
Inst. Oceanog. Scien., Report No.30.

Fox, L., 1966.
"Characteristics in three independent variables",
Advances in Programming and Non-numerical Computation,
Chapt.28, Pergammon Press.

Francis, J.R.D., 1951.
"The aerodynamic drag of a free water surface",
Proc. Roy. Soc., A.206, pp.387-406.

Groen, P., and Groves, G.W., 1962.
"Surges", The Sea, Vol.I, pp.611-646.
Interscience Publications, New York.

Hahn, S.G., 1958.
"Stability criterea for difference schemes",
Commun. Pure and Appl. Math., Vol.11, p.243.

Hansen, W., 1956.
"Theorie zur Errechnung des Wasserstandes und der
Stromungen in Randmeeren nebst Anwendungen",
Tellus, 8., pp.287-300.

Hansen, W., 1957.
"A method of calculation of long period waves",
Proc. Nineteenth Int. Nav. Congress., S2-C1, p.5.

Harcourt, V.L.F., 1889.
"Physical estuary modelling",
Proc. Roy. Soc., Vol.45.

Harris, D.L., 1966.
"Hurricane storm surges",
Hurricane Symp. Amer. Soc. Oceanog. pp.200-224.

Hartree, D.R., 1953.
"Some practical methods of using characteristics in the
calculation of non-steady compressible flow",
U.S. Atomic Energy Comm., Report No. AECU - 2713.

Heaps, N.S., 1965.
"Storm surges on a continental shelf",
Phil. Trans. Roy. Soc., A.257, pp.351-383.

Heaps, N.S., 1967.
"Storm Surges",
Oceanog. Mar. Biol. Ann.Rev., Vol.5., pp.11-49.

Heaps, N.S., 1969.
"A two-dimensional numerical sea model",
Phil.Trans. Roy.Soc., A.265, pp.93-137.

Heaps, N.S., 1973.
"Three dimensional numerical model of the Irish Sea",
Geophs. J.Roy. Astron. Soc., Vol.35, pp.99-120.

Heaps, N.S., and Ramsbottom, A.E., 1966.
"Wind effects on the water in a narrow two-layered lake",
Phil. Trans. Roy. Soc.,A 259, pp.391-430.

Hellstrom, B., 1941.
"Wind effects on lakes and rivers",
Bull. No.41., Inst. Hydraul., Roy.Inst. Technol., Stockholm.

Henderson, F.M., 1966.
"Open Channel Flow", MacMillan Publishers.

Ippen, A.T., 1966.
"Estuary and Coastline Hydrodynamics",
McGraw - Hill Book Co., New York.

Jelesnianski, C.P., 1967.
"Numerical computations of storm surges with bottom stress",
Mon. Weather Rev. Vol.95, pp.740-756.

Katepodes, N., and Strelkoff, T., 1978.
"Computing two-dimensional dam-break flood waves",
Proc. A.S.C.E., Vol.104, Hy9, pp.1269-1288.

Katepodes, N., and Strelkoff, T., 1979.
"Two-dimensional shallow water wave models",
Proc. A.S.C.E., Vol.105, EM2, pp.317-333.

Lai, C., 1965.
"Solution by method of characteristics for flows in tidal reaches",
U.S. Dept. of Interior. Geol. Surv.

Lamb, H., 1932.
"Hydrodynamics",
6th Ed., Camb. Univ. Press, London.

Lax, P.D., 1958.
"Differential equations, difference equations, and matrix theory",
Commun. Pure and Appl. Math., Vol.11, p.175.

Lax, P.D., and Richtmyer, R.D., 1956.
"Survey of the Stability of linear finite difference equations",
Commun. Pure and Appl. Math., Vol.9, p.267.

Le Blond, P.H., and Mysak, L.A., 1978.
"Waves in the Ocean",
Elsevier, Amsterdam, Oxford.

Leendertse, J.J., 1967.
"Aspects of a computational model for long period water wave propagation",
R.M-5294-PR., Rand Corpn., Santa Monica, California.

Leendertse, J.J., 1970.
"A water quality simulation model for well-mixed Estuaries
and coastal seas; Vol.1, Principles of Computation",
RM-6230-RC., Rand Corpn., Santa Monica, California.

Leendertse, J.J., and Lui, S.K., 1975.
"Modelling of three-dimensional flows in estuaries",
In "Modelling Techniques" A.S.C.E., pp.625-642.

Leendertse, J.J., and Lui, S.K., 1978.
"Numerical Modelling of Estuaries and Seas",
Advances in Hydroscience, Vol.11, pp.95-164.

Lennon, G.W., 1963.
"The identification of weather conditions associated with the generation of major storm surges along the west coast of the British Isles",
Quart. Journ. Roy. Met. Soc., Vol.89, pp.381-395.

Liggett, J.A., and Woolhiser, D.A., 1967.
"Difference solutions of the shallow-water equation",
J. Eng. Mech. Div., Proc. A.S.C.E., Vol.93, EM2, pp.39-71.

Lorentz, H.A., 1926.
"Report of the Government Zuiderzee Commission",
Alg. Lansdrukkerij, The Hague.

Lynch, D.R., and Gray, W.G., 1978.
"Analytical solutions for computer flow model testing",
Proc. A.S.C.E., Vol.104, Hy10, pp.1409-1428.

Massau, J., 1889.
"Memoire sur l'integration graphique des equations aux derivees partielles",
Annales Ass. Ingen. Ecoles de Gand, p.95.

Matsoukis, P., 1980.
"The analysis and application of the method of characteristics for simulating long wave propagation in two-dimensional space",
PhD thesis, Strathclyde University.

McIntyre, R.J., 1979.
"Analytical models for west coast storm surges with application to events of January 1976",
Appl. Math. Modelling, Vol.3, pp.80-98.

Meteorological Office,
"Daily weather reports and synoptic charts for the periods 5th Dec 1972 and 7th-9th March 1979."

Milne, P.H., 1971.
"Storm surge research on the Scottish west coast",
Dock and Harbour Auth., Vol.52, No.610, pp.150-152.

Mitchell, A.R. 1969.
"Computational methods in partial differential equations",
Wiley.

Munk, W., 1955.
"Wind stress on water: An hypothesis",
Quart. J. Roy. Met. Soc., Vol.81, pp.320-332.

Myers, V.A., and Overland, J.E., 1977.
"Storm tide frequency",
Proc. A.S.C.E., Vol.103, WW4, pp.519-535.

Prandle, D., 1975.
"Storm surges in the southern North Sea and the River Thames",
Proc. Roy. Soc., A.344, pp.509-539.

Prandle, D., 1978.
"Residual flows in the southern North Sea",
Proc. Roy. Soc., A.359, pp.189-229.

Proudman, J., 1955.
"The propagation of tide and surge in an estuary",
Proc. Roy. Soc. A.231, pp.8-24.

Proudman, J., and Doodson, A.T., 1926.
"Time relations in meteorological effects on the sea",
Proc. Lond. Math. Soc., Vol.24(2), pp.140-149.

Reid, R.O., 1956.
"Approximate response of water level on a sloping shelf
to a wind fetch which moves directly towards shore".,
U.S. Army Corps.

Reid, R.O., and Bodine, B.R., 1968.
"Numerical model for storm surges in Galveston Bay",
Proc. A.S.C.E., Vol.94, WW1, pp.33-57.

Richtmyer, R.D., 1957.
"Difference methods for initial value problems",
Interscience Tracts in Pure and Applied Mathematics, No.4.

Richtmyer, R.D., and Morton, K.W., 1967.
"Difference methods for initial - value problems",
2nd Ed., Wiley, New York.

Riemann, G.F.B., 1860.
"Partielle differentialgleichungen und deren Anwendung
auf Physikalische Fragen: Vorlesungen.

Rossiter, J.R., 1954.
"The North Sea storm surge of the 31st January
and the 1st February 1953",
Phil. Trans. Roy. Soc., A.246, pp.371-400.

Rossiter, J.R., 1959.
"Research on methods of forecasting storm surges on the east and south coasts of Great Britain",
Quart. J. Roy. Met. Soc., Vol.85, No.365, pp.262-278.

Rossiter, J.R., 1961.
"Interaction between tides and surges in the Thames",
Geophys. J. Roy. Ast. Soc., 6, pp.29-53.

Rossiter, J.R., and Lennon, G.W., 1965.
"Computation of tidal conditions in the Thames Estuary by the initial value method",
Proc. Inst. Civil Eng., Vol.31, pp.25-56.

Shepard, F.P., 1963.
"Submarine Geology",
Harper and Row, New York, 2nd edit, p.348.

Sheppard, P.A., 1958.
"Transfers across the earth's surface and through the air above",
Quart. J. Roy. Met. Scc., Vol.84, pp.205-244.

Silvester, R., 1974.
"Coastal Engineering",
Vol.II, Elsevier Scientific Publ. Co., New York, pp.178-190.

Sivaloganathan, K., 1979.
"Channel flow computations using characteristics"
Proc. A.S.C.E., Vol.105, Hy7, pp.899-910.

Stetter, H.J., 1961.
"On the convergence of characteristic finite-difference methods of high accuracy for quasi-linear hyperbolic equations",
Numerische Mathematik, Vol.3, p.321.

Stoker, J.J., 1957.
"Water Waves", Interscience Publications, New York.

Strang, G., 1964.
"Accurate partial difference methods - II. Nonlinear problems",
Numerische Mathematik, Vol.6, p.37.

Sverdrup, H.U., 1942.
"Oceanography for Meteorologists"
Prentice-Hall, Englewood Cliffs, New Jersey.

Taylor, G.I., 1916.
"Skin friction of the wind on the Earth's surface",
Proc. Roy. Soc., A.92, pp.196-199.

Taylor, G.I., 1919.
"Tidal friction in the Irish Sea",
Phil. Trans. Roy. Soc., A.94.

Taylor, G.I., 1920.
"Tidal oscillations in gulfs and rectangular basins",
Proc. London Math. Soc., 20,(2), pp.148-181.

Thorade, H., 1926.
"Flutwellen uber unebenem grund",
Ann. Hydr. Mar. Met., Vol.54., p.217.

Thornhill, C.K. 1948.
"The numerical method of characteristics for hyperbolic
problems in three independent variables",
Aero. Res. Council, Reports and Memoranda No.2615.

Townson, J.M., 1974.
"An application of the method of characteristics to
tidal calculations in 'x,y,t' space",
J. Hydraul. Res., 14(4), pp.499-523.

Vantroys. L., 1959.
"Structure formelle attachee a l'equation due
probleme des marees",
La Houille Blanche., No.5, p.533.

Vardy, A.E., 1977.
"On the use of the method of characteristics for
the solution of unsteady flows in networks",
Proc. of the second Int. conf. on press. surges.
B.H.R.A., Fluid Eng., Bedford, England.

Veltkamp, C.W., 1954.
"De invloed van stationaire windvelden op een
zee van op delen constante diepte",
Math. cent. Amsterdam, Rep., TW24.

Watson, G.N., 1923.
"Theory of the Bessel Function",
Cambridge Univ. Press.

Webster, J.A., 1968.
"An application of the method of characteristics to tidal
computations in estuaries",
Unpublished Ph.D thesis, University of Aberdeen.

Weenink, M.P.H., 1954.
"Bijdrage tot de theorie der opwaaiing in een
baai of randzee bij een inhomogeen windveld",
Koninkl. Ned. Met. Inst., Met. Rapp. Stormvloed 1, pp.40-57.

Wiggert, D.C., and Sundquist, M.J., 1977.
"Fixed grid characteristics for pipeline transients",
Proc. A.S.C.E., Vol.103, Hyl2, pp.1403-1416.

Wilson, B.W., 1960.
"Note on surface wind stress over water at
low and high wind speeds",
J. Geophys. Res., 74, pp.444-455.

Wilson, B.W., 1972.
"Seiches",
Advances in Hydroscience, Vol.8, pp.1-94.